EPITAXIAL GROWTH OF SILICON ON OXYGEN IMPLANTED SUBSTRATES

By

Kalyankumar Das

A thesis submitted in partial fulfilment
of the requirements for the degree of
Doctor of Philosophy
of the Council for National Academic Awards
October 1982

Microelectronics Centre
Middlesex Polytechnic

Collaborating Establishment:
University of Kent at Canterbury.

ACKNOWLEDGEMENTS

The author would like to express his sincere gratitude to the following who contributed in various ways towards a successful completion of the programme of study undertaken.

Dr. J.B. Butcher for providing supervision, taking a keen interest in the work and securing continued financial support throughout the tenure of the programme.

Dr. K.V. Anand for originating the concept upon which the study was based, his critical assessment of progress as an external supervisor, providing motivation and a sense of direction.

R. Nuttall of Electrogas Systems for his help in redesigning and commissioning the epitaxial reactor.

Dr. E. Franks for his advice and assistance in running the epitaxial reactor.

The late R. A. Sinclair for providing the initial tuition on electron microscopy and diffraction work and creating a lasting interest in these techniques.

K.E.G. Pitt for his interest in the work and providing a background on infra-red absorption spectroscopy of silicon oxides.

Dr. J.E. Penney for permitting the use of an infra-red spectrophotometer and his comments on the results.

Professor K.G. Stephens, Department of Electronic and Electrical Engineering, University of Surrey, for providing the facilities of their Accelerator Laboratory.

Drs. P.L.F. Hemment and D W Wellby for their advice and assistance with the implantation and Rutherford back-scattering experimental work and help with the interpretation of results at the early stage.

Dr.G.R. Booker and M.C. Wilson, Department of Metallurgy and Science of Materials, University of Oxford for the transmission electron microscopy work.

Drs. R.H. West and J. Castle, Department of Metallurgy and Materials Technology, University of Surrey, for the Auger electron spectroscopy work.

T.J. Distler, J.F. Sheridan and G.V. Rouse, Harris Semi-conductor Products Division, Melbourne, Florida, for the low-pressure anneal treatment and spreading resistance measurement.

D.G. Hart, Plessey Allen Clark Research Centre, Caswell for the X-ray topography work.

Dr.P. Arrowsmith, BTRL, for his interest in the work and his advice and assistance in the device processing work.

I. Rafferty for his assistance in setting up the epitaxial reactor.

J. Benstead for the construction of the reflection electron diffraction specimen holder.

C H Freshwater and E.W. Lee for their assistance with the electron microscopy work.

G P Shorthouse, J.F. Linnell, Dr. P.J. Revell, M.P. Taylor, Miss S. Haywood, Mrs. L.Sless, S. McClelland, J. Mynard (University of Surrey), M. Chapman (University of Surrey) for their assistance, in the experimental work and in the preparation of the manuscript, so willingly provided.

Mrs. V. Norman for typing the manuscript with great care and patience.

Finally, the author's wife, Mandira, who made it all possible.

The programme was supported by the Science and Engineering Research Council and the Advanced Computer Technology Projects unit of the Department of Industry.

CONTENTS

ABSTRACT

The feasibility of growing epitaxial layers of silicon on silicon substrates with a buried oxide layer formed by the implantation of oxygen ions, has been studied.

Conditions for epitaxial growth from a silane source in a reactor, built and commissioned as a part of the programme, have been established.

Buried implanted oxide layers have been formed by high dose implantation of oxygen ions in silicon. The effects of dose at a given energy, energy for a given peak concentration, and temperature on the distribution profile of oxygen have been studied. An approximate Gaussian distribution is observed at doses contributing less than the stoichiometric requirement of oxygen for the formation of silicon dioxide. A saturation in the oxygen content is reached when the stoichiometric requirement is exceeded. A consequent reduction in the interface damage is also observed. Other parameters being equal, at higher substrate temperatures the interface damage is decreased.

It has been attempted to optimise conditions for a dose of 1.4×10^{18} $O^{+}.cm^{-2}$ at 200 keV which provides the stoichiometric concentration only at the peak of the distribution.

The epitaxial layers deposited on substrates maintained at $\sim 550^{\circ}C$ during implantation have a crystalline quality comparable to those of layers on untreated substrates. Fabricated p-n junction diodes have low leakage currents and high breakdown voltages. The minority carrier lifetime is comparable to that in diodes processed similarly but without an implanted oxide layer.

INTRODUCTION

Initially the objective of the programme was to study the feasibility of depositing device quality silicon epitaxial layers on oxygen implanted substrates. Having successfully demonstrated the feasibility the objective shifted towards optimisation of the implantation conditions enabling subsequent epitaxial deposition and developing an understanding of the physical processes involved during implantation. Electrical evaluation of the layers and fabrication of devices were not considered to be the primary objective. However, some preliminary measurements were made on diode structures.

A thin layer of crystalline silicon on a dielectric substrate is highly desirable as the starting material for the fabrication of integrated circuit devices. The feasibility of an alternative to the presently available techniques for achieving this has been studied. A buried dielectric layer was formed in a single crystal silicon substrate by high dose implantation of oxygen ions. An epitaxial layer subsequently grown produced a silicon/oxide/silicon structure and enabled the fabrication of

of active devices. Since it involves only homoepitaxy of silicon on silicon substrates, the structure should at least be free from mismatch defects other than those arising from the oxygen implantation. The orientation of the epitaxial layer should be the same as that of the substrate crystal. For CMOS devices a final structure as shown in Fig. I.1. is proposed. In bipolar circuits, lateral isolation could be obtained by various means, e.g. by forming countersunk oxide trenches around the active areas, as indicated in Fig. I.2.

As a part of the present programme, as epitaxial reactor was set up, commissioned and growth conditions were studied. Subsequently, oxygen implantation, annealing and epitaxial deposition on appropriately annealed samples were carried out and evaluated.

In the first chapter various aspects of epitaxial deposition of silicon on silicon substrates (autoepitaxy or homoepitaxy are reviewed. A description of the reactor, the experimental details, growth conditions and an analysis of the growth data are given in the second chapter. The

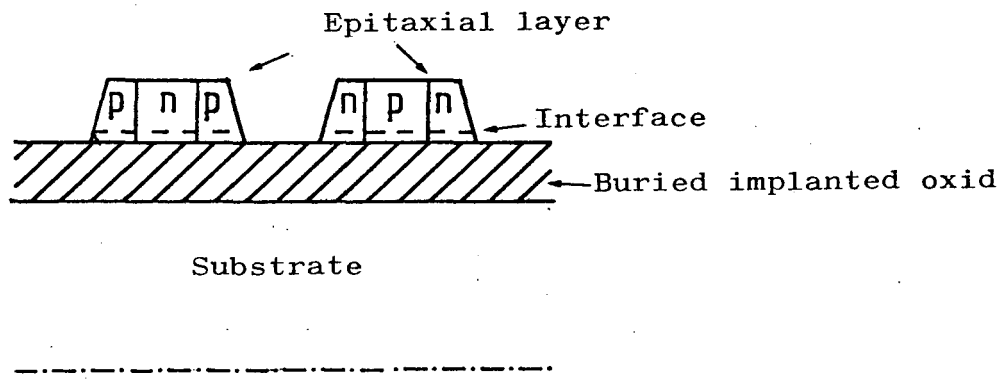

Basis for

Fig I.1. /CMOS device structure in the epitaxial layer deposited on substrates with buried implanted oxides.

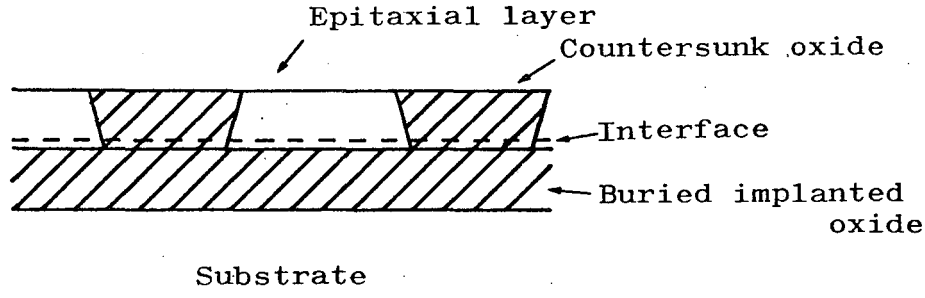

Fig. I.2. Countersunk oxide lateral isolation.

later chapters are concerned with oxygen implantation, anneal treatment, assessment techniques and, finally, with measured electrical characteristics.

In the following paragraphs dielectrically isolated structures currently in use and those being developed by others are considered in brief.

In the 'classical' dielectrically isolated process,[1] islands of single crystal silicon surrounded by thermally grown silicon dioxide, are used for the fabrication of the active devices. A thick layer of polycrystalline silicon acts as a substrate. Although a high degree of isolation between components is obtainable, the process is complex and expensive.

Epitaxially deposited silicon on single crystal sapphire substrates (SOS)[2] has been used for the fabrication of MOS type devices[3]. These devices are almost free from parasitic elements. Unfortunately, due to mismatch of the crystallographic planes of sapphire and silicon, a high density of misfit dislocations, stacking faults and micro-twins[4] is generated at the interface, resulting in low carrier lifetimes and mobilities[5]. Certain upgrading treatments have improved the quality of the silicon films[6,7] but it still falls short of the requirements for dynamic logic and bipolar applications.

A novel dielectrically isolated structure based on oxidized porous silicon has been reported by Imai[8]. The surface layer of a p-type substrate with n^+ areas formed by diffusion or implantation is exposed to an anodizing treatment using concentrated hydrofluoric acid as the electrolyte. The p - type material surrounding and underlying the n islands is converted into porous silicon leaving the n^+ areas unaffected. Subsequently the substrates are oxidized.

The porous silicon oxidizes at a much faster rate than the single crystal n - type islands, resulting in complete isolation of the islands by porous oxide. For CMOS applications, selected p-type areas are temporarily converted to n-type by proton implantation and activation at a temperature between 300&500°C. Following anodization the proton implanted regions are reconverted to p-type by annealing at a temperature above 700°C. The resulting structure is shown schematically in Fig. I.3. It is believed that there are problems associated with the surface planarity of the structure.

A considerable amount of effort is also being directed towards developing an alternative structure consisting of a recrystallized layer of deposited amorphous or polycrystalline silicon on thermally oxidized silicon substrates. Large grain polycrystalline silicon has been obtained from amorphous or fine grain polycrystalline silicon by scanned laser [9,10] or electron beam[11] induced heating, in some cases involving localised melting. Various schemes have been employed to orientate the layer in the desired direction. Lateral epitaxial regrowth[12,13] of strips ~ 80μm x 30μm has been obtained from exposed areas of the single crystal substrate as indicated in Fig. I.4. Amorphous silicon films have been recrystallized into crystallites of average grain size of ~100μm by laser annealing in conjunction with a technique known as graphoepitaxy, in which a surface relief structure is employed to orientate the crystallites in the desired direction[14]. A temperature slightly below the melting point of silicon and a thin layer of silicon dioxide as a cap are required for graphoepitaxy. Crystallites of an average size of a few millimetres have been formed by graphoepitaxy using rapid heating to a temperature between 1100° & 1300°C using carbon strip heaters above and below the sample[15].

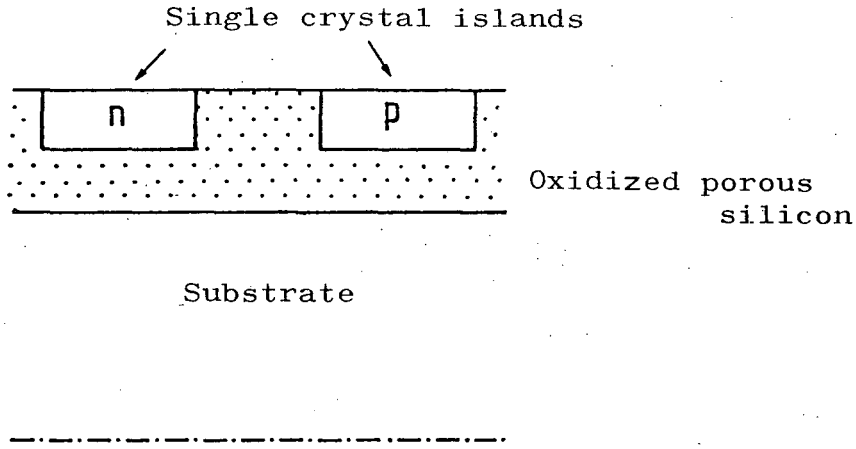

Fig. I.3. Isolation by oxidized porous silicon

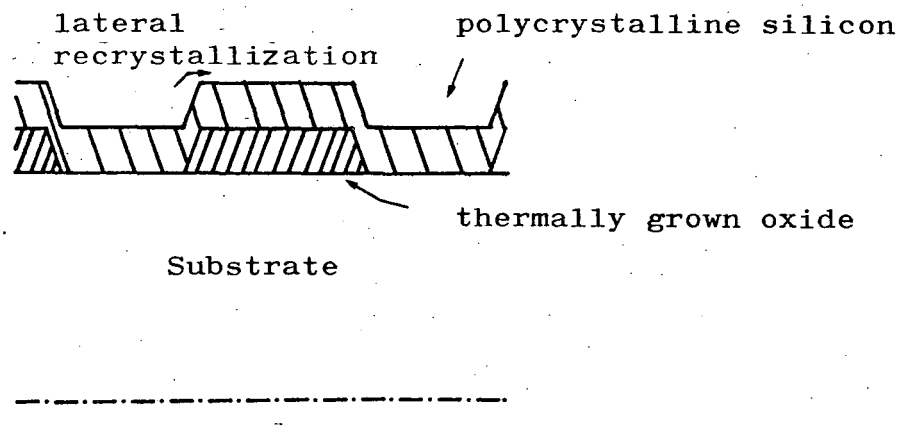

Fig. I.4. Structure employed for lateral epitaxial recrystallization.

Observation of (100) oriented crystalline areas typically ~ 2 mm x 1 cm, has been reported[16], formed by a moving melt zone recrystallization technique without any lateral seeding or a surface relief structure on the substrate surface. The structure, as shown in Fig. I.5, is placed on a carbon strip heater and a thin movable heater strip is used for translating the molten zone across the sample. An MOS channel mobility of 520 cm^2/V Sec has been obtained from the recrystallized material produced by this technique. Characteristics of MOS transistors fabricated in laser recrystallized materials have also been reported[17,18] but these are not as good as those of the melt zone recrystallized material. Vertically stacked CMOS transistors with a common gate,using laser recrystallized material, have also been reported[19,20]. One of the transistors is fabricated in the single crystal substrate and the other directly above in the recrystallized material on the common gate oxide.

A dielectrically isolated structure, based on a buried implanted nitride layer and a subsequently grown epitaxial layer, has also been reported[21]. However, electrical characteristics of this structure are not available.

Formation of oxides by the implantation of oxygen in silicon has been studied and it was suggested that the buried oxide layers could also be used for dielectric isolation in integrated circuits[22]. This served as the basis for the present investigation. Earlier work on oxygen implantation has been reviewed in Sec. 3.1. During the course of this programme characteristics of devices fabricated in the epitaxial layer deposited on substrates with buried implanted oxide layers have been reported (See Chapter 5) mainly by a group in Japan. However, implantation conditions and process details have not been available. It has, therefore, been attempted here to establish conditions necessary to obtain reproducible results and develop an understanding of the physical processes involved.

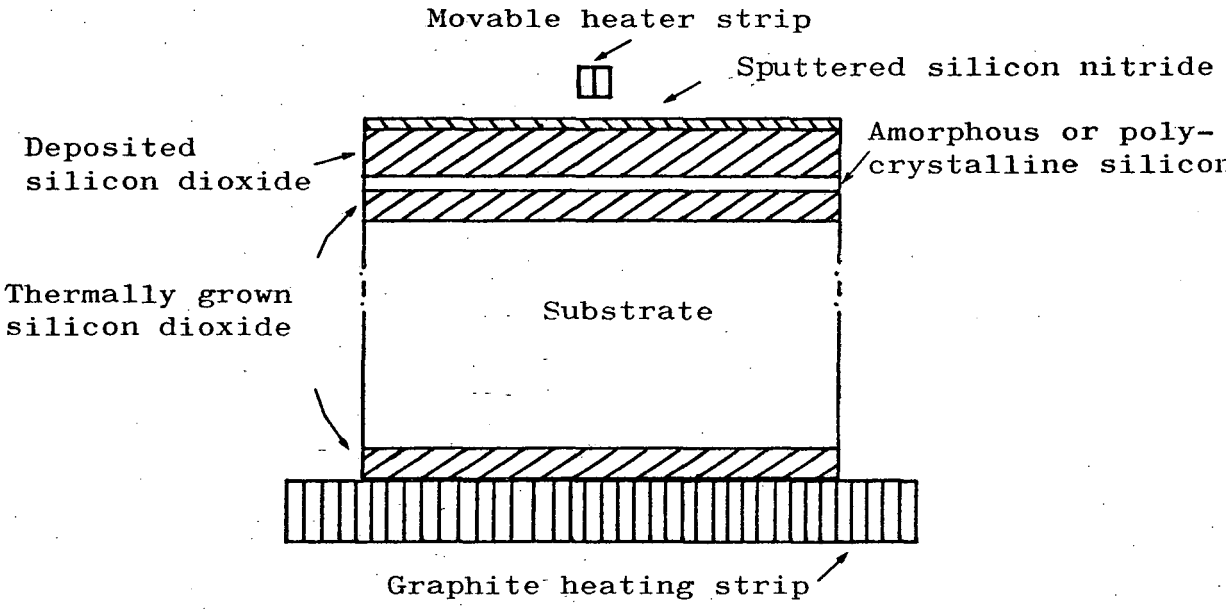

Fig. I.5 Structure used for moving melt zone recrystallization.

CHAPTER 1

SILICON EPITAXY

1.1 Introduction

Uniformly-doped single crystal layers with practically any desired impurity concentration ($\sim 10^{14}$ - 10^{20} atoms cm^{-3})[23,24] can be formed by epitaxial deposition on single crystal substrates with almost any given concentration of impurity atoms. A lower limit to the impurity concentration in the deposited layer is set by the cleanliness of the deposition system and the purity of chemicals used, whereas at very high concentrations, imperfections such as misfit dislocations are generated at the interface[25]. Epitaxial deposition on highly doped substrates results in topographical defects[23] and autodoping of the growing layer[26].

Historically, the availability of epitaxy as a process step provided a simple solution to the problem of contradicting requirements for high BV_{CBO} (high resistivity) and low $V_{CE\ (SAT)}$ (low resistivity) in discrete bipolar transistors[23,27]. In bipolar integrated circuits low resistivity n^+ regions are formed in the p substrate prior to the deposition of a high resistivity (1 - 10 Ωcm) n epitaxial layer[23,28]. Present day device applications of the epitaxy process include discrete transistors, bipolar and certain MOS integrated circuits and microwave devices.

In this chapter the nucleation mechanisms, various techniques available and some of the problems associated with the epitaxial deposition of silicon on silicon substrates are reviewed.

1.2 Nucleation

The nucleation process at the very early stage of epitaxial growth has been studied[29] using direct evaporation of silicon and pyrolysis of silane under U.H.V. conditions. Chemical vapour deposition systems were considered unsuitable as precise control of such growth conditions at the early stages is impossible.

Joyce et al[30,31] and Charig and Skinner[32] have shown that with atomically clean surfaces, epitaxial growth proceeds by the lateral motion of monatomic steps of the deposited material on the substrate crystal. Surface steps on the substrate would occur as a result of slight misorientations from an exact array of low index planes and adsorbed atoms diffusing over the surface would be captured at existing steps. An active step could also be produced by a high temperature $\sim 1250^{\circ}C$ treatment of the substrates before deposition. Steps are provided also by randomly formed nuclei. In (111) substrates, growth proceeds by the lateral expansion of (111) layers in the $[11\bar{2}]$ direction. The step edges are perpendicular to the direction of expansion and lie in the [110] direction.

However, the presence of carbon contamination on the surface impedes the lateral growth and three dimensional growth centres/nuclei of both discrete crystallographic and irregular shapes are formed[29]. These centres grow laterally and vertically, eventually coalescing to form a continuous film with crystallographic and non-crystallographic topographical features.

The carbon contamination can be removed by a heat treatment at a temperature of $\sim 1150^{\circ}$- $1200^{\circ}C$ for a short time before deposition and a two dimensional growth mode is then initiated.[30,31,32]

Nucleation of epitaxial layers in chemical vapour deposition (CVD) systems is expected to be similar to that in UHV systems, although in the early studies a three dimensional nucleation process was observed[29]. This could well have been due to carbon contamination although at the time, the contaminant was suspected to be oxygen[29].

The presence of silicon dioxide or adsorbed oxygen on the substrate surface also affects the initial growth[33,34]. At low growth temperatures ($\sim 1000^{o}C$) for a low rate of arrival of silicon atoms, silicon dioxide reacts with the incoming silicon to form volatile silicon monoxide. Deposition starts when all the silicon dioxide has been removed. At higher temperatures ($\sim 1150^{o}$) silicon dioxide is probably removed by reaction with the substrate. In CVD systems at a comparable temperature, the hydrogen carrier gas reacts with silicon dioxide to form silicon monoxide and water vapour[23].

1.3 Chemical Vapour Deposition (CVD)

Chemical vapour deposition (CVD) is the general term used for describing techniques in which the silicon for deposition is obtained through a heterogeneous chemical reaction at the heated substrate surface. Thermal decomposition of silane or hydrogen reduction of silicon tetrachloride or chlorosilanes are commonly employed.[23,35]. Deposition from organosilanes has also been reported[36]. Normally CVD is carried out in a dynamic flow open tube reactor at atmospheric pressure. Reactors operating under reduced pressure conditions, are becoming available commercially and offer improved deposition and doping uniformity and autodoping characteristics[35]. Purified hydrogen is used as the carrier gas even in the thermal decomposition of silane. Prediluted hydrides of boron, phosphorus or arsenic in hydrogen are used for the doping of epitaxial layers[35]. Antimony doping from

trimethylstibine vapour has been reported[37]. For deposition, thoroughly cleaned substrates are placed on silicon carbide coated graphite susceptors and inductively or radiantly heated in the reactor. A predeposition hydrogen chloride etch and/or a high temperature pre-treatment at $\sim 1200^{o}C$ is normally used[23].

CVD is almost universally used for silicon epitaxy for the following advantages[29].

1. Layers of high crystalline quality can be obtained, without the use of UHV systems, at temperatures well below the melting point of silicon thereby reducing the probability of contamination and dopant redistribution by diffusion.

2. Excellent control of layer thickness is obtained.

3. Precise control of dopant incorporation in the range 10^{14} - 10^{20} atoms cm^{-3} is possible.

1.3.1 Theoretical Model of the CVD Process

In developing a theoretical model of the CVD process a nearly stagnant gas layer is assumed to exist in contact with the susceptor on which the wafers rest[38]. The deposition chemicals are transported to the upper surface of the stagnant layer by the main carrier flow and the following sequence of events is assumed :

1. Mass transport of reactants through the stagnant layer to the substrate surface.

2. Adsorption of the reactants to the surface.

3. Reaction or a series of reactions at the surface.

4. Desorption and transport of the reaction product molecules

into the main gas flow.

5. Surface diffusion and addition of silicon atoms to growth steps.

The growth rate is expected to be controlled by a step which is slower than the others. At high temperatures the mass transfer of the reactants is the controlling factor. The mass transfer rate is influenced by the gas flow rate but is relatively independent of temperature. At low temperatures the adsorption rate is the controlling factor and the growth rate is determined by the surface reaction rate.

1.3.1.1. Stagnant Layer Model

The stagnant layer model developed by Eversteyn, Severin, v.d. Brekel and Peek[38] adequately explains the kinetics of epitaxial deposition. Although developed and verified for a reactor of rectangular cross-section using silane, the model is widely applicable in the solution of CVD reactor problems[39].

It has been observed experimentally that in the reactor cell the space above the susceptor is divided into a convective and a stagnant layer as shown in Fig.1.1. The following assumptions, substantiated mainly by observation of flow patterns, are used in deriving expressions for growth rates.

1. Due to thermal convection, the carrier gas velocity V_M and the temperature T_M are constant over the height $(b - \delta)$ and in the length direction of the reactor cell. The assumption regarding the temperature is valid for a water cooled reactor.

2. The gas velocity in the stagnant layer is zero. The temperature rises linearly with y from T_M to the susceptor

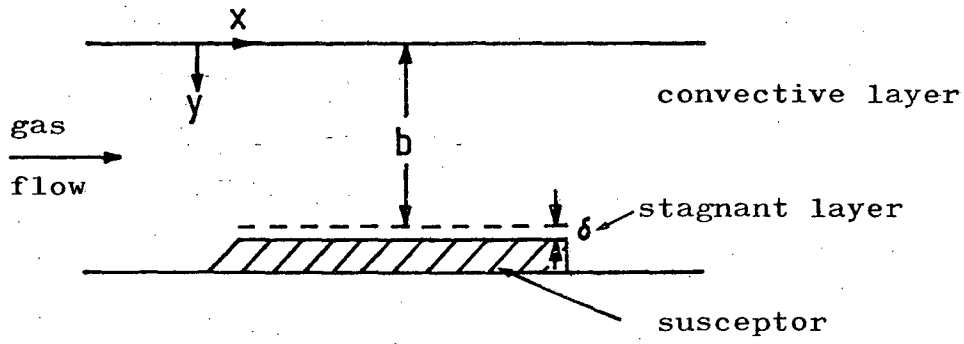

Fig. 1.1. Stagnant layer model for a horizontal reactor.

temperature T_S. The temperature T (y) at any point in the stagnant layer is given by

$$T(y) = T_S - (T_S - T_M) \frac{(b - y)}{\delta}$$

3. Silane diffuses through the stagnant layer to the susceptor surface and decomposes instantaneously maintaining zero silane concentration at the susceptor surface. Thus the rate of deposition of silicon is controlled by the diffusion through the stagnant layer. It is assumed that no dissociation takes place in the gas phase.

With the above assumptions and using the equation of continuity in the convective layer and the diffusion equation in the stagnant layer and balancing them at the interface, the rate of epitaxial growth in a horizontal reactor is given by

$$G(x) = 7.23 \times 10^6 \frac{D_o T_s p_o}{R T_o^2 \delta} \exp\left(- \frac{D_o T_s x}{T_o V_o b \delta}\right) \quad (1.1)$$

where G is the growth rate in (μm/min.)

D_o, the diffusion coefficient of silane in hydrogen at $300^oK = 0.2\ cm^2/s$

T_s, the susceptor temperature (^oK)

$T_o = 300^oK$

p_o, the partial pressure of silane (dynes/$cm^2 \approx 10^{-6}$ atm) at the inlet.

V_o, the mean velocity (cm/s) of the gas as calculated from the incoming gas flow and the free cross-section of the reactor cell,

R, the gas constant (8.3×10^7 erg/^oK)

b, the free height (cm) above the susceptor and

δ is the thickness of the stagnant layer.

Eversteyn et al[38] determined δ experimentally from the flow pattern experiments. The flow pattern was made visible by injecting titanium dioxide particles into the reactor. The particles were observed to flow in a region separated from the susceptor by a stagnant layer. It was observed that the thickness of the stagnant layer decreased with increasing gas flow velocity. δ can also be determined from the growth rate at x = 0 and from the slope of a plot of growth rate G as a function of x. For calculating G from eqn. (1.1) an empirical expression for δ was used

$$\delta = A/(V_T)^{\frac{1}{2}} - B \qquad (1.2)$$

where A = 7 $cm^{3/2}$ $s^{-\frac{1}{2}}$ and B = 0.2 cm and V_T is the mean gas velocity in the reactor corrected for the rise in temperature.

It can be seen from eqn. (1.1) and also is experimentally observed that growth rate decreases with increasing values of x. The magnitude of this effect is dependent on the gas flow rate. This decrease in growth rate is due to the reduction of silane concentration in the gas stream as deposition proceeds along the length of the susceptor. This effect could be compensated for by tilting the susceptor as shown in Fig. 1.2. The tilting restricts the free space available above the susceptor and brings in a gradual increase in the flow velocity with increasing x. This effectively reduces δ with increasing x which brings about an enhancement of growth rate downstream. The growth rate with a tilted susceptor is given by

$$G(x) = 7.23 \times 10^{6} \frac{D_o \; T_s \; P_o}{R T_o^{2} \; \delta(x)} \cdot$$

$$\exp\left[-\frac{2 \; D_o \; T_s \; T_m}{4 \; g \; T_o^{2} \tan\psi}\left(\delta(0) - \delta(x) + 0.2 \; \ln \frac{\delta(o)}{\delta(x)}\right)\right] \qquad (1.3)$$

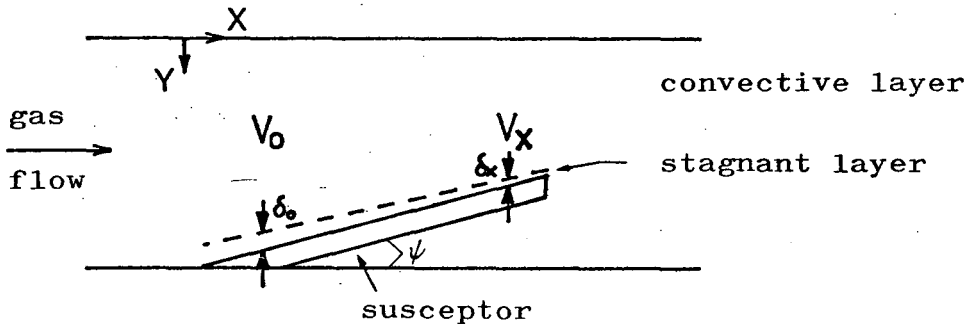

Fig.1.2. Stagnant layer model for a horizontal reactor with a tilted susceptor.

where g is the acceleration due to gravity and ψ the angle of tilt.

It has been shown from eqn. (1.3) and also experimentally that for a given value of tilt angle it is possible to adjust the gas flow velocity to a value for which uniform growth rate can be obtained over almost the entire length of the susceptor.

The reactor efficiency, η , defined as the fraction of the incoming silane decomposed on the heated substrate is given by

$$\eta = \frac{C}{d}\left[1 - \exp\left(-\frac{D_o\, T_s\, L}{b\, V_o\, \delta\, T_o}\right)\right] \qquad (1.4)$$

where C is the width of the susceptor and d the width of the reactor and L the length of the susceptor.

At low gas velocities η decreases with increasing V_o, tending to be a constant at $\sim 35\%$ for high velocities.

1.3.2 CVD Reactor System

There are three major types of reactor geometry[35] to be found in research, development and production.

1. Horizontal reactor with inductive or radiant heating.
2. Vertical "pancake" reactor with inductive heating.
3. Cylinder or barrel reactor with radiant heating.

The horizontal reactors and more recent barrel type inductively heated reactors are favoured for high volume production. The older inductively heated pancake type are still used in research and development. Schematic diagrams of these reactor types are shown in Fig. 1.3 , though individual designs vary considerably. High purity fused quartz reactor cells and silicon carbide graphite susceptors are used.

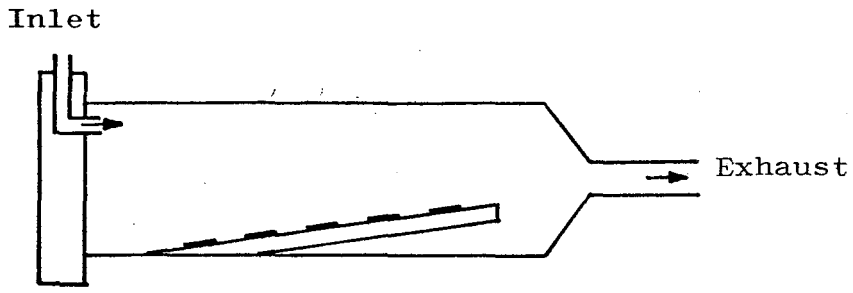

(a) Horizontal reactor with inductive or radiant heating.

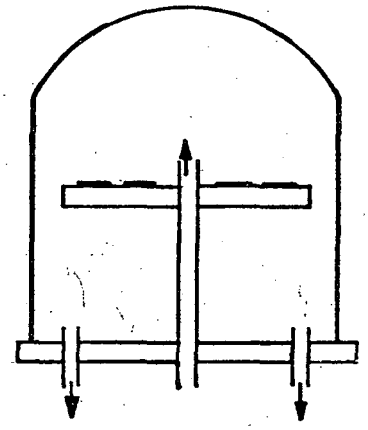

(b) 'Pancake' reactor with inductive heating.

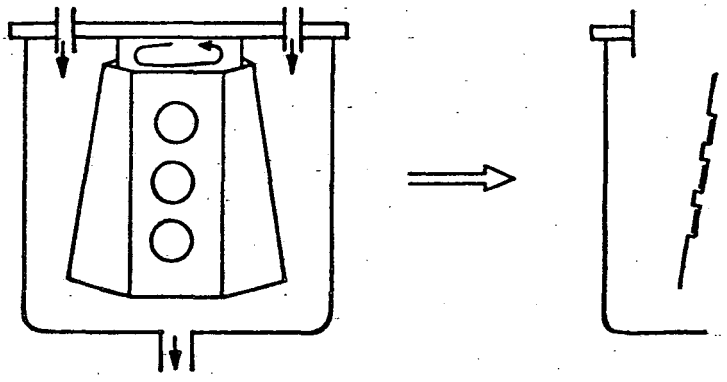

(c) Barrel reactor with radiant heating.

Fig. 1.3. Epitaxial reactors in common use.

Since the early development of epitaxial reactors inductive heating has been employed to achieve cold wall reactors. Radiant heating has been employed in recent designs and is gaining popularity as this mode of heating avoids the generation of certain crystal defects in the deposited film[35].

1.3.3. CVD Chemicals

Typical growth rates, temperature ranges and allowed oxidant level for normally used deposition source chemicals are given in Table 1.1[35].

Silicon tetrachloride is the most commonly used source because of its ready availability in a highly purified form in bubbler containers[35]. It is less sensitive to residual water vapour and oxygen content in the gas supplies. The reaction involved is

$$Si\ Cl_4 + 2H_2 \rightleftharpoons Si + 4\ HCl$$

The growth rate increases with increasing concentration of silicon tetrachloride, reaching a maximum at high concentrations. Etching instead of deposition takes place at very high concentrations[23,41,42]. The probable reaction is

$$Si + Si\ Cl_4 \rightleftharpoons 2\ Si\ Cl_2$$

Trichlorosilane[40,43] is less commonly used although it offers marginal benefits[35] of slightly faster growth rate and somewhat lower temperature than silicon tetrachloride. Rapid formation of deposit downstream from the deposition zone is a disadvantage[35].

Dichlorosilane[35,44,45,46,47] gives a fast growth at a lower temperature through an irreversible reaction

$$Si\ H_2\ Cl_2 \longrightarrow Si + 2\ HCl$$

and is finding increasing use in the industry.

TABLE 1.1

Deposition source chemical	Normal growth rate $\mu m.min^{-1}$	Temperature range ^{o}C	Allowed oxidant level ppm
Silicon tetrachloride	0.7 - 1.5	1150 - 1250	5 - 10
Trichloro-silane	0.7 - 2.0	1100 - 1200	5 - 10
Dichloro-silane	0.7 - 3.0	1050 - 1150	<5
Silane	0.2 - 0.3	950 - 1050	<2

Dichlorosilane also provides the most efficient source of silicon[46].

Thermal decomposition[23] of silane occurs according to the reaction

$$Si\ H_4 \longrightarrow Si + 2H_2$$

Silane permits epitaxial deposition[35,48,49] at temperatures lower than those required for chlorosilanes. Epitaxial growth of ~ 0.1 µm/min. has been reported with silane in a hydrogen carrier[52] at a temperature of 960°C and 0.01 µm/min. at 860°C[50]. A growth rate of 3 µm/min. at 900°C has been achieved in the absence of the retarding action of hydrogen on silane decomposition in a helium carrier gas[51]. Sharper impurity profiles and better performance in terms of autodoping[52] and pattern shift[35] are obtainable. However, a number of disadvantages are encountered[35,53]:

- a powdery deposit in the line which could be transported by the gas stream on to the substrates thereby giving rise to defects;

- at high temperatures and high concentration of silane, particles of silicon are formed in the gas phase and can settle on the substrate surface initiating overgrowths;

- defects are formed due to trace amounts of moisture or oxygen in the gas stream;

- fast build up of deposit in the reactor requires frequent cleaning.

A faster growth rate at a temperature comparable to that required for silane has been obtained using a mixture of silane and hydrogen chloride[54]. Hydrogen chloride inhibits the gas phase decomposition.

Irrespective of the type of equipment and experimental conditions, with silicon tetrachloride and the chlorosilanes the deposition is generally surface reaction controlled, whereas with silane it is diffusion controlled[29,48].

Thermal decomposition of tetramethylsilane[36] in a helium carrier has been employed for epitaxial deposition of silicon in an attempt to remove the problem of hydrogen adsorption on the substrate surface and a consequent high deposition temperature. Although initial experiments were carried out at temperatures between 1100°C and 1300°C a deposition temperature below 1000°C should be adequate. A growth rate of 0.4 μm /min. has been obtained for a tetramethylsilane to helium ratio of 0.05 at 1150°C.

1.3.4. Doping of CVD Grown Layers

Epitaxial layers with impurity concentration in the range of 10^{14} - 10^{20} .cm^{-3} can be obtained by adjusting the dopant to silicon ratio in the gas phase between 10^{-7} to 10^{-1}. Highly reproducible results with a desired doping concentration can be easily achieved although the dopant incorporation mechanism is not well understood. The dopant density in the growing epitaxial layer is controlled by

- dopant/silicon ratio in the gas phase
- temperature
- growth rate
- gas flow velocity

For a given growth rate the dopant concentration[55] in the epitaxial layers increases linearly with dopant-to-silicon ratio, with a slope of unity. At ratios greater than 10^{-3} the slope decreases to 0.5. For a constant dopant to silicon ratio, dopant concentration decreases with increasing temperature. At low growth rates, doping concentration is independent of growth rate but at high growth rates it is inversely proportional to growth rate[56].

Gas flow velocity in the reactor is expected to have a significant effect, although no systematic study has been reported. The gas velocity controls the thickness of the stagnant layer through which the reactant molecules must diffuse to the substrate surface. Also the stagnant layer is slow to respond to variations in the composition of the gas phase above the stagnant layer[56].

The dopant incorporation into the growing epitaxial layer is likely to involve a mechanism analogous to the transfer of silicon from the gas stream to the gas/solid interface during epitaxial growth. At low growth rates, a near thermodynamic equilibrium is maintained whereas at high growth-rates rate limitation is imposed probably by surface mechanisms[56,57] i.e. adsorption, surface chemical reaction, surface diffusion and site incorporation. A mass-transport controlled mechanism has been proposed by other workers[58].

Boron, arsenic or phosphorus doping of epitaxial layers is readily achieved by introducing diborane ($B_2 H_6$), arsine (AsH_3) or phosphine (PH_3), respectively, prediluted in hydrogen to ppm levels. Further one or two stage dilution is normally used before mixing with the main carrier gas flow. Neutron transmutation doping (NTD) has been used for precise and homogeneous phosphorus doping of initially undoped epitaxial layers on heavily arsenic-doped substrates[59]. The stable silicon isotope Si^{30} is converted to Si^{31} by neutron bombardment in a reactor. The Si^{31} subsequently decays to stable phosphorus P^{31}, thereby doping the material n-type. Antimony doping has been obtained from trimethylstibine ($Sb(CH_3)_3$)[37] vapour picked up by passing hydrogen over the liquid maintained at -78°C.

1.3.5 Autodoping

Unintentional incorporation of dopant in the growing epitaxial layer may arise from various sources, such as the susceptor, the reactor walls, deposition chemicals and substrates[35,60]. The contribution from the substrates is

generally called autodoping. Autodoping normally occurs through vaporization of the dopant species into the stagnant layer or the presence of reaction products of HCl etching reincorporated into the growing layer[60,61]. Solid state diffusion at high deposition temperature could also be a contributing factor[52,62,63,64]. Some authors use the term autodoping to describe only the vapour phase process[60,61,65,66,67].

As the stagnant layer is fairly stable and static, the vaporized autodopant atoms have a long residence time[61] depending on the temperature, flow rate and the dimensions of the reactor. A steady state concentration is established. This contributes to the formation of an adsorbed layer[65] at the growth interface which is subsequently incorporated in the epitaxial layer.

The problem of autodoping is severe in the preparation of lightly doped layers on heavily doped substrates. The general effect is a graded impurity profile at the interface. This is not desirable for microwave applications[52]. Lateral as well as vertical autodoping from selected area buried layer structures has been observed and studied by a number of workers[61,66].

Autodoping cannot be totally eliminated but various techniques have been suggested for minimizing the effect[35,52,60,65,66,67]. HCl etching before deposition and a polycrystalline silicon coating on the susceptor are generally useful[60]. Sealing of the back surface of the substrates with a layer of polycrystalline silicon,silicon dioxide or silicon nitride reduces the surface area for dopant evaporation[60]. Sealing is also achieved through the presence of a thin layer of silicon which grows during predepositon hydrogen chloride etch from a silicon coated susceptor in r.f. heated reactors[67].

The use of silane and/dichlorosilane permits deposition at

lower temperatures than that required for silicon tetrachloride. At a lower deposition temperature, the vapour pressure of the evaporated dopant from the susceptor is reduced[35] and the rate of solid state diffusion is also reduced[52]. A two-stage technique with an intermission in the growth process permits the escape of the undesired autodopant from the stagnant layer into the main gas flow[60]. The use of antimony doped substrates reduces autodoping since antimony has a lower vapour pressure and solid state diffusivity than phosphorus and arsenic[35]. Reduced-pressure epitaxy improves both lateral and vertical autodoping by allowing rapid escape of the autodopant from the stagnant layer[35,68]. Good quality epitaxial growth at temperatures lower than 900°C can be achieved under reduced pressure[69].

1.4 Other Deposition Techniques

The Molecular Beam Epitaxy (MBE) technique under UHV conditions has been reported to have produced defect-free epitaxial layers at temperatures as low as 600°C. The problems of autodoping and outdiffusion are practically eliminated. Liquid Phase Epitaxial (LPE) growth from a saturated solution of silicon in tin has been studied as a potentially low temperature technique[71,72]. Epitaxial deposition of silicon has been obtained by the electrolysis of molten fluorides at a temperature of 750°C.[73]

Solid Phase Epitaxial (SPE) growth[74] has been investigated by a number of workers for the fundamental scientific interest in the physical mechanisms involved and as a potentially useful low temperature process. SPE regrowth of small grain polycrystalline and sputter-deposited silicon layers on crystalline silicon substrates has been reported[75,76]. Epitaxial growth has been obtained on (100) and (111) silicon substrates using a crystalline silicon/metal/amorphous silicon structure. An SPE growth occurs by the precipitation of silicon transported through the metal film typically

300Å - 1000Å thick, during a post deposition anneal at a temperature between 400° and 600°C[74].

1.5 Orientation Dependence of Growth Rate[29]

Orientation dependence of growth rate is not expected when the growth rate is limited by the mass transport of reactant molecules to the growing surface. This is confirmed experimentally when silane is used as the deposition chemical. On the other hand, deposition from silicon tetrachloride and chlorosilanes are surface mechanism controlled where the nature of the growing surface is likely to have an effect. Orientation dependence of growth rate has indeed been observed for deposition from silicon tetrachloride, with the (111) being the slowest growing surface and the (110) the fastest.

1.5.1 Pattern Shift and Pattern Obliteration[35,77]

Pattern shift and pattern obliteration occur, when an epitaxial layer is deposited on buried layer structures formed by diffusion, as a direct result of the orientation dependence of growth rate. Buried layers in selected areas are required for low collector resistance in bipolar integrated circuits. These are normally formed by diffusion through windows in an oxide layer. The exposed silicon in the window areas is oxidized during drive-in in an oxidising ambient. Shallow, flat depressions bounded by steps result when the oxide over the entire substrate is removed. The orientation of the sides and the bottom of the depression will be different for all substrate orientations, except (100), with consequent distortion and displacement of the depression during epitaxial growth. In some cases complete obliteration of the pattern occurs.

The pattern shift can be minimised by a careful selection of

- deposition temperature
- growth rate
- substrate orientation
- deposition source chemical

Using silicon tetrachloride at a temperature of 1200°C ± 90°C with a growth rate of 1 μm/min. substrates misoriented from a (111) plane towards the nearest (011) plane show very little temperature dependence and minimal distortion. With silicon tetrachloride at 1240°C, substrates with precise (100) orientation show little distortion. Substrates orientated 4° off (100) towards the (110) plane show minimum distortion with dichlorosilane at 1100°C. No distortion has been observed with silane either in (100) or (111) wafers.

1.6 Defects in Epitaxial Layers

Defects are introduced into the epitaxial layer as a result of any departure from ideally clean conditions of the substrate surface; e.g. the presence of particulate materials, contaminants like carbon in the form of silicon carbide, clusters of silicon dioxide[29], trace amounts of metals, presence of oxidants in the carrier gas[35]. These impurities probably affect the post-nucleation growth by retarding the lateral growth of steps resulting in dislocations, line defects, stacking faults, pyramids/hillocks, cones, polycrystalline areas etc.,[29] The growth of whiskers or spikes is initiated by particulate impurities, mostly silicon precipitates from an unclean system[35,53].

The presence of defects affects carrier mobility, lifetime and hence device characteristics[29]. Although with the high quality of substrates and with improved cleaning and handling techniques most types of defect have largely been eliminated, some still persist.

A common defect in epitaxial silicon is an edge dislocation which is the localized distortion of the lattice due to the abrupt termination of a layer of atoms[23,29]. Normally, with a clean substrate, the number of dislocations in the epitaxial film is substantially the same as in the substrate[35]. However, it has been shown that diffusion-induced dislocation

networks in {111} planes particularly at the edge of a heavily doped/diffused buried layer propagate in the growing layers in the <110> directions[78]. These dislocations move away from the interface in the $[11\bar{2}]$ direction which is the fastest growth direction as opposed to $[\bar{1}\bar{1}2]$ which is the slowest growth direction. Diffusion induced defects can be eliminated by implanting the buried layer instead of diffusing from a chemical source[79].

In inductively heated reactors a thermal gradient exists through the thickness and substrates warp to a dish-shape[35]. This problem is severe in wafers of 3" diameter or above. The thermal stress arising from this radial temperature gradient results in dislocation movement or slip. The stress increases with temperature and wafer size. The situation is improved by introducing uniform back-surface damage which makes the wafers mechanically stronger and more resistant to dislocation motion. Pancake reactors perform well up to ~ 1100°C and are better than horizontal slab reactors, because the rate of heating is slower. Radiant heating largely eliminates this problem up to a temperature of 1200°C. The wafers are heated first and then the susceptor, initially at a slow rate from a remote source. The temperature gradient between the front and back surfaces is not enough to initiate thermally induced dislocation movement[35].

A high dopant concentration in silicon produces a change in the lattice constant due to a difference in atomic radii of the dopant and silicon atoms. When a highly doped layer is epitaxially deposited on a lightly doped substrate or vice-versa, the latticemismatch can cause sufficient strain to generate misfit dislocations which may adversely affect device characteristics. Using an electrically inactive impurity of appropriate atomic radius, the lattice constant of the epitaxial layers can be matched with that of the substrate, thereby eliminating misfit dislocations[25]. Germanium up to a concentration of 1×10^{20} atoms.cm^{-3}

has been used in layers highly doped with boron or phosphorus. Tin at a level of 2×10^{19}. cm^{-3} has been used in layers with 4×10^{19} P.cm^{-3} [80]. Carbon at a concentration of 7.6×10^{18} has successfully been used in antimony doped layers to a concentration of 9.5×10^{18}.cm^{-3} [25]. Apparently these co-dopants do not affect the electrical characteristics of the layers.

Another commonly occurring defect in epitaxially grown silicon is the stacking fault[23,29]. Selective chemical etching is normally necessary to reveal the stacking faults[81]. The intersections of the fault planes with the surface etch faster than the unfaulted perfect crystal and are made visible as grooves[82]. In (111) substrates the stacking faults appear as equilateral triangles, semi-triangles, single lines parallel to the sides of the triangles and complex polygons arising from the interaction of two or more faults. Normally stacking faults originate on a discontinuity in the stacking sequence of the $\{111\}$ planes at the substrate/epitaxial interface. The discontinuity occurs whenever silicon atoms are deposited in the incorrect sequence at one of the nucleating centres[83]. The incorrect sequence is associated with mechanical damage, the presence of silicon dioxide and metallic impurities in the surface[29] and also the presence of oxygen or water vapour in the carrier gas. As the growth process continues the mismatched area grows. The mis-match boundaries propagate along adjacent inclined $\{111\}$ planes and are equivalent to stacking faults in these planes. The intersection of these three $\{111\}$ planes with the epitaxial layer surface forms a tetrahedron in the layer with one apex at the interface. Partial triangles and single line defects are formed when only two or one of the $\{111\}$ faulted planes propagate into the growing layer. The intersections of the stacking fault planes with the surface lie in the $\langle 110 \rangle$ directions. Stacking faults can also originate in the growing layer, in addition to those formed at the interface[83].

Faults corresponding to single line etch figures terminate at partial dislocations having Burger's vectors $a/6$ $\langle 112 \rangle$ whereas in equilateral triangular defects one (111) fault plane is connected to another through a 'stair rod' partial dislocation with Burger's vector $a/6$ $\langle 110 \rangle$. Corresponding to the triangle etch figure formed on (111) substrates a square figure is formed in epitaxial layers on (100) substrates.

A high density of epitaxial stacking faults ($\sim 10^4$ cm^{-2}) has been observed in dislocation-free silicon when the substrates were oxidized before epitaxy. These stacking faults are almost totally eliminated in substrates containing $\sim 1.5 \times 10^{18}$ O atoms.cm^{-3} and in selected areas where buried layers were created by antimony implantation or diffusion[84]. For the implantation process the elimination extends laterally for 50 μm to 100 μm beyond the buried area. In the former case the gettering of nucleation sites for stacking faults has been attributed to the presence of silicon dioxide precipitates, whereas in the latter, some complex interaction between implantation damage and oxidation induced nucleation sites must have taken place resulting in elimination of faults in the epitaxial layer.

Stacking faults in the active area of a device are known to contribute to poor characteristics[85,86,87]. Stacking faults can generally be eliminated by proper substrate cleaning techniques and pre-annealing in a hydrogen ambient or by hydrogen chloride etching prior to epitaxial deposition[23].

Overgrowths in the epitaxial layers in the form of tripyramids of many variations are quite common[23,29]. These defects occur only in (111) substrates and may have only one high or low point at the centre and may also consist of one or two pyramids. Tripyramids originate from initially

mismatched deposition and subsequent twinning of the bounding {111} planes or by the interaction of neighbouring growth regions. These overgrowths in (111) substrates are attributed to the presence of β - silicon carbide. In (100) material β - silicon carbide initiates stacking faults.

CHAPTER 2

EPITAXIAL DEPOSITION FROM SILANE IN A HORIZONTAL REACTOR

A major part of the experimental programme involved setting up an epitaxial reactor and establishing the conditions for successful deposition of epitaxial layers.

2.1 Description of the Reactor

The reactor and gas flow diagram using silane premixed with hydrogen is shown in Fig. 2.1. An alternative scheme for use with silicon tetrachloride is also indicated if faster growth and thicker layers are required. The thermal decomposition of silane occurs in an RF heated, water-cooled fused quartz reactor cell of circular cross-section. Facilities for hydrogen chloride etching of the substrates and phosphorus doping from phosphine have been included. After the gas flow rates are set manually while purging them through the waste line, flow sequences and process times can be controlled electrically from a programmer unit. However, an override facility has been built in to permit manual operation throughout.

2.1.1. The Gas Flow System

Stainless steel tubing of $\frac{1}{4}$" diameter has been used for all gas lines with PTFE inlet and outlet tubes and couplings for connection to the fused quartz glass reactor cell. Solenoid valves are used for controlling nitrogen, hydrogen and phosphine flows. Hydrogen chloride and silane are controlled by stainless steel pneumatic valves operated by nitrogen line pressure which are turned on by solenoid valves (not shown in Fig. 2.1) for automatic operation. Pneumatic valves have lower leakage and hence are better suited than solenoid valves for corrosive gases such as hydrogen chloride and

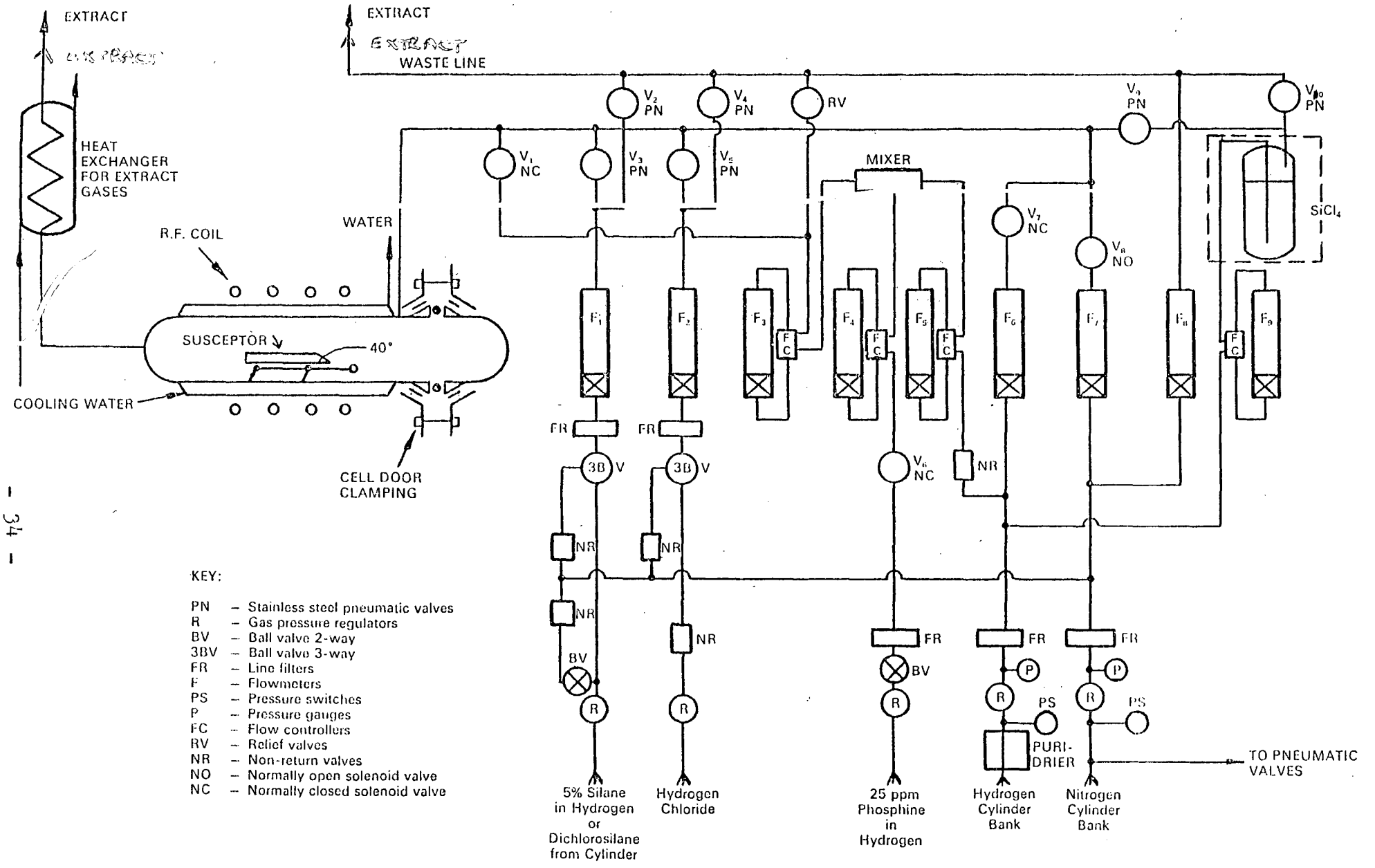

Fig. 2.1. Epitaxial reactor and gas flow diagram.

hydrogen saturated with silicon tetrachloride. Silane and hydrogen chloride lines have provision for nitrogen purging by means of three-way ball valves. Nitrogen is also introduced into the reactor cell through a normally open solenoid valve. This acts as a safety feature in case of power failure or operation of any of the safety interlocks described later. The waste line also is purged continuously with nitrogen when the system is operating. This is to provide a carrier and dilution flow for the small volumes of toxic gases released into the waste line during flow adjustments and sometimes during automatic operation. The hydrogen carrier is passed through a palladium diffuser and a molecular sieve to remove any oxygen and moisture present. Small quantities of oxygen and/or moisture tend to produce polycrystalline films or films with a high density of stacking faults. These impurities also raise the minimum temperature at which epitaxial films can be deposited. Phosphine at 25 ppm in hydrogen is further diluted with hydrogen in a mixing tube and the required portion of the dilute gas is injected into the cell. Any portion discarded escapes to the waste manifold through the relief valve RV. Since only a low volume is required for the diluted phosphine, flow controllers are included for flow stabilization.

2.1.2. Other Major Components

Table 2.1 gives a brief description of the various components and consumables.

Table 2.1

Component	Brief Details
1. Reactor tube	Fused quartz, double walled, internal diameter 4.5 cm.
2. Susceptor	High purity graphite of dimensions 20.3 cm x 3.8 cm x 1 cm with a wedge shaped end at the gas entry side,

Table 2.1 (cont'd)

Component	Brief Details
	as shown in Fig.2.1, coated with a thin film of polycrystalline silicon (6 - 10 μm) in situ.
3. Susceptor pedestal	Fused quartz tilted at an angle of 2^{o}
4. RF generator	12kVA at 400kHz
5. Consumables	'Oxygen free' nitrogen; 'high purity' hydrogen; electronic grade 5% silane in hydrogen; 25 ppm phosphine in hydrogen; electronic grade hydrogen chloride.

2.1.3 Safety features

Any accidental leak of hydrogen into the atmosphere or inward leak of air into the system could be hazardous, since high temperatures are involved. Therefore, all joints and seals must be airtight and should be leak-tested with a hydrogen detector. Silane and phosphine gases are highly toxic and pure silane is also pyrophoric. However, silane at 5% in hydrogen is not pyrophoric and the phosphine is at only 25 ppm in hydrogen. Therefore, the same precautions as those taken for hydrogen alone are applicable.

For safe running of the system, several safety interlocks have been included :

1. 50 psi nitrogen and 25 psi hydrogen pressures are sensed by pressure switches. Nitrogen and hydrogen pressures are reduced to 6 psi before entry into the system.

2. Extraction fan operation is sensed by pressure switches.

3. The cooling water supply to the reactor cell is sensed.

4. There is a microswitch sensor on the loading port of the reactor tube.

5. The reactor has an aluminium front panel for protection of the operator from RF burns. This has a microswitch sensor.

If any of the above fail to operate, the 24 d.c. supply for the solenoid valves and the power supply to the RF generator will be unobtainable and only nitrogen will be allowed into the reactor cell.

2.2 Operation

For a typical run, the system is taken through the following stages :

1. Before the first run of the day the susceptor alone is heated to 1200°C for 15 minutes. This drives off adsorbed moisture and other gases which would lead to poly-crystalline rather than epitaxial growth.

2. The reactor cell is loaded with up to 4 x $1\frac{1}{4}$" slices. (Following a slice cleaning schedule.)

3. The cell is purged with nitrogen.

4. All interlocks are made and seals checked visually.

5. Hydrogen flow is turned on and adjusted and seals are checked for leaks with a hydrogen detector.

6. The silane line is purged with nitrogen, the silane cylinder is turned on (15 psi output pressure) and the flow is directed to waste while being adjusted.

7. If phosphorus doping is required, the phosphine is turned on (15 psi output pressure). The dilution hydrogen flow, phosphine flow and the flow into the reactor cell are adjusted while allowing flow to the cell.

8. The gas flow sequence is selected and the process timers are adjusted on the automatic sequence control panel.

9. The RF induction heating is switched on and the power slowly increased to the required value as determined by the desired susceptor/slice temperature. The latter is measured with an optical pyrometer.

10. Automatic operation is started. This introduces the gases into the reactor cell in the following order :

    a. Hydrogen carrier alone for 5 minutes;

    b. Silane and dopant gas (if required) to waste for 1 minute;

    c. Silane to waste and dopant gas to cell for $\frac{1}{2}$ minute (to prevent initial growth of a high resistance layer);

    d. Both silane and dopant to cell for required deposition time.

11. RF power is switched off at the end of the process.

12. The susceptor is allowed to cool for 15 minutes.

13. Nitrogen flow is turned on and allowed to purge for 2 minutes.

14. Slices are unloaded.

2.3 Evaluation of Grown Layers

The quality of the grown layers has been assessed by 10 second

Sirtl etching[81] (50g CrO_3 in 100 ml H_2O, mixed with equal volume of HF just before use) and examination under an optical microscope fitted with a Nomarski interference contrast objective.

The thickness of layers has been obtained from the measurement of stacking fault triangles[23] revealed by Sirtl etch. If L is the measured length of one side of a triangle, the thickness, t, of the layer is given by

$$t = L \ (2/3)^{\frac{1}{2}} = 0.816 \ L$$

As hardly any stacking faults are found when the reactor is correctly "tuned", test slices were scratched before epitaxial deposition to obtain visible stacking faults.
The thickness obtained from stacking fault measurement shows a good correlation with that calculated from weight gain. Uniformity of thickness from slice to slice and run to run is well within the limits of error ($\pm$ 10%) in the stacking fault measurement.

2.4 Dependence of Layer Growth Kinetics on Experimental Conditions

The conditions for epitaxial growth on (111) 9-10 Ωcm n-type slices have been established and the effects of temperature, silane concentration and flow-rate on growth of undoped layers have been studied. It has been found that a minimum temperature of 1050°C and a typical flow-rate of 30 litres per minute of hydrogen (63 cm.sec.$^{-1}$ flow velocity) is required for epitaxial deposition in the system. At lower temperatures poly-crystalline deposition takes place. Even at this temperature some growth features are present but the stacking fault density is low ($\sim 100.cm^{-2}$). Films grown at 1100°C at a silane concentration of 0.1% and at a total flow-rate of 30 litres (or more) per minute are virtually free from growth features and stacking faults ($< 2.cm^{-2}$) except on the edges of the slices.

2.4.1. Effect of Substrate Temperature, Silane Concentration and Flow Rate on Growth Rate and Quality of Layers

It was observed that varying the temperature between 1050°and 1200°C with a silane concentration of 0.1% for two values of flow-rate (15 and 30 litres per minute) had no effect on growth rate though the higher flow rate gave a higher growth rate as would be expected. This suggests that in this range the growth rate is mass transfer controlled rather than surface reaction controlled[23]. This independence of growth rate on temperature has previously been observed by Joyce and Bradley[48] for temperatures above 1100°C.

The quality of the films grown above 1100°C remains the same as far as stacking fault count is concerned, but at a temperature of 1200°C for the lower flow rate, in some areas of the slices a high density (10^7 - $10^8.cm^{-2}$) of small etch pits ($\sim$ 0.25 μm) was revealed by Sirtl etching .

The effect of silane concentration variation from 0.05% to 0.2% on growth rate for total flow rates of 15, 30 and 60 litres per minute is shown in Fig. 2.2. Under these conditions the growth rate is proportional to $(\text{concentration})^{1.15}$. The factor 1.15 for the order of the reaction is probably due to the retarding action of hydrogen on a second order reaction[48]. At concentrations higher than 0.2% for 30 litres per minute flow, particles of silicon form in the gas stream and deposit on the cooler part of the reactor cell downstream. At higher temperatures this particle formation takes place at a lower concentration of silane. This imposes a limit on the maximum silane concentration usable at a given temperature and total flow. Conditions which give rise to these deposits are to be avoided since particles can settle on the substrate surface initiating overgrowths

As shown in Fig. 2.3 growth rate was found to vary linearly with$(\text{gas velocity})^{\frac{1}{2}}$, for a total gas flow in the range

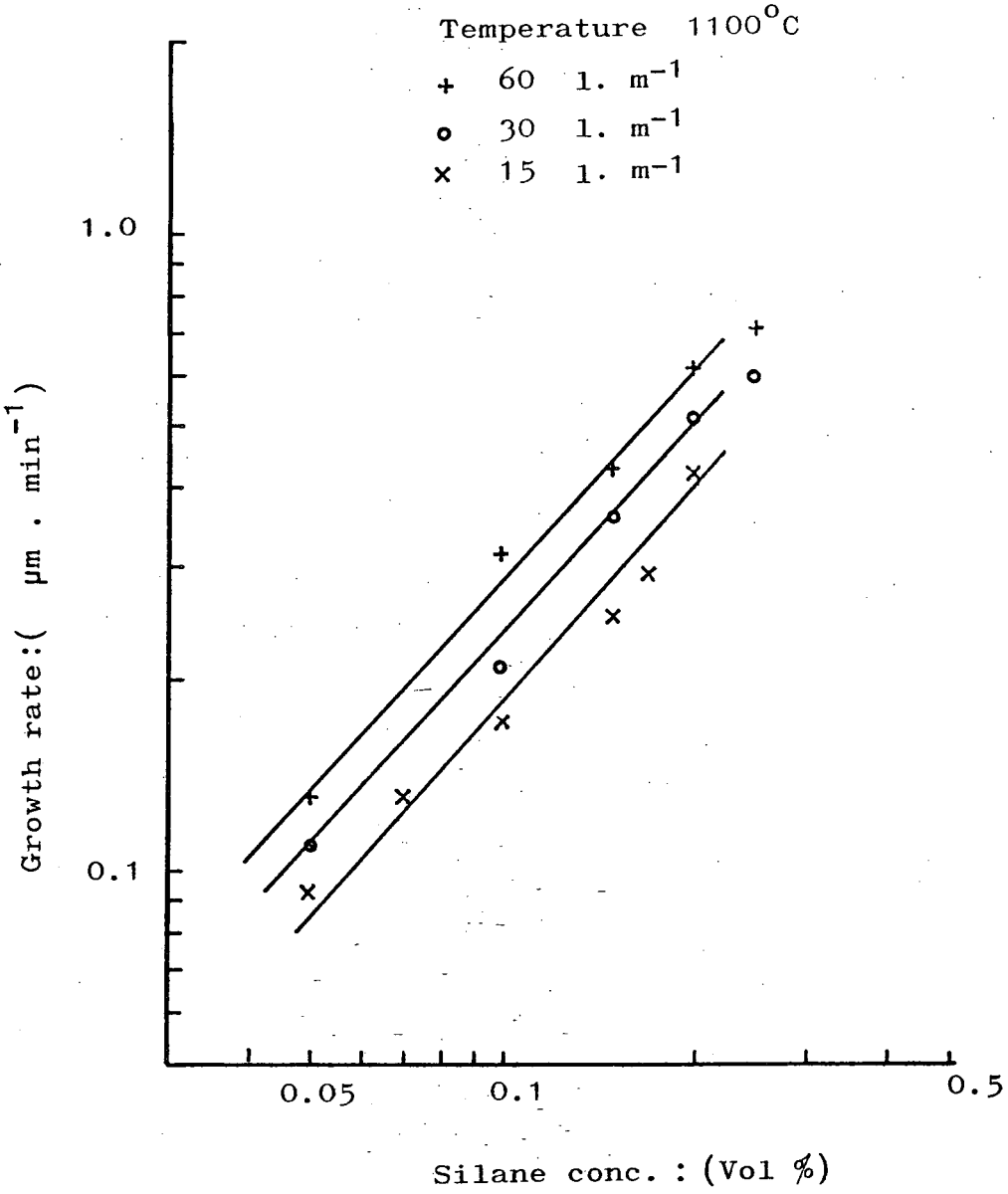

Fig. 2.2. Growth rate as a function of silane concentration. The straight lines have been drawn through points calculated using equations (2.1) and (2.5).

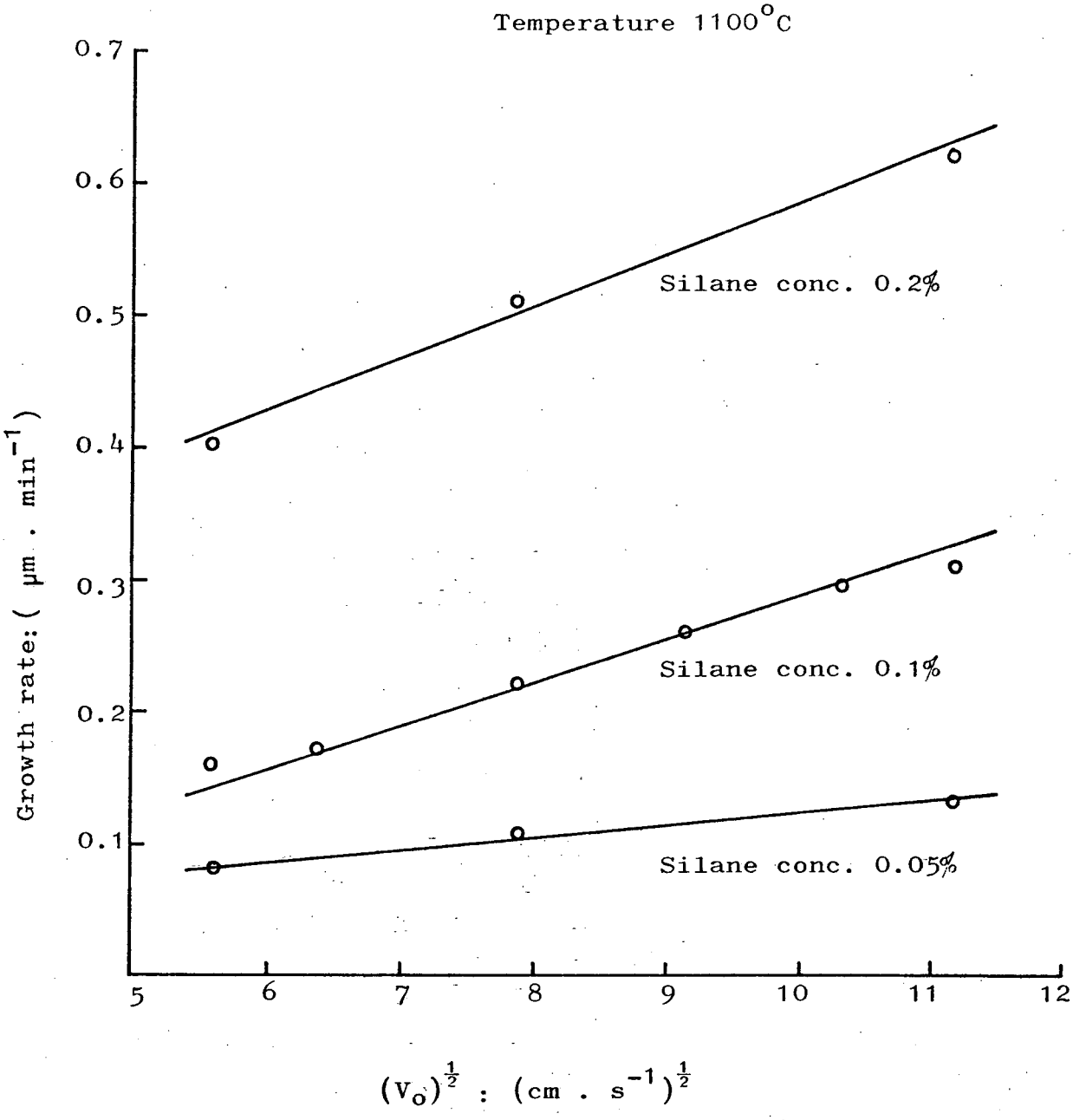

Fig. 2.3. Effect of flow velocity on growth rate.

15 to 60 litres per minute (flow velocity 31.5 - 126 $cm.sec^{-1}$). This could be interpreted on the basis of the stagnant layer model for epitaxial growth[38].

2.5 Analysis of Growth Rate Using the Stagnant Layer Model

An attempt was made to analyse/interpret the growth kinetics on the basis of the stagnant layer model developed by Eversteyn, Severin, v.d. Brekel and Peek[38].

The observed independence of the growth rate with temperature indicates that the reaction is controlled by the mass transfer of the reacting species through the stagnant layer. The linear dependence of the growth rate with $(V_o)^{\frac{1}{2}}$ indicates that the thickness of the stagnant layer is proportional to $(V_o)^{\frac{1}{2}}$.

Expression (1.1) as obtained from the stagnant layer model[38]

$$G(x) = 7.23 \times 10^6 \frac{D_o T_o p_o}{R T_o^2 \delta} \exp\left(-\frac{D_o T_s x}{T_o V_o b\delta}\right) \quad (1.1)$$

predicts the growth rate at a position x = 0 on the susceptor and an exponential decay for the growth further along the susceptor. The exponential part of the above expression is dependent on the geometry of the reactor and corresponds to a reactor with a rectangular cross-section. Therefore, this cannot be directly applied to a reactor with a circular section as used in the present study. However, the pre-exponential part does not contain any geometrical parameters except that δ is dependent on the gas flow velocity which, in turn, is determined by the free cross-sectional area not occupied by the susceptor. It was decided, therefore, to use only the pre-exponential part of the expression which is expected to predict the growth rate at x = 0 , although in most experiments only one wafer, placed at x = 10 cm, was used.

In developing the model Eversteyn et al[38] have taken the growth rate to be directly proportional to the partial pressure/volume concentration of silane in the gas flow. However, it was observed in this study that the growth rate was proportional to the (volume concentration)$^{1.15}$ up to a volume concentration of 0.2%. Above this concentration the slope of the growth rate concentration curves tends to drop probably due to the decomposition of silane in the gas phase forming a deposit of amorphous silicon on the reactor cell wall. The factor of 1.15 is not evident from linear plots of growth rate as a function of the partial pressure or volume concentration below 0.1% as shown by Eversteyn et al[38].

Therefore, it was necessary to modify the pre-exponential part of expression (1.1) as

$$G(x_o) = 7.23 \times 10^6 \frac{D_o T_s (p_o)^{1.15}}{R T_o^2 \delta} \qquad (2.1)$$

Eversteyn et al have obtained an empirical relation between the stagnant layer thickness δ and V_T,

$$\delta = A/(V_T)^{\frac{1}{2}} - B \; . \qquad (1.2)$$

It is difficult to estimate V_T, as the temperatures involved in the gas flow system are unknown. Only the susceptor temperature T_s is known and the reactor cell wall temperature T_o is assumed to be close to the ambient, 30°C, for a water cooled reactor. For a susceptor temperature of 1050°C Eversteyn et al[38] have taken $V_T = 2.5\ V_o$. Since the observed growth rate as a function of $(V_o)^{\frac{1}{2}}$ produced a good straight line, an empirical approach was used in this study to obtain an expression relating δ and V_o, as follows :-

Eqn. (2.1) may be written as

$$G(x_o) = 7.23 \times 10^6 \; K(p_o)^{1.15} \; , \qquad (2.2)$$

where K stands for $D_o T_s / R T_o^2 \delta$. K could be obtained from

the experimentally determined growth rate.

Thus δ may be calculated, since R, D_o T_o and T_s are known and can be given by

$$\delta = \frac{X}{(V_o)^{\frac{1}{2}}} \qquad (2.3)$$

X was obtained for three values of V_o for p_o of 2000 dynes or a silane concentration of 0.2%. A straight line as shown in Fig. 2.4 was obtained when X was plotted as a function of $(V_o)^{\frac{1}{2}}$. This plot shows the effect of V_o on δ and its influence on the growth rate. X also incorporates any correction factor arising from the use of V_o instead of V_T. X from Fig. 2.4 is given by

$$X = 1.43\ (V_o)^{\frac{1}{2}} + 15.5 \qquad (2.4)$$

substituting (2.4) in (2.3)

one obtains

$$\delta = 1.43 + \frac{15.5}{(V_o)^{\frac{1}{2}}} \qquad (2.5)$$

Using (2.5) for determining δ , growth rates were calculated from (2.1) for silane concentration of 0.1% and 0.05%. These calculated values agree well with experimentally obtained growth rates, as shown in Fig. 2.2.

In most of the growth experiments only one wafer was used, placed at X = 10 cms. In a limited number of experiments three wafers were used, placed at x = 6.5, 10 and 13.5 cms. No variation of growth rate with x was observed. This probably is attributable to the susceptor tilt of 2^o. As the expression given by Eversteyn et al[38] for non-tilted susceptor adequately explains the results, no attempt was made to incorporate the tilt angle. This complicates the calculations and involves a number of parameters not easily determined.

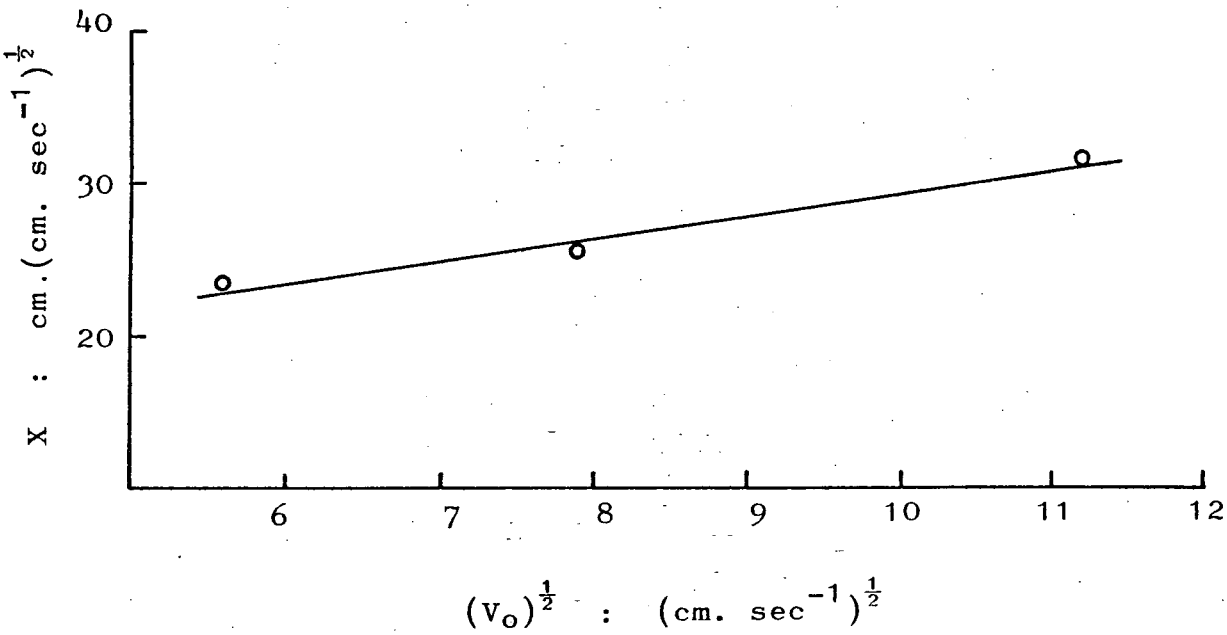

Fig. 2.4. X, for a silane concentration of 0.2%, as a function of $(V_o)^{\frac{1}{2}}$.

CHAPTER 3

FORMATION OF SILICON OXIDE BY THE IMPLANTATION OF OXYGEN

3.1 Introduction

Introduction of group III and V impurities into silicon by ion implantation in silicon is well established in the manufacture of integrated circuit devices[88,89,90,91]. The formation of silicon dioxide and silicon nitride dielectric layers on the surface of silicon wafers by implantation has also been investigated[22,92-101]. IMPLanted OXides (IMPLOX) produced in the early experiments were of poor quality[93,94]. Subsequently it was suggested[22,99] that low ion dose, high beam currents, rise in substrate temperature and non-optimized anneal treatment etc.,[93,94] may have caused the poor characteristics. More recently Badawi and Anand[22], Dylewski and Joshi[9,96,97], and Kirov et al[98] reported the formation of IMPLOX of quality comparable to that of thermally grown oxides. This improvement was attributed to the implantation being carried out at room temperature and a suitable high temperature anneal treatment (800°C - 1100°C) in dry nitrogen ambients. In some cases Badawi and Anand[22] observed the formation of Buried IMPLanted OXides (B-IMPLOX). They suggested that the IMPLOX layers could be used for device isolation in integrated circuits. If the surface layer of a substrate with a B-IMPLOX layer could be recrystallized, it should be possible to initiate the deposition of epitaxial layers which will be dielectrically isolated from the substrate, but whose orientation is determined by the substrate. The structure thus formed would be expected to be at least free from mismatch defects since the deposition of silicon epitaxial layers on silicon substrates only is involved.

3.2 Implanted Oxygen Profile

The buried nature of the IMPLOX may be visualized by considering the implanted impurity profile[22]. The implanted impurity concentration N(x), using a Gaussian approximation of the LSS projected range distribution[102], is given by

$$N(x_p) = \frac{\Phi}{\Delta R_p (2\pi)^{\frac{1}{2}}} \cdot \exp\left[-\frac{(x_p - R_p)^2}{2\,\Delta R_p^2}\right] \qquad (3.1)$$

where x_p is measured in the direction of the incident ion and

Φ = ion dose. cm^{-2}

ΔR_p = standard deviation in the projected range

R_p = projected range

The peak impurity concentration will be

$$N(R_p) = \frac{\Phi}{\Delta R_p (2\pi)^{\frac{1}{2}}} \simeq \frac{0.4\Phi}{\Delta R_p} \qquad (3.2)$$

Gaussian distribution profiles could be constructed from the table of ordinates given in Table 3.1 using computed values of average projected range and the standard deviation as given by Gibbons, Johnson and Mylroie[103].

Table 3.1

Ordinates for the Gaussian Distribution

$\frac{x_p - R_p}{R_p}$	0	1	2	2.15	3.03	3.72	4.29	4.80	5.26	5.68
$\frac{N(x_p)}{N(R_p)}$	1.0	0.606	0.135	10^{-1}	10^{-2}	10^{-3}	10^{-4}	10^{-5}	10^{-6}	10^{-7}

It should be pointed out that the LSS range theory although valid for targets with a random distribution of atoms i.e. amorphous materials only, can be applied to crystalline

targets provided the ion beam is not incident along any major crystallographic direction[88,89,91,102]. If the incident beam direction coincides with any low index crystallographic direction i.e. parallel to close packed rows or planes, the ions will penetrate deep into the crystal and are said to be channelled. Implanted impurity distributions in crystals are likely to have two peaks, one due to channelling and the other arising from the randomised component resulting from wide angle collisions with surface atoms.

Distribution of oxygen in silicon using the above approach has been obtained by Badawi and Anand[22]. They have shown that the profile obtained on the assumption that the molecular state is retained upon implantation of O_2^+ is identical to that obtained using the more realistic situation in which the O_2 dissociates upon impact into two O atoms with half the energy of the incident O_2^+.

For the formation of silicon dioxide which has a typical concentration of 2.3×10^{22} molecules.cm^{-3} a minimum of 2.3×10^{22} $O_2^+.cm^{-3}$ or 4.6×10^{22} $O^+.cm^{-3}$ must be provided. Therefore, only the part of the profile above the concentration of 4.6×10^{22} O. cm^{-3} will give rise to stoichiometric silicon dioxide formation. Formation of buried oxide (B-IMPLOX) is shown schematically in Fig. 3.1. A B-IMPLOX layer of thickness d_{ox} at a depth d below the surface is indicated[22]. A saturation in the oxygen content is reached when the stoichiometric requirement for the formation of silicon dioxide. is exceeded[99]. In other words a given volume of silicon cannot accomodate an amount of oxygen greater than the stoichiometric requirement for silicon dioxide formation. When the anticipated profile is as indicated in Fig.3.1(a) the observed profile is as shown in Fig. 3.1(b) (see Sec. 4.6.2.5). Gill and Wilson[99] have observed that under very high dose conditions a surface IMPLOX layer of a maximum thickness of $2\ R_p$ (for $O^+ \longrightarrow$ silicon dioxide target) is obtained.

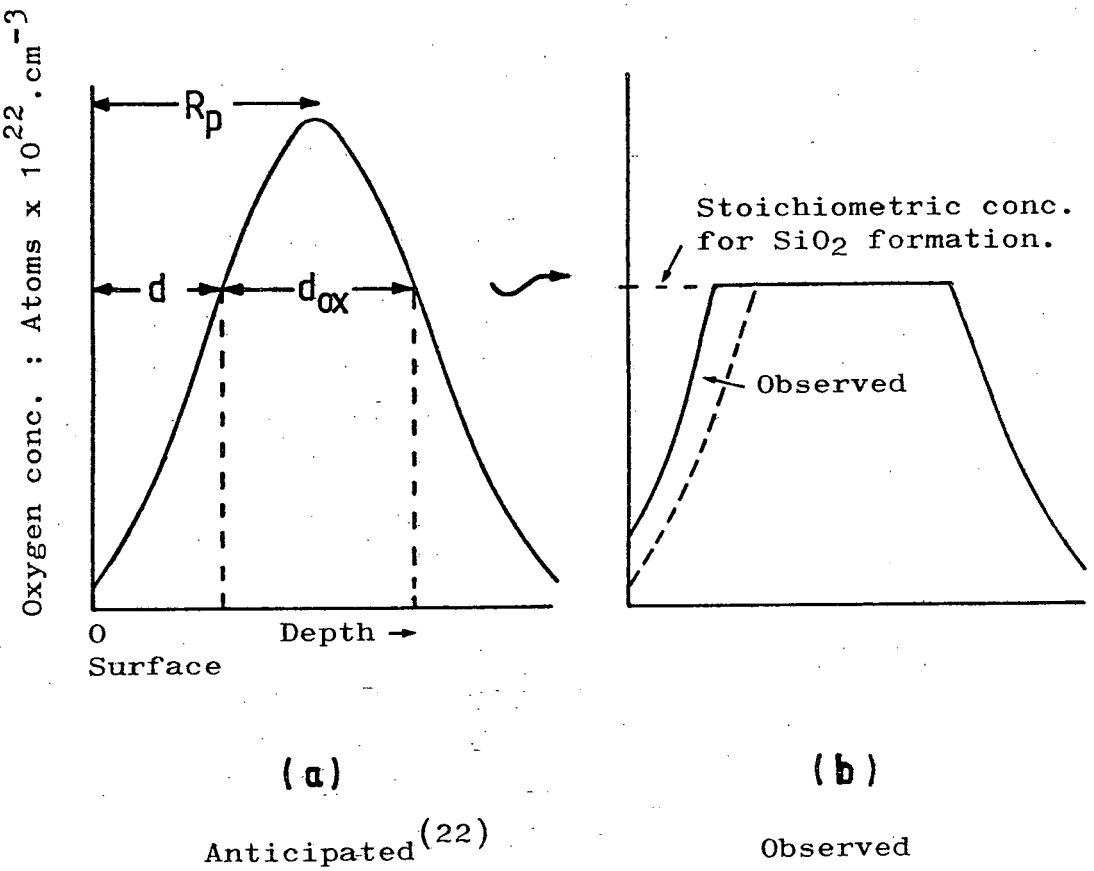

Fig. 3.1. Schematic distribution profile of implanted oxygen.

3.3 Implantation Damage[89,104]

High energy implanted ions in the process of slowing down in a solid target lose energy through inelastic and elastic collisions with the target atoms. The inelastic processes dominate at high energies, resulting in electronic excitation of the target atoms. At low energies the elastic collisions dominate. The elastic processes result in displacement of target atoms and collision cascades are formed. A critical energy at which energy losses by the two processes become equal depends on the ion mass for a given target material. In a single crystal target any displacement of the lattice atoms leads to damage of the periodic structure. When a large number of atoms are displaced in a small volume of the target material, the material changes from crystalline to amorphous form. Individual zones of apparent amorphous form may be seen at relatively low doses. As the ion dose increases the number of these zones increases until they overlap and form a continuous layer extending to a depth approximately equal to the penetration depth of the ions. Amorphous layers produced in silicon by high dose implantation have characteristics similar to amorphous silicon layers produced by r.f. sputtering[105]. The formation of an amorphous layer is generally desirable for the implantation of electrically active species into silicon if high post-anneal activation is to be achieved[106].

The dose required for amorphization depends on the ion mass and temperature of the target[107,108]. At high dose-rate it is also dependent on the dose-rate[107]. There is only a small dependence on ion energy[109] except that the thickness of the amorphous layer depends on the range of the ions at a given energy. At an elevated temperature, re-ordering of the damaged regions takes place due to defect migration (mainly vacancy out-diffusion) and bond rearrangement[107]. At a given temperature there is a critical dose required for the formation

of a continuous amorphous layer. Also, at or above a critical temperature it is impossible to form an amorphous layer[107].

3.3.1. Amorphizing dose

To obtain a simple mathematical expression[104] for the amorphizing dose, it is assumed that each implanted ion produces a right circular amorphous cluster of length R_p and area A_i projected on the surface. The rate at which the amorphous material spreads over the entire surface is given by

$$(dN_A/dN) = A_i(1 - A_A/A_o) \qquad (3.3)$$

where N is the total dose, A_A the total surface area covered by the amorphous clusters and A_o the total area being implanted. The factor $(1 - A_A/A_o)$ is the probability that a given ion is incident upon the undamaged area. The solution of (3.3) may be given as

$$A_A = A_o\,(1 - e^{-A_i\Phi}) \qquad (3.4)$$

where Φ is the dose per unit area. Mayer et al[110] have shown that for an A_i of $(19\ \mathring{A})^2$ this simple theory provides a very good fit for experimental data. For practical purposes it is convenient[104] to define a dose Φ_o, required to convert 0.9 (nine tenths) of the total area (A_o) into amorphous material, as the amorphizing dose, which is then given by

$$\Phi_o = 2.2/A_i = 2.2/\pi R_o^2 \simeq R_o^{-2} \qquad (3.5)$$

On the other hand, an expression for Φ_o can be written directly by assuming that all of the target atoms must be displaced to produce an amorphous layer[107]

$$\Phi_o = \bar{E}\, n_2\, (dE/dx)_o^{-1} \quad cm^{-2} \qquad (3.6)$$

where $\bar{E}$ is the effective energy to displace a target lattice atom, n_2 is the density of the target material in atoms. cm^{-3}, and $(dE/dx)_o$ is the energy-independent nuclear energy loss per unit path length. For practical purposes the nuclear energy loss is given by an approximation[110] to the Nielson equation, i.e.

$$(dE/dx)_o \simeq 7 \times 10^8 \; g_2 \; Z_2^{\frac{2}{3}} \; M_1 (M_1 + M_2)^{-1} \; e \; V.cm^{-1} \qquad (3.7)$$

where Z_1, Z_2, M_1, M_2 are the atomic numbers and masses of the projectile and target, respectively, and g_2 is the density of the target material in $gm.cm^{-3}$. $\bar{E}$ is taken as 25eV for silicon which is roughly twice the estimated threshold energy required to break all bonds.

3.3.2. Temperature dependence of amorphizing dose

The temperature dependence of the amorphizing dose has been considered by Morehead and Crowder[107]. The displaced atoms in the highly disordered or 'amorphous' cylindrical volume of radius R_o surrounding the ion track re-form bonds and relax to form a stable amorphous core. Also, simple defects, i.e. vacancies from the peripheral regions of highly disordered clusters, diffuse out, thereby reordering an outer sheath of width δR, as shown in Fig. 3.2. These events take place in a period of time of the order of 10^{-9}s.

δR is assumed to be of the order of the diffusion length for the vacancies

$$\delta R \simeq (D_v \tau)^{\frac{1}{2}} \qquad (3.8)$$

Fow low substrate temperatures during implantation, out-diffusion of vacancies may be considered to be absent and the δR term does not arise, whereas at elevated temperatures the radius of an amorphous cluster is given by

$$R(T) = R_o - \delta R(T) \qquad (3.9)$$

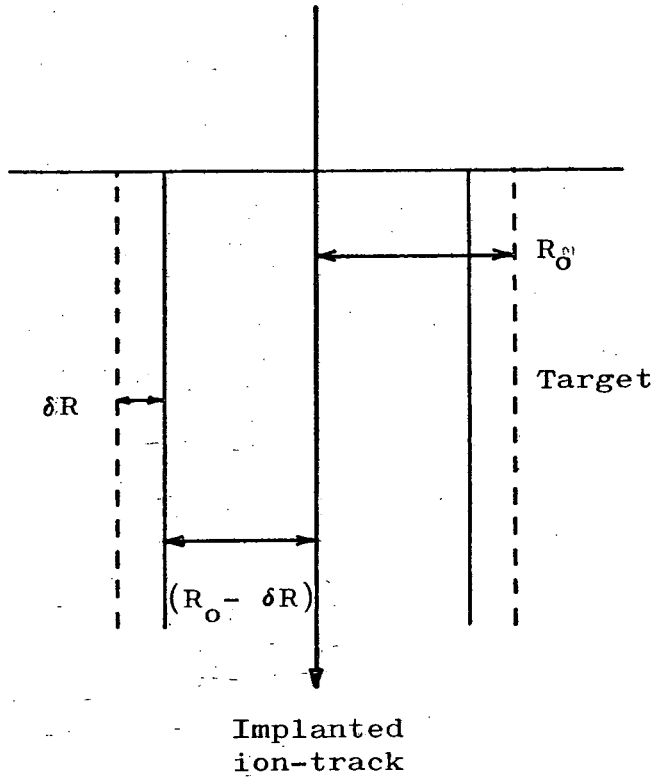

Fig. 3.2. Reordered outer sheath of a cylindrical amorphous region surrounding the ion-track.

The amorphizing dose given by (3.5) will have to be modified according

$$\Phi_T = \left[R_o - \delta R(T)\right]^{-2}$$

$$= R_o^{-2}\left[1 - \delta R(T)/R_o\right]^{-2}$$

$$= \Phi_o\left[1 - \delta R(T)/R_o\right]^{-2} \qquad (3.10)$$

The temperature dependence of δR is obtained by substituting

$$D_{vT} = D_{vo}\ \exp\left(-E_{df}/kT\right) \qquad (3.11)$$

in (3.8). D_{vo} is a constant and E_{df} is the activation energy for the diffusion. Φ_T will then be given by

$$\Phi_T = \Phi_o\left[1 - K'(d\,E/dx)_o^{-\frac{1}{2}}\ \exp\left(-U/kT\right)\right]^{-2} \qquad (3.12)$$

with K' and U as two adjustable constants given by

$$K' = 2\left(\tau\ D_{vo}\ \bar{E}\ n_2\right)^{\frac{1}{2}}$$

$$U = E_{df}/2$$

At a temperature T_∞ such that

$$K'\ (dE/dx)^{-\frac{1}{2}}\ \exp\ (-U/kT) = 1$$

Φ_T will be ∞ , i.e. an amorphous layer will not form. Calculated values of Φ_o, Φ_T at 27^oC and T_∞ for oxygen ion implantation in a silicon target are given in Table 3.2 along with other ions[107] of interest in silicon technology.

TABLE 3.2

Amorphizing dose for ions of interest in silicon technology[107] and oxygen.

Ion	Amorphizing dose. cm^{-2}			T_∞
	low temp.	300°K	300°K measured	°K
Boron	9×10^{14}	4×10^{17}	2×10^{16}	306
Oxygen	5×10^{14}	7×10^{15}	-	350
Phosphorus	2×10^{14}	8×10^{14}	5×10^{14}	430
Arsenic	1×10^{14}	2×10^{14}	2×10^{14}	600
Antimony	6×10^{13}	1×10^{14}	1×10^{14}	730
Bismuth	4×10^{13}	6×10^{13}	5×10^{13}	910

A plot of the amorphizing dose as a function of 1/T for these ions is shown in Fig. 3.3. In these calculations

$$K' = 3.6 \times 10^5 \ (e\ V/cm)^{-\frac{1}{2}}$$

and $U = 0.06$ eV

have been used[107].

It should be mentioned here that the above model, although developed for heavy ions, nonetheless gives a reasonable estimate of the amorphizing dose for light ions. A higher dose will be required for light ions not producing individual amorphous clusters without predamage[104]. An ' energy deposition model' developed by Stein et al[111] does not specifically require the formation and overlap of amorphous clusters. By depositing a critical energy of $\sim 10^{21}$ keV/cm^3, a phenomenon akin to melting occurs in the formation of an amorphous layer provided all the damage produced by the implanted ions is retained as stable disorder[104]. This indeed is the case at low substrate temperatures[107].

3.4 Initial Considerations

It was considered, before embarking on implantation experiments, that if good isolation characteristics were to be achieved, a stoichiometric silicon dioxide layer must be formed. For the subsequent nucleation of an epitaxial layer the crystallinity of the Relatively oxygen-free Surface Layer (RSL) must not be totally destroyed as a result of implantation damage. The concentration of oxygen at the surface also should be kept well below the stoichiometric requirement for the formation of silicon dioxide. Even at a lower concentration of oxygen, the formation of localized clusters of silicon dioxide or other silicon-oxygen complexes is possible[112,113]. The disruptive effect of these clusters on the surface crystallinity should also be kept to a minimum. In an ideal situation the surface concentration of oxygen should not be

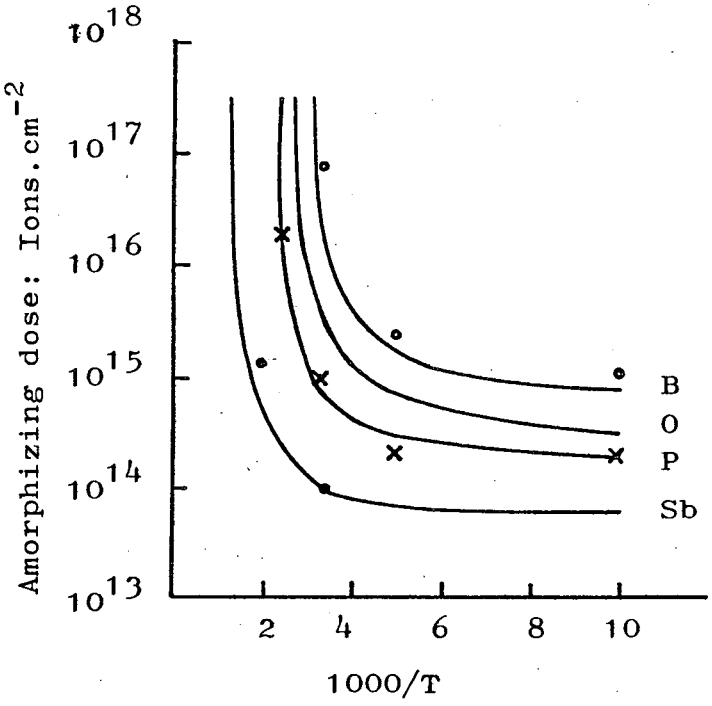

Fig.3.3. Amorphizing dose as a function of 1/T in silicon target, for ions of interest in silicon technology[107] and oxygen ion.

allowed to exceed that in the worst case Czochralski grown crystals i.e. $\sim 2 \times 10^{18}$ O. cm^{-3}[113]. However, the maximum tolerable surface concentration will have to be determined experimentally.

A high energy beam would normally produce a deep buried layer with a low surface concentration. But in order to produce a stoichiometric layer of silicon dioxide of a given thickness, as defined by Badawi and Anand[22] and schematically shown in Fig.3.1(a) a very high dose will be required. This will take long implantation times on the low current multi-user type implanter used in this study. Therefore, dose requirements, shown in Table 3.3, for various energies between 50 keV - 240 keV were worked out so that a stoichiometric concentration of oxygen is available only at the peak of the distribution profile. This is indicated schematically in Fig. 3.4.

It could be seen from Table 3.3 that with a 240 keV beam and a dose of 1.55×10^{18} O^+. cm^{-2} the low surface concentration criterion is well satisfied, but the dose of 1.55×10^{18} $O^+.cm^{-2}$ was considered to be a little too high. It was felt that 200 keV or 180 keV might be a suitable compromise. Initial experiments with 200 keV proved satisfactory. Therefore, it was attempted to optimise conditions for a dose of 1.4×10^{18} O^+. cm^{-2} at 200 keV. Other groups subsequently reported device quality epitaxial layers on substrates with 1.2×10^{18} O^+. cm^{-2} at 150 keV[114,115]. It was also proposed to carry out implantation at lower energies in order to establish the maximum tolerable surface concentration for subsequent epitaxy and the effect of dose variation at a given energy.

At the high doses, of the order of 1×10^{18} ions. cm^{-2} considered here, it is expected that ion bombardment damage would create a continuous amorphous surface layer if the implantations were carried out at $\sim$room temperature[107,108] (section 3.3). Using a model developed by Morehead and

TABLE 3.3

Energy and dose for stoichiometric oxide formation at the projected range.

Energy keV	Dose $O^+.cm^{-2} \times 10^{18}$	Peak conc. $O.cm^{-3} \times 10^{22}$	Surface conc. $O.\ cm^{-3}$
50	0.5	4.6	1.2×10^{21}
70	0.65	4.64	6.5×10^{20}
100	0.86	4.7	2.5×10^{20}
130	1.05	4.7	7.0×10^{19}
150	1.15	4.7	3.4×10^{19}
180	1.3	4.7	2.35×10^{19}
200	1.4	4.76	6.3×10^{18}
240	1.55	4.65	2.3×10^{18}

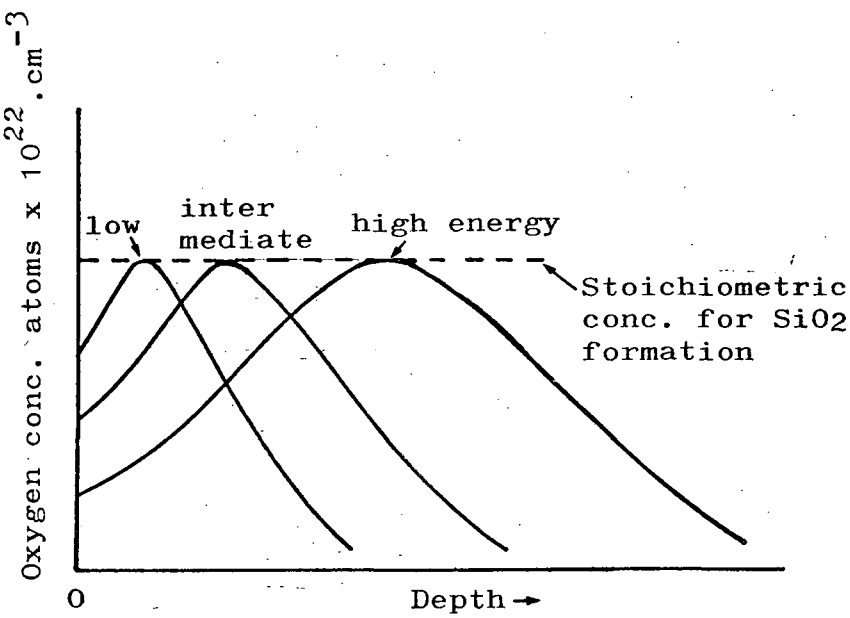

Fig. 3.4. Desired oxygen profile providing stoichiometric requirement of oxygen for the formation of silicon dioxide at the peak of the distribution.

Crowder[107] a temperature of 77°C was obtained above which, for oxygen implantation in a silicon target, an amorphous layer cannot be formed however high the dose might be (Table 3.2). It was decided to determine experimentally the required substrate temperature at which a good degree of surface crystallinity will be maintained.

3.5 Implantation Experiments

A 500 keV general purpose implanter designed and built at the University of Surrey Accelerator Laboratory was used in this work. The description and performance of this machine is well documented[116,117,118]. An r.f. plasma type oxygen source was employed. A typical mass spectrum of the source is shown in Fig. 3.5. An O_2^+ beam was used in preference to an O^+ beam as the former species produced a consistently higher beam current. As a result an accelerating voltage of 400 keV had to be used to obtain an effective beam energy of 200 keV for the atomic species. The implantation parameters are quoted in terms of the effective energy and the corresponding dose for the atomic species, through the entire text. Electrostatic beam scanning was used. A 1 sq. cm central area of 2 cm x 2 cm or 3.7 cm diameter 3-5 Ωcm n-type (111) substrates was exposed to the beam through a stainless steel mask.

Implantation parameters and conditions are given in Tables 3.4 - 3.7. The initial experiments were carried out with a 200 keV beam and a dose of 2.5×10^{17} $O^+ . cm^{-2}$. The dose was gradually increased to 1.4×10^{18} $O^+ . cm^{-2}$ as shown in Table 3.5. At a later stage an estimated dose of up to 2.5×10^{18} $O^+ . cm^{-2}$ was implanted.

A small specimen holder with a low thermal mass was used in the early experiments. This could accommodate only a small number of 2 cm x 2 cm substrates and had a low thermal mass. A substantial temperature rise, estimated at a later stage to be ~ 550°C was obtained due to beam induced heating. Successful epitaxial deposition following a short anneal

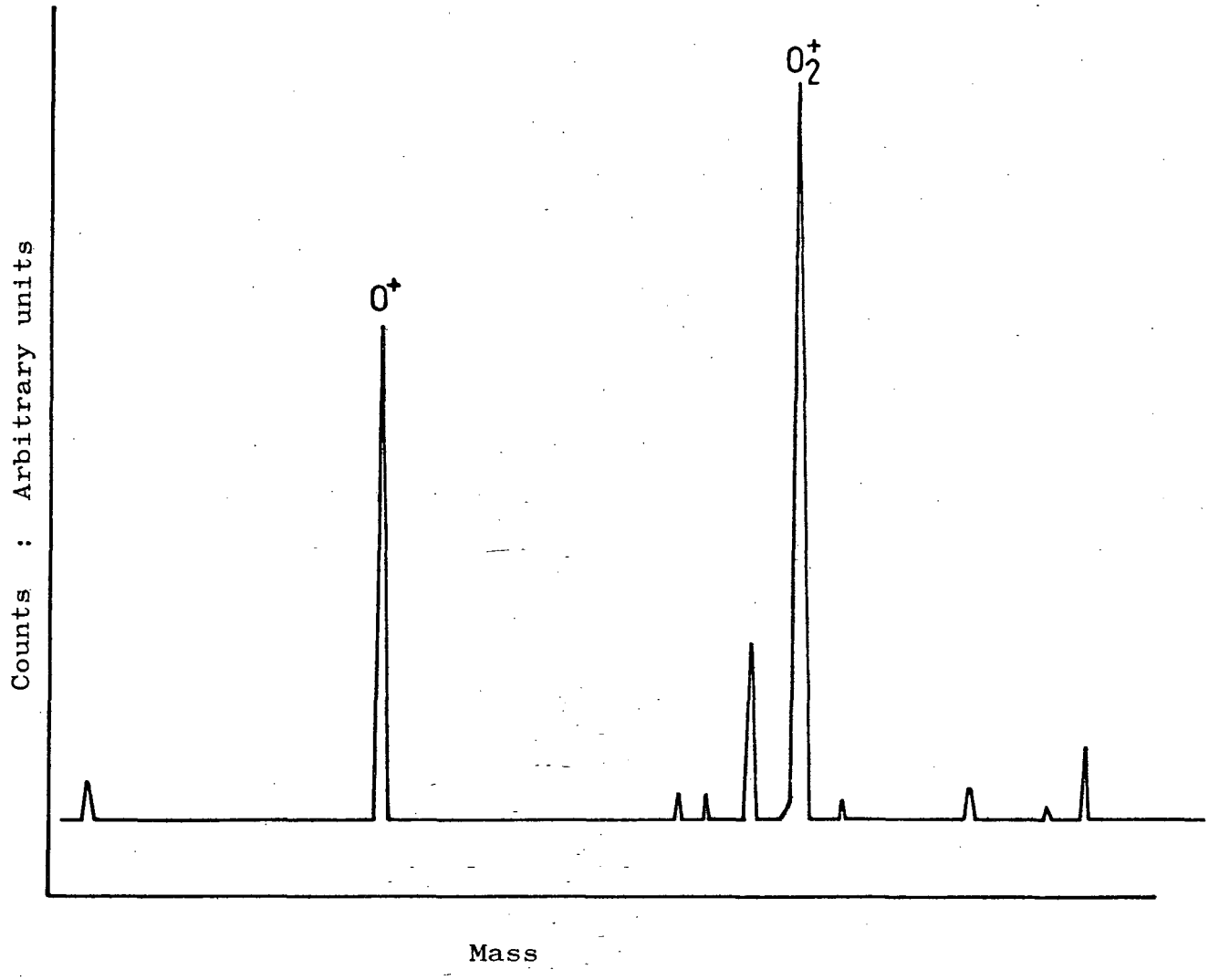

Fig. 3.5. Mass spectrum of oxygen ion source.

TABLE 3.4

Implantation conditions for the study of the effect of beam energy with corresponding doses to provide the stoichiometric requirement of oxygen to form silicon dioxide at the peak of the distribution. Normal incidence was used except where mentioned.

Specimen holder	Energy keV	Dose $O^+.cm^{-2} \times 10^{18}$	Beam current μA		Substrate temp. °C
			Total	scanned	
No.2 carousel-type holder providing good heat-sink.	50	0.5	20-30	10-15	-room temp.
	70	0.65	"	"	" "
	100	0.86	"	"	" "
	130	1.05	"	"	" "
	150	1.15	"	"	" "
	180	1.3	"	"	" "
	200*	1.4	"	"	" "
	240	1.55	"	"	" "

* also implanted at a tilt of 8° from the normal but this did not appear to affect either the distribution of oxygen or the surface crystallinity.

TABLE 3.5

Implantation conditions for the study of the effect of dose at a given energy. The beam was normally-incident on the substrate.

Specimen holder	Energy keV	Dose $O^+ . cm^{-2}$ x 10^{18}	Beam current μA		Substrate temp. ^oC
			total	scanned	
No.1 low thermal mass	200	0.25	40-45	15-17	not estimated
	"	0.5			"
	"	0.75			"
		1.0			"
No.3 Heated sp. holder with heater dis-connected	200	1.4	20-30	10-15	~550°
	"	1.9	30-35	25	-
	"	2.5	30-35	25	~750°

TABLE 3.6

Implantation conditions for determining the effect of substrate temperature for a dose of 1.4×10^{18} $O^{+}.cm^{-2}$ at 200 keV.

Specimen holder	Beam current μA		Mode of heating	Substrate temp. °C
	total	scanned		
No.2 Carousel type	20-30	10-15	heat-sink	~room temp.
No.3 Substrate heated	6-8	3-4	substrate heating	~200
No.3 Substrate heated	10-12	5-6	" "	~275
No.3 heater disconnected	20-30	10-15	beam heating with min. contact.	~550

TABLE 3.7

Implantation conditions for determining the effect of substrate mounting with minimal thermal contact. The beam was normally-incident. A dose of 1.4×10^{18} $O^{+}.cm^{-2}$ at 200 keV was used.

Specimen holder	contact	Beam current μA	
		total	scanned
No.3 Heated sp. holder with heater disconnected	normal	20-25	10-12
	minimum	20-25	10-12

treatment in a hydrogen ambient was achieved in all cases.

Subsequently a carousel-type specimen holder accommodating up to 17 3.7/5.0 cm diameter wafers was used for increased throughput. The use of 3.7 cm diameter whole wafers still with 1 cm^2 implanted area, improved the subsequent handling to a large extent. A number of wafers were implanted to a dose of 1.4 x 18 O^+ cm^{-2} at 200 keV and also some implants were obtained with a selection of energy-dose combinations as shown in Table 3.4. Unfortunately this specimen holder dissipated beam-induced heat rather efficiently; as a result the wafers were implanted at near room temperature. A continuous, amorphous surface layer was formed which could not be recrystallized by a subsequent anneal treatment (see Section 3.6.5.)

Implantation to a dose of 1.4 x 10^{18} O^+. cm^{-2} at 200 keV was also carried out at temperatures of~200°C and~275°C using a heated substrate holder accommodating two 3.7/5 cm diameter wafers. A maximum temperature of~275°C was obtainable.

A combination of substrate heating and beam heating was also attempted in order to produce a higher substrate temperature as a high enough beam current (~ 10 μA scanned beam) was not always available to bring about a rise in temperature to ~ 550°C. The major problem encountered with the heated specimen holder was that the specimen interchange mechanism became inoperative at the high implantation temperatures. It had to be allowed to cool below ~100°C before substrate interchange could take place, thus reducing throughput.

In some experiments the heated specimen holder was used with the heater turned off and it was attempted to obtain the maximum effect of beam-induced heating. In these experiments the substrates were mounted with a minimal thermal contact with the holder plate. Small pieces of thin stainless steel wire spacers were introduced between the substrate and the

holder plate, while the substrates were held in position by stainless steel clips making only point contacts. The arrangement is shown schematically in Fig. 3.6. In a control experiment it was attempted to determine the effect of these spacers, a first substrate with, and a second without, spacers, while other conditions were maintained as identical as possible. A minimum scanned beam current of ~10 μA was used in this experiment. In a number of cases 15 - 17 μA was obtainable.

Under similar implantation conditions a 2 cm x 2 cm substrate was expected to have a higher temperature rise than a 3.7 cm diameter wafer. This would arise directly from the reduction of the radiative area available outside the 1 cm^2 implant area. Also, with experience, it appeared that with 3.7 cm diameter wafers the temperature across the implanted area was non-uniform, the central ~7 mm region being hotter than the outlying region. The quality of the subsequently deposited epitaxial layer on the outlying region was visibly inferior to that on the central region.

To obtain a high degree of dose uniformity over the exposed area about two-thirds of the total beam current had to be sacrificed in over-scanning. However, in most of the above experiments, about one half was used thereby compromising on the uniformity, still approximately 8 mm x 8 mm area of uniform dose distribution was obtained.

In some experiments, using minimal beam scanning, currents up to 25 μA were obtained. This way temperatures up to ~ 750°C were obtained and high doses up to ~2.5 x 10^{18} ions.cm^{-2} could be introduced in a localized central area (2 - 3 mm dia.) for the same number of counts normally required for a dose of 1.4 x 10^{18} $O.^{+}$ cm^{-2} over 1 sq. cm. area. With high doses the damage at the interface between the B-IMPLOX and the surface silicon layer is reduced (Section 4.6.2.10). Thus better interface characteristics will be expected and a higher degree of isolation than that provided by 1.4 x 10^{18} O^{+}.cm^{-2}

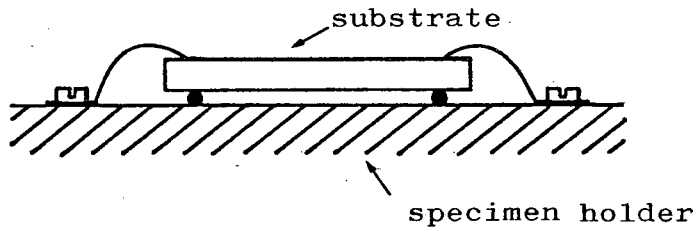

Fig. 3.6. Arrangement used for minimizing thermal contact between substrate and specimen holder, during implantation.

will be obtainable.

3.6 Anneal Treatment

The role of an anneal treatment is seen as threefold:

1) To provide the activation energy for the chemical reaction between the implanted interstitial oxygen and silicon to form silicon dioxide and also for the re-arrangement of distorted SiO_4 tetrahedra (see Section 4.5.1).

2) To recrystallize the relatively oxygen free silicon surface layer.

3) To minimize the damage at the interface between the surface silicon and the B-IMPLOX layers.

[Broadly speaking steps (2) and (3) may be considered as a single physical process but (2) taking place in a relatively short time 5 - 15 mins. at 1100°C. No systematic study has been undertaken for the optimization of step (3)].

So far only thermal annealing has been considered in the present programme, except for very recent preliminary work on laser beam annealing. The anneal temperature, time, the ambient and the crystalline state of the as-implanted substrate are likely to have a critical effect on the B-IMPLOX/recrystallized surface layer structures. The various anneal schedules attempted are given in Table 3.8 and described in sub-section 3.6.5.

An anneal treatment for 5 mins. at a temperature of 1100°C in a hydrogen ambient appeared to be satisfactory. This permitted the use of the epitaxial reactor under normal operating conditions for both annealing and subsequent epitaxial deposition (see section 3.6.1.).
This anneal treatment was also adequate for the formation of silicon dioxide (Sec. 3.6.2 and 4.5.1) and recrystallization of the surface layer (see sections 3.6.3 and 4.6.2.7).

3.6.1. Use of the Epitaxial Reactor for Annealing

The reactor was normally run at 1100°C. The susceptor was initially heated in a low hydrogen flow. The output r.f. power was increased manually to the required level in about 7-10 minutes. Then the hydrogen carrier flow was increased to 60 l/m. A period of 5 mins. was allowed to achieve thermal equilibrium before introducing the silane and dopant gases. The use of this 5 min. period sometimes extended to 15 mins. as the anneal time, eliminated a separate anneal schedule and accompanied heating and cooling cycle. Thus the anneal and epitaxial deposition was combined into a single process step.

3.6.2 Formation of Silicon Dioxide

For the formation of electrically-inactive silicon dioxide precipitates in Czochralski grown silicon crystals, an anneal treatment at a temperature between ~650° and 1150°C is necessary[112,113,119]. At higher temperatures ~1350°C the SiO_4 tetrahedral bonds are broken and the oxygen atoms return to interstitial positions[112]. On the other hand, at low anneal temperatures 300° - 500°C electrically active donor type silicon-oxygen complexes are formed[112,120]. A very long anneal at 600°C for 60 hours tends to arrange the SiO_4 tetrahedra in a α- quartz type crystallographic form[121]. At a temperature of 1100°C the formation of silicon dioxide as indicated by the characteristic absorption spectrum, is complete (see Sec.4.5.1) in ~5 min. (disregarding the heating up time in the epitaxial reactor). An 1100°C anneal treatment has also been reported to have produced IMPLOX layers of quality comparable to that of thermally grown oxides[22].

3.6.3 Recrystallization of the Surface Layer

In the case of silicon, an amorphous layer produced by low temperature, high dose implantion of group III and V ions, can be subsequently recrystallized by solid phase epitaxial

regrowth from the undamaged substrate at relatively low anneal temperatures between ~500° and 650°C[104,105,106]. At a higher anneal temperature (900° - 1150°C) a random nucleation of crystallites takes place[122,123]. These crystallites grow in size until neighbouring grains of varying orientations meet a common grain-boundary at which point any further growth stops. The resulting material is, at best, polycrystalline. A two-stage anneal with an initial long low temperature step followed by a short high temperature treatment produces better crystallinity[122,124].

At a substrate temperature of 500° - 650°C, during implantation, in addition to the vacancy out-diffusion[107], solid-phase epitaxial regrowth of the damaged region also takes place. This may be considered to be the first step of a two-step anneal process.

In the case of implantation of oxygen in silicon to a sufficiently high dose a new phase, i.e. silicon dioxide, is formed. This new phase is likely to be amorphous particularly if the stoichiometric level of oxygen for the formation of silicon dioxide is approached. The relatively oxygen-free surface layer will be separated from the undamaged substrate by the amorphous B-IMPLOX layer. Therefore the substrate will not be available for the initiation of the low temperature solid phase epitaxial regrowth. Even at high anneal temperatures only very small crystallites are formed (Section 4.4.1.2). If, however, the implantation is carried out at a temperature between 500° and 650°C the crystallinity of the surface layer is expected to be retained to a reasonable degree through vacancy out-diffusion and, probably through lateral and downward epitaxial regrowth of the damaged regions particularly when the oxygen concentration builds up and the crystalline continuity between the undamaged substrate and the surface layer is lost. This 'in-situ continued anneal' at elevated implantation temperatures appears to be absolutely essential if a good degree of surface crystallinity were to be main-

tained at the high implantation doses of the order of 10^{18} O^+ cm^{-2} considered here (Sec. 4.6.2.6.). A subsequent high temperature anneal further enhances the surface crystallinity permitting an epitaxial deposition (see Sec. 4.6.2.7.).

For the purpose of recrystallization, the B-IMPLOX structure may be considered in a way similar to that of a deposited thin silicon layer on oxidized silicon substrates. The thin silicon layer may be amorphous, polycrystalline or a damaged crystal depending upon the implantation temperature and also the IMPLOX itself requires an anneal treatment to allow for the formation of silicon dioxide.

Recrystallization of deposited silicon layers by thermal annealing has been studied by a number of workers[125-128]. The transition from amorphous to crystalline silicon films is a function of both time and temperature. Feldman and Plachy[125] have estimated a crystallization time of 3 seconds at 850°C. Amorphous layers deposited on fused silica substrates held at 300° - 500°C under high vacuum conditions have been crystallised to form grains of 0.5 - 1 µm in diameter at temperatures of 850° - 1000°C[125]. Recrystallization of thick poly-silicon layers of 50 - 100 µm in thickness with initial grain size of 0.1 - 1 µm at temperatures between 1150° and 1250°C produced an average grain size of 20 µm[127]. At anneal temperatures of 1350°C average grain size of ~100 µm was obtained[127,128].

It is also interesting to note that 'crystalline silicon' (crystallites) has been observed following the decomposition of deposited 'silicon monoxide' in vacuum or inert ambient at 800° - 900°C. The reaction, $2SiO \rightarrow Si + SiO_2$, has been suggested. There is some controversy in the literature regarding the existence of 'silicon monoxide' in the solid phase[121,129,130]. Some authors have suggested that deposited 'silicon monoxide' is a mixture of silicon and silicon dioxide with a 1:1 silicon: oxygen ratio[121]. The observed

crystallinity may relate to grain formation of the silicon component during anneal. As-implanted low temperature IMPLOX is identical to deposited 'silicon monoxide' as far as the infra-red absorption characteristics are concerned. Non-stoichiometric regions of the IMPLOX following anneal will probably be similar to annealed 'silicon monoxide', i.e. a mixture of silicon crystallites and clusters of silicon dioxide.

Considering the above observations relating to the recrystallization of deposited silicon layers it would seem reasonable to expect an enhancement of surface crystallinity of the B-IMPLOX structures by an anneal treatment at 1100°C. A very high-temperature anneal at ~1350°, although desirable from the crystallinity considerations would be detrimental to the IMPLOX layer as SiO_4 tetrahedral bonds will be broken and the oxygen will return to interstitial states, also a diffusion of oxygen away from the IMPLOX region may take place.

3.6.4. Pre-anneal Cleaning

No particular cleaning treatment seemed necessary prior to implantation except for blow cleaning with a filtered nitrogen pressure jet to remove particulate material. Pre-anneal cleaning of implanted wafers appeared to be very critical in eliminating some topographical defects in the epitaxial layer.

The normal cleaning procedure involved ultrasonic agitation in isopropyl alcohol, five minutes in concentrated sulphuric acid/hydrogen peroxide (1/1) mixture, deionised water rinse, 30 sec. dip in 10% hydrofluoric acid followed by a final deionized water rinse. The sulphuric acid/hydrogen peroxide treatment were repeated three times in most cases. A very thin layer of silicon was thus removed and the surface topography of the deposited epi-layer improved generally. A final spin drying seemed almost essential as water droplets tended to adhere to the implanted damaged area. It was difficult to accommodate 2 cm x 2 cm pieces in the spin drier, therefore,

a cold nitrogen jet had to be used carefully to remove the adhering water. The wafers were finally blow-dried in hot nitrogen.

3.6.5. Anneal Schedules (Table 3.8)

The early low-dose implants (Table 3.5)were annealed in the epitaxial reactor at a temperature of 1000°C for 30 minutes in oxygen-free nitrogen. At the end of the anneal treatment the carrier was changed to hydrogen and an epitaxial layer was deposited at 1100°C. The surface of the epitaxial layer had an interesting topography as shown in Fig.4.12 (Sec.4.4.1.3). This was probably due to the effect of localized presence of silicon dioxide on the post nucleation growth of the epitaxial layer (see section 1.2). The oxide may have formed during anneal in nitrogen which contained residual (ppm) quantities of moisture and oxygen.

The use of dry, oxygen-free hydrogen as the anneal ambient for 30 minutes at 1000°C improved the surface topography to a large extent, as viewed by an optical microscope.

Subsequently, for considerations outlined in Sec.3.6.1 - 3.6.4 an anneal treatment for 5 - 15 minutes at 1100° was carried out before the introduction of silane and dopant gases in the reactor. This procedure reduced the epitaxial deposition on the B-IMPLOX substrates to a single step operation.

At this stage a large specimen holder affording an increased throughput of 3.7 cm dia.wafers was used.This specimen holder acted as a good heat sink, thereby maintaining the wafers at a temperature very close to room temperature (Section 3.5). These substrates, during anneal treatment in a hydrogen ambient at 1100°C lost the B-IMPLOX layer probably through the permeation of the hydrogen through the amorphized surface layer and a reaction with the B-IMPLOX, producing 'volatile' silicon monoxide and water vapour[131] (see Section 4.5.1).

TABLE 3.8

Anneal Schedules

All samples were implanted to a dose of $1.4 \times 10^{18} O^+.cm^{-2}$ at 200 keV except where stated otherwise.

Sample	Temp. °C	Ambient	Time	Effect
Low dose implants (Table 3.5)	1000	N_2	30 min.	High incidence of overgrowths in deposited epi-layer
	1000	H_2	30 min.	Surface conc. of overgrowths reduced.
room temp. implant	1100	H_2	5 min.	B-IMPLOX lost
	1150	H_2	2 hrs.	B-IMPLOX lost, surface recrystallized.
	550 +	N_2	40 hrs.	
	1150 +	N_2	2 hrs.	B-IMPLOX retained
	1100	H_2	5 min.	B-IMPLOX lost
200°C implant	550 +	N_2	40 hrs.	
	1150 +	N_2	2 hrs.	
	1100	H_2	5 min.	B-IMPLOX retained
275°C implant	550 +	N_2	40 hrs.	
	1150 +	N_2	2 hrs.	
	1100	H_2	5 min.	B-IMPLOX retained
550°C implant	550	N_2	8 hrs.	No improvement in surface crystallinity.
	550 +	N_2	8 hrs.	
	1150	N_2	2 hrs.	Surface suspected to be degraded.
	1100	H_2	5 min.	B-IMPLOX retained, surface crystallinity enhanced.

The surface layer could, however, be recrystallized to a high degree by prolonged anneal at 1100° for the low energy/low doses. A dose of 1.4×10^{18} O^+ cm^{-2} at 200 keV required two hours at 1150°C. The B-IMPLOX layer was retained in these substrates by the use of a nitrogen ambient although the surface layer could not be recrystallized by a one-stage anneal treatment at 1150° for two hours or even a two-step treatment initially at 550°C for 40 hours, followed by another 2 hours at 1150°C (see Section 4.6.2.6.).

A comparison of the infra-red absorption spectra of the substrates implanted using specimen holders no. (1) and (2) to a dose of 1.4×10^{18} O. cm^{-2} at 200 keV indicated that the early implants on specimen holder (1) had undergone an in-situ anneal at an approximate temperature of 550°C (Section 4.5.3). In other words, considerable sample heating took place in the specimen holder as the beam heating could not be dissipated efficiently. At high substrate temperatures the surface layer retains a good degree of crystallinity and appeared to act as a barrier to the permeation of hydrogen to the B-IMPLOX layer.

Subsequent implants to a dose of 1.4×10^{18} at 200 keV carried out at~200°C and~275°C were annealed at 550°C for 40 hours followed by 2 hours at 1150°C both in nitrogen ambients. These substrates also had a 5 minute pre-deposition anneal in the epitaxial reactor. The B-IMPLOX layer was retained but the quality of the epitaxial layer was poor (Section 4.6.2.6).

In the latest implants a temperature of ~550°C was obtained with a minimal contact between the substrate and the specimen holder. A five minute anneal in hydrogen at 1100°C retained the B-IMPLOX and also enhanced surface crystallinity and enabled epitaxial deposition of a high quality. A two-step anneal treatment, with 8 hours at 550°C followed by 2 hours at 1150°C both in nitrogen ambients, was also attempted. The 550°C step did not contribute to any enhancement of surface

crystallinity whereas the 1150°C step appeared to have degraded the surface layer.

3.7 Epitaxial Deposition

Epitaxial deposition was carried out at 1100°C. A flow of 60 l/m of hydrogen giving flow velocity of 126 $cm.sec^{-1}$ was used. A silane concentration of 0.2% by volume in hydrogen was used to obtain growth rate 0.66 μm. The layers were doped with phosphorus to give a resistivity of approximately 2 Ω cm.

CHAPTER 4

ANALYTICAL TECHNIQUES

EXPERIMENTAL DETAILS AND RESULTS

4.1 Introduction

The analytical techniques to be used were selected with the following objectives :

1. To study the crystalline quality of the surface layers of implanted and annealed wafers in order to assess the suitability for subsequent epitaxial deposition and also the quality of deposited epitaxial layers.

2. To obtain the distribution profile of the implanted oxygen and study the nature of the oxide formed.

3. To study the nature of crystallographic defects in the deposited epitaxial layer, requiring both destructive and non-destructive sample preparation.

The techniques used are listed below :

a) Visual inspection under normal ambient lighting and strong focussed illumination for a qualitative assessment of the surface damage.

b) Optical and scanning electron microscopy for topographical study.

c) Infra-red absorption spectroscopy, of as-implanted and annealed substrates, for establishing the nature of the implanted oxide and comparison with other forms of silicon dioxide particularly thermally grown layers.

d) Rutherford back-scattering spectroscopy using a 1.5 MeV He^+ ion beam for determining the oxygen distribution profile and assessing the crystalline quality of the surface layer.

e) Reflection electron diffraction using a 80 keV beam in a transmission microscope for establishing the crystalline nature of the surface layer.

f) Sirtl etching of deposited epitaxial layers to reveal stacking faults and other defects.

g) Transmission electron microscopy of thinned cross-sectional samples with epitaxial layers for studying crystallographic defects.

h) X-ray topography of deposited epitaxial layers for non-destructive study of the defects.

i) Auger electron spectroscopy of an as-implanted sample for oxygen profiling.

Some of the above techniques such as infra-red absorption spectroscopy, Rutherford back-scattering and reflection electron diffraction etc., were used extensively. The other techniques were used for a limited number of samples. Almost all the samples were initially inspected visually and with an optical microscope. The experimental details of the above techniques are described and results obtained are given in the following sections.

4.2 Visual Inspection under Ambient Illumination

As-implanted and annealed wafers implanted to a dose of 1.4×10^{18} O^+. cm^{-2} at an energy of 200 keV (and particularly those implanted at a substrate temperature of $\sim 550^{\circ}C$) do not look substantially different from unimplanted wafers. In some

samples a variation in colour over the implanted area, and more frequently, with high dose implants ($\sim 2.5 \times 10^{18}$ $0.cm^{-2}$), brightly coloured rings were observed, as shown in Fig.4.1. These are probably due to thickness variations of the crystalline surface layer, the subsurface damaged layer and the buried oxide layer brought about by the nonuniformity of dose distribution and variations in the substrate temperature[132,133]. Lower energy implants showed more prominent oxide colouration. The boundaries of the implanted areas were always observable by oblique viewing. In a small number of (111) substrates implanted at $\sim 550^{o}C$, macroscopic surface damage, as shown in Fig. 4.2,was observed. A higher incidence of similar defects was observed in (100) substrates. These are probably cracks originating from severe slip resulting from sharp temperature gradients.

4.3 Visual Inspection under Strong Illumination

Samples were placed under an optical microscope with a x10 objective. The surface was brought into focus and viewed obliquely as indicated in Fig. 4.3. Any departure from optical flatness caused diffuse reflection of the incident beam making the surface appear milky or hazy. The degree of haziness is qualitatively assessed and loosely related to a degradation of the surface crystallinity. An amorphous surface appears very hazy indeed. Under high dose conditions the surface haze is sometimes apparent even with normal ambient illumination[105]. The appearance of haze is an indication of the onset of amorphization. Visual inspection has been considered to be more sensitive than electron diffraction studies, as amorphous diffraction patterns are obtained at a dose approximately an order of magnitude lower than that required to produce saturation disorder in silicon[105].

4.3.1 Results

Visual inspection under strong illumination is very simple and one of the most effective techniques for the observation and qualitative assessment of surface roughness or a departure

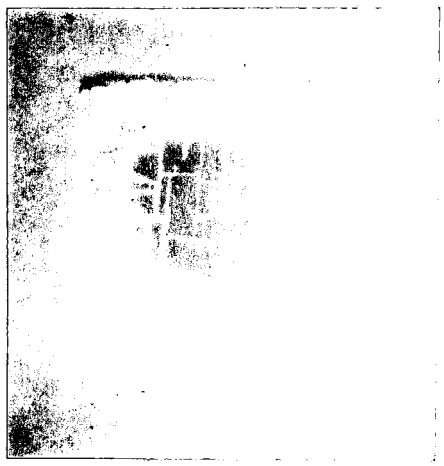

Fig. 4.1. Interference colour rings in substrates implanted to a high dose and macroscopic surface damage in (100) substrates.

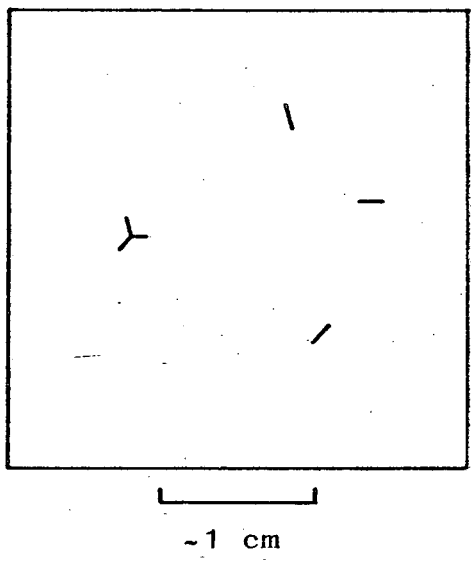

Fig. 4.2. Macroscopic surface damage in (111) substrates. The sample was implanted to a dose of 1.4×10^{18} $O^{+}.cm^{-2}$ at 200°C.

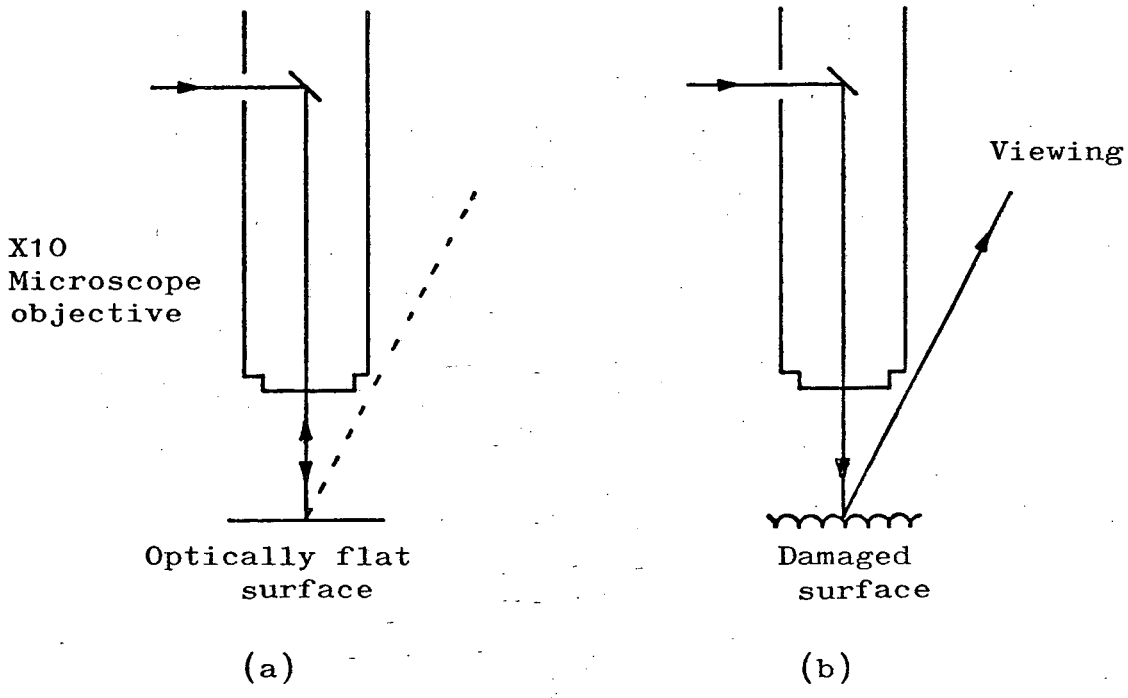

Fig. 4.3. Visual inspection under strong illumination.

from crystallinity of the surface layer. Polycrystalline or amorphous surface layers produced by high dose implantation normally do not retain the high degree of optical flatness of the starting material, resulting in a diffuse reflection of the incident light. A qualitative assessment of the surface haze as a function of substrate temperature during implantation is given in Table 4.1. Implantation in a substrate at $\sim 550^{\circ}C$ produced an almost haze-free surface, whereas lower temperature implants at $\sim 275^{\circ}C$ or lower had hazy surfaces.

4.4 Optical and Scanning Electron Microscopy

Optical and scanning electron microscopy techniques were used for studying the surface topography and its dependence on implantation conditions and anneal treatment. A Leitz Metallux microscope fitted with a Nomarsky objective, a polariser and an analyser was used. Angle-lapped B-IMPLOX samples were investigated using a Carl Zeiss Epival Interphako microscope. Some samples were investigated using an ISI SUPER III scanning electron microscope operated in the conventional secondary electron mode.

4.4.1. Results

Results produced in this section relate to an implant dose of $1.4 \times 10^{18}\ O^{+}.\ cm^{-2}$ at 200 keV. Thickness of the epitaxial layers investigated was 1 μm.

4.4.1.1. Angle-lapped Samples

$\sim 0.65^{\circ}$ angle lapped samples with buried implanted oxide layers showed a distinct interference contrast arising from the B-IMPLOX layer, as shown in Fig.4.4. The substrate during implantation was held at near room temperature and subsequently annealed at $1150^{\circ}C$ for 2 hours in a nitrogen ambient. For samples implanted with the same dose and energy the observed contrast did not appear to vary with substrate temperature during implantation and anneal treatment. From Fig. 4.4 a

Table 4.1

Qualitative assessment of surface-haze.
Samples implanted to a dose of 1.4×10^{18} $O^+.cm^{-2}$ at 200 keV.

Sample	Appearance in the as-implanted state
~Room-temp. implant	hazy
~200°C implant	hazy
~275°C implant	hazy
~550°C implant	almost haze-free

Fig. 4.4. 'Interphako' micrograph of the B-IMPLOX layer in an angle-lapped sample.

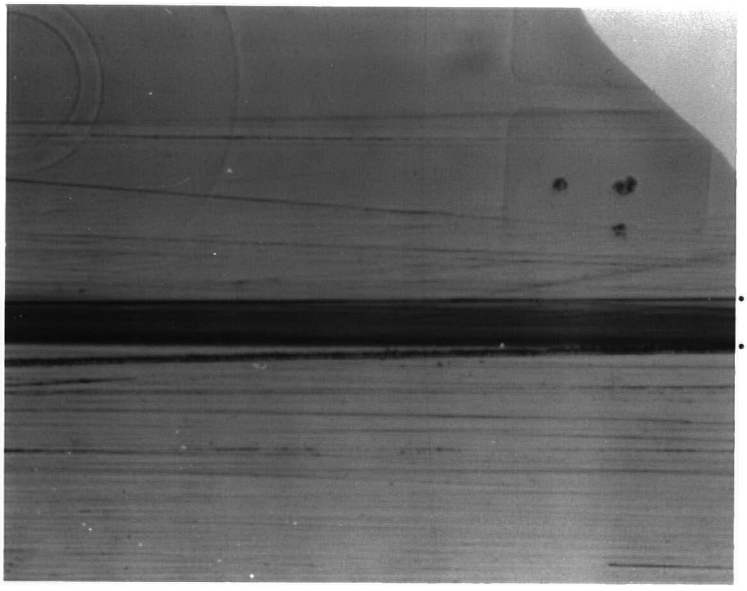
B-IMPLOX
100μm

B-IMPLOX thickness of ~0.3 μm and a depth of ~0.35 μm below the surface were worked out.

4.4.1.2. As-implanted and Annealed Samples

As-implanted samples except the ~200°C implant had hardly any features observable with an optical microscope. The surface features contributing to a hazy appearance were suspected to be below the limit of resolution of an optical microscope. These features apparently did not contribute to any contrast in the scanning electron micrographs.

Samples implanted at room temperature following an anneal treatment in a nitrogen ambient for 2 hours at 1150°C showed a definite change in topography. A fine 'orange-peel' type structure just resolved by the optical microscope was observed as shown in Fig.4.5(a). It is speculated that this structure is due to the formation of isolated pyramidal crystallites with rounded features of the type shown in the sketch in Fig.4.5(b). It is also speculated that the height h of these crystallites is directly related to the thickness of the relatively oxygen-free surface layer. A high density of etch pits, delineating the edge of the implanted area, was observed in the SEM as shown in Fig.4.6, although no other features were observed in the implanted area. These etch-pits are very similar in appearance to dislocation etch-pits in (111) silicon normally revealed by Sirtl etching and probably are indicative of a high density of dislocations at the high-stress implant boundary region. The mechanism of the preferential etching process is not understood but speculated to be thermally induced.

The as-implanted~200°C sample had a fine 'orange-peel'surface as shown in Fig.4.7(a). Following the intermediate anneal at 550°C for 40 hours in a nitrogen ambient, the sample showed a feature as shown in Fig. 4.7(b) The subsequent 1150°C anneal further modified the topography as shown in Fig.4.7(c). Formation of closely-spaced crystallites as indicated in the sketch in Fig.4.7(d) is speculated.

Fig. 4.5 (a). Fine orange-peel type surface in samples implanted to a dose of 1.4×10^{18} $O^+.cm^{-2}$ at 200 keV at $\sim$ room temperature following an anneal treatment for 2 hours at 1150°C in a nitrogen ambient.

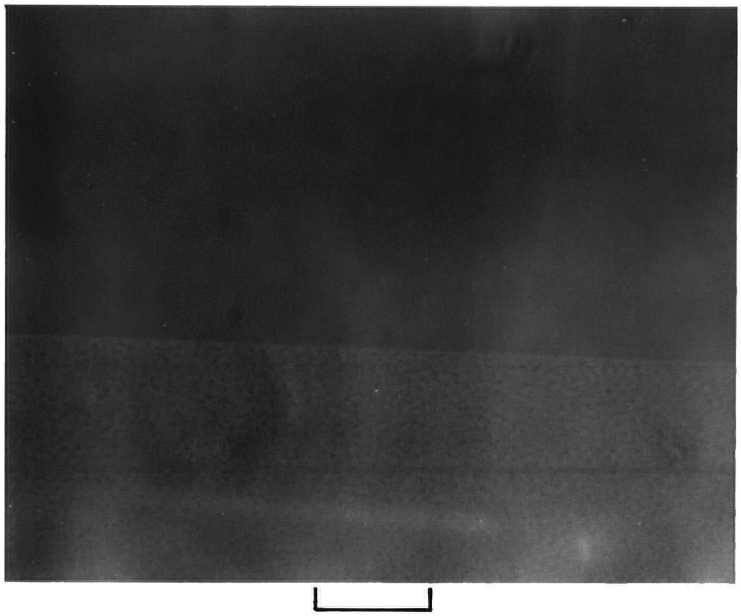
Implanted
area
20μm

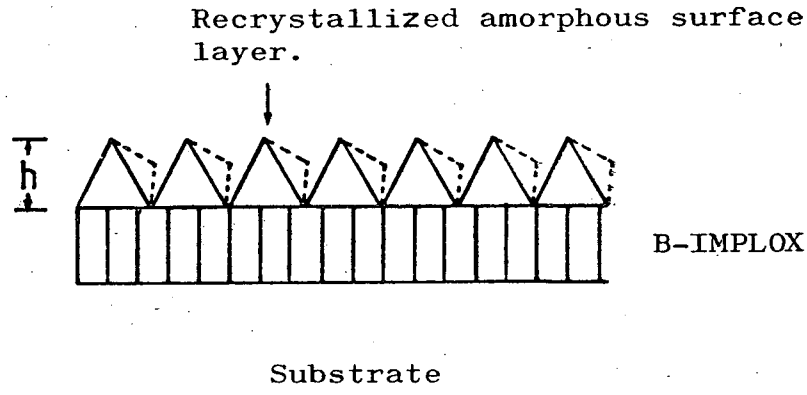

Fig. 4.5 (b). Formation of pyramidal crystallites during anneal treatment.

Fig. 4.6. Scanning electron micrograph of etch-pits at the implant-boundary in annealed samples.

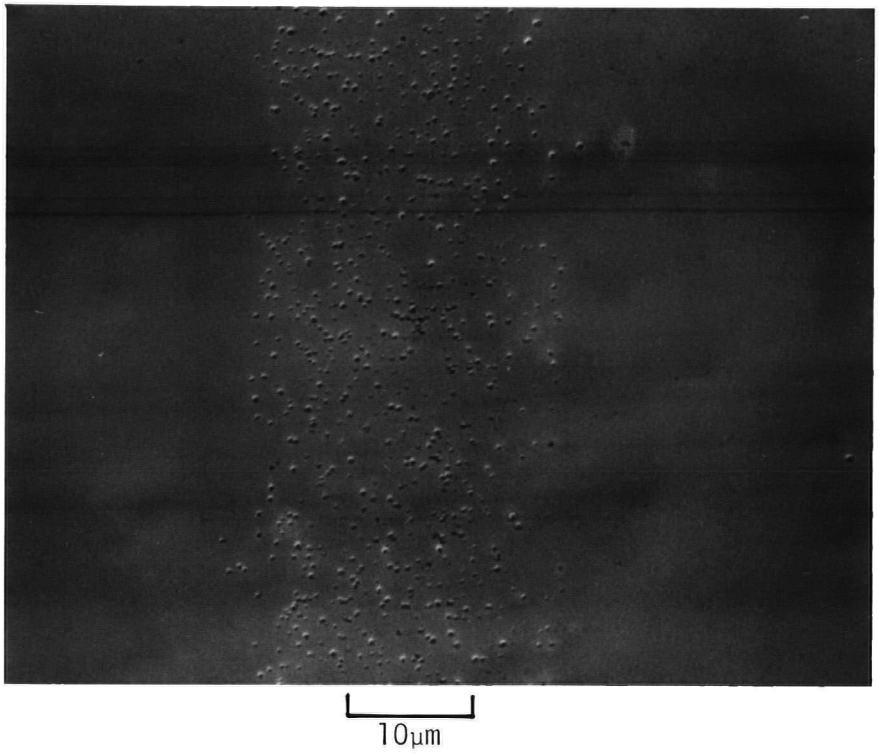
Edge of the implanted area
Implanted area
10μm

Fig. 4.7 (a). Surface structure of the 200°C implant in the as-implanted state.

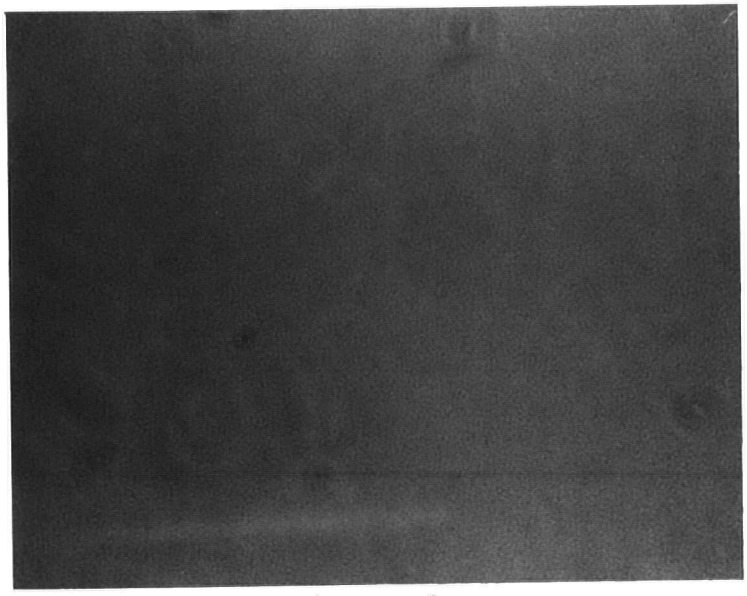

20μm

Fig. 4.7 (b). Surface structure of the 200°C implant following an intermediate anneal at 550°C.

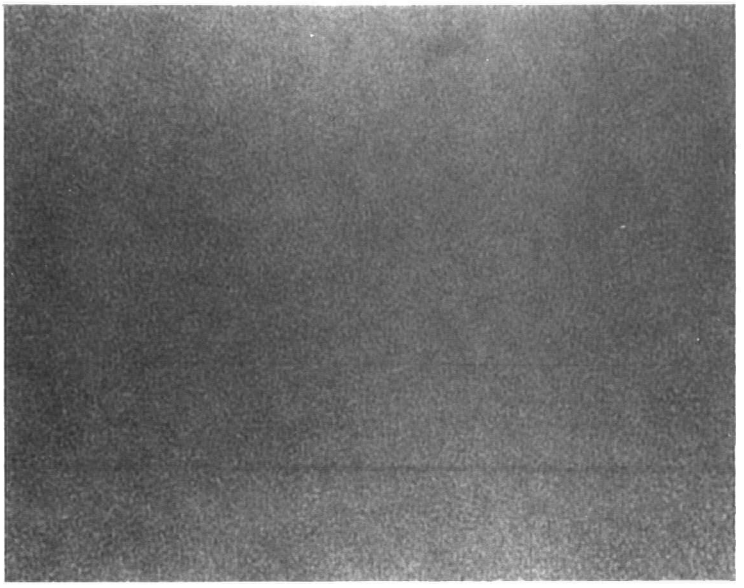
20μm

Fig. 4.7 (c). Surface structure of the 200°C implant following the final anneal at 1150°C.

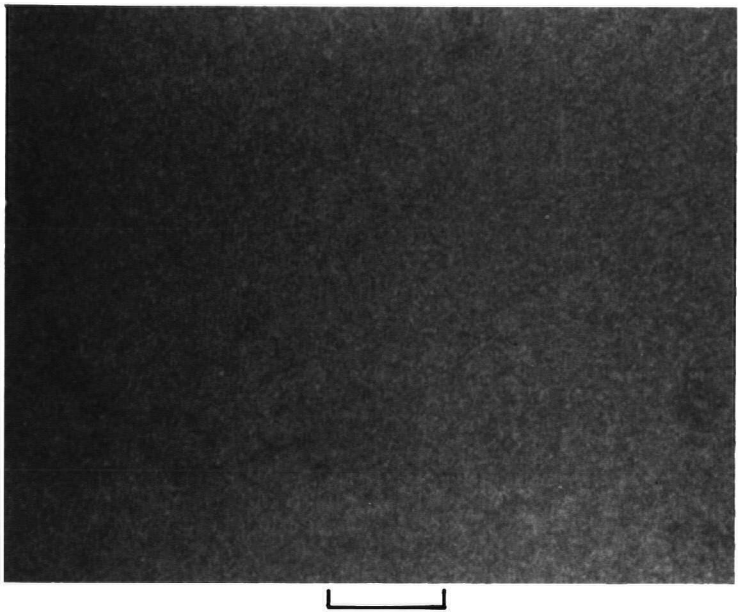
20 µm

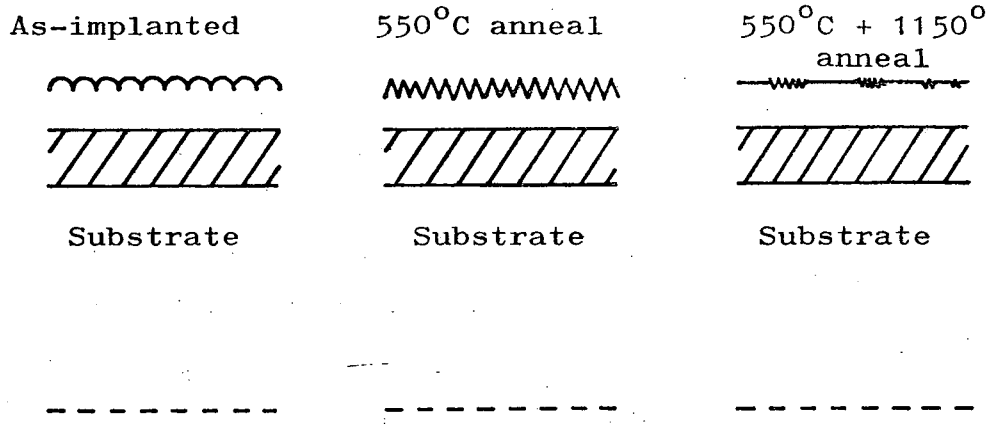

Fig. 4.7 (d). Surface structure of the 200°C implant in the as-implanted state and following anneal treatments, shown schematically.

The ~275°C implant had no particular optically-resolvable feature. However, following a two step anneal treatment (550°C + 1150°C) a fine structure, as shown in Fig. 4.8, was observed in the scanning electron micrographs of samples coated with 25 - 50Å thick layer of gold.

Substrates implanted at ~550°C following an anneal treatment at 1100°C for 5-15 mins. in a hydrogen ambient had mainly a featureless surface except for an occasional incidence of 'blisters'. Samples annealed in a reduced pressure hydrogen ambient of 80 torr in an AMR 7600 epitaxial reactor at 1100°C were apparently free from these 'blisters'.*

4.4.1.3. Epitaxial Layers

The epitaxial layer deposited on the substrate implanted at ~200°C had a surface topography as shown in Fig. 4.9. The sample had undergone a two-stage anneal treatment, at 550°C for 40 hours followed by 2 hours at 1150°C, prior to a 5 min. treatment at 1100°C in a hydrogen ambient immediately followed by epitaxial deposition. The presence of features, as sketched in Fig. 4.10 in the micrograph in Fig. 4.9 is interpreted as evidence of twinned growth. Twinned growth is probably initiated by existing re-crystallization microtwins formed during post-implantation anneal treatment of the partially damaged surface layer.

The epitaxial layer on the ~275°C implant which had undergone the same anneal treatment as the ~200°C sample, showed a varied topography. Certain areas, as shown in Fig. 4.11(a) were comparable to the ~200° sample, whereas in other areas the surface tended to be featureless as shown in Fig. 4.11(b)

Epitaxial layers deposited on substrates implanted at ~550°C following an anneal treatment at 1100°C for 5-15 mins. in a hydrogen ambient had about $10^3 . cm^{-2}$ growth pyramids of the type appearing in Fig. 4.12. The surface was otherwise featureless. In some early samples, annealed in a nitrogen ambient

*Work carried out by T J Distler, Harris Semiconductor Products Division, Melbourne, Florida.

Fig. 4.8. Scanning electron micrograph of the 275°C implant following a two-step anneal treatment (550° + 1150°C). The specimen was tilted at an angle of 55° for micrography.

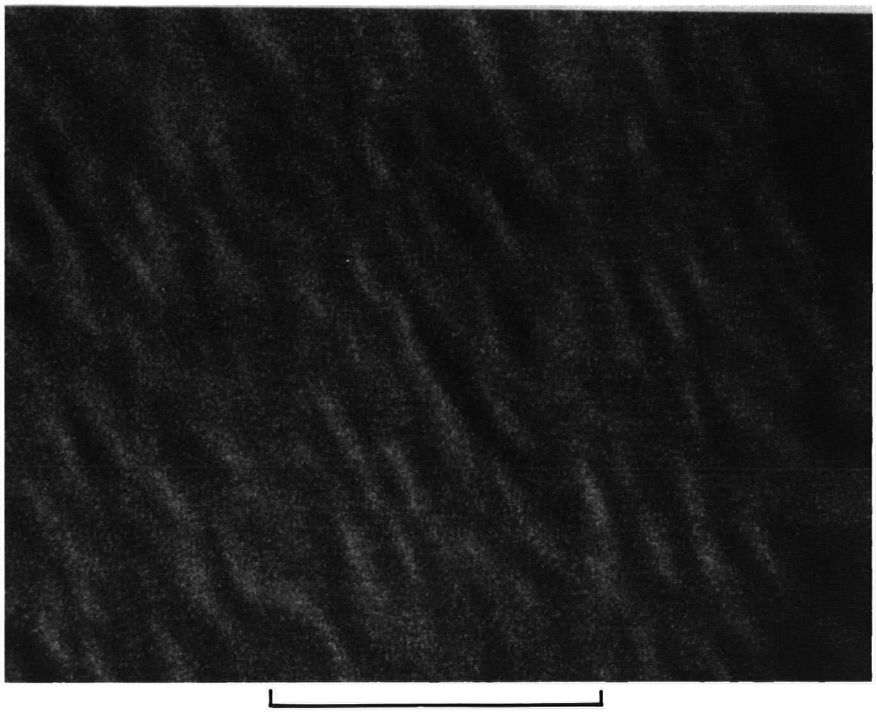

1.0μm

Fig. 4.9. Scanning electron micrograph of an epitaxial layer deposited on the 200°C implant.

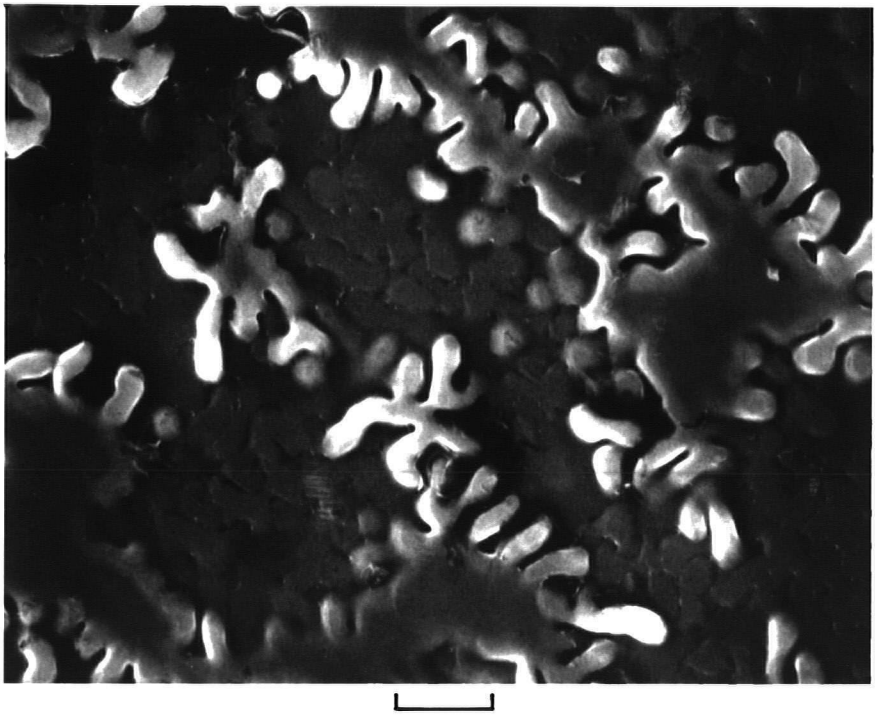
10μm

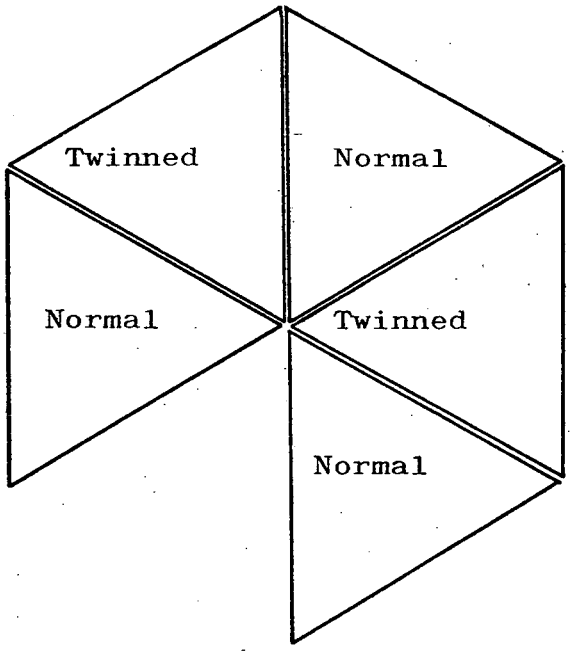

Fig. 4.10. Twinned overgrowth in the epitaxial layer.

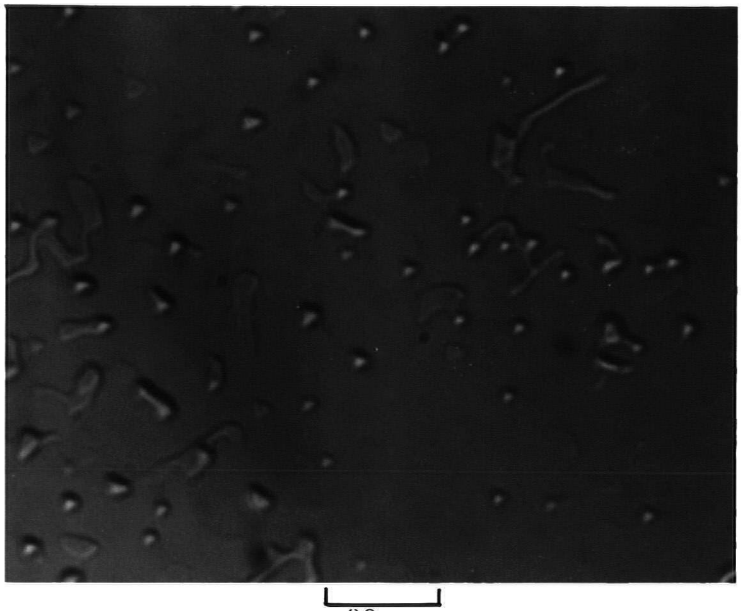
20μm

Fig. 4.11 (a). Scanning electron micrograph of an epitaxial layer deposited on the 275°C implant. The area shown is comparable to the layer on the 200°C implant.

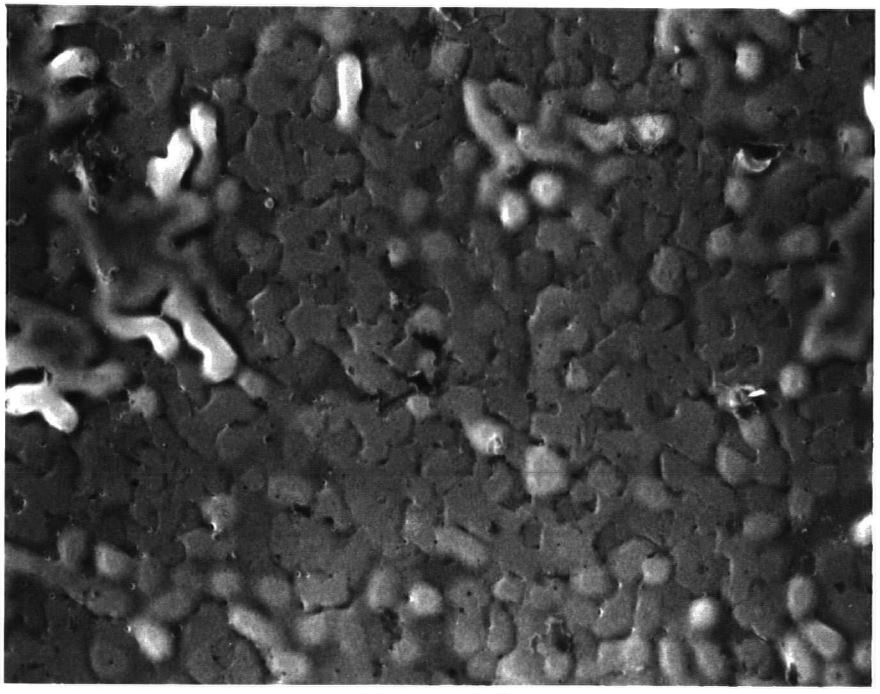

10μm

Fig. 4.11 (b). Scanning electron micrograph of an epitaxial layer deposited on the 275°C implant. The area shown has a lower incidence of topographical features than that deposited on the 200°C implant.

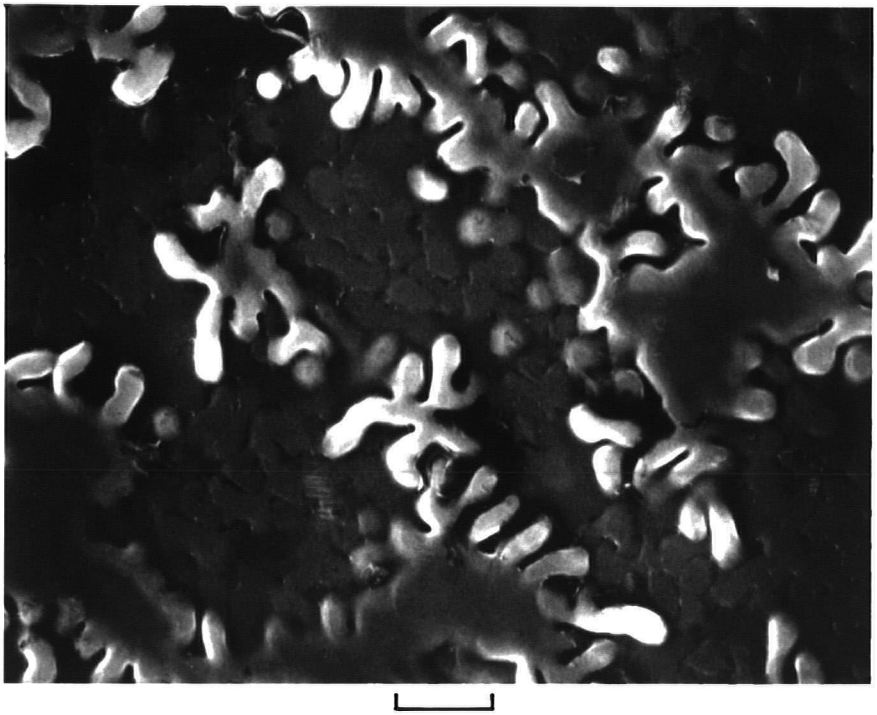
10μm

Fig. 4.12. Optical micrograph of the epitaxial layer deposited on a low-dose implant (5×10^{17} $O^+.cm^{-2}$ at 200 keV) annealed in a nitrogen ambient.

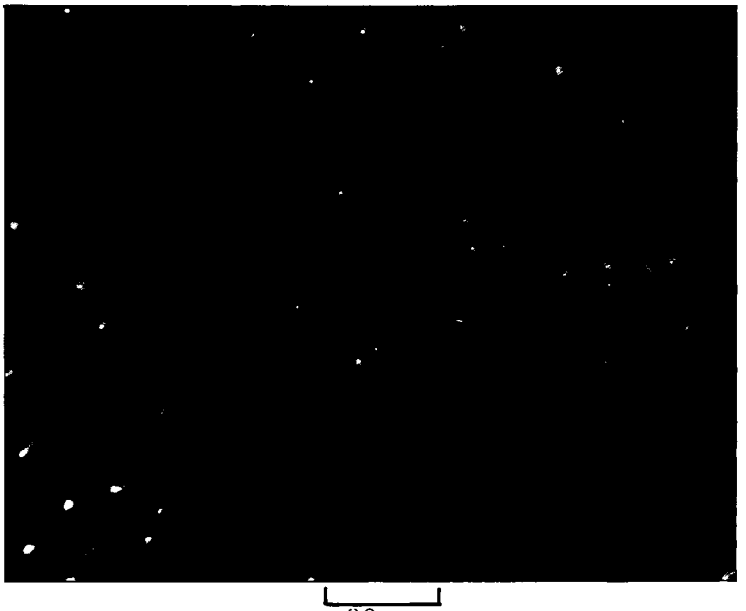
20μm

at 1000°C prior to epitaxial deposition, a high density of growth pyramids and other crystallographic overgrowths was observed, as shown in Fig.4.12.These are considered to be the effect of trace amounts of oxygen or moisture, in the nitrogen anneal ambient, on the post-nucleation growth of the epitaxial layer (see Section 1.2). A dry, oxygen-free hydrogen ambient improved the topography significantly, as shown in Fig.4.13. A lower incidence of overgrowths in the implanted area is attributed to defect gettering by the implantation damage[79,84]. Subsequently, a combination of a hydrogen ambient anneal and repeated treatment in concentrated sulphuric acid and hydrogen peroxide mixture followed by a dip in 10% hydrofluoric acid produced featureless epitaxial deposition, as mentioned above.

4.5 Infra-red (IR) Absorption Spectroscopy

IR absorption spectra were obtained from all implanted samples in the as-implanted state and following an anneal treatment, using a Perkin-Elmer 297 dual-beam spectrophotometer, in the 2.5 μm - 16 μm range. Wafers with oxide layers between 0.04 and 0.5 μm in thickness, grown in a dry oxygen ambient at 1000°C were also studied for comparison. A high overall transmittance could be obtained using a beam attenuator or a matching silicon wafer, in the reference beam, without an oxide layer either thermally grown or implanted. However, it was observed that exact matching of general absorption was extremely difficult as absorption was somewhat dependent on orientation with respect to the beam, the exact position of the wafer under the beam and also on slight variation of thickness between the sample and reference wafers. It was also observed that absorption peaks with a silicon reference or a beam attenuator shifted to slightly higher wavelengths than those obtained with air as a reference. Therefore, most of the experiments were carried out with air as a reference, although a relatively lower transmittance was obtained. Also samples with lapped-back surfaces scattered the beam severely and hardly any transmission was obtained. Fortunately the wafers

Fig. 4.13. Epitaxial layer deposited on a low-dose implanted sample (5×10^{17} $O^+.cm^{-2}$ at 200 keV) annealed in a hydrogen ambient. The implanted area has a lower incidence of overgrowths.

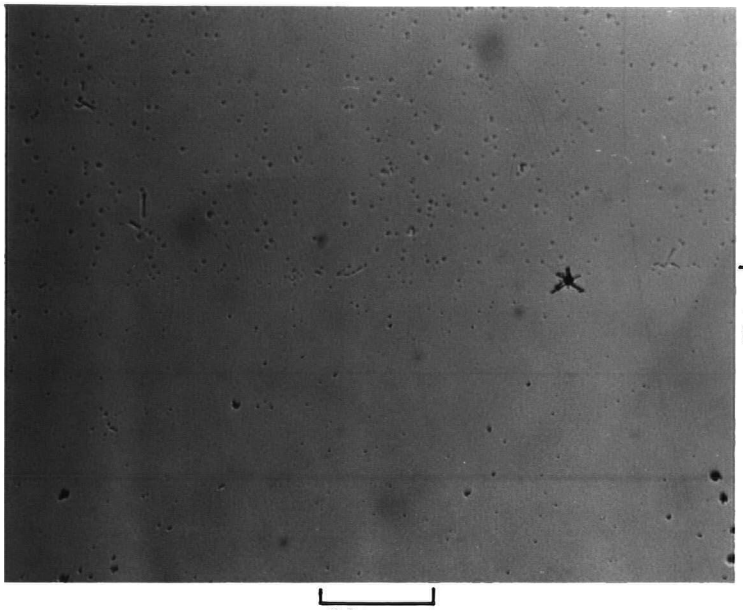
Implanted
area
200μm

used in this work had chemically polished back surfaces. However, it should be noted that lapping damage may prove to be efficient in gettering subsequent process induced defects[134]. A silicon wafer from the same batch must be used as reference if lapped wafers are used and the shift in the peak position also will have to be taken into consideration.

4.5.1. Results

A small absorption peak at ~9μm was observed in the substrates in the unimplanted state, as shown in Fig. 4.14. This absorption is probably due to the presence of oxygen, in Czochralski grown crystals, in the form of silicon dioxide clusters and/or an Si_2O (Si-O-Si) complex formed with oxygen atoms which might still be in solid solution. It is not possible to distinguish between silicon dioxide and Si-O-Si absorption from the room temperature spectra[135].

In implanted samples the wavelength of the absorption peak in the as-implanted state at a given implant temperature depends on the dose, whereas at a given dose it is determined by the temperature during implantation. A sample implanted to a dose of 1.4×10^{18} $O^+.cm^{-2}$ at 200 keV at near room temperature had an absorption peak at ~10μm, as shown in Fig. 4.14. The higher temperature implants show a shift of the peak towards shorter wavelength, as shown by the spectra in Fig. 4.14, also in Table 4.2. This shift of the peak indicates a partial in-situ annealing of the implanted oxide. Absorption spectra arising from lower dose implants are also shown in Fig. 4.14. The dose dependence of the peak position is broadly in agreement with the observation reported by Dylewski and Joshi[95]. A pronounced shoulder at 9 μm also occurred in these spectra, the corresponding absorbance, $\ln(I_o/I_{tr})$ for higher temperature implants being greater, as shown in Table 4.2. This is probably indicative of an enhancement of the Si-O-Si type bonds with temperature.

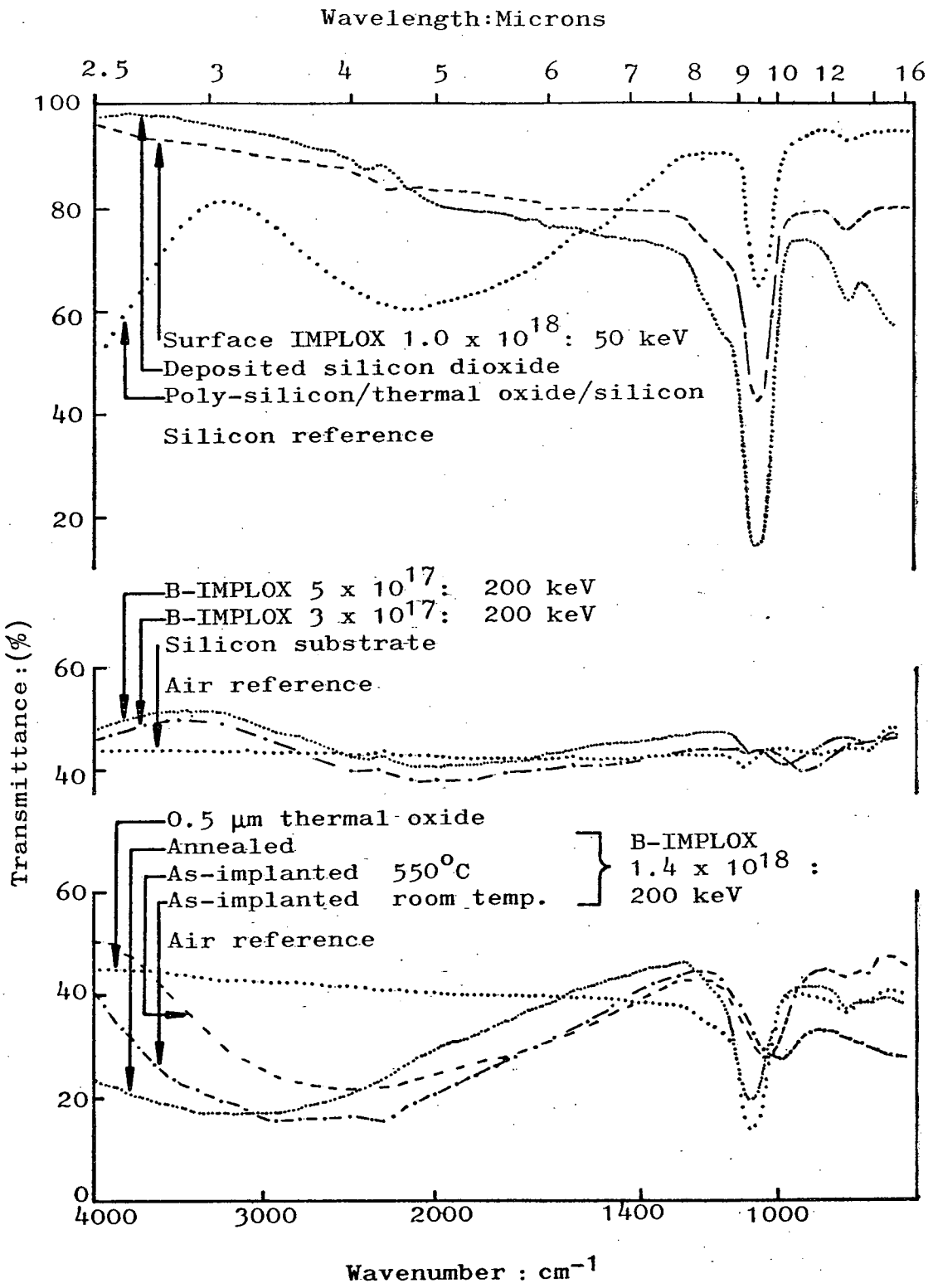

Fig.4.14. Infra-red absorption spectra of the substrate, implanted oxides in the as-implanted an annealed states, thermal and deposited oxides and buried thermal oxides.

TABLE 4.2

Infra-red peak position and absorbance at 9 μm as a function of substrate temperature during implantation.

Samples implanted to a dose of 1.4×10^{18} $O^{+}.cm^{-2}$ at 200 keV.

Sample	IR peak as-impl.	position μm annealed	Absorbance at 9 μm in the as-implanted state
~Room temp. implant.	10.1	9.2	0.08
~200°C implant	10.0	9.2	0.08
~275°C implant	9.9	9.2	0.14
~550°C implant	9.7	9.2	0.15

The absorption peak at ~10 μm obtained from the room temperature implants is almost identical to that observed by Hass and Salzberg[129] and Garski[121] in evaporated films of silicon monoxide.

The implant samples annealed at a temperature of 1000°C or above gave rise to a prominent peak at 9.2 μm (Fig. 4.14) regardless of the substrate temperature during implantation. A weaker peak at 12.5 μm is also observed. Another peak at ~ 8.4 μm seems to be present but is not entirely resolved, due to the proximity of the more prominent peak at 9.2 μm. However, these peaks are not observed in samples implanted at room temperature following an anneal treatment in a hydrogen ambient, indicating a total loss of the B-IMPLOX layer.

The absorption spectra of annealed, oxygen-implanted samples are almost identical to those obtained from oxides thermally grown in a dry oxygen ambient. Spectra similar to those obtained from thermal oxides were observed by Hass and Salzberg[129] from silicon monoxide films heat treated in air and also from chemically prepared silicon dioxide films (prepared by condensing fumes produced by exposing silicon tetrachloride to moist air and then baking the film for 8 hours at 350°C). Silicon dioxide layers, formed by reacting silane with oxygen at 450°C and annealed at 1000°C for 10 minutes, also produced similar absorption spectra, as shown in Fig. 4.14.

The 9.2 μm peak in a thermal oxide appears to be somewhat sharper than that of the implanted oxide. At a point where the absorbance is one-half of the peak absorbance the IMPLOX peak is approximately 10% broader than the thermal oxide peak. This is probably due to the environment in which the absorbing bonds are situated, particularly at the B-IMPLOX-Si interfaces where some bonds are likely to be unsatisfied and strained, thus giving rise to an effect of 'not too tight a coupling'.

Buried implanted oxides, both in the as-implanted and in the

annealed state, also have a broad absorption band in the 2.5 μm - 7.5 μm region. This appears to be due to the buried nature of the oxide. A similar broad band, as shown in Fig.4.14, has been observed in a poly-silicon/thermal oxide/ silicon structure. Implanted surface oxides do not show this broad absorption band as seen in the spectrum of a sample implanted to a dose of 1×10^{18} O^+. cm^{-2} at 50 keV, Fig. 4.14.

Infra-red absorption of silicon dioxide in various crystallographic forms, and as fused silica[136-138] and silicon monoxide[121,129,130,139], has been studied by a number of investigators. The tetrahedral SiO_4 group is considered to be the principal building block in all forms of silicon dioxide. Neighbouring SiO_4 groups are connected by bridging oxygen atoms. Various polymorphs of silicon dioxide are characterised by the value of the angle between neighbouring SiO_4 tetrahedra. In fused silica the SiO_4 tetrahedra are randomly distributed. The exact nature of the absorption spectra varies somewhat from one form to the other, but, in general, silicon dioxide in any form has characteristic absorption in the following regions of the infra-red spectrum[136-138]

8 μm - 10 μm	Si-O	stretching modes associated primarily with the motion of the oxygen atoms
12 μm - 17 μm	Si-O-Si	stretching modes associated with the movement of the silicon atoms, and
17 μm - 25 μm	Si-O-Si	bending bonds.

The longest wavelength region falls outside the range of the instrument used in the present work.

The 10 μm absorption peak observed in silicon monoxide films evaporated from a mixture of silicon and silicon dioxide, giving a 1:1 silicon to oxygen ratio, is believed to be due to Si-O stretching mode vibrations in isolated SiO_4 groups

separated by clusters and chains of silicon atoms[121]. The SiO_4 tetrahedra are also likely to be highly distorted. There is a considerable disagreement in the literature over the existence of silicon monoxide as a stoichiometric compound (see section 3.6.3.). However, silicon monoxide may exist in the vapour phase at temperatures between 1100° and 1200°C as a product of the reactions[23]:

1. $Si + SiO_2 \longrightarrow 2\ SiO$
2. $SiO_2 + H_2 \longrightarrow SiO + H_2O$

During the oxidation treatment of evaporated silicon monoxide films, the number of SiO_4 groups increases and, depending upon time and temperature, interlinking of the SiO_4 tetrahedra takes place. On prolonged heating, a crystalline quartz-like structure is approached[121].

Although as-implanted silicon shows a 10 μm peak identical to silicon monoxide, following an anneal in an inert or reducing ambient, a silicon dioxide-type absorption is observed. The shift of the 10 μm peak to 9.2 μm, with significant sharpening of the peak, indicates that the distortion of the individual SiO_4 tetrahedra is substantially reduced. In addition, an ordering and interlinking of the neighbouring tetrahedra is likely to have an effect. The appearance of the 12.5 μm absorption peak in the annealed material is interpreted as a direct indication that a degree of interlinking, comparable to that in thermally grown oxides, takes place. It appears from the absence of the 12.5 μm absorption peak that hardly any interlinking between the SiO_4 tetrahedra exists in the as-implanted material. The peak at 8.4 μm, which is not well resolved, falls well within the range of the Si-O bond stretching absorption. This is probably due to the influence of interlinking of the SiO_4 tetrahedra on the Si-O bond stretching absorption.

4.5.2. Estimation of Buried Oxide Layer Thickness from IR Spectra

Infra-red absorption spectra of silicon dioxide films grown in a dry oxygen ambient and those of annealed IMPLOX layers were found to be very similar in nature (see Section 4.5.1) Therefore, an attempt was made to obtain a measure of the IMPLOX thickness from the experimentally-obtained absorbance at 9.2 μm by comparison with those obtained from thermally grown oxide layers of various thicknesses.

The transmitted intensity through an absorbing medium (I_{tr}) is given by

$$I_{tr} = I_o e^{-\alpha t}$$

$$\text{or} \quad \ln(I_o/I_{tr}) = \alpha t$$

where I_o is the incident intensity

α is the absorption coefficient

and t is the thickness of the absorbing material.

A plot of $\ln(I_o/I_{tr})$ as a function of t is thus expected to be a straight line passing through the origin.

Thermal oxides of various thicknesses, ranging between 0.04μm and 0.5μm were grown in a dry oxygen ambient at a temperature of 1000°C. The measured absorbances plotted as a function of thickness produced a straight line passing through the origin, as shown in Fig.4.15. Thickness values obtained for IMPLOX layers using this plot are given in Table 4.3. Thicknesses obtained from RBS spectra and those calculated on the assumption that all the implanted oxygen contributed to the formation of silicon dioxide are also given. The values obtained from the infra-red absorbance are consistently higher than those from the RBS spectra. Thicknesses from the RBS spectra are in good agreement with the calculated values.

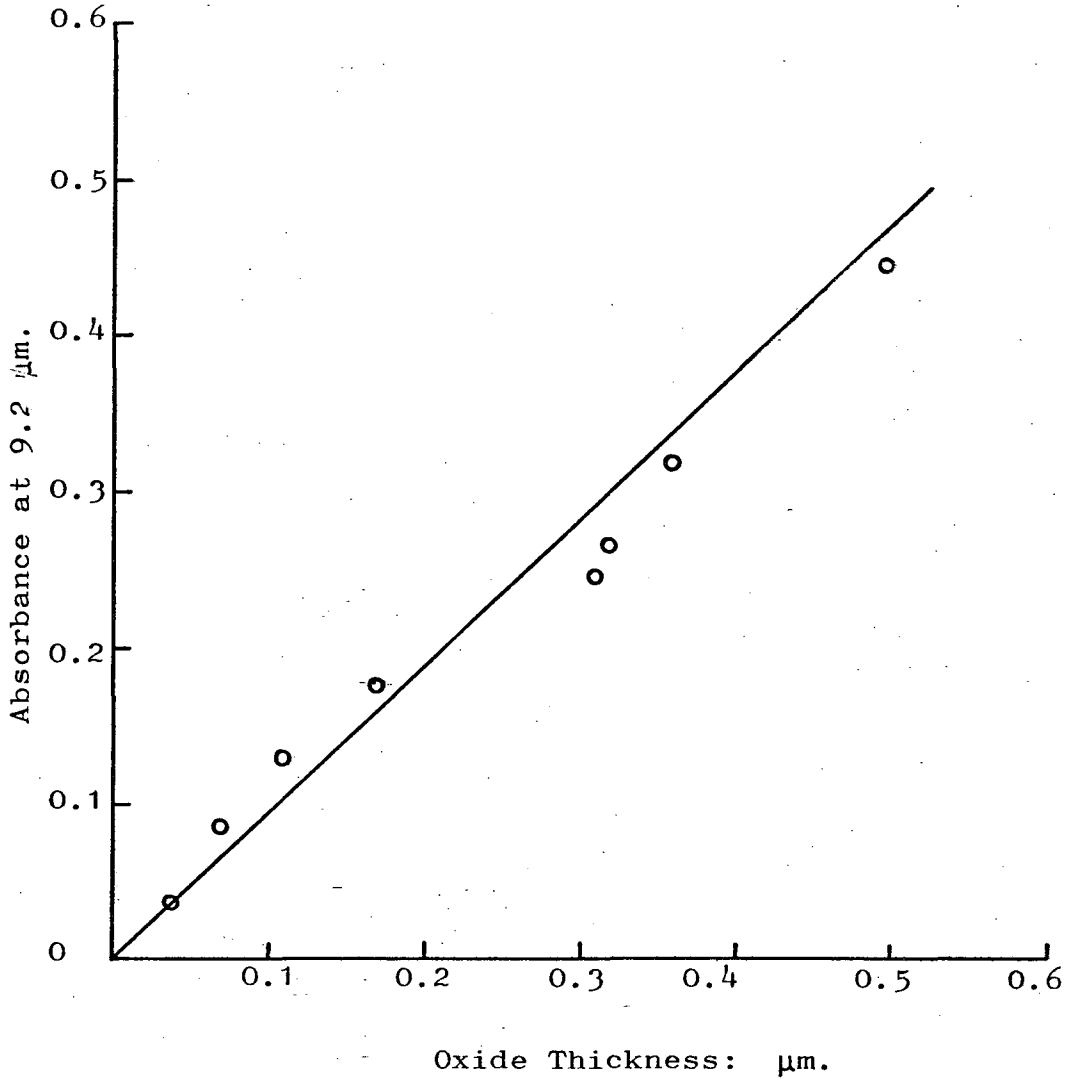

Fig. 4.15. Thermal oxide absorbance at 9.2 µm as a function of thickness.

TABLE 4.3

IMPLOX thickness as measured by various techniques.

Dose:energy $O^+.cm^{-2}$:keV	IR absorbance (±0.05 μm)	Angle-lapping μm	TEM μm	RBS (±0.015 μm)	Expected μm
1.15×10^{18}: 150	0.37	-	-	0.258	0.2826
1.4×10^{18} : 200	0.40	~0.3	0.38	0.28	0.3043

4.5.3 Estimation of Substrate Temperature during Implantation

Substrate temperature measurements during ion implantation have been reported by Parry[140] and Wada, Usui and Ashikawa[141]. In these measurements the infra-red radiation emitted by the heated silicon wafers was collected by an infra-red pyrometer which displayed the temperature. Wada et al[141] observed a temperature rise as high as 730°C for an implant beam power of 6W/cm^2. Parry measured temperatures close to the melting point of silicon with beam powers up to 200 W/cm^2.

An infra-red pyrometer was not available in the present study, therefore, it was attempted to estimate the substrate temperature during implantation indirectly from the observed temperature dependent shift in the infra-red absorption peak of the as-implanted wafers. This shift appears to be due to partial in-situ annealing of the IMPLOX at elevated implantation temperatures brought about by beam heating or substrate heating or a combination of both. A 'calibration curve' was produced using the following approach:

A sample, implanted under good heat-sink conditions whereby the temperature rise was low, was isochronally annealed at temperatures of 200° - 1000°C at 100° intervals and at 1150°C for 2 hours in nitrogen ambients. Infra-red absorption spectra were obtained after each anneal step. The position of the peak as a function of temperature is shown in Fig.4.16.

Substrate temperatures during implantation were obtained by noting the position of the infra-red absorption peak in the as-implanted state and reading the corresponding temperature from the 'calibration curve' in Fig. 4.16.

The assumption involved is that the physical processes taking place during implantation into a hot substrate as far as the oxide is concerned, are the same as would occur during an

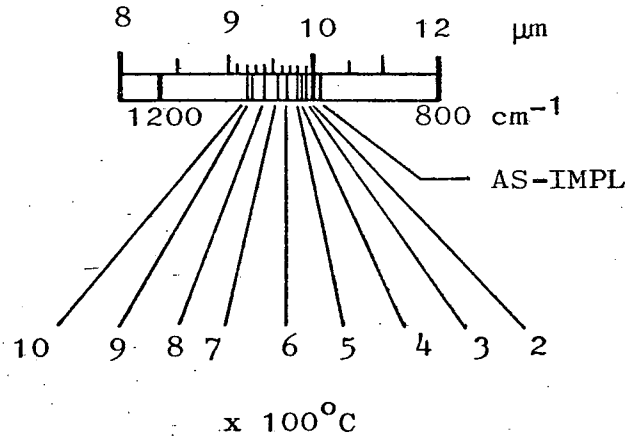

Fig. 4.16. Position of IR absorption peaks as a function of anneal temperature.

anneal treatment at the same temperature for times comparable to the implantation time, if initially implanted at a lower temperature. The implication is that a substrate implanted at a high temperature would retain a degree of surface crystallinity, even at high doses, due to out-diffusion of vacancies from the damage core[107] and solid phase epitaxial regrowth of damaged regions. Thus, infra-red absorption spectroscopy should serve as a useful non-destructive technique for the assessment of the suitability of a sample for subsequent epitaxial deposition.

With the heated specimen holder (heater not in use) for an average beam power of $4W/cm^2$ a temperature of $\sim 550^oC$ and for $5W/cm^2$ a temperature of $\sim 650^oC$ were estimated. These figures are in good agreement with results reported by Parry[140] and Wada et al[141], although conduction losses, which would depend on the design of the individual substrate holder and the target chamber,are expected to be different.

Two samples implanted under identical conditons, (see Table 3.6) but one with a minimal thermal contact and the other in good contact with the substrate holder, produced identical infra-red absorption spectra. However, the damage distribution, as seen from the RBS spectra (see Section 4.6.2.10) indicated that a higher temperature rise occurred in the sample in minimal thermal contact. This points to the insensitivity of the infra-red peak position to a difference in temperature probably less than 100^oC, which appears to be high enough to influence the damage distribution.

4.6 Rutherford Back-Scattering (RBS) Analysis

Elastic back-scattering of light, high energy ions, usually called Rutherford back-scattering has proved to be a very useful tool for the study of implantation damage and annealing, the location of impurity atoms in a crystal and the investigation of surfaces and thin films[89,142,143,144].

The experimental arrangement is shown schematically in Fig.4.17.

A well-collinated beam of singly ionized 1-3 MeV helium ions is used. The specimen to be analysed is placed on a goniometer and exposed to the beam in a target chamber at a pressure of $\sim 10^{-6}$ torr. Information about the specimen is contained in the energy spectrum of the ions back-scattered through an angle of $\sim 150^{o}$. These ions are detected by a silicon surface barrier detector. The signal is amplified and analysed, stored, displayed and recorded.

A silicon sample, for example, exposed to the beam of energy E_o, gives rise to a spectrum consisting of a sharp edge at $0.59\ E_o$, corresponding to helium ions elastically scattered by surface silicon atoms and deflected into the detector. The sharp edge is followed by a smoothly varying yield at lower energies, as shown in Fig.4.18 by the curve designated as 'random'. Helium ions not scattered at the surface penetrate into the target, losing energy through inelastic collisions and are scattered elastically in the bulk. They eventually leave the target to be detected after losing more energy inelastically on the way out. If the stopping power of the target and the geometry of the system are known, the energy scale can be converted to a depth scale.

If the ion beam is incident in a low index direction of a high quality crystal specimen, it would appear to the beam to be a very open structure consisting of hollow 'tubes' or 'channels' with lattice atoms forming the walls of the tubes. 'Channelling' minimises collisions of incident ions with target atoms and reduces the observed back-scattered yield for all depths in the crystal, as shown in Fig.4.18, by the curve labelled as 'channelled'. A small surface damage peak observed only in the channelled spectrum is due to localized surface disorder. Even high quality crystal samples show this surface disorder peak. If the crystal has been damaged e.g. by ion implantation, and the displaced atoms occupy

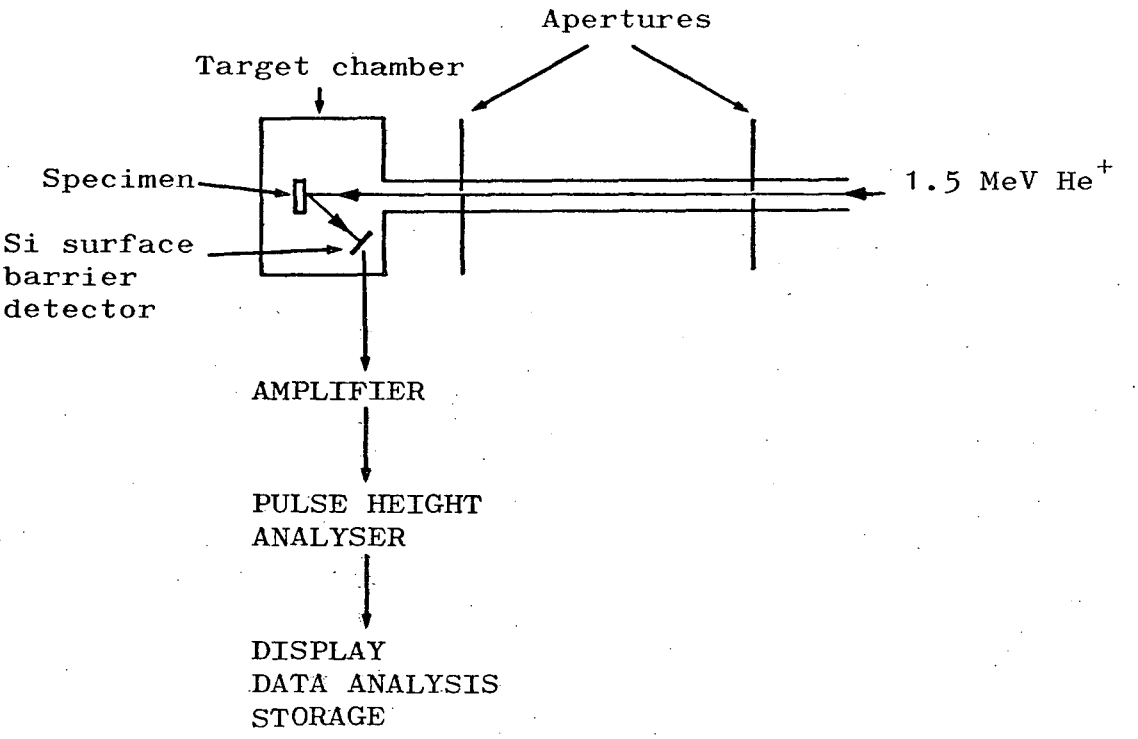

Fig.4.17. Schematic diagram of the experimental arrangement used for RBS analysis.

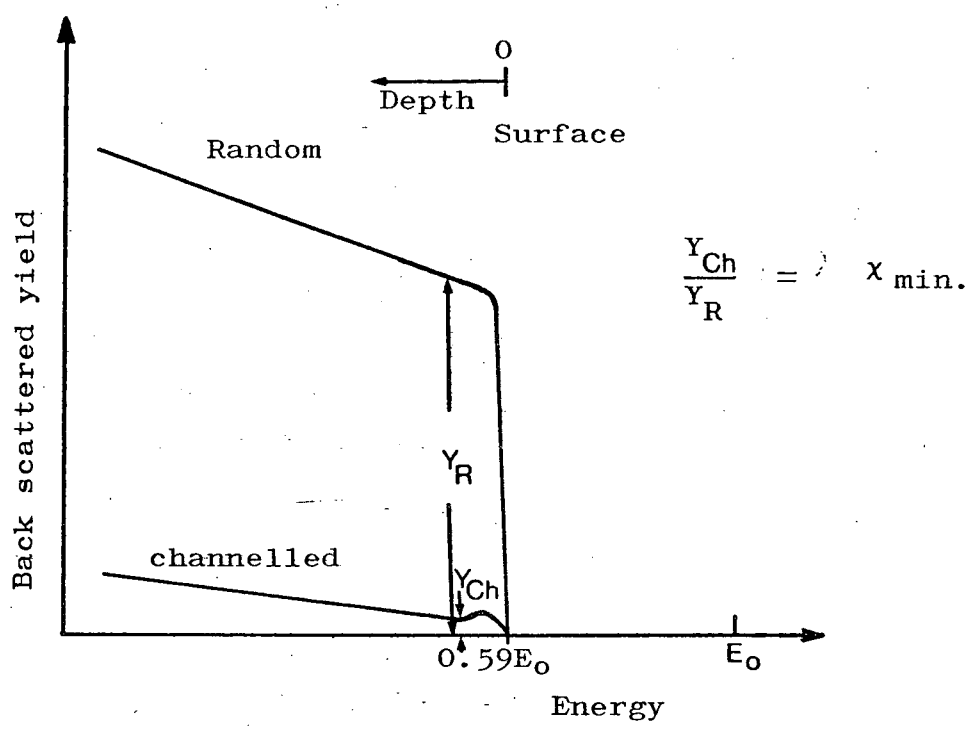

Fig. 4.18 Schematic energy spectra of back-scattered helium ions from a crystalline target.

sites in the channel areas, the channelled ions suffer elastic collisions with these atoms resulting in a higher scattered yield. The ratio of the yields in the channelling and random (non-channelling) directions is a measure of the quality of single crystal specimens. For good quality silicon, this ratio, often referred to as χ_{min}, is ~ 0.03.

RBS, in conjunction with channelling, can also be used to determine the concentration and position of impurity atoms in the crystal, the technique being more sensitive for heavier elements. This technique has also been applied to a variety of surface and thin film problems.[145-147].

4.6.1. Experimental

RBS analysis was carried out at the University of Surrey Accelerator Laboratory. A collimated beam of 1.5 MeV He^+ ions was used. Specimens in the form of 5 x 5 mm square pieces were mounted with 'silver dag' on a stainless steel plate which was then clamped in position with spring clips. The holder fits on to a goniometer stage in the target chamber which is pumped down to a pressure of $\sim 10^{-6}$ torr. The goniometer is driven by stepping motors enabling specimen tilting from -30° to 30° about two mutually perpendicular axes as indicated in Fig. 4.19.

The specimens are held at ground potential and a suppressor plate with a square window measuring 6 mm x 6 mm is placed in front of the specimen. The suppressor is maintained at -300V to suppress secondary electron emission.

In all the specimens investigated an attempt was made to obtain a channelling spectrum. Initially the goniometer was set at $\Phi = 0$ and θ was scanned from -7° to 7° and the total signal from the amplifier was monitored on a chart recorder. A typical trace is shown in Fig. 4.20. When a minimum in the signal output, corresponding to a minimum yield of back-scattered He^+ ions was obtained, the scanning

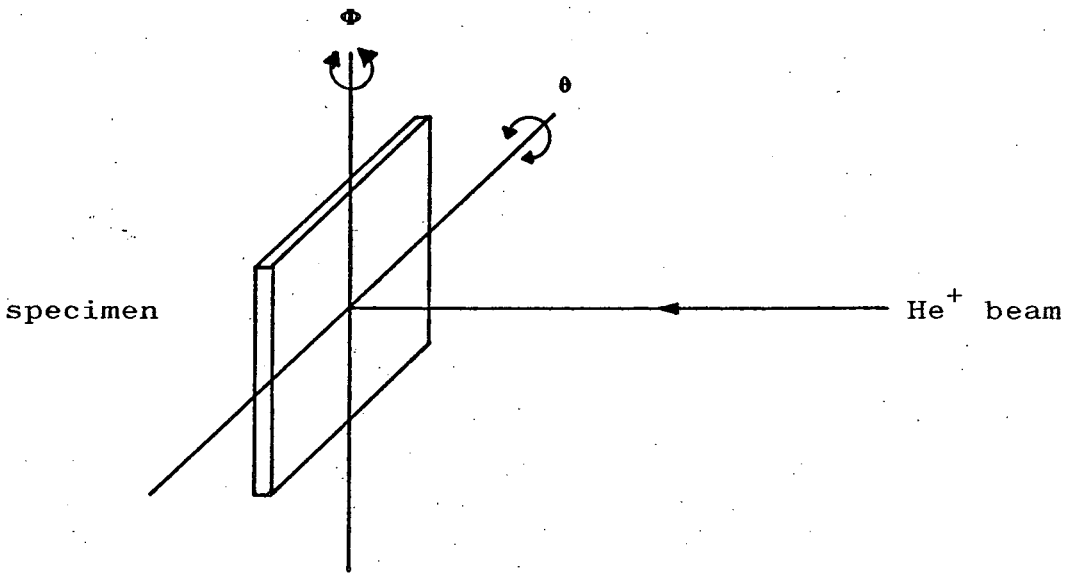

Fig.4.19. RBS specimen tilting in two mutually perpendicular directions.

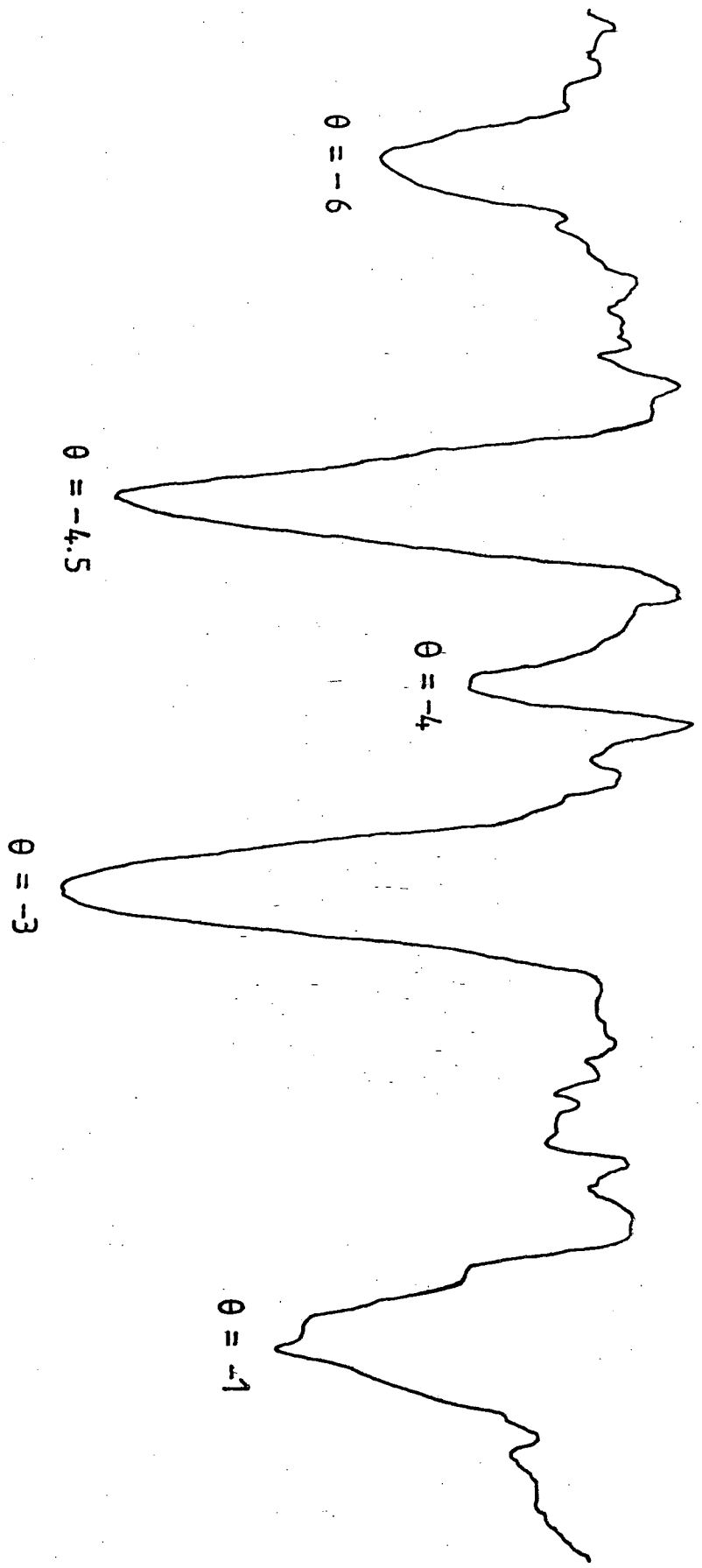

Fig.4.20. Back-scattered yield as a function of θ with Φ = 0.

was stopped. Having obtained a setting for θ, Φ was scanned between -3^0 to 3^0. Scanning was stopped when a new minimum was observed. After obtaining approximate settings for both Φ and θ the procedure was repeated several times with a much reduced scan and at lower speeds to obtain optimum settings.

A data collection programme 'RBS1' on a PDP 11 computer was used for obtaining the spectra[148]. A preset charge of 8 μC was collected in both the channelling and random directions. The random spectrum was obtained by tilting the specimen away from the channelling direction.

On completion of data collection the spectrum is displayed on a visual display unit. The data were stored on a floppy disc and could subsequently be analysed using a programme 'RBS2', plotted on a Tektronix plotter and a printed version obtained from a line printer. 'RBS2' enables one to assign a depth scale[89,148] to the energy spectrum. The programme also permits analysis of impurities and integration of counts over a selected number of channels. A third programme 'RBS3' enables simulation of back-scattering experiments[148].

4.6.2. Results

RBS analysis was used generally for obtaining the distribution profile of implanted oxygen and for assessing the crystalline quality of the surface layer.

The following, in particular, were studied :

1. Unimplanted silicon substrates, thermally oxidized substrates and deposited polycrystalline silicon on thermally oxidized substrates for the purpose of comparison.

2. The effect of implant energy on oxygen distribution profile for a given peak oxygen concentration.

3. The effect of dose on distribution profile for a given energy.

4. The effect of temperature on surface crystallinity for a given dose at a given energy.

5. The effect of anneal treatment on surface crystallinity and oxygen distribution.

6. The crystalline quality of deposited epitaxial layers on unimplanted and on annealed, implanted substrates.

7. A qualitative comparison of the extent of damage at the surface silicon/IMPLOX interface in various samples implanted under different conditions of temperature and dose at a given energy.

4.6.2.1. Spectra from the Substrate

RBS spectra obtained from an unprocessed silicon substrate are shown in Fig.4.21. Scattering of helium ions from silicon atoms at the surface occur at an energy of 0.89 MeV for a primary beam energy of 1.5 MeV. Channelled and random spectra were obtained with a χ_{min} value of 0.03.

4.6.2.2. Spectrum from Thermally Oxidized Silicon

A random spectrum, obtained from a thermally oxidized substrate is shown in Fig.4.22. No channelling was observed due to total randomization of the beam by the presence of the relatively thick oxide layer. Region(1)of the spectrum is the scattering yield from silicon atoms in the thermally grown silicon dioxide. As there are only 2.3×10^{22} silicon dioxide molecules. cm^{-3} (each with one silicon atom) compared with 5×10^{22} silicon atoms.cm^{-3} in crystalline silicon, a proportionally reduced silicon scattering yield is obtained from the silicon dioxide layer. Region (2) in the spectrum

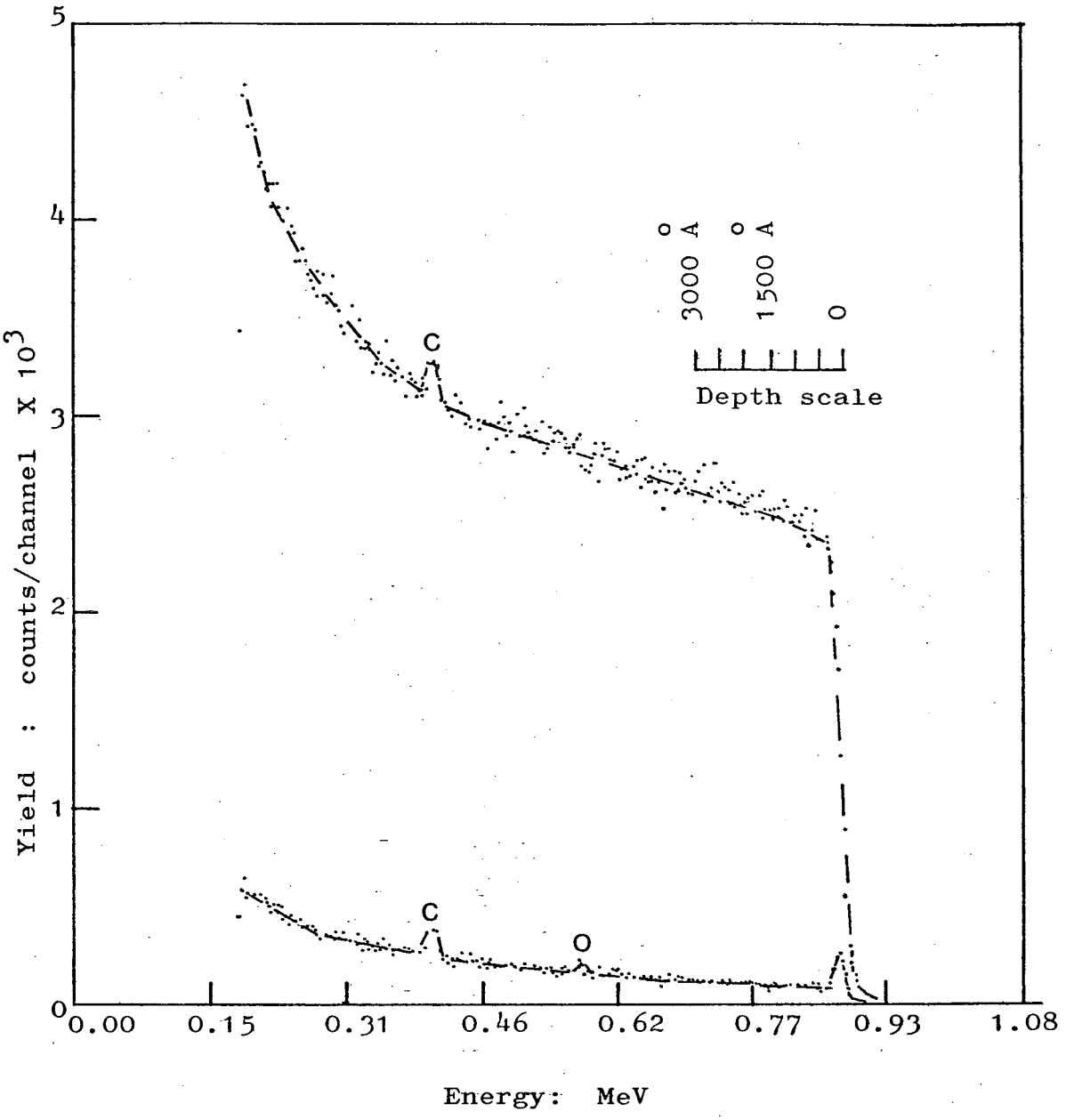

Fig.4.21. Random and channelled spectra obtained from untreated single crystal silicon substrates. Presence of carbon and a very small oxygen peak, arising from an extremely thin surface oxide layer are observed.

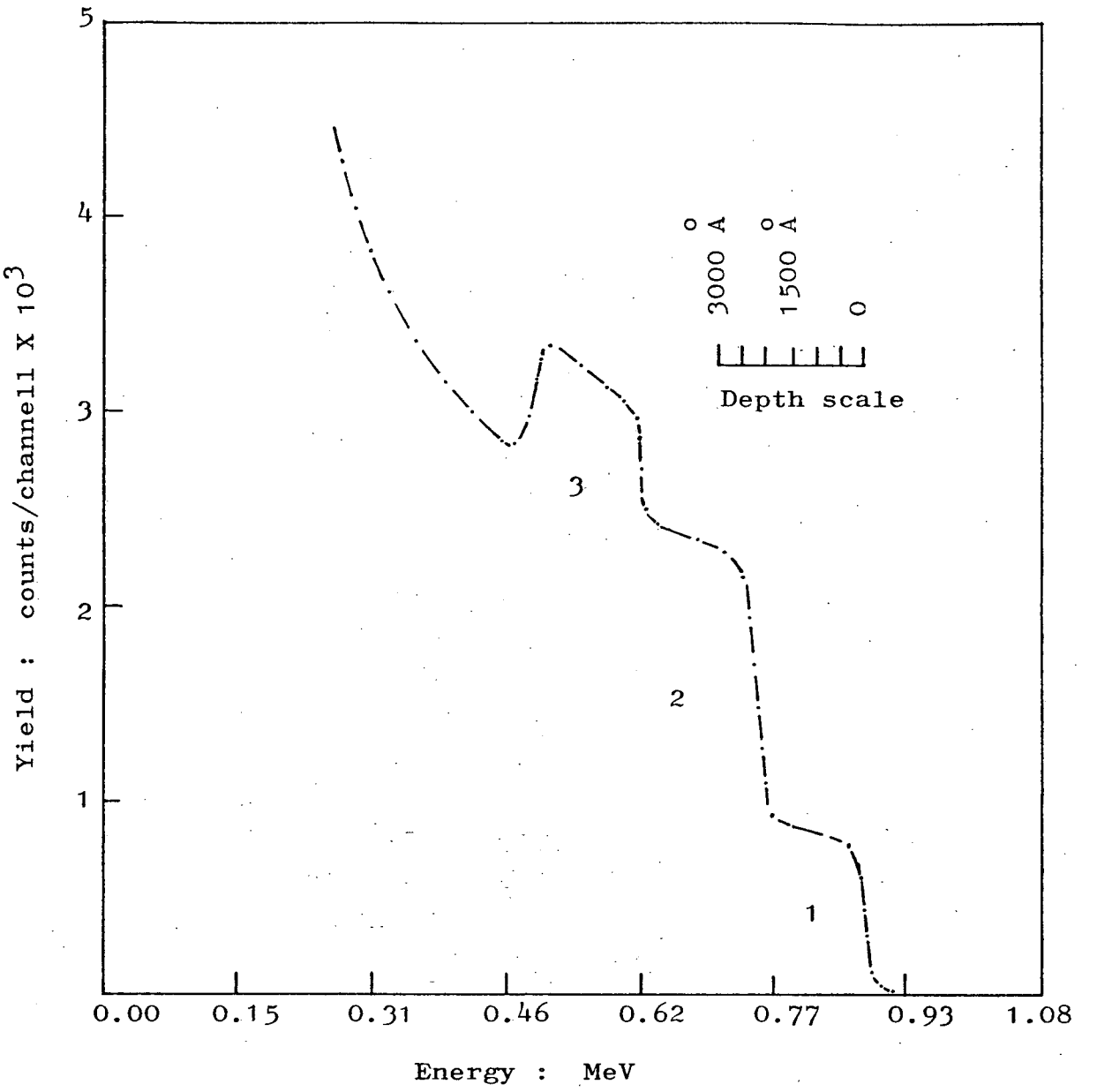

Fig.4.22. RBS spectrum from thermall oxidized silicon. Region (1) corresponds to silicon yield from the oxide, (2) to silicon yield from the substrate underlying the oxide and (3) to yield due to scattering from oxygen atoms in the oxide.

is due to scattering by silicon atoms in the substrate just below the oxide layer. Scattering yield in this region is essentially the same as that arising from corresponding depths in an untreated silicon substrate. Oxygen atoms, being lighter than silicon atoms, scatter at a lower energy of 0.58 MeV which is the characteristic energy of helium ions scattered from oxygen atoms located at the surface of the sample. The oxygen peak is superimposed on the silicon background yield originating from a region deeper in the substrate. Depth scales inserted in the spectrum indicate that the oxide thickness is~0.27 μm. This value is in good agreement with that expected from the growth conditions.

4.6.2.3. Spectrum of Polycrystalline Silicon/ Thermal Oxide/Silicon

Polycrystalline silicon was deposited on part of the thermally oxidized substrate used in the preceeding experiment. During the five minute heat treatment at 1100°C in a hydrogen ambient prior to deposition (used as a standard procedure in epitaxial deposition) partial removal of the oxide is expected. Also, a reaction is expected between initially arriving silicon atoms and silicon dioxide molecules [29]

$$Si + SiO_2 \longrightarrow 2\ SiO$$

resulting in further removal of silicon dioxide. These reactions are likely to have an effect on the interface structure.

The spectrum obtained from the structure is shown in Fig.4.23 No channelling was observed. The spectrum can be considered to arise from a silicon substrate with a buried oxide layer. The region(1)of the spectrum is the yield due to scattering from the silicon atoms in the polycrystalline silicon layer. This is followed by a region of reduced silicon yield arising from the scattering from silicon atoms in the buried oxide. Region(3)is due to scattering from silicon atoms in the substrate below the oxide. Region(4)is

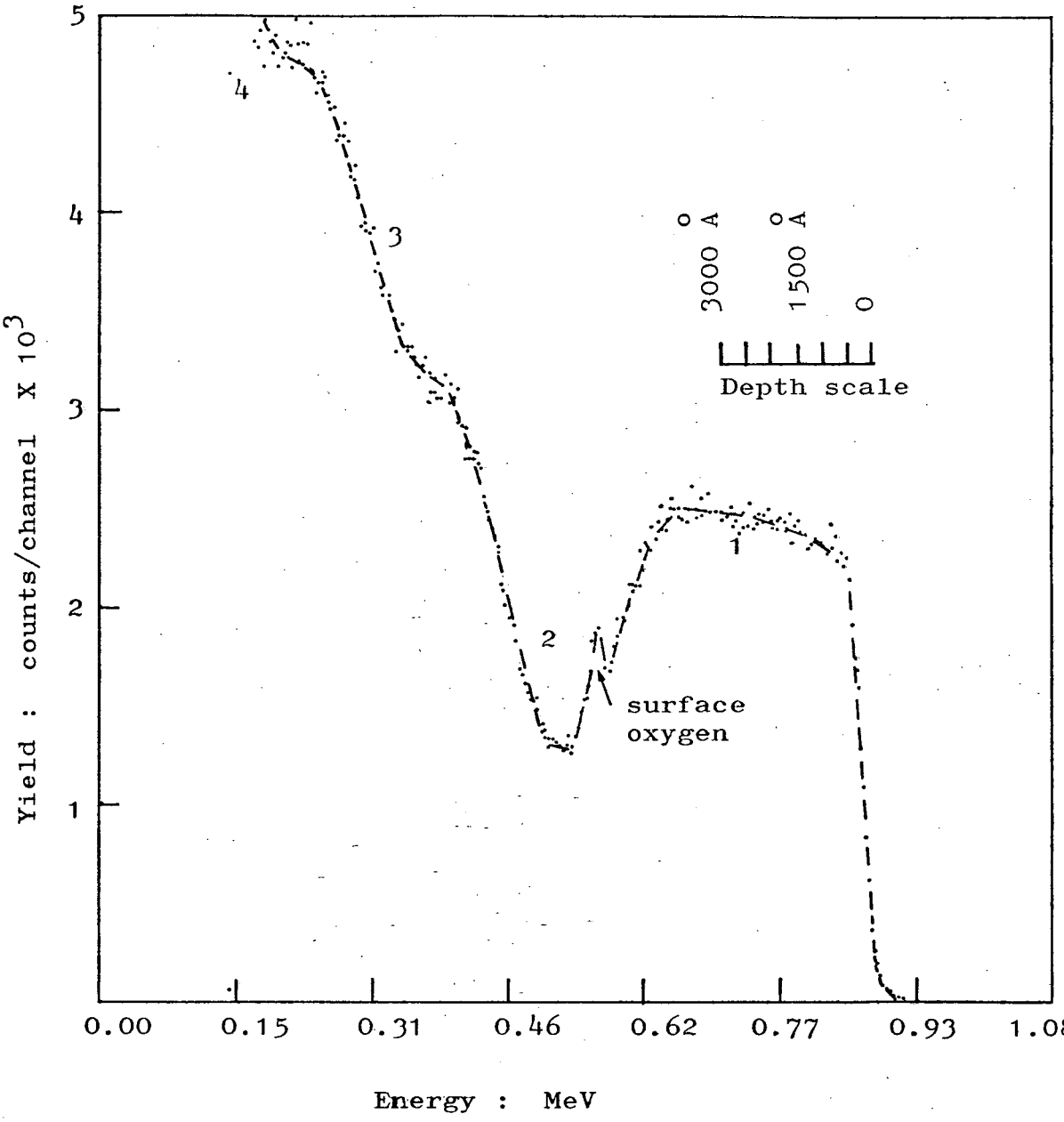

Fig. 4.23. RBS spectrum of polycrystalline silicon/thermal oxide/silicon. Region (1) corresponds to yield from surface silicon, (2) to reduced silicon yield from the oxide, (3) to silicon background yield from the underlying silicon and (4) to scattering yield from oxygen in the oxide.

the peak due to oxygen in the oxide layer. Due to the buried nature of the oxide, the oxygen peak occurs at a lower energy than that for a surface oxide and is not well resolved because it is superimposed on the sloping part of the background silicon yield.

4.6.2.4. Effect of Implant Energy on Oxygen Distribution Profile

Implantations were carried out at various energies ranging from 50 keV - 200 keV. The corresponding doses were calculated to give a concentration of $\sim 4.6 \times 10^{22}$ $O.cm^{-3}$ at the peak of the distribution as shown in Table 3.3. In addition to the effect on distribution, it was expected that this experiment would enable the determination of the maximum surface concentration of oxygen consistent with satisfactory subsequent deposition of epitaxial layers. However, the desired result could not be obtained as all these implants were carried out at ~room temperature, thereby amorphizing the surface layer and resulting in a total loss of the implanted oxygen during anneal in a hydrogen ambient (see section 3.6.5). The B-IMPLOX was retained in annealed samples, for RBS analysis, by a treatment in a nitrogen ambient for 2 hours at $1150^{o}C$.

The spectra from annealed samples are shown in Fig.4.24. As-implanted samples produce almost identical spectra. No channelling was observed except in the 50 keV and 70 keV implants where channelling was obtained from the substrate underlying the IMPLOX layer. Buried oxide layers were formed in all cases. Back-scattering yield from the relatively oxygen-free surface layers is comparable to the random yield from crystalline silicon substrates. The silicon yield gradually decreases as the implanted oxide is approached, attaining a minimum corresponding to the projected range of the implanted oxygen, then rising again to the normal random yield following an approximate Gaussian curve. The oxygen peak occurs at a lower back-scattered energy and is

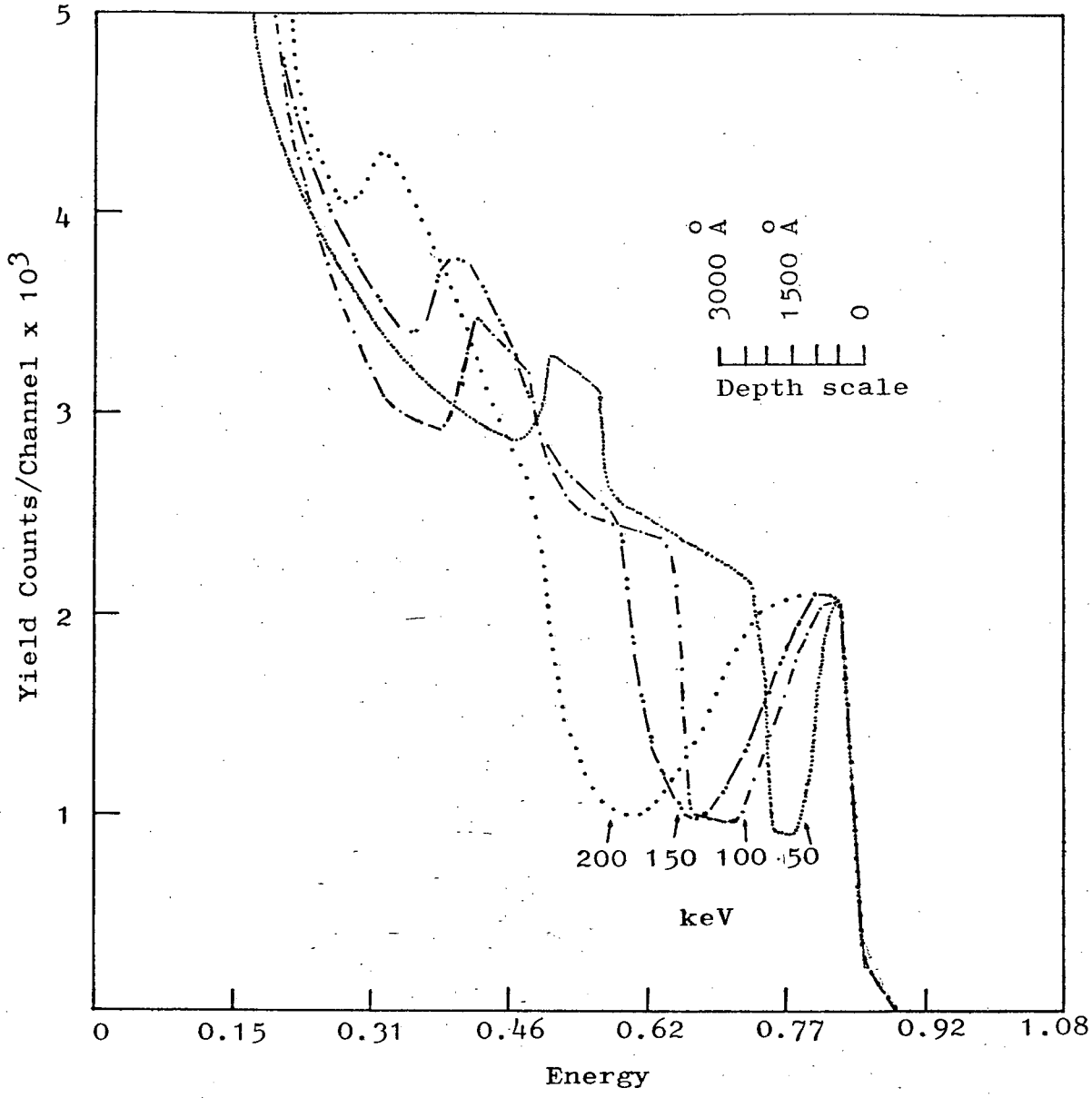

Fig. 4.24. Effect of implant energy on the RBS spectra for a given peak concentration of 4.6×10^{22} 0.cm^{-3}. A saturation in oxygen content is observed in the 50 and 100 keV implants.

superimposed on the silicon yield curve. At higher implant energies, the implanted oxygen is buried deeper and back-scattering occurs at lower energies where the background silicon yield is high and the curve is highly sloped. Consequently, the oxygen peak becomes less and less well-defined with increasing implant energy. Therefore, all the parameters relating to the oxygen distribution are determined from the complement of the yield/energy curve arising from silicon in the implanted oxide. The background yield is subtracted and the curves are inverted, as shown in Fig.4.25. R_p and ΔR_p obtained from the curves are shown in Table 4.4, and are compared with the values given by Gibbons, Johnson and Mylroie[103]. Implanted oxide thickness is estimated from the area under these curves assuming that all the oxygen present is bonded to form silicon dioxide and contributes to a total stoichiometric oxide thickness. The relatively oxygen-free surface layer thickness is estimated from the surface to a point where the silicon yield drops by $\sim$1%. The oxide thickness and the thickness of the oxygen free layer for various energies are given in Table 4.5.

4.6.2.5. Effect of Dose on Distribution Profile

Most of the implantations were carried out at an energy of 200 keV to a dose of 1.4×10^{18} O^+. cm^{-2}. In a limited number of implants a much higher localized dose was obtained by minimising the beam scanning. This also made the dose distribution highly non-uniform across the exposed area of the wafer, ranging from $\sim 2 \times 10^{17}$ O^+. cm^{-2} at the edge to $\sim 2.5 \times 10^{18}$ O^+. cm^{-2} at the centre. Although these figures were estimated from the spectra, giving rise to probable errors, a general trend could be seen. In Fig.4.26 spectra obtained from various points along a straight line through the centre of the exposed area are shown. The spectra for a dose of 1.4×10^{18} O^+. cm^{-2} are also shown. For doses $\leq 1.4 \times 10^{18}$ O^+. cm^{-2} a Gaussian-type distribution was obtained as would be expected from projected range and standard deviation figures given by Gibbons, Johnson and Mylroie[103].

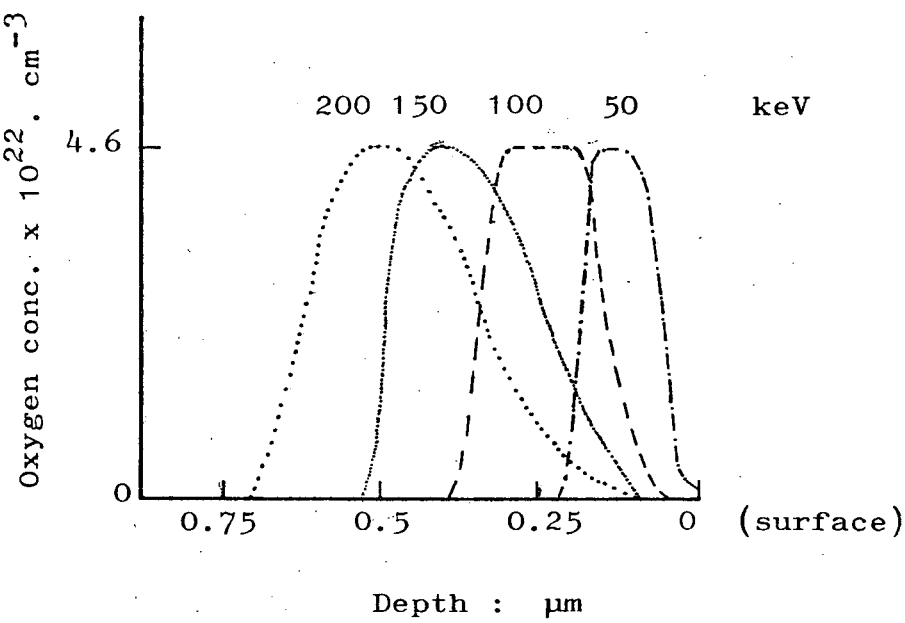

Fig.4.25. Approximate oxygen distribution profile from the RBS spectra shown in Fig.4.24.

TABLE 4.4

Projected range and standard deviation for oxygen ions in silicon target.

Energy keV	R_p from RBS μm ± 0.015 μm	R_p computed (103) μm	ΔR_p from RBS μm ± 0.015 μm	ΔR_p computed (103) μm
50	0.118	0.1142	0.052	0.0429
70	0.177	0.1645	-	0.0560
100	0.251	0.2415	-	0.0735
130	0.325	0.3190	0.110	0.0887
150	0.369	0.3707	0.103	0.0978
180	-	0.4478	-	0.1105
200	0.487	0.4989	0.118	0.1182

TABLE 4.5

Approximate oxide thickness from the RBS spectra.

Energy keV	Dose $O^+.cm^{-2}$ x 10^{18}	Approx. Oxide Thickness from RBS μm	Expected Oxide Thickness μm	Approx. thickness of surface Si layer μm
50	0.5	0.133	0.109	0.044
70	0.65	0.162	0.140	0.052
100	0.86	0.207	0.187	0.059
130	1.05	0.236	0.228	0.103
150	1.15	0.258	0.283	0.118
200	1.4	0.280	0.304	0.162

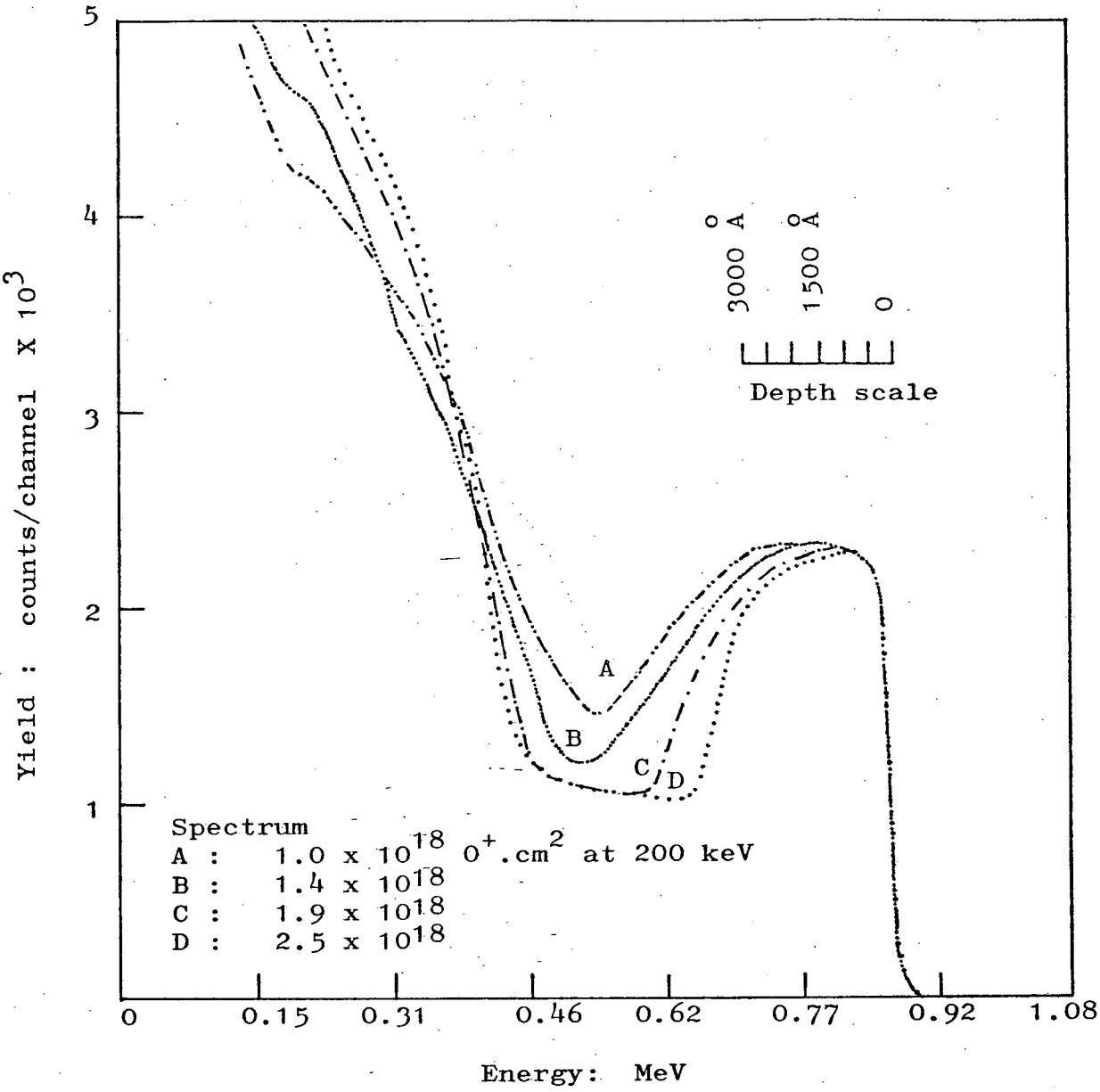

Fig.4.26. Effect of dose on the RBS spectra. Saturation in the oxygen content is observed for doses above 1.4 x 10^{18} $O^+.cm^{-2}$.

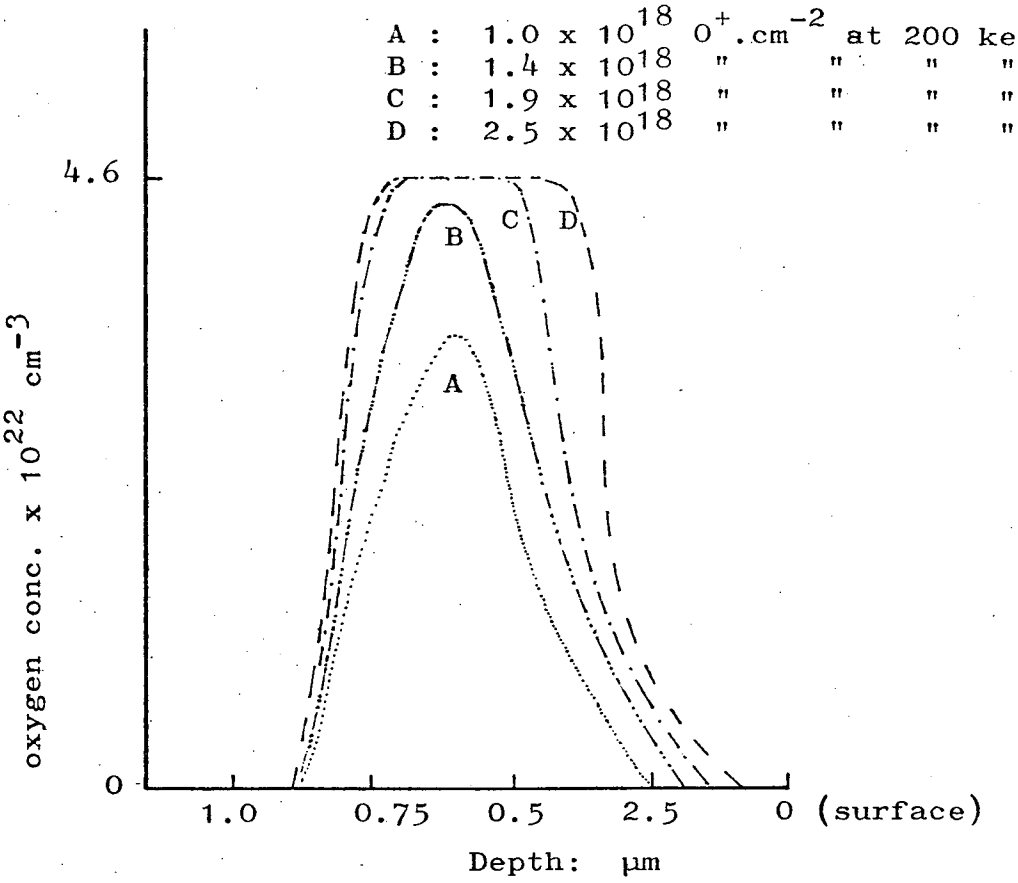

Fig.4.26(a). Approximate oxygen distribution profile from the RBS spectra shown in Fig.4.26.

At doses $>1.4 \times 10^{18}$ a box-type distribution is obtained. These results are in general agreement with those reported by Hayashi and his co-workers[149,150]. They used doses between 3.0×10^{17} and 2.7×10^{18} $O^+.cm^2$ at 150 keV. The oxygen profile was obtained by Auger electron spectroscopy. The box-type distribution appears to correspond to a volume of silicon where an amount of oxygen sufficient to form stoichiometric silicon dioxide is present. The B-IMPLOX thickness increases with increasing dose. With extremely high doses a surface oxide is formed[99]. The mechanism associated with the movement of the excess implanted oxygen is not clearly understood. However, it is evident that a given volume of silicon cannot accommodate more oxygen than that required for the formation of SiO_4 tetrahedra, i.e. stoichiometric silicon dioxide. The excess oxygen movement may involve a 'preferential' diffusion[135] towards nucleation centres i.e. silicon dioxide clusters at the upper interface.

The stoichiometry is established by comparison with the spectrum from thermally oxidized silicon. The criterion used is that the minimum silicon yield from the B-IMPLOX must drop to the level of the extrapolated yield from silicon in the silicon dioxide of a thermally oxidized sample, as indicated in Fig. 4.27. Formation of stoichiometric oxide took place at a lower dose for a lower implant energy. In Fig. 4.28 spectra of stoichiometric oxide formed by a 100 keV implant to a dose of 1×10^{18} $O^+.\ cm^{-2}$ is shown. In this case, as expected, the oxide is nearer the surface than for 200 keV implants. Also, no channelling was observed, probably because the implantation was carried out at near room temperature. Therefore, whether the high surface concentration of oxygen $\sim 3 \times 10^{20}$ atoms.cm^{-3} had any effect on the surface crystallinity remained unresolved. In the 200 keV implants good channelling spectra were obtained even for doses as high as$\sim 2.5 \times 10^{18}$, since considerable beam heating (up to $\sim 750^{\circ}C$) took place (Fig.4.29).

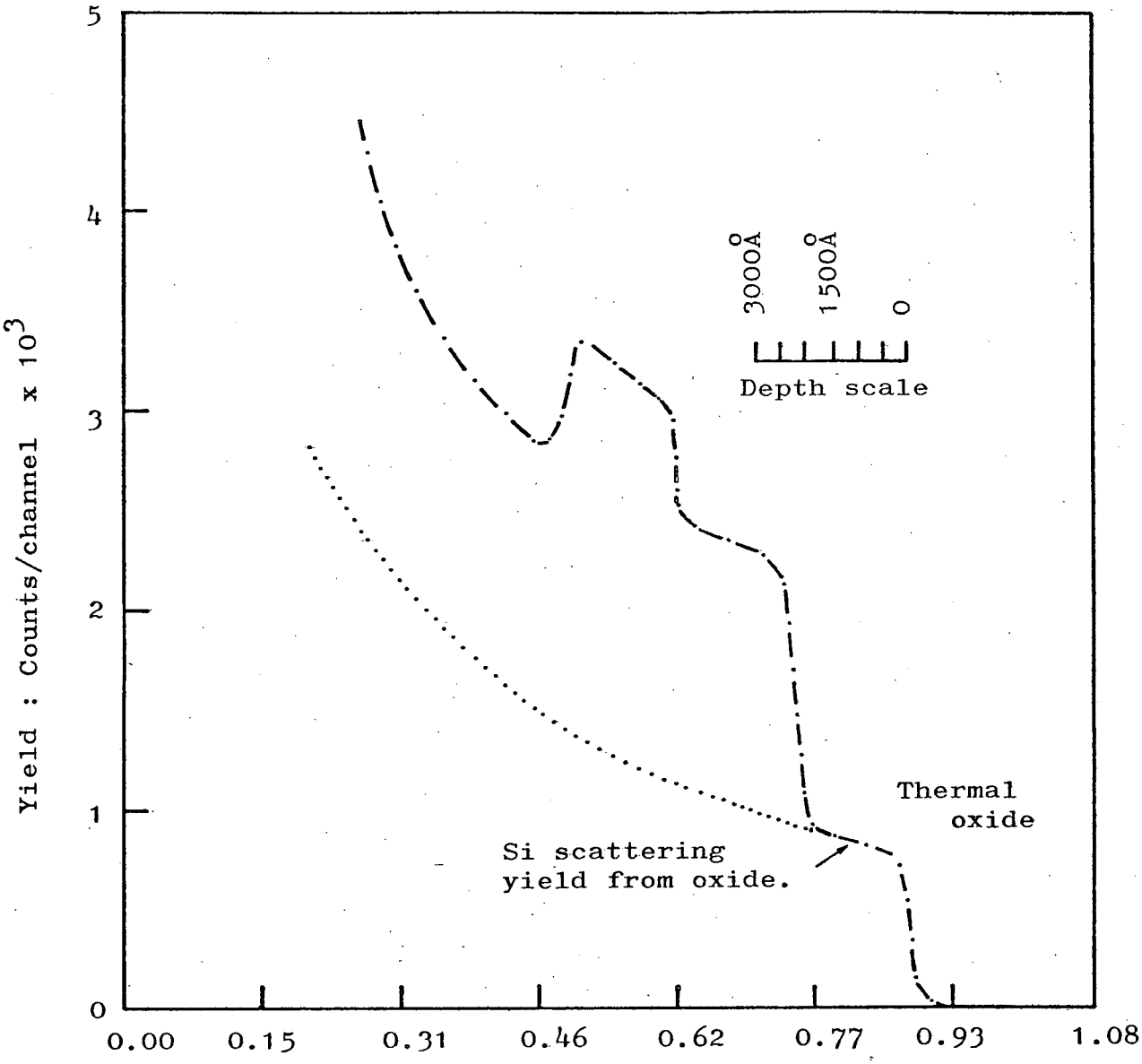

Fig.4.27. Extrapolated reduced silicon yield from stoichiometric oxide. Stoichiometry in the buried implanted oxide is achieved when the silicon yield drops to this level.

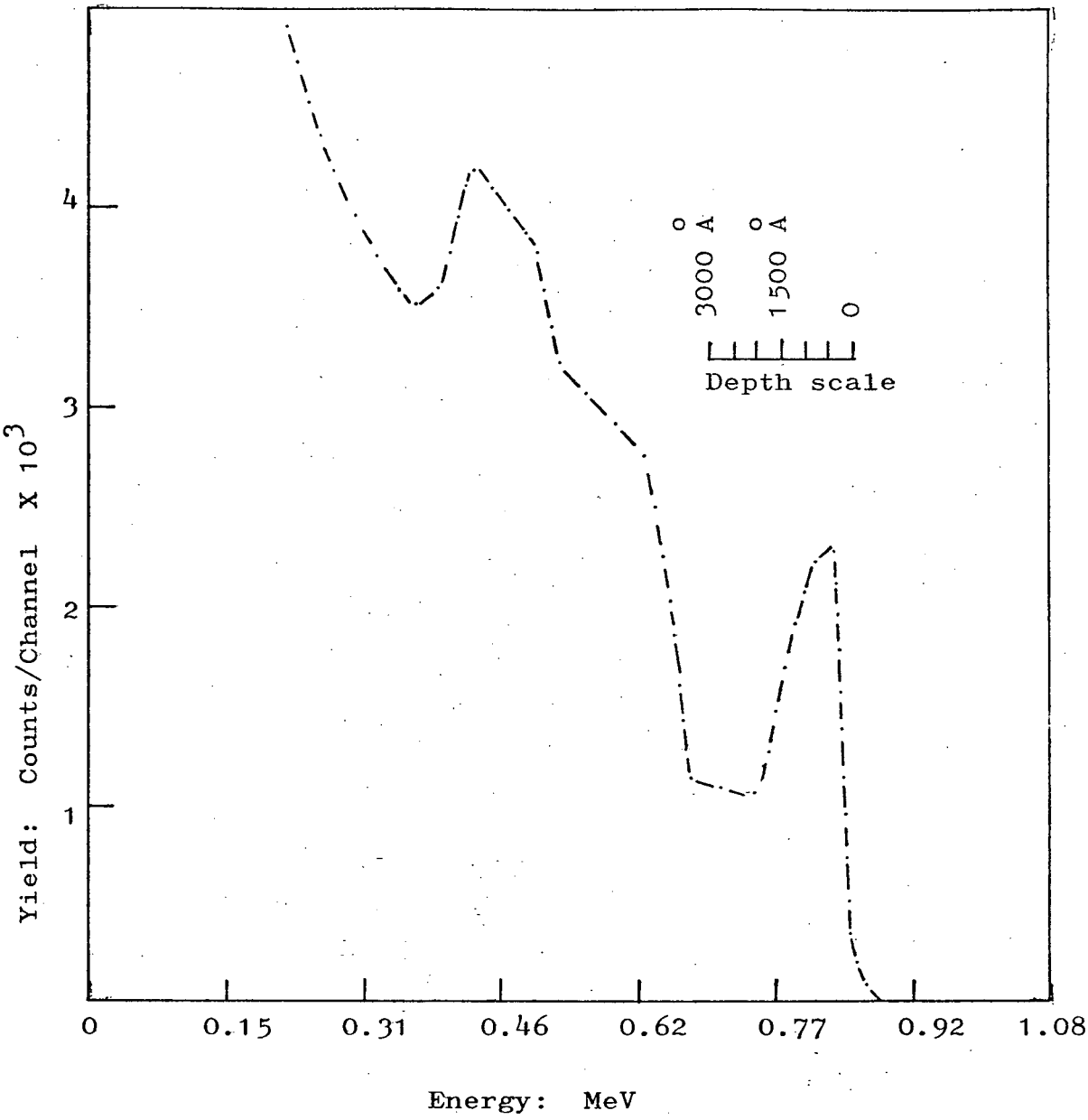

Fig. 4.28. RBS spectrum of buried stoichiometric oxide formed by a dose of 1.0 x 10^{18} $O^+.cm^{-2}$ at 100 keV.

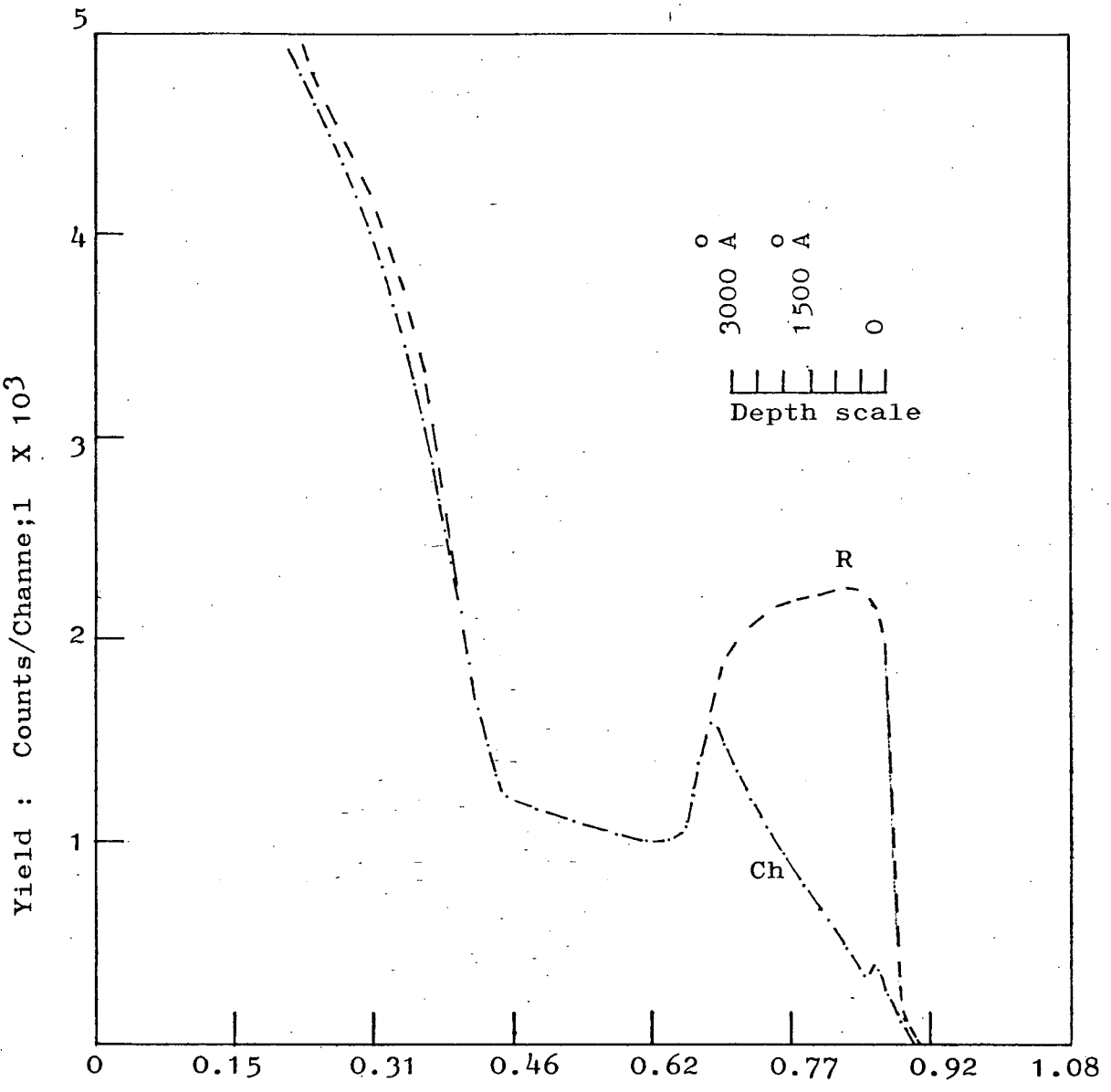

Fig. 4.29. Random and channelled spectra for a dose of ~2.5 x 10^{18} $O^+.cm^{-2}$ at 200 keV.

The oxygen profile constructed using a Gaussian approximation for a dose of 2.5 x 10^{18} $O^+.cm^{-2}$ at 200 keV is shown in Fig. 4.30. In Table 4.6 certain parameters from the constructed profile along with those obtained from the experimental RBS spectra are given.

4.6.2.6. Effect of Temperature on Surface Crystallinity

As shown in Table 4.7 in samples implanted at room temperature, ~200°C and~275°C, to a dose of 1.4 x 10^{18} $O^+.cm^{-2}$ at 200 keV, no channelling was observed in the as-implanted state nor following various anneal treatments. Good channelling spectra, as shown in Fig. 4.31 arising from the surface layer were obtained from the as-implanted~550°C samples, giving a χ_{min} of 0.12 - 0.16. This indicates that a good degree of surface crystallinity had been retained in the ~550°C implants.

Although a channelling direction was not found in the back-scattering experiments, the~200°C and~275°C implants must have retained some degree of surface crystallinity enabling the nucleation of a poor quality epitaxial layer following anneal. Channelling was observed in these epitaxial layers. The layer on a specimen implanted at~275°C had a lower $\chi_{min.}$ than the one processed at~200°C (see Sec.4.6.2.9). This indicates that a better degree of crystallinity is retained at a substrate temperature of~275°C. The room temperature sample would hardly be expected to retain any crystal order at the high doses involved.

4.6.2.7. Effect of Anneal on Surface Crystallinity

The channelled spectra from substrates implanted at ~550° in the as-implanted state and following an anneal treatment at 1100°C for 5 and 15 minutes in hydrogen are shown in Figs.4.31, Fig. 4.32(a) and (b) respectively. A reduction in back-scattered yield from the surface layer is observed. Correspondingly the $\chi_{min.}$ improved from 0.12 - 0.16 in the as-implanted state

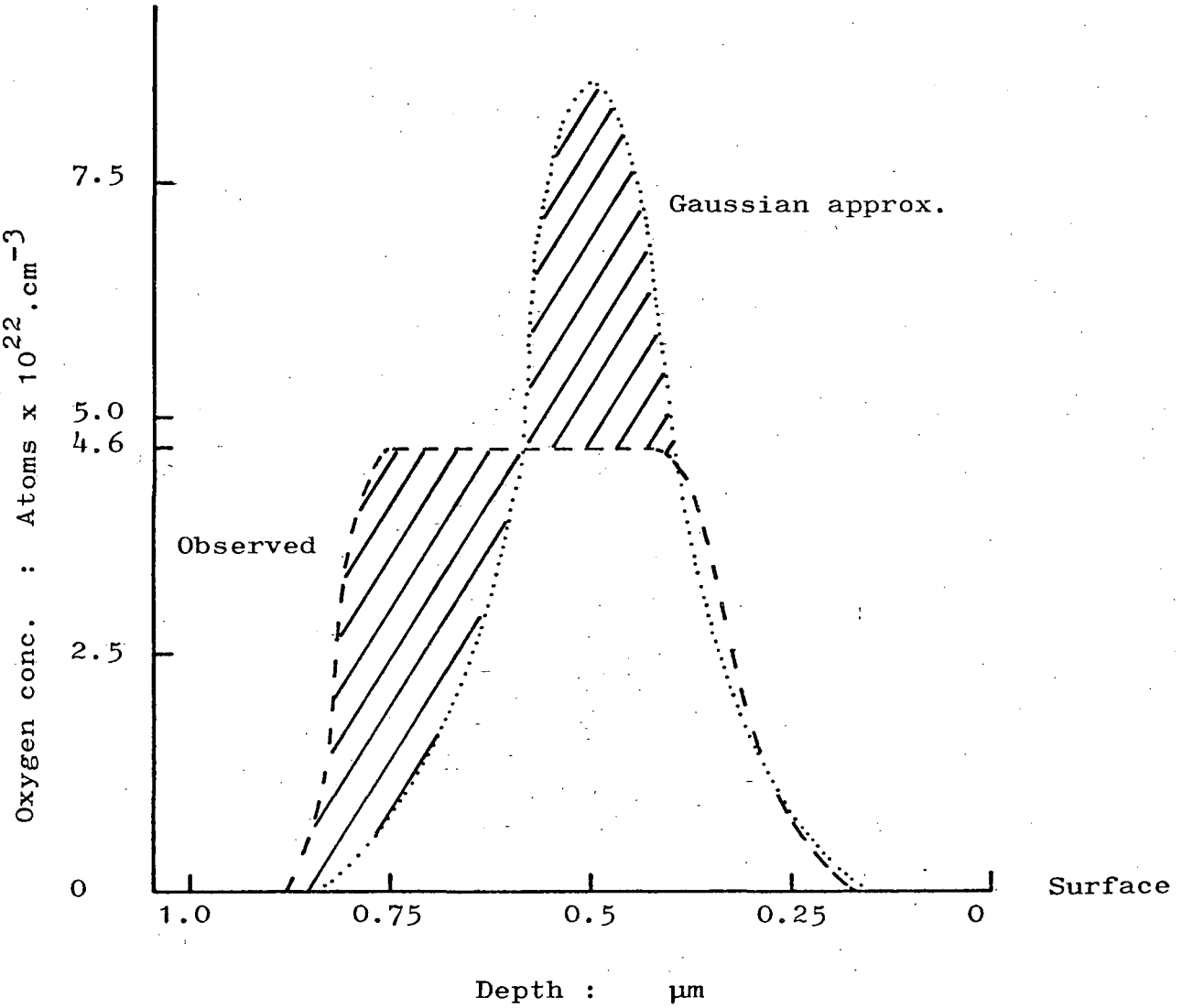

Fig.4.30. Observed and calculated profile using a Gaussian approximation, for a dose of 2.5 x 10^{18} O^+.cm^{-2} at 200 keV. The shaded areas are approximately equal. This, in conjunction with the spectra shown in Fig.4.26, indicates that the excess oxygen accumulates at the upper interface which approaches the substrate surface with increasing dose. The figure gives the misleading impression that the excess oxygen accumulates at the back interface. This arises probably due to the use of a depth scale not corrected for the change in stopping-power in the stoichiometric silicon dioxide.

TABLE 4.6

Oxygen distribution parameters for a dose of 2.5×10^{18} $O^{+}.cm^{-2}$ at 200 keV.

Profile	Centre of Distribution μm	Peak conc. $O.cm^{-3} \times 10^{22}$	Oxide Thickness μm	Thickness of Si Surface layer μm	Surface conc. of oxygen $O.cm^{-3}$
Gaussian approx.	0.4989	8.5	0.26	0.16	1×10^{19}
Experimental RBS	~0.585	~4.6	~0.55	~0.10	-

TABLE 4.7

Surface crystallinity in the as-implanted state from RBS and channelled spectra.

Samples implanted to a dose of 1.4×10^{18} $O^{+}.cm^{-2}$ at 200 keV.

Sample(as-implanted)	Channelling	$\chi_{min.}$
~Room temp. implant	no channelling observed	-
~200°C implant	" " "	-
~275°C implant	" " "	-
~550°C implant	Channelling observed	0.12 - 0.16

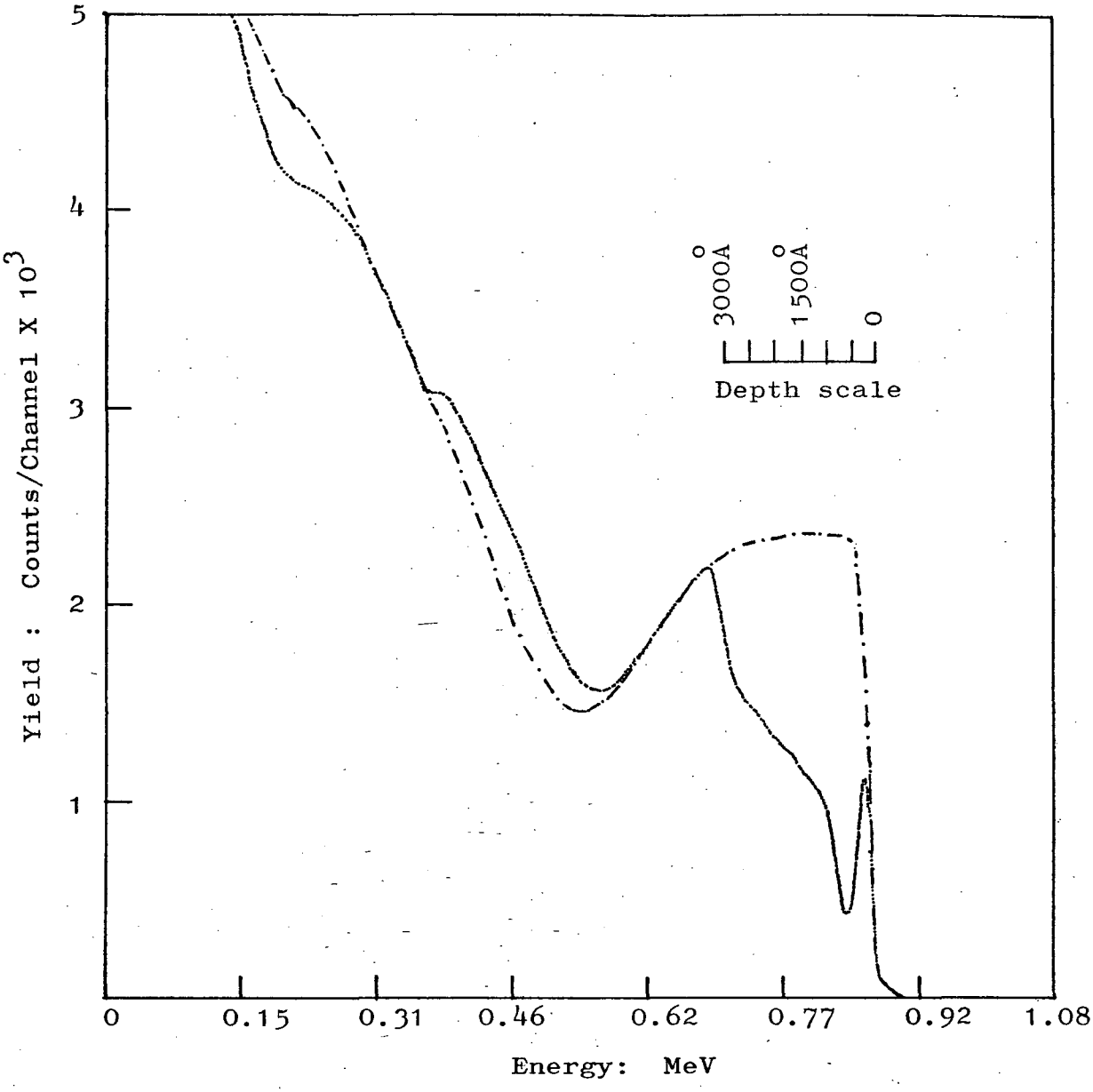

Fig. 4.31. Random and channelling spectra from the ~ 550°C implant, in the as-implanted state (dose ~1.4 x 10^{18} $O^+.cm^{-2}$ at 200 keV). Non-uniformity of dose-distribution is observed in the spectra.

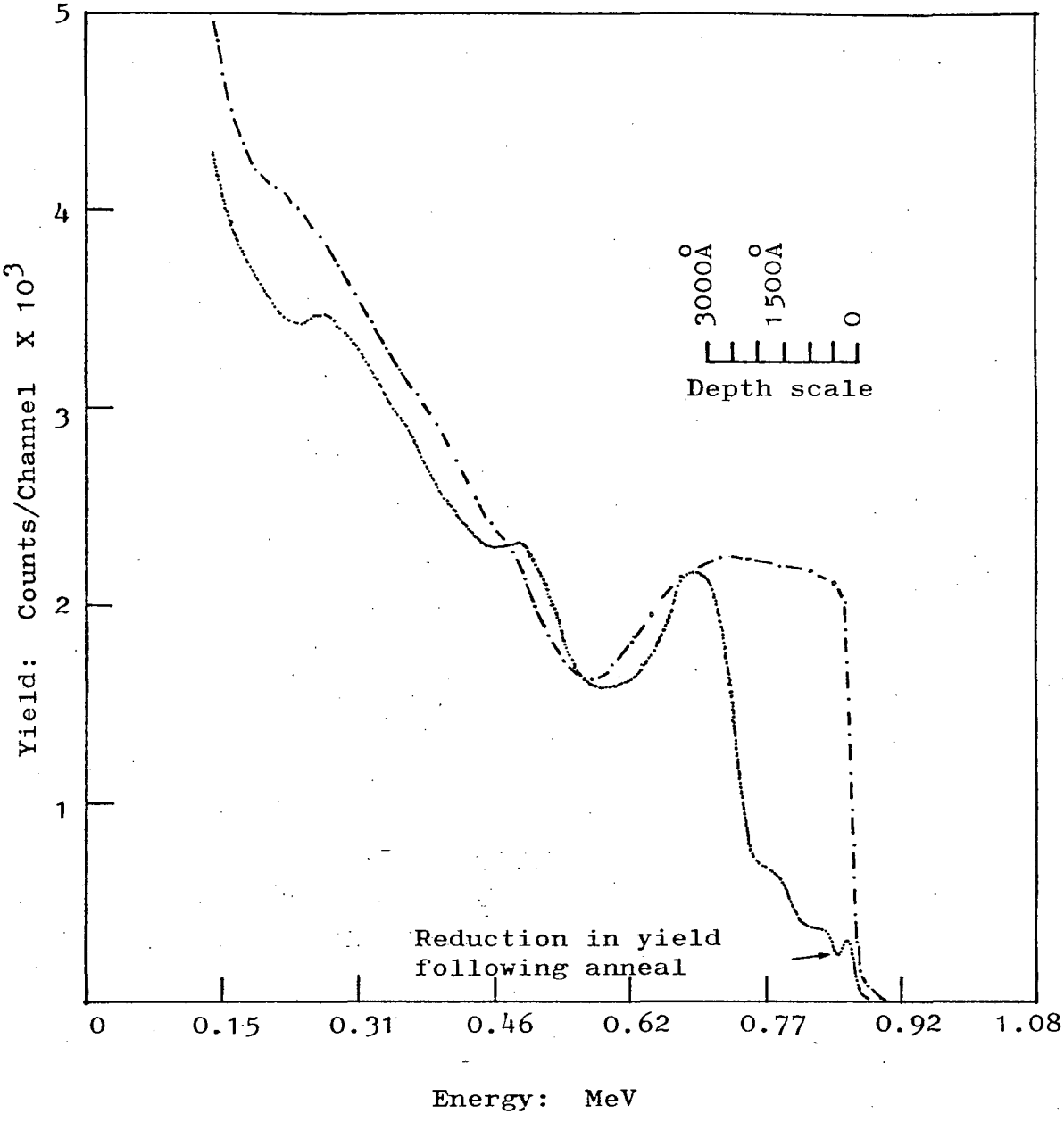

Fig. 4.3.2 (a). Random and channelled spectra from an implanted sample annealed for 5 min. The actual area samples by the helium beam had received a substantially lower dose than the intended 1.4×10^{18} $O^+.cm^{-2}$ at 200 keV.

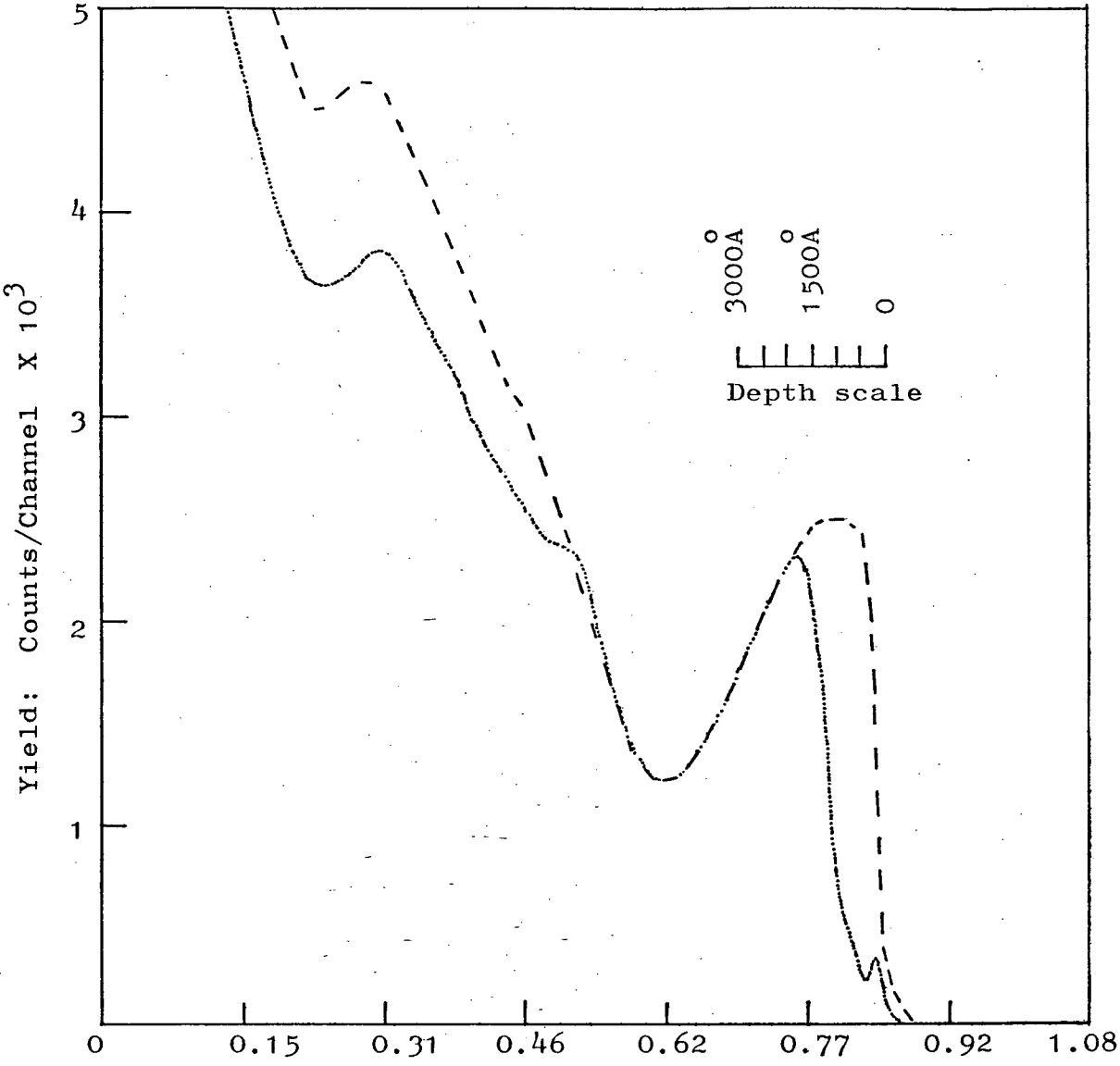

Fig.4.32 (b). Random and channelled spectra from a sample implanted to a dose of 1.4×10^{18} $O^+.cm^{-2}$ at 200 keV, following anneal for 15 min. at 1100°C. A thin layer of oxide, had formed at the surface during anneal, which was etched in buffered HF before obtaining the spectra.

to 0.07 in annealed samples, as shown in Table 4.8. This indicates a significant enhancement of surface crystallinity. An intermediate anneal treatment at 550°C for 8 hours in a nitrogen ambient does not contribute any further improvement. Substrates implanted at~room temperature,~200°C and~275°C, did not show any channelling effect either in the as-implanted or in the annealed states. The~200°C and~275°C implants retained some degree of surface crystallinity. A subsequent anneal treatment (see Table 3.8.) is likely to have some enhancing effect, still below the level of detection by the channelling technique (see Sec. 4.6.2.9.).

4.6.2.8. Effect of Anneal on Oxygen Distribution

Samples implanted to a dose of 1.4×10^{18} $O^+.cm^{-2}$ at 200 keV at lower temperatures did not show any change in the oxygen distribution following an anneal treatment, whereas the ~550°C implant showed a shift of the oxygen distribution towards the surface, as shown in Fig.4.33 although the profile remained unaltered. A similar shift is not evident in all~550°C samples investigated. This effect is probably masked by the effect on the spectrum of non-uniformity of the dose distribution. Non-uniformity is known to exist in some samples, particularly in the vicinity of the edge of the 1 cm^2 implant area. Also, two different samples were used for obtaining as-implanted and annealed spectra, although they came from the same implanted wafer.

The observed shift in the oxygen distribution is probably associated with a change in volume of the surface layer during recrystallization.

4.6.2.9. Crystalline Quality of Deposited Epitaxial Layers

Channelled and random spectra obtained from epitaxial layers deposited on substrates implanted at~550°C are shown in Fig.4.34. These are indistinguishable from those obtained from epitaxial layers on unimplanted substrates (see Table 4.9).

TABLE 4.8

Surface crystallinity following anneal treatment (Table 3.8)
Samples implanted to a dose of 1.4×10^{18} $O^{+}.cm^{-2}$ at 200 keV.

Sample (annealed)	Channelling	$\chi_{min.}$
Room-temp. implant	no channelling observed	-
200°C implant	" " "	-
275°C implant	" " "	-
550°C implant	channelling observed	0.05 - 0.07

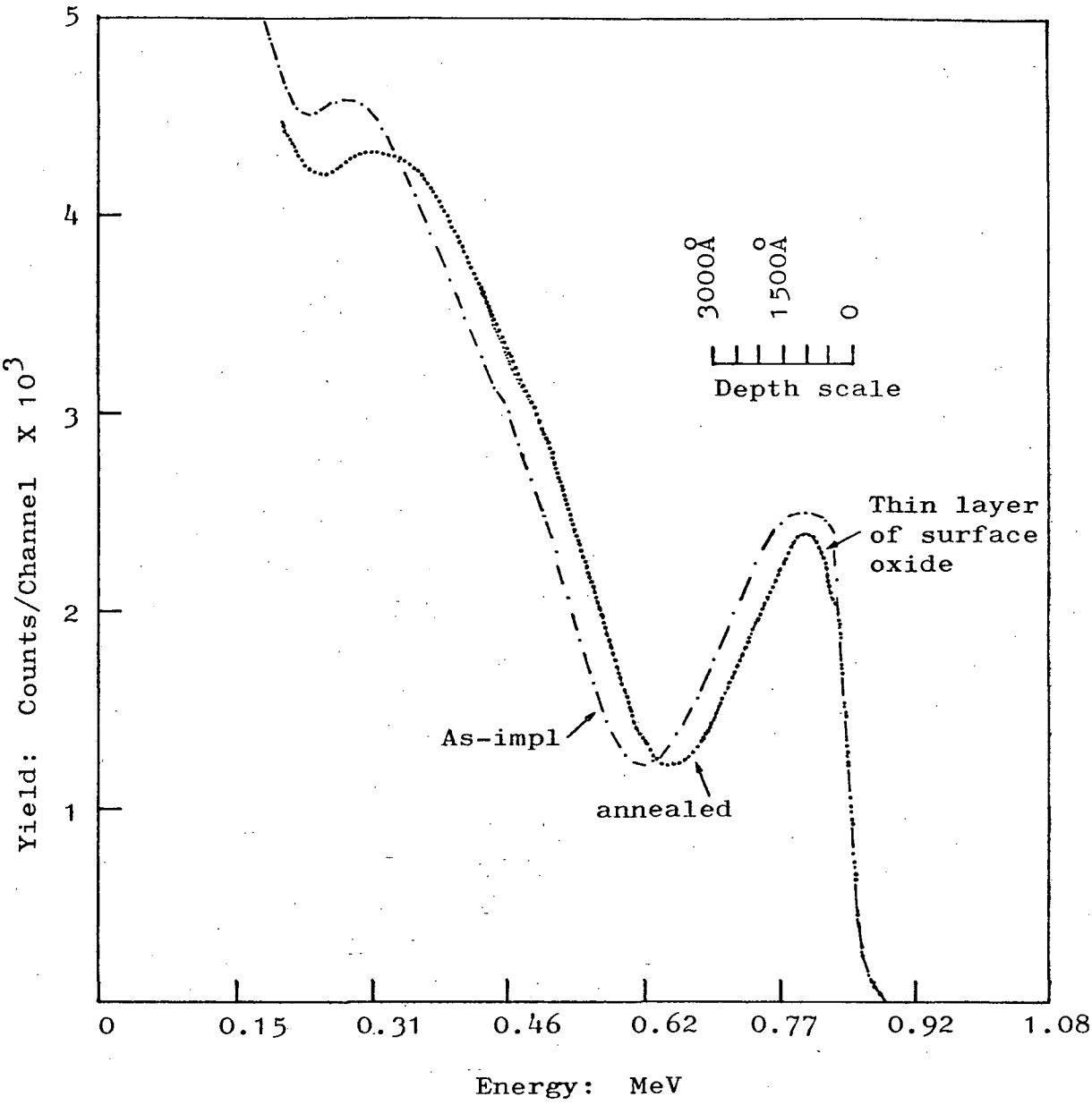

Fig. 4.33. Random spectra for a dose of 1.4 x 10^{18} $O^+.cm^{-2}$ at 200 keV showing a shift in the oxygen distribution following anneal treatment (15 min. at 1100°C).

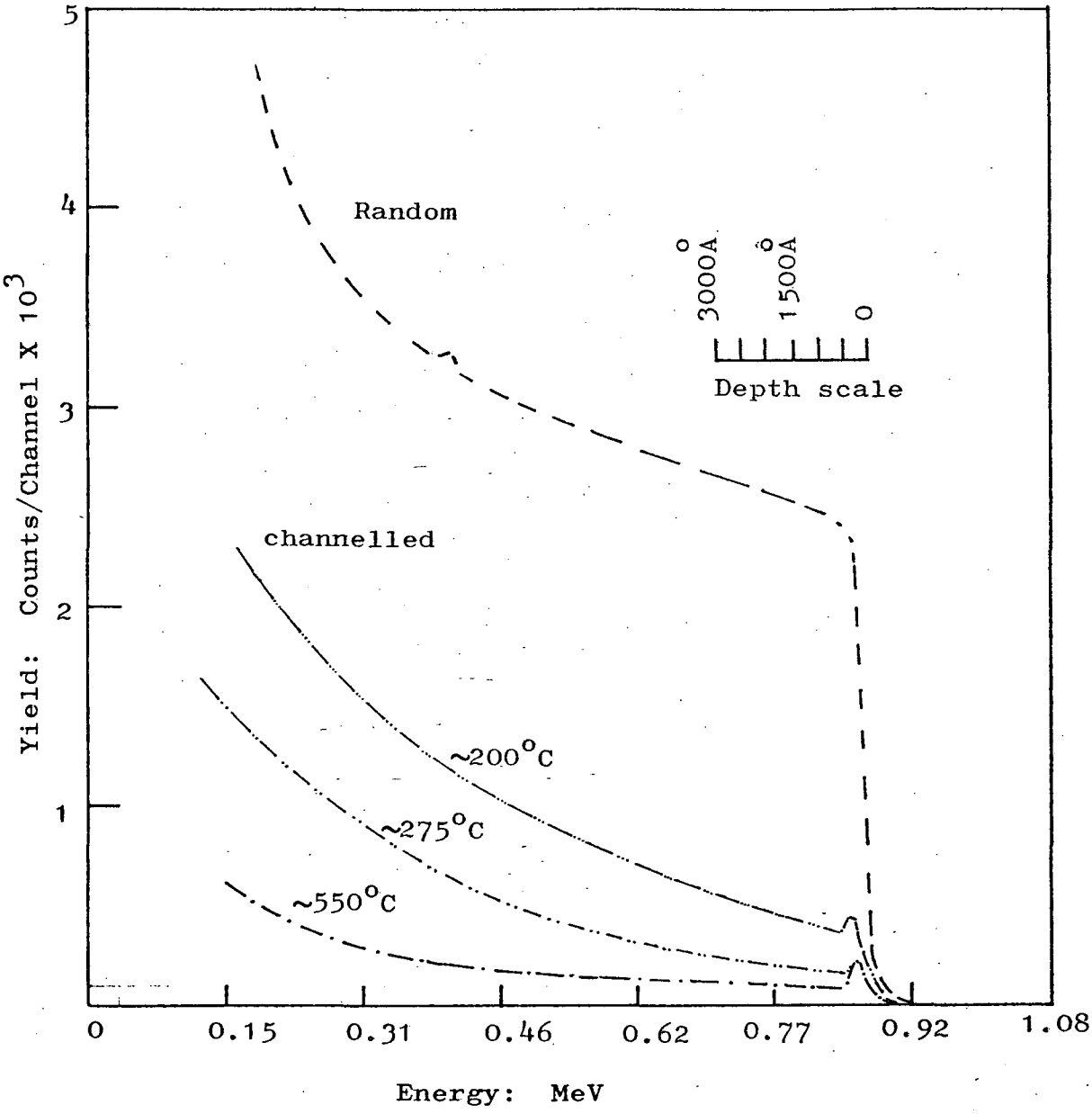

Fig. 4.34. Random and channelled spectra obtained from epitaxial layers deposited on substrates implanted at various temperatures to a dose of 1.4×10^{18} $O^+.cm^{-2}$ at 200 keV.

This indicates that good quality epitaxial layers were grown on the B-IMPLOX substrates. Epitaxial layers deposited on substrates implanted at~200°C and~275°C show some degree of channelling, as shown in Fig.4.34, although no channelling was observed in the as-implanted or annealed states. A $\chi_{min.}$ of 0.12 was obtained for the layer deposited on the ~200°C implant compared with 0.07 for the~275°C implant.

4.6.2.10. Interface Damage

The channelling spectra, as shown schematically in Fig.4.35 can be seen to be composed of :

1. a reduced yield regime, immediately following the silicon edge, arising from the crystalline surface layer,

2. a damage peak from the surface layer/B-IMPLOX interface damage,

3. a reduced silicon yield regime from the B-IMPLOX layer,

4. a second damage peak from the B-IMPLOX/substrate interface

5. an oxygen peak superimposed on the background silicon yield curve.

The surface layer, the damaged layer and the IMPLOX can all be seen directly in the transmission electron micrographs as shown in Fig.4.44 (see section 4.9.1).

The spectra shown in Fig.4.36, were obtained from two samples, both implanted to a dose of 1.4×10^{18} $O^{+}.cm^{-2}$ at an energy of 200 keV. One was mounted with a good thermal contact with the specimen holder plate during implantation, whereas the other was only in indirect contact via thin stainless steel spacers. A rise in temperature occurred in both the samples. The one in good thermal contact was expected to be at a lower temperature than the sample with minimal contact,

1. Yield from surface silicon.
2. Damage peak.
3. Reduced silicon yield from B-IMPLOX.
4. Damage peak.
5. Oxygen peak.

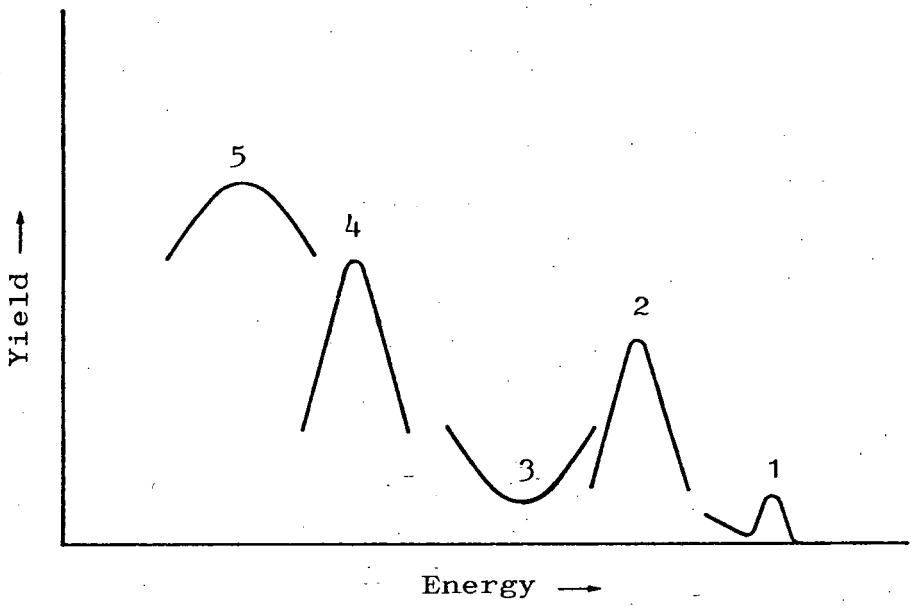

Fig. 4.35. Schematic representation of channelled spectrum from oxide layers formed by implanting oxygen ions into silicon substrates at high temperatures.

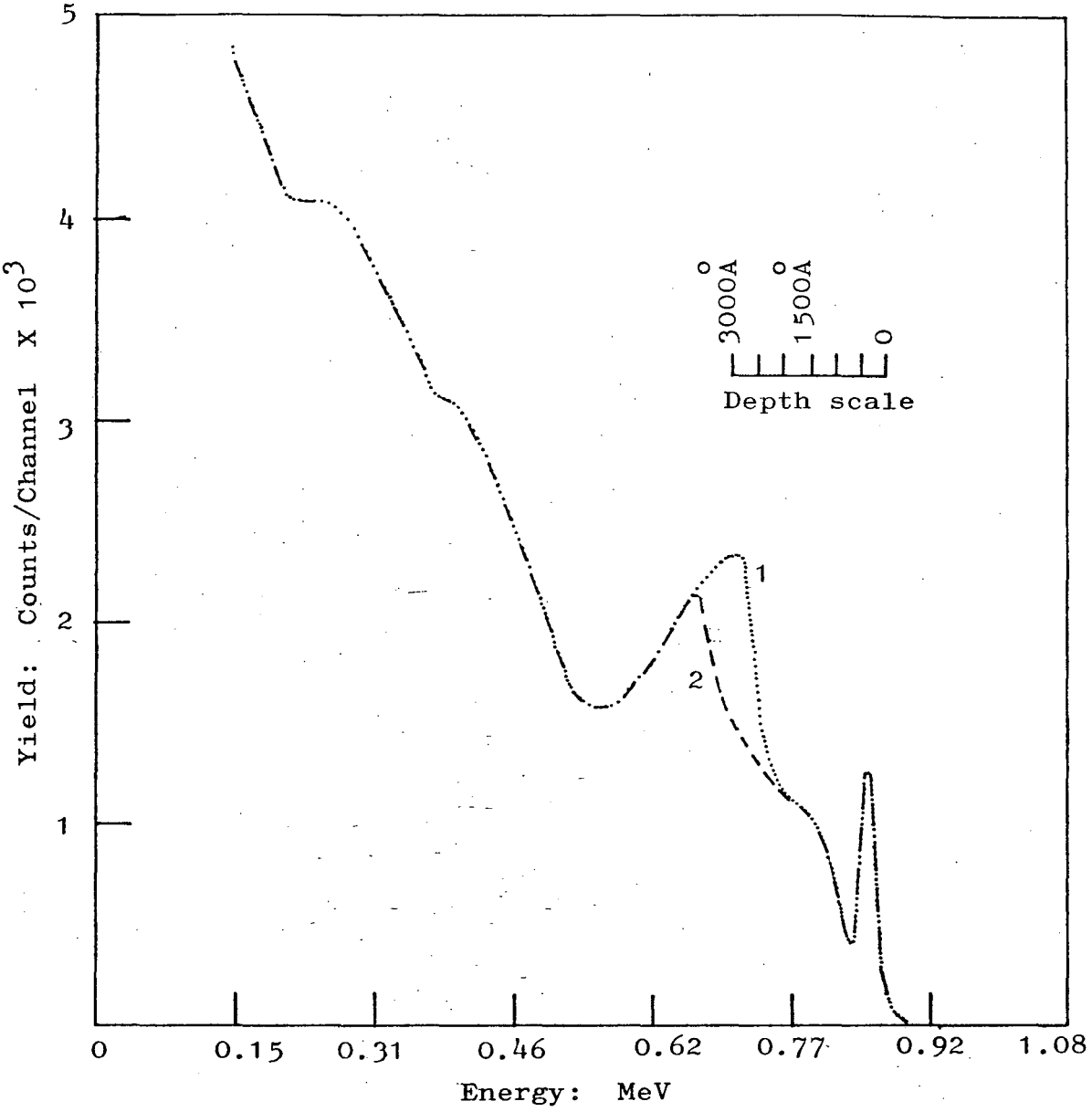

Fig.4.3 6. Channelled spectra from samples implanted to a dose of 1.4×10^{18} $O^+.cm^{-2}$ at 200 keV; (1) in good thermal contact and (2) in minimal contact with the specimen holder; other conditions remaining the same. A lower degree of interface damage is observed in the sample in minimal contact with the substrate holder indicating a higher substrate temperature during implantation.

although a temperature of 550°C was estimated from the infra red spectra (Sec.4.5.3.) in both the cases. Comparison of the two spectra shows that the damage peak is deeper and smaller in magnitude in the sample which was in minimal contact during implantation, indicating a lesser extent of interface damage at a higher temperature. A χ_{min} of 0.12 was obtained from both the samples.

The effect of high doses on the interface damage can be seen in the channelled spectra corresponding to 2.5×10^{18} $O^+.cm^{-2}$ in Fig.4.37. The channelled spectrum corresponding to 1.4×10^{18} $O^+.cm^{-2}$ is also superimposed in Fig.4.37. The magnitude of the damage peak is much smaller for $2.5 \times 10^{18} O^+.cm^{-2}$ than for $1.4 \times 10^{18} O^+.cm^{-2}$. In the high dose case the oxygen concentration rises from the surface concentration to the peak concentration in a relatively short distance, whereas in the Gaussian distribution corresponding to 1.4×10^{18} $O^+.cm^{-2}$ the oxygen distribution is of a sloping nature. In this region a gradually increasing concentration of silicon dioxide clusters is likely to damage the crystal and give rise to the damage peak in the channelled spectra. In the high dose implant the distribution being sharper, the damage is confined to a smaller volume.

In the high dose experiments a minimum scanning produced a higher beam current of 23-25 μA, as opposed to 10-15 μA in most of the experiments. This produced a temperature of $\sim 750^{\circ}$ at the central part of the substrate. This high temperature may have a contributory effect in reducing the interface damage. It was suspected that temperature a few mm. away had been much lower, as reflected by a lower χ_{min}.

4.7 Reflection Electron Diffraction

Reflection electron diffraction, also termed as Reflection High Energy Electron Diffraction (RHEED), was used to study the surface crystallinity of as-implanted and annealed samples

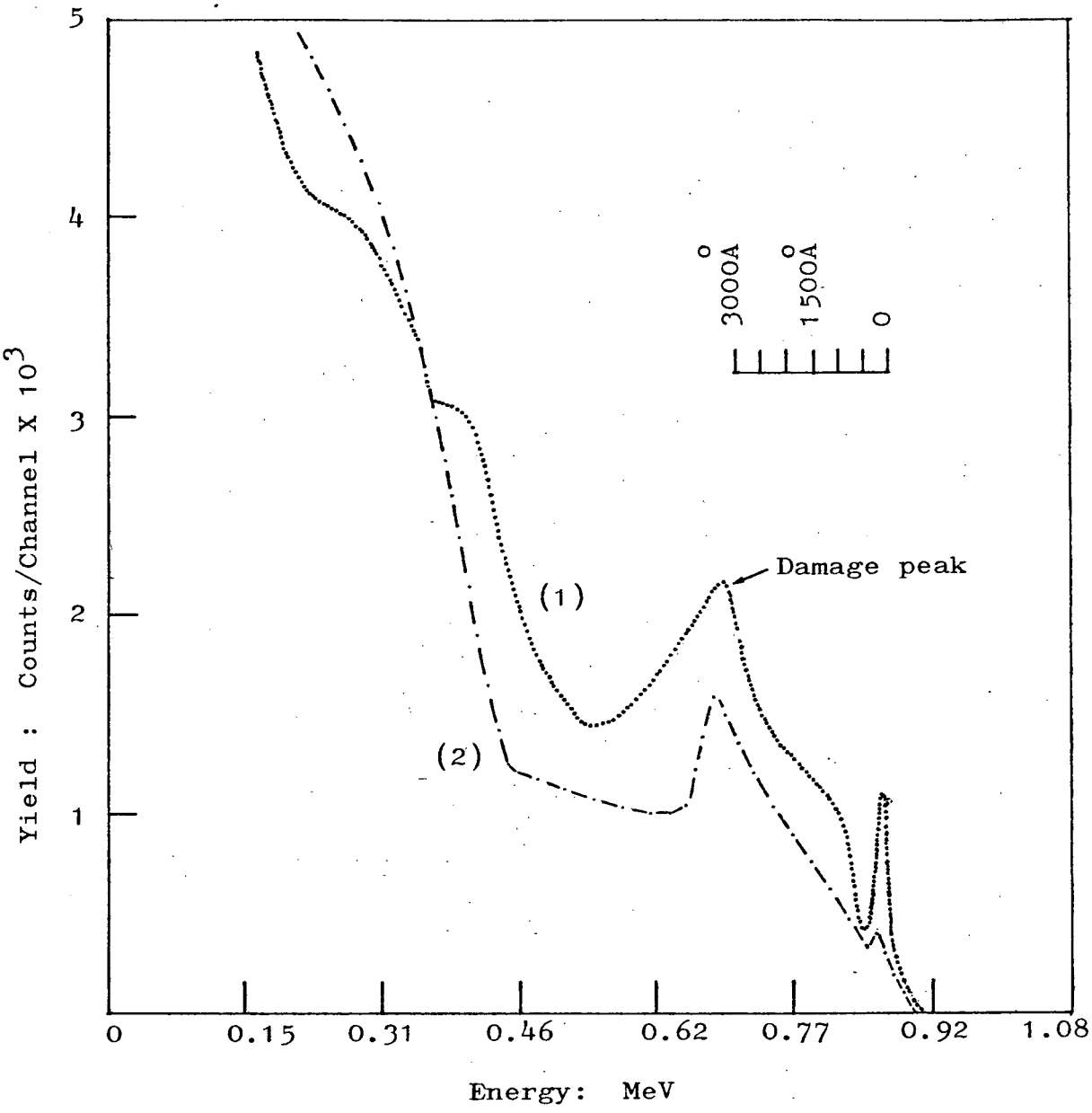

Fig. 4.37. Channelled spectra showing interface damage as a function of dose. Spectrum (1) corresponds to a dose of 1.4×10^{18} $O^+.cm^{-2}$ and (2) to $\sim 2.5 \times 10^{18}$ $O^+.cm^{-2}$, both at 200 keV and in the as-implanted state.

and deposited epitaxial layers. An AEI EM6G transmission electron microscope was used, at first with a commercially available reflection stage. Then, due to the following experimental difficulties, a new specimen holder was designed and constructed. The problems were :

1. Conversion of the instrument from normal transmission to reflection work was highly time consuming.

2. The instrument had to be let up to atmospheric pressure and the transmission specimen stage with all the precision drive mechanisms had to be replaced by the reflection stage and then pumped down again. At each specimen change, air had to be admitted into the instrument and the stage had to be completely detached from the instrument.

3. Manipulation of a specimen in the beam was difficult because the direct shadow of the edge of the specimen was not observable on the screen.

The new reflection specimen holder could be used in the air lock facility available for quick transmission specimen interchange and the change-over from transmission to reflection was as simple as interchanging transmission specimens.

The upper part of the new reflection specimen holder, shown in Fig. 4.38(a), is identical to the transmission specimen holders so that no modification to the support and entry mechanisms was necessary. It is made in one piece, as opposed to the two piece construction of the transmission specimen holder, as shown in Fig. 4.38(b).The narrow tubular part which accommodates the specimen in transmission is replaced by a semicircular solid rod of the same length and diameter, so that half the field could be blocked by placing the holder centrally in the beam. The specimen in the shape of a 4 mm x 4 mm plate is mounted by 'silver dag' on the lowest part of the flat of the semicircular rod.

Fig. 4.38(a) The new reflection electron diffraction specimen holder.

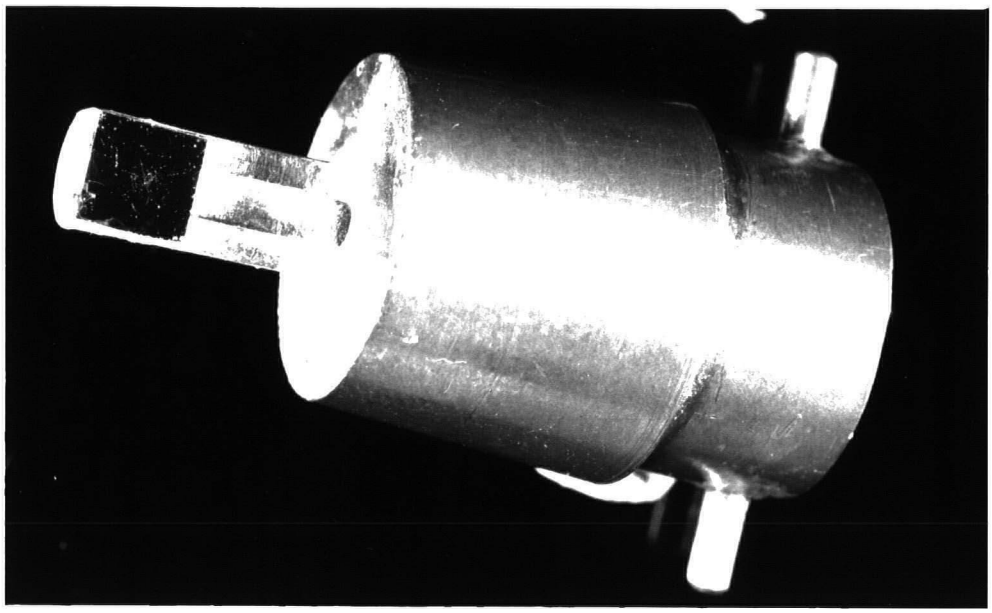

1 cm

Fig. 4.38 (b) AEI EM6G specimen holder for normal transmission electron microscopy. (Reproduced by permission from Kratos Ltd: AEI Scientific Instruments.)

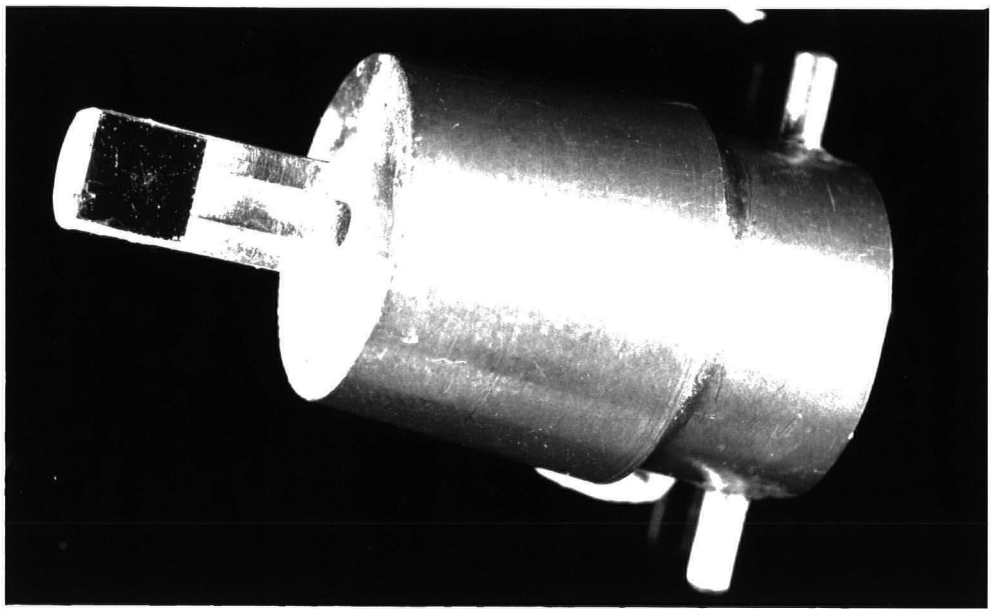

1 cm

Using the normal transmission specimen drive mechanism, the following movements can be obtained, but rotation about an axis, normal to the specimen surface, is not available.

- x-y movement
- in/out of beam
- 360^{o} rotation about an axis parellel to the beam or at a selected tilt and
- -5^{o} to $+5^{o}$ tilt with respect to the beam.

The RED pattern is obtained in almost the same way as a normal transmission electron diffraction pattern using the following procedure :

1. Align instrument in transmission, withdraw objective aperture, and spread beam in low magnification.

2. Introduce specimen, bring specimen into the beam so that half the field is blocked, and establish the position of 'no tilt', as '0' reading on the tilt angle dial does not necessarily mean that the beam is parallel to the surface. With experience, the shadow of the upper and lower edge of the specimen, as shown in Fig.4.39 can easily be recognised. The tilt position at which the two shadow edges coincide is taken as the zero position.

3. Having set the specimen parallel to the beam, i.e. at zero tilt and magnification selector to 'diffraction', adjust condenser C_2 to bring the beam to a spot and tilt specimen so that the lower edge casts a shadow on the screen. When an appropriate tilt is obtained, a diffraction pattern should be visible on the screen. Slight movement of the specimen and the beam may be necessary while tilting.

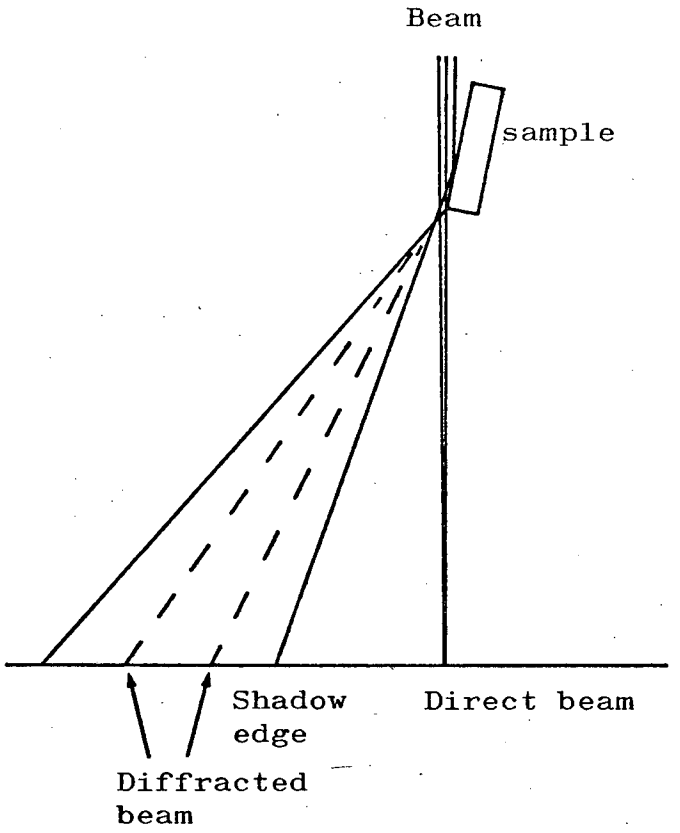

Fig. 4.39(a) Simple geometry for the formation of reflection electron diffraction patterns.

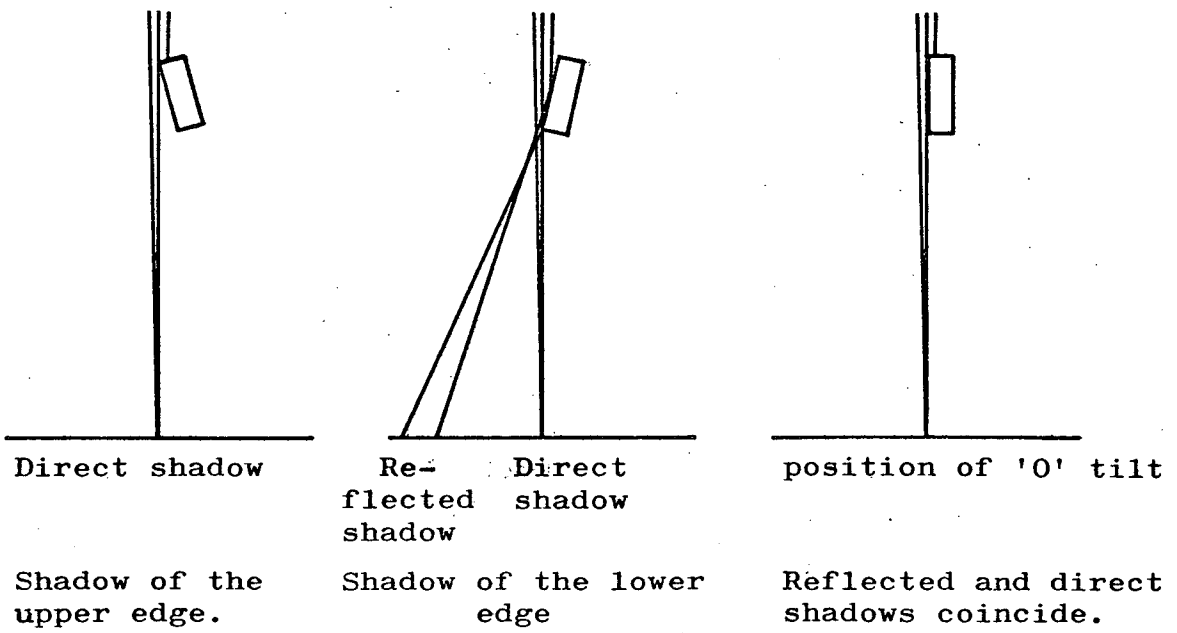

Fig.4.39(b) Establishing proper tilt-angle for reflection diffraction with beam spread for low-magnification microscopy.

4. Focus the diffraction pattern using projector 1 (diffraction control) and defocussing condenser C_2.

4.7.1. Results

Implanted samples, having energy/dose combinations, as given in Table 3.4 were studied, using reflection electron diffraction (RED). It was realised at a later stage that the substrate holder used in these implantation experiments did not allow any substantial rise in substrate temperature. As a result, at these high doses, the substrate surface was totally amorphized. Samples implanted to a dose of 1.4×10^{18} $O^+.cm^{-2}$ at an energy of 200 keV with beam heating and subsequently deposited epitaxial layers were also studied.

No RED pattern was obtainable from samples listed in Table 3.4 in the as-implanted state. However, if a sample were exposed to the electron beam for a few minutes, a diffuse ring pattern developed. This pattern originated from a layer of carbon contamination building up on the beam-bombarded surface. A thin layer of vacuum deposited carbon on a clean silicon substrate gave rise to an identical diffraction pattern.

These samples, following anneal treatment for 2 hours at 1150°C in a nitrogen ambient, showed diffraction spot patterns. The spots corresponded to a (100) surface of silicon, although the starting material was (111). At low energies of 50-70 keV only one or two spots of low intensity were observed as shown in Fig. 4.40. The number of spots and their intensity increased with increasing ion beam energy.

Samples implanted at a temperature of ~550°C to a dose of 1.4×10^{18} $O^+.cm^{-2}$ at an energy of 200 keV showed a strong Kikuchi band and, in some cases, also low intensity spots, as shown in Fig. 4.41(a). The intensity increased, as shown in Fig. 4.41(b), following anneal treatment for 5-15 mins.

Fig. 4.40. Reflection electron diffraction patterns from annealed samples implanted at various energies.

(a) 5×10^{17} $O^{+}.cm^{-2}$ at 50 keV.

(b) 8.6×10^{17} $O^{+}.cm^{-2}$ at 100 keV.

(c) 1.3×10^{18} $O^{+}.cm^{-2}$ at 180 keV.

(a)

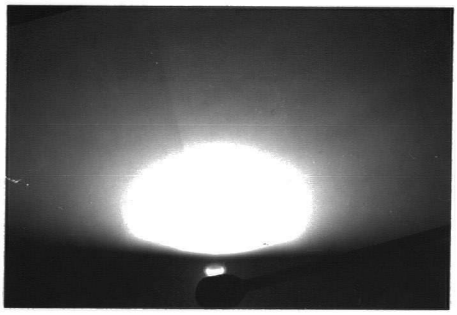

(b)

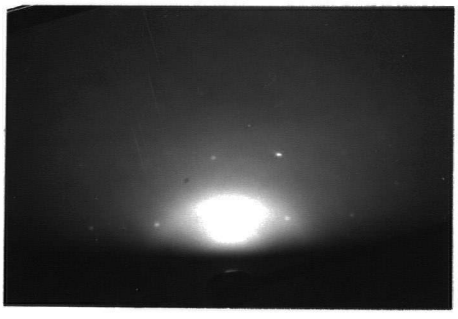

(c)

Fig. 4.41. Reflection electron diffraction patterns from as-implanted and annealed samples implanted at 550°C.

(a) As-implanted

(b) Annealed

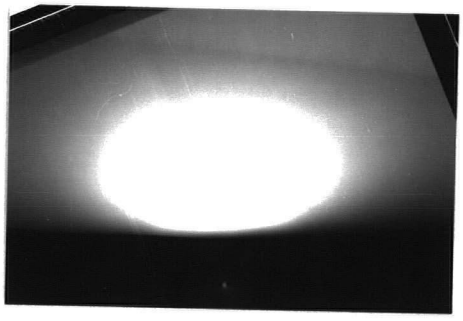

(a)

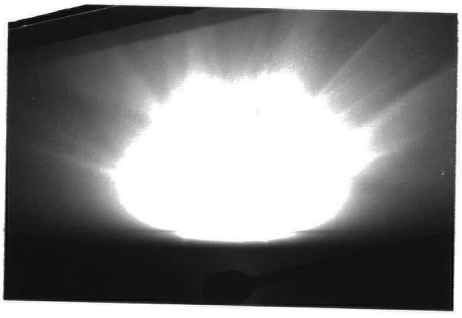

(b)

at 1100°C in a hydrogen ambient. The deposited epitaxial layers (Fig.4.42) showed diffraction patterns indistinguishable from that of untreated silicon wafers.

The appearance of (100) diffraction spots from annealed samples, listed in Table 3.4, may probably be due to a change in crystallographic morphology during recrystallization of the amorphous layer. As indicated by low magnification optical micrographs, shown in Fig.4.7, closely-spaced, isolated pyramidal crystallites bounded by three (111) planes are formed on the B-IMPLOX layer. Under the geometrical conditions of the reflection diffraction experiments, one set of (100) planes is nearly perpendicular to the electron beam, as indicated in Fig. 4.43. The resulting diffraction pattern, therefore, corresponds to (100) planes.

The low intensity of the spots from the lower energy implants is probably due to the extremely small thickness of the surface silicon layer. At higher energies the thickness of the surface layer increases, contributing to the enhancement of the diffraction spots.

The Kikuchi lines for the case of the elevated temperature implants, indicate that a good degree of long-range order[151,152] is maintained even in the as-implanted state. The surface crystallinity is further enhanced by a short anneal treatment for 5 min. at 1100°C.

4.8 Sirtl etching

Sirtl etching[81] revealed a high density of stacking faults of the order of 10^6 . cm^{-2} in the epitaxial layers deposited at the early stage of the work, on implanted substrates annealed in a nitrogen ambient. These layers also had topographical overgrowth, as shown in Fig.4.12. In later samples the stacking fault density was reduced to an order of $10^3 . cm^{-2}$, using careful cleaning and handling procedures (see sec. 3.6.4).

Fig. 4.42. Reflection electron diffraction patterns from deposited epitaxial layers on annealed implanted substrates.

(a) Substrate implanted at 200°C

(b) Substrate implanted at 275°C

(c) Substrate implanted at 550°C

(a)

(b)

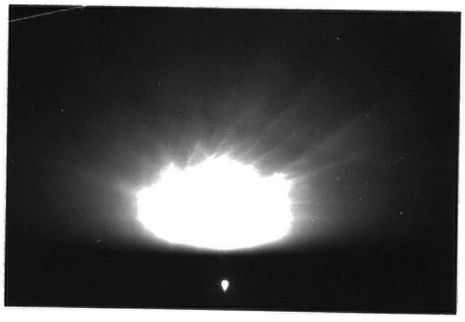

(c)

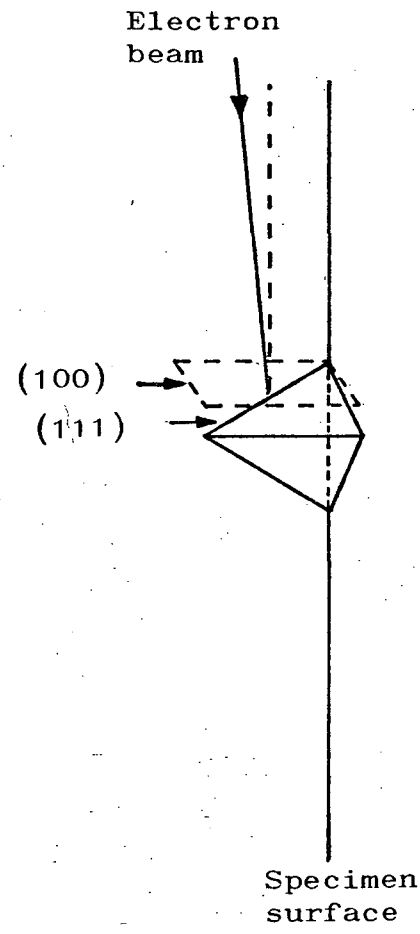

Fig.4.43. Reflection electron diffraction arising from pyramidal crystallites.

4.9 Transmission Electron Microscopy (TEM)*

Transmission electron microscopy was carried out on some cross-sectional samples of epitaxial layers deposited on substrates in which a buried implanted oxide was formed. Oxygen was implanted to a dose of 1.4×10^{18} $O^+.cm^{-2}$ at 200 keV in the central area (1 x 1 cm) of a 2 x 2 cm substrate. The estimated substrate temperature during implantation was $\sim 550^{\circ}C$. This temperature rise was brought about by beam induced heating. The samples were annealed in the epitaxial reactor in a hydrogen ambient at a temperature of $1100^{\circ}C$ prior to the deposition of an epitaxial layer of thickness in the range o.6 μm - 1.0 μm. The layers were phosphorus doped during growth to give a resistivity of ~2 Ωcm.

Specimens were prepared for TEM examination by standard procedures[153] involving mechanical polishing followed by low energy ion-beam thinning. The cross-section plane was close to $(2\bar{1}\bar{1})$. The specimens were cut from the border region of the implanted area so that both implanted and unimplanted regions could be examined. These were examined in a Philips EM300 TEM operated at 100 kV and using standard diffraction contrast procedures[154,155]. Micrographs taken for different specimen tilts, diffraction conditions, etc., are shown in Figs.4.44 and 4.45. Selected-area diffraction patterns arising from specimen areas ~0.5 μm across were also obtained to provide information on the crystallography of different regions of the specimen.

4.9.1 Results

The transmission electron micrographs in Figs. 4.44 and 4.45 showed the presence of a well-defined central region, appearing as a dark band approximately parallel to the surface of the original specimen. This region undoubtedly corresponds to the buried oxygen-implanted layer. The upper and lower boundaries of this buried implanted oxide layer are ~1.02 and 1.40 μm from the surface giving a layer thickness

*Work carried out by M C Wilson and G R Booker, Dept. of Metallurgy and Science of Materials, University of Oxford.

Fig.4.44(a) Transmission electron micrograph (bright-field, near a $\langle 211 \rangle$ type pole, 220 reflection, s+Ve) of a cross-sectional sample. 'D1' is the damaged layer above and 'D2' is the one below the implanted oxide layer. The interface between the original substrate and the epitaxial layers is not delineated. The substrate was implanted to a dose of 1.4×10^{18} $O^+.cm^{-2}$ at 200 keV.

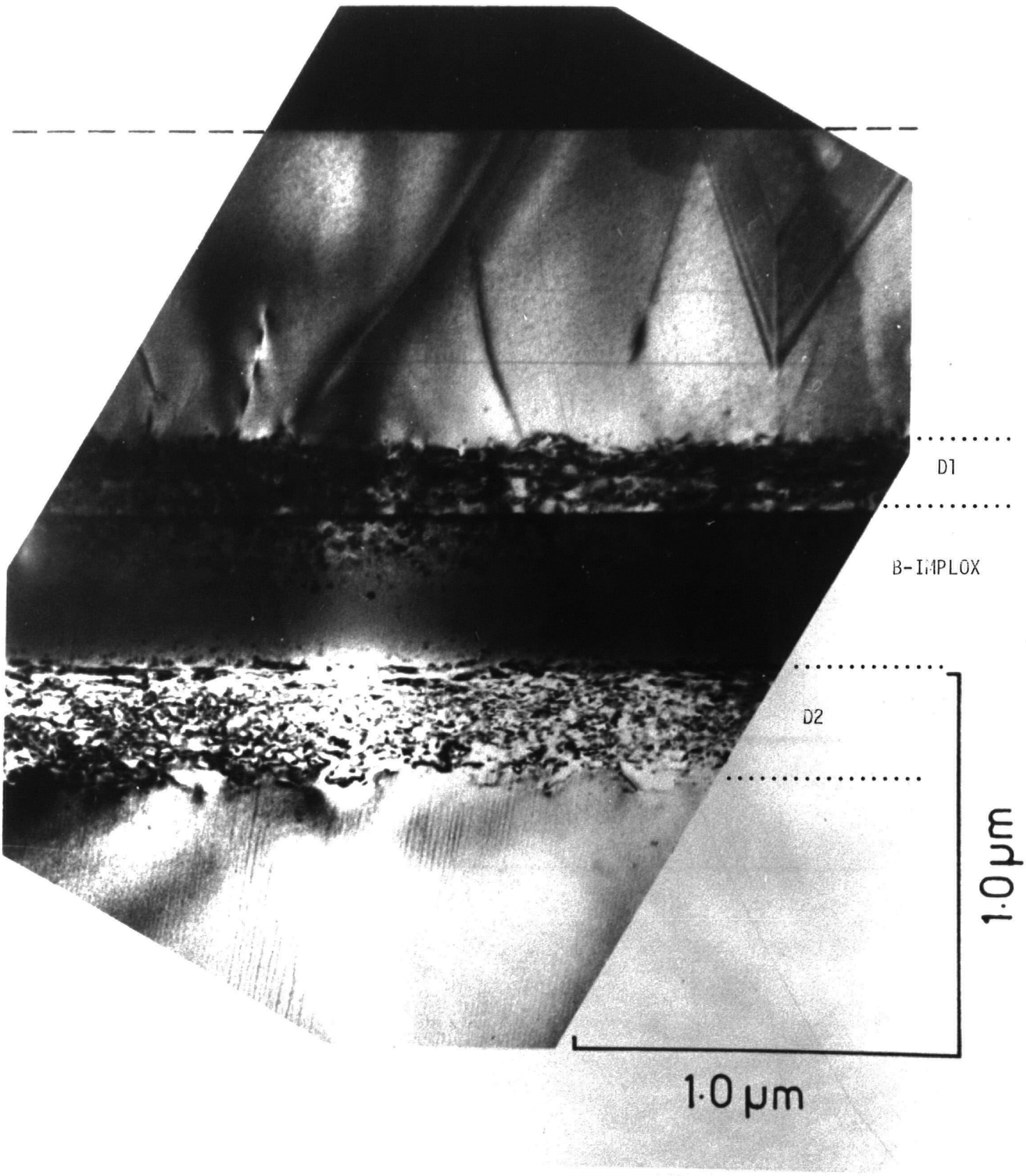
D1
B-IMPLOX
D2
1.0 µm
1.0 µm

Fig.4.44(b) Dark-field micrograph (near a ⟨211⟩ type pole, 220 reflection, s+Ve) of the same area as (a).

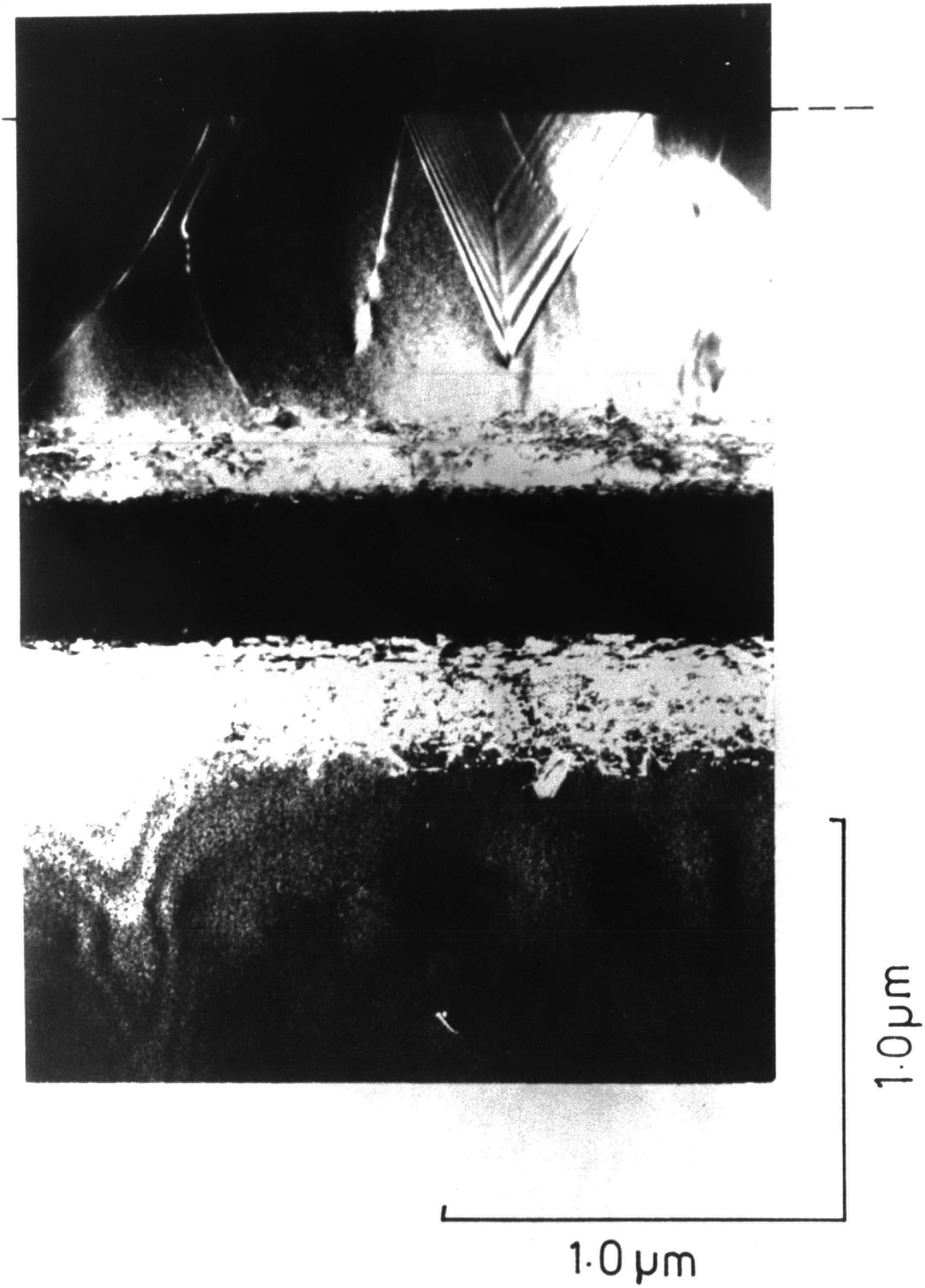
1.0 µm
1.0 µm

Fig. 4.44(c) Dark-field, weak-beam micrograph (near a ⟨211⟩ type pole, 220 reflection, 5/5g) of the same area as (a) and (b).

1.0 μm
1.0 μm

Fig. 4.44(d) Bright-field micrograph (near a $\langle 110 \rangle$ type pole, 220 reflection, s+Ve) of a region outside the implanted area.

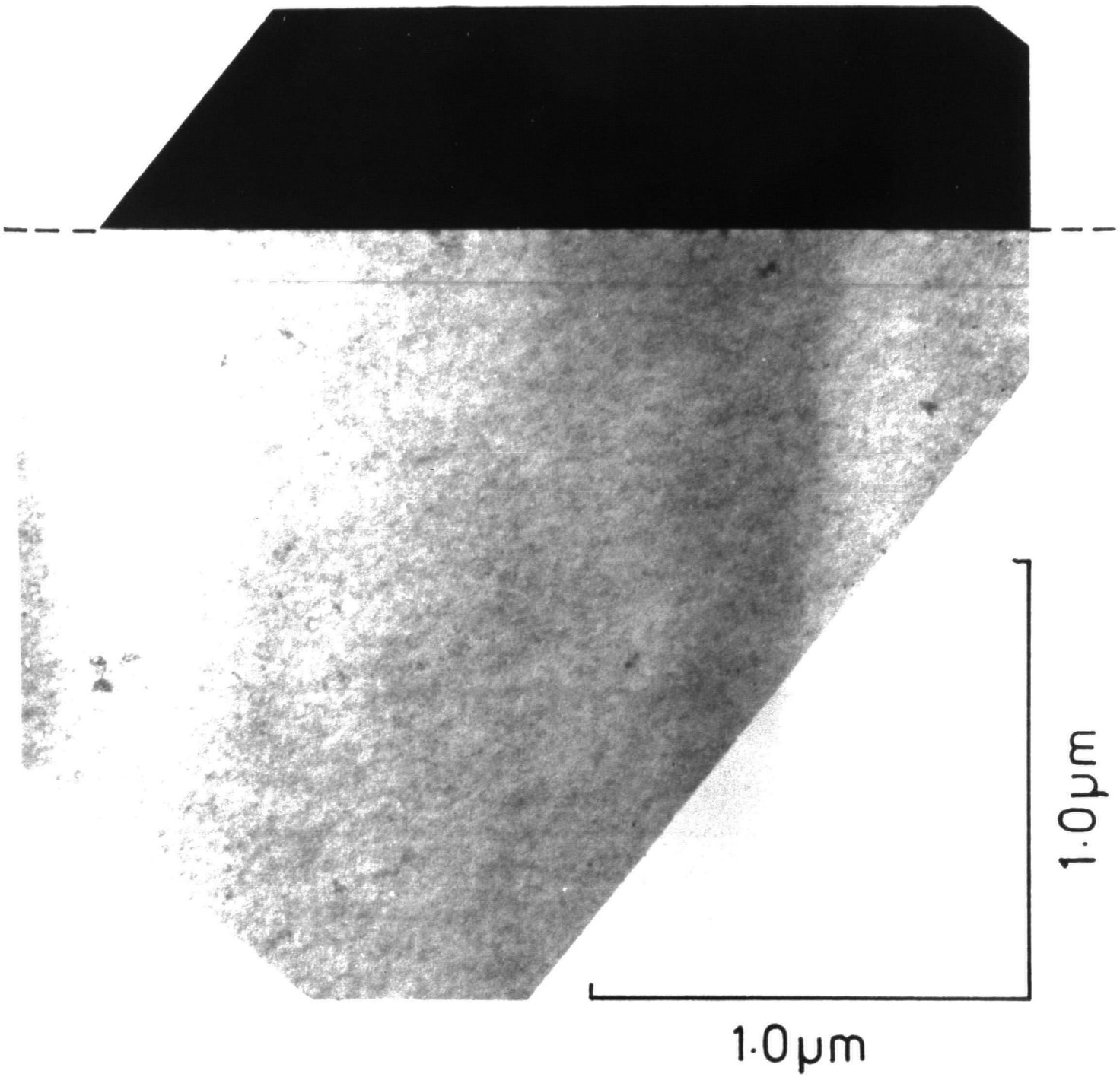
1.0μm
1.0μm

Fig.4.45(a) Bright-field micrograph of a cross-sectional sample showing striated oxide. (Near a <211> type pole, 220 reflection, s+Ve.)
The substrate was implanted to a dose of 1.0×10^{18} $O^{+}.cm^{-2}$ at 200 keV.

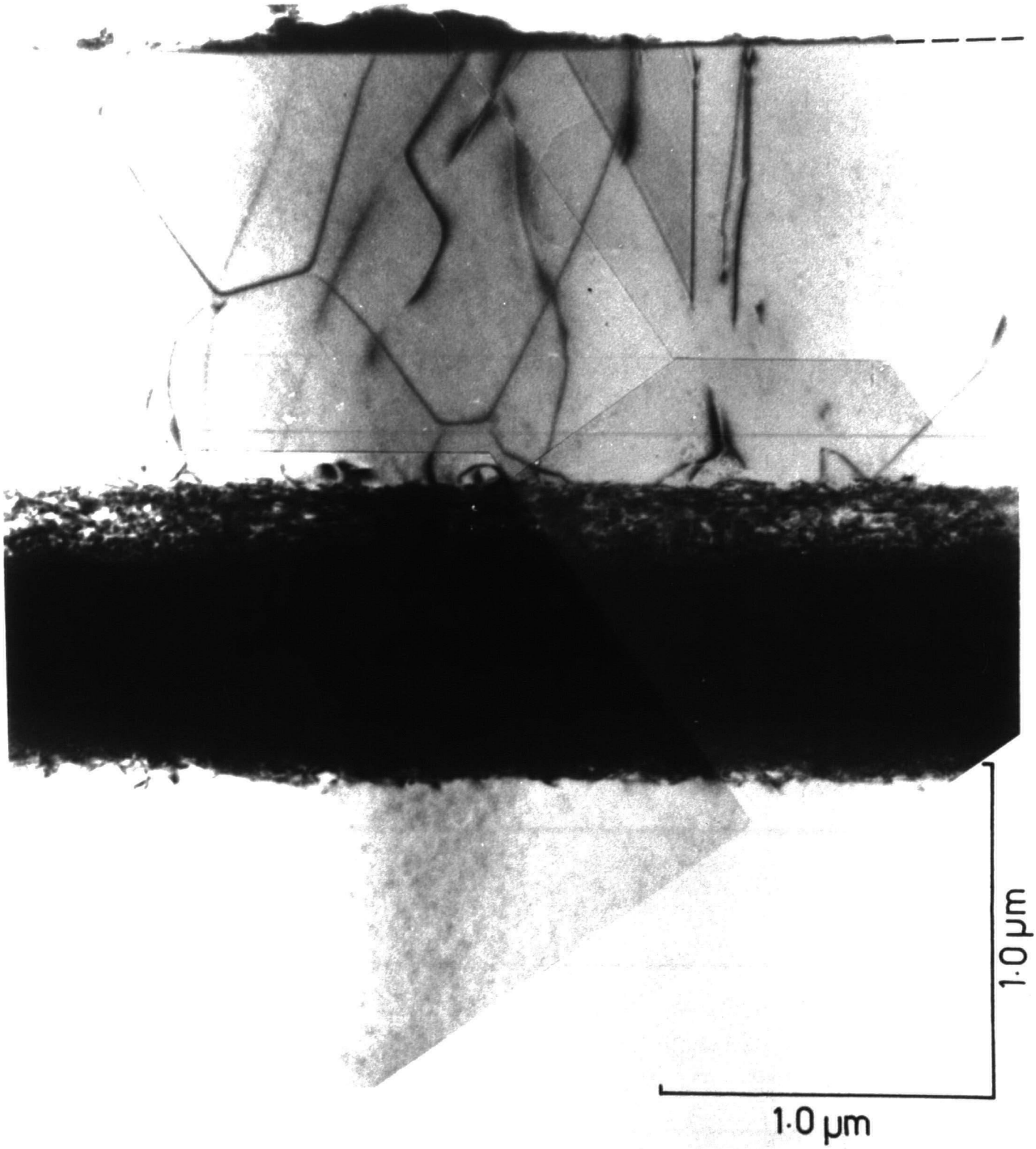
1·0 μm
1·0 μm

Fig.45(b) Dark-field, weak-beam micrograph of the same area as (a). (Near a $\langle 211 \rangle$ type pole, 220 reflection, g/5g .

1.0 μm
1.0 μm

of ~0.38 μm. On either side of this buried oxide layer there are heavily damaged regions, the one above the oxide being ~0.19 μm thick and the one below being~0.32 μm thick. Above the upper damaged region is the epitaxial layer and below the lower one is the substrate.

The damaged regions consist of polycrystalline material, low angle boundaries, irregular dislocation arrays, etc. The buried implanted oxide region contains polycrystalline material (most probably crystallites of silicon) near the upper and lower boundaries, with grain sizes in the range 500Å and downwards. On going towards the middle of this zone, grains can still be observed down to the resolution limit of ~20Å in the weak beam micrograph of Fig.4.43(c) These grains are very likely to be crystallites of silicon. It is speculated that the variation in size of these crystallites arises from the approximate Gaussian nature of the oxygen distribution. The tails of the distribution correspond to the edges of the oxide, where the oxygen content is much lower than the stoichiometric requirement for oxide formation. It is probable that large clusters of silicon dioxide would form during anneal, due to 'preferential' diffusion[135] of oxygen atoms towards existing nuclei of silicon dioxide. These silicon dioxide clusters would be surrounded by unreacted silicon clusters or vice versa depending on the amount of oxygen present in a given volume of the substrate. As the peak of the Gaussian distribution is approached, little silicon would remain unreacted with a consequent reduction of grain size. The unreacted silicon would be expected to form crystallites during anneal at temperatures above ~800°C[129]. The striated nature of the oxide, as shown in Figs.4.45 corresponding to a lower dose of ~1 x 10^{18} $O^{+}.cm^{-2}$, (other processing steps were the same as the previous sample) is probably due to a higher incidence of crystallites of unreacted silicon.

Selected-area transmission electron diffraction patterns from the epitaxial layer and the substrate showed only single

crystal silicon having the same crystallographic orientation. Diffraction patterns from a region covering simultaneously the buried oxide and parts of the damaged layers above and below it, showed both single crystal and polycrystalline silicon. Characteristic, broad, diffuse rings of amorphous silicon dioxide were not observed, but this could not be ascertained without a micro-diffraction pattern from a much smaller selected area.

Dislocations in the epitaxial layer, originating from the damaged region below it and threading through the layer, were observed. The density of these dislocations referred to the original specimen surface was estimated to be $\sim 5 \times 10^{8}$ cm^{-2}. A small number of epitaxial stacking faults was also observed. The precise position of the interface between the original implanted substrate and the subsequently grown epitaxial layer was not clearly delineated in the micrographs. A few dislocations in the substrate were also observed. These originated from the damaged region below the implanted oxide layer.

The corresponding micrographs from the unimplanted region showed good quality silicon. No defects were observed in the area examined, as shown in Fig.4.44(d).

4.10 X-ray topography

X-ray topography appears to be the only non-destructive technique available for examining defects in semiconducting materials[156]. Either reflection or transmission mode can be used. The crystal mounted on a goniometer is orientated to satisfy the Bragg reflection condition for a desired set of planes. The diffracted beam is recorded on a photographic plate, the primary beam being transmitted through the crystal does not strike the plate. Any localised deviation from the exact Bragg condition, due to the presence of faults, will cause a variation in the otherwise uniform diffracted

intensity. For a given orientation only those dislocations with a component of their Burger's vector perpendicular to the diffracting plane will be imaged. By oscillating the crystal and the film together, large areas, like whole wafers, can be examined.

The transmission topographs, as shown in Fig.4.47, were obtained using molybdenum K_α radiation and the (220) reflection. The experimental arrangement is shown schematically in Fig.4.46(a). Copper K_α radiation and the (440) plane were used for obtaining reflection topographs. The reflection arrangement is shown in Fig.4.46(b).

Three samples were examined, all of which were prepared from 3-5 Ωcm n-type (111) silicon. Two samples were oxygen implanted, one to a dose of 1.4×10^{18} $O^+.cm^{-2}$, the other to 1.0×10^{18} $O^+.cm^{-2}$, both at 200 keV, at a substrate temperature of ~550°C. The implanted samples were annealed at 1100°C for 5 minutes in a hydrogen ambient. An n-type epitaxial layer of 1.5 μm in thickness was grown on the implanted samples and on an untreated substrate, in the same run. Subsequently enhancement and depletion mode MOS transistors were fabricated. Following testing of the devices the metallisation and the oxide layer were removed and topographs obtained.*

4.10.1 Results

The topographs are shown in Fig. 4.47. Only a transmission topograph was obtained from the unimplanted sample. No defects were observed. From the topographs of the implanted samples the central implanted area was clearly recognisable from a grainy appearance, probably arising from the sub-surface damaged region at the upper B-IMPLOX interface (see transmission micrographs in Fig. 4.44). The reflection topographs showed greater contrast. The triangular areas of null contrast are probably due to pyramidal hillocks as shown in Fig. 4.12. The dark triangular areas are probably due to contrast arising from stacking faults.

* Work carried out by D.G. Hart, Plessey Allen Clark Research Centre, Caswell.

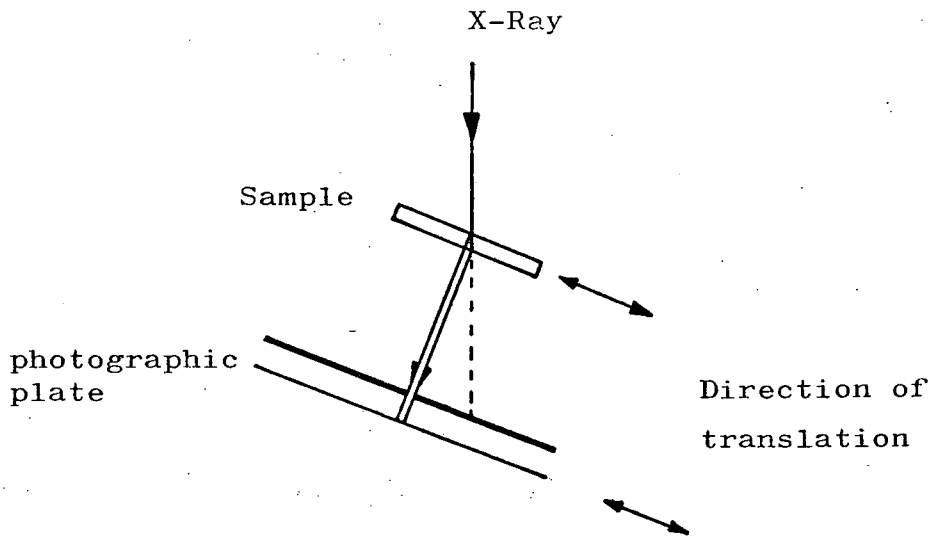

(a) Transmission

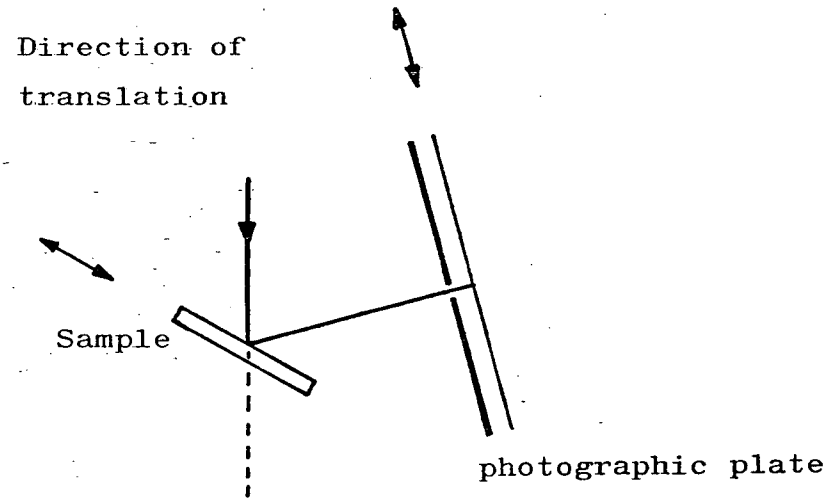

(b) Reflection

Fig.4.46. Schematic arrangement used for obtaining X-ray topographs.

Fig. 4.47(a) Transmission topograph of a sample without a buried implanted oxide.

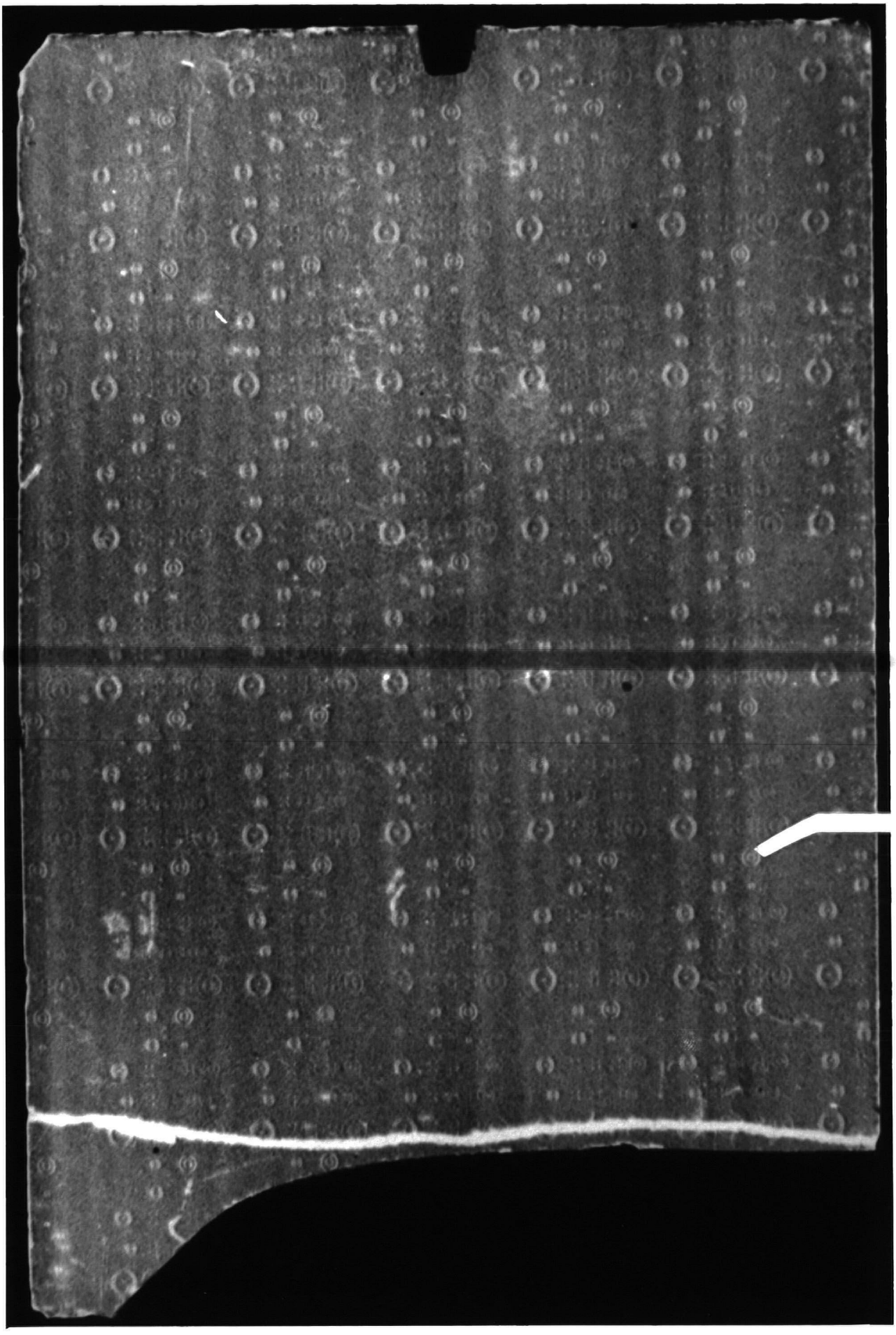

Fig. 4.47(b) Transmission topograph of a sample implanted to a dose of $1.4 \times 10^{18} O^{+}.cm^{-2}$ at 200 keV. The $1 cm^{2}$ implanted area is clearly recognizable from the granular appearance.

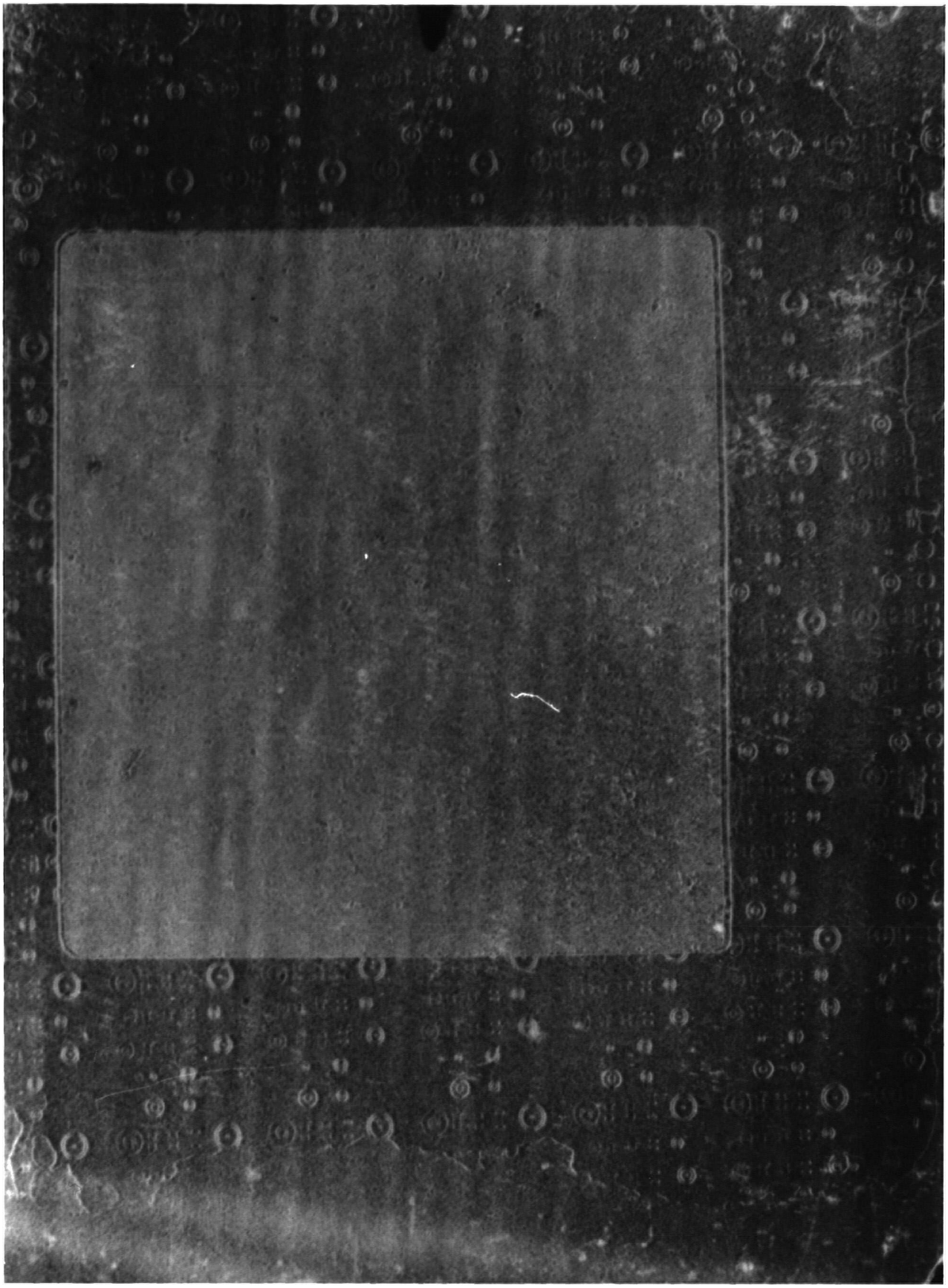

Fig. 4.47(c) Reflection topography of the same sample as (b). A stacking fault density of ~1 x 10^3 and pyramidal hillock density of ~1 x 10^3 are estimated from the observed defect contrast.

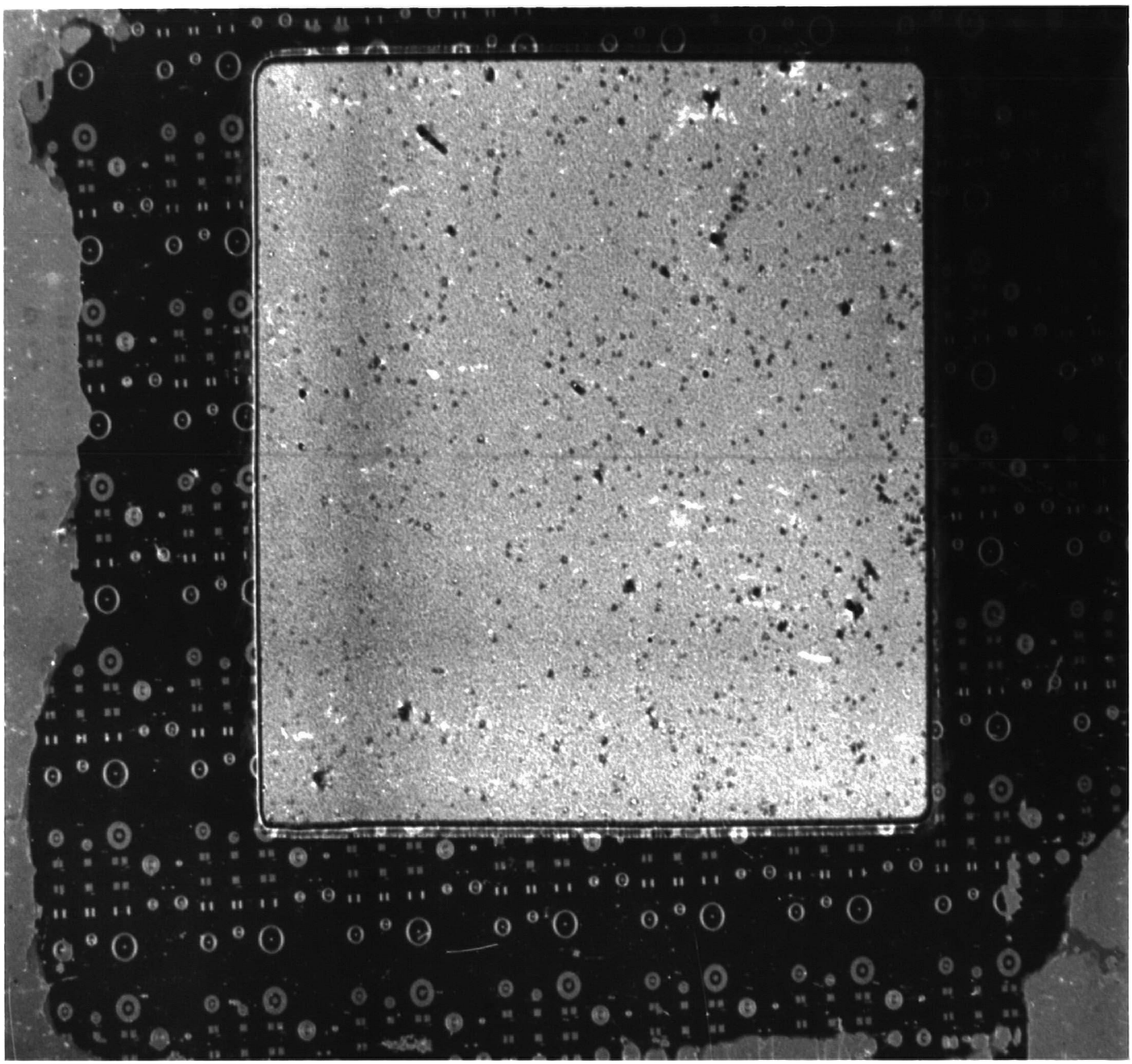

4.11 Auger Electron Spectroscopy[157,158]

Auger electrons are generated by bombarding the specimen with low energy electrons (1 - 10 keV). Electron transitions giving rise to an Auger electron are shown schematically in Fig.4.48. If an electron from the K level is ejected by primary bombardment, an electron from the L_2 level may fill the vacancy releasing an amount of energy $E_K - E_{L2}$. This energy may now be transferred to another electron in the L_3 level which is then ejected from the solid. The ejected electron is the Auger electron and its energy is given by :

$$E = E_K - E_{L2} - E_{L3}$$

Since the energy levels are characteristic of a particular element, it is possible, by measuring the energies and the number of Auger electrons, to determine the elemental composition of a given sample.

The energy of Auger electrons lies in the range between 20 and 1000 eV. Only those produced within the first two or three atomic layers ($\sim 20\text{Å}$) will escape without losing a substantial part of the original energy. Thus Auger electron spectroscopy is essentially a surface analytical technique, but coupled with sputter etching, it can be used for depth profiling. The detection limit of the technique is ~0.1 At.%.

An Auger electron spectrometer consists of a vacuum chamber with an electron gun (1-10 kV) to produce the primary beam and an electron spectrometer for energy analysis of the emitted electrons. An ion gun is provided for sputter cleaning the sample surface and for etching in composition-depth profiling. A number of samples are mounted on a carousel holder attached to a manipulator for sample positioning. Pressures better than 10^{-8} torr are used to minimise adsorption of residual gas atoms on the sample surface.

The general character of the electron energy spectrum produced by the primary incident electrons is shown in Fig.4.49 (a).

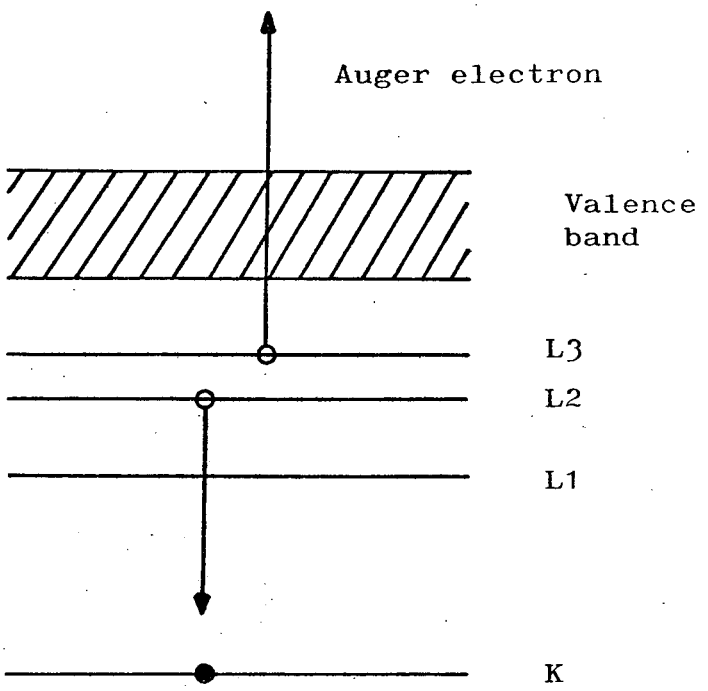

Fig.4.48. Auger electron emission .

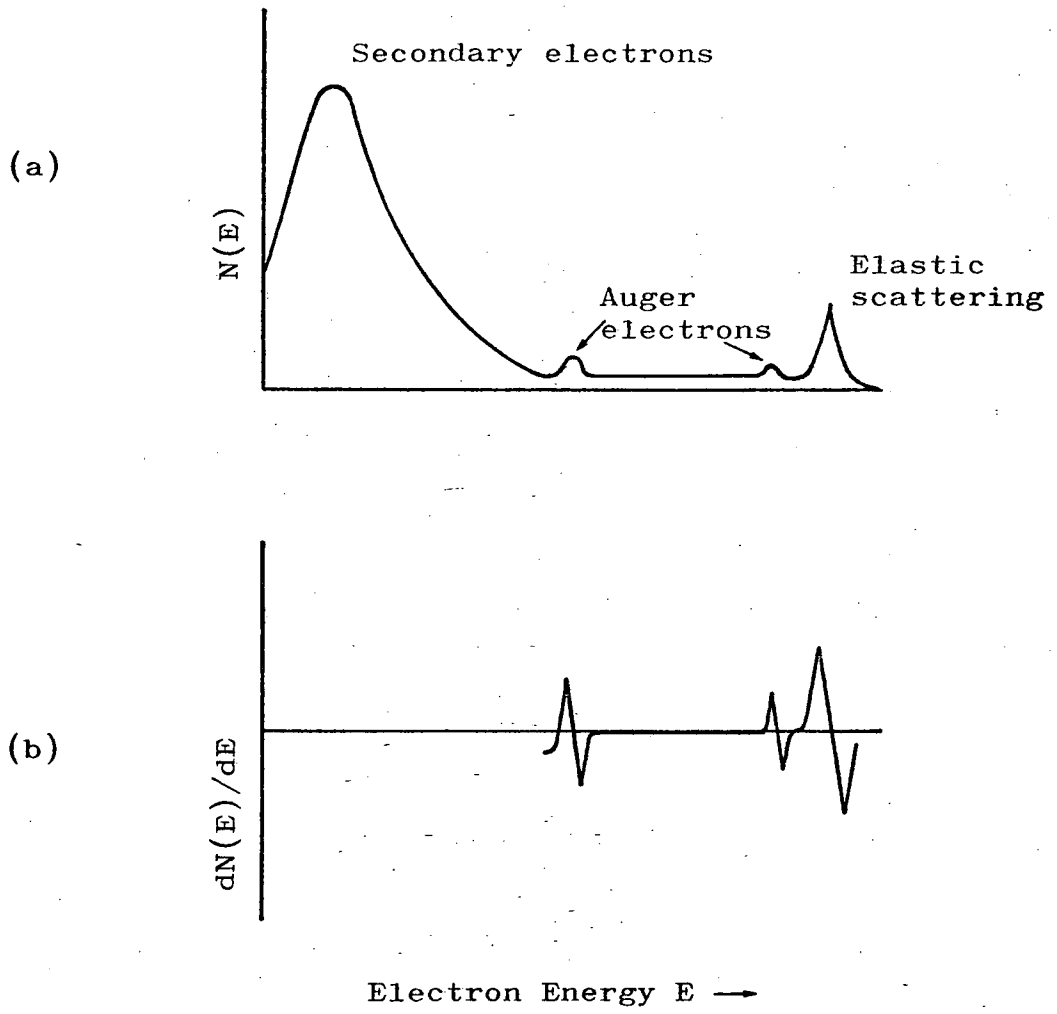

Fig. 4.49 (a) Electron energy spectrum produced by incident electrons.

(b) Corresponding derivative signal.

Auger transitions appear as a fine structure between the secondary and elastically-scattered primary electron peaks. Auger peaks are comparatively small in amplitude. Therefore, the derivative $dN(E)/dE$ is used to enhance the detectability. By convention, the energy of the Auger peak is taken to be the energy corresponding to the minimum of the negative part of the Auger transition since this is usually the most sharp and prominent. For most elements, a number of Auger transitions occur and different elements are identified by characteristic peaks at well-defined energies. Composition-depth profiles are normally obtained by sequential ion-beam sputter-etching and surface analysis.

A Vacuum Generators ESCA III instrument was used to analyse* samples implanted to a dose of 1.3×10^{18} $O^+.cm^{-2}$ at 100 keV, (1) in the as-implanted state (2) following an anneal treatment for 15 minutes at 1100°C in a hydrogen ambient. During implantation the substrate temperature was maintained near room temperature. A 9 kV, 200 μA cm^{-2} Ar^+ ion beam was used for etching. For silicon an etch rate of 5Å ±1Å per μA per minute is expected under these conditions. A target current of 50 μA was obtained while etching through silicon for a 5 mm x 5 mm sample. The sample was sequentially etched and analysed at 30 sec. intervals. The following three Auger peaks were monitored :

Channel	1	2	3
Peak	O_{KLL}	C_{KLL}	Si_{LVV}
Position	510 eV	288 eV	91 eV

The target current dropped to an average of 17 μA when the implanted oxide was reached.

4.11.1 Results

In the as-implanted sample, the O_{KLL} peak was first observed at a depth of 1250Å (± 250Å). The approximate interface between the surface silicon and buried implanted oxide was

*Work carried out by R H West, Dept. of Metallurgy and Materials Technology, University of Surrey.

established to be 1500Å (± 300Å). The oxide layer extended to a depth of 2400Å (± 400Å). A typical spectrum from the oxide is shown in Fig.4.50. The peak-to-peak heights of the O_{KLL} an Si_{LVV} peaks, as a function of the number of 30 second-etches, are shown in Fig.4.51.

An oxygen concentration profile as shown in Fig.4.52 can be constructed from the Auger peak heights in Fig.4.51. It is assumed that stoichiometric silicon dioxide is formed where the O_{KLL} (SiO_2) and Si_{LVV} (SiO_2) curves in Fig.4.51 reach a plateau. The long tail at the deep side of the oxygen profile is probably due to surface roughness which increases with etch time, resulting in greater error in the depth calculations. However, the distribution is similar to that shown in Fig. 4.30. The part of the Gaussian curve above the stoichiometric level is not observed.
The presence of oxygen was not detected in the annealed sample. This indicated the loss of oxygen during anneal treatment (see Sec. 4.5.1.).

4.12 Summary of Results (also see Table 4.9.)

Buried implanted oxide layers were formed by the implantation of oxygen ions in silicon substrates at various doses and energies. The distribution profile of the oxygen was obtained by Rutherford back-scattering of 1.5 MeV helium ions and by Auger electron spectroscopy in conjunction with sputter-etching.

An approximate Gaussian distribution was obtained for doses up to that required for providing the stoichiometric amount, i.e. $\sim 4.6 \times 10^{22}$ O. cm^{-3}, at the peak of the distribution, for the formation of silicon dioxide. The peak of the distribution occurred at greater depths with increasing

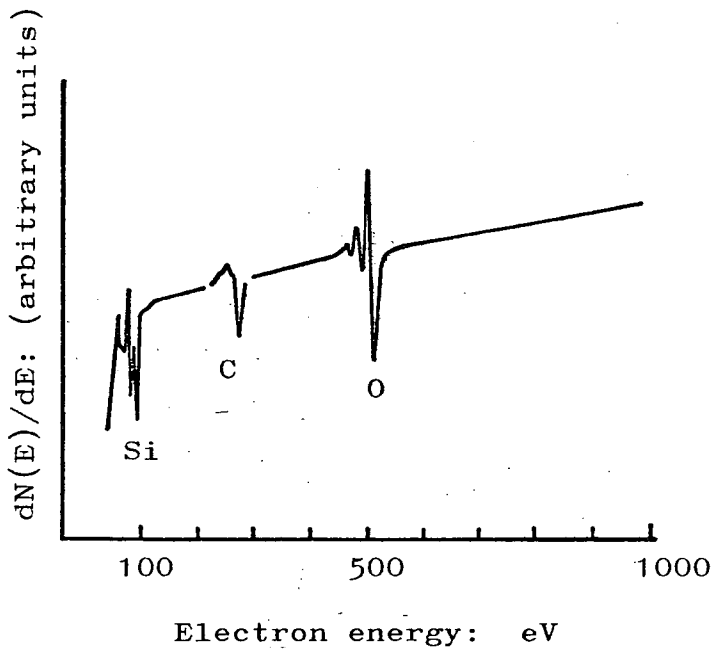

Fig. 4.50. Typical Auger spectra obtained fom an oxygen implanted substrate. Carbon was present in a very thin surface layer.

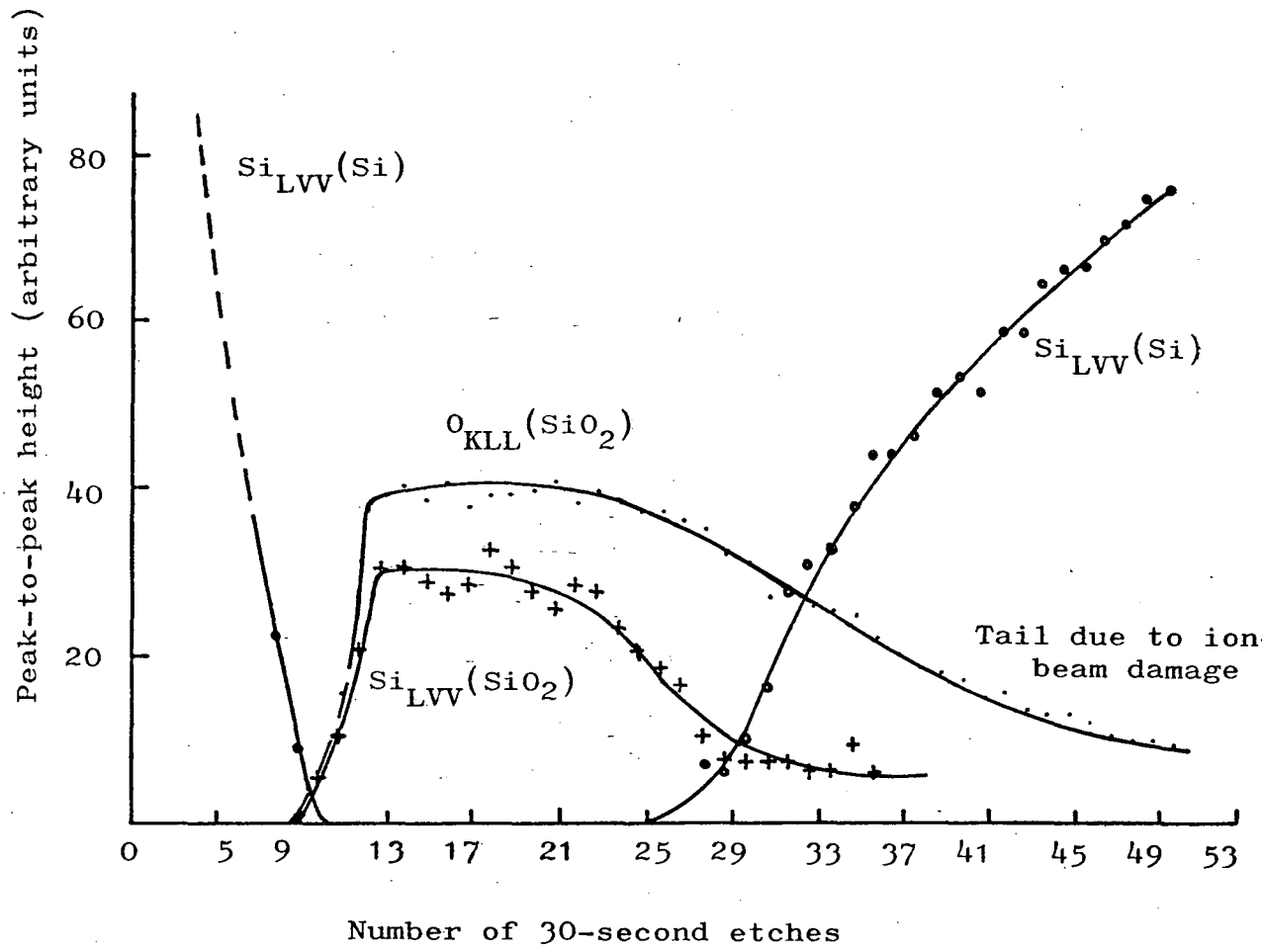

Fig. 4.5.1. Peak-to-peak heights of the O_{KLL} and Si_{LVV} Auger peaks from an oxygen implanted substrate as a function of 30-second etches.

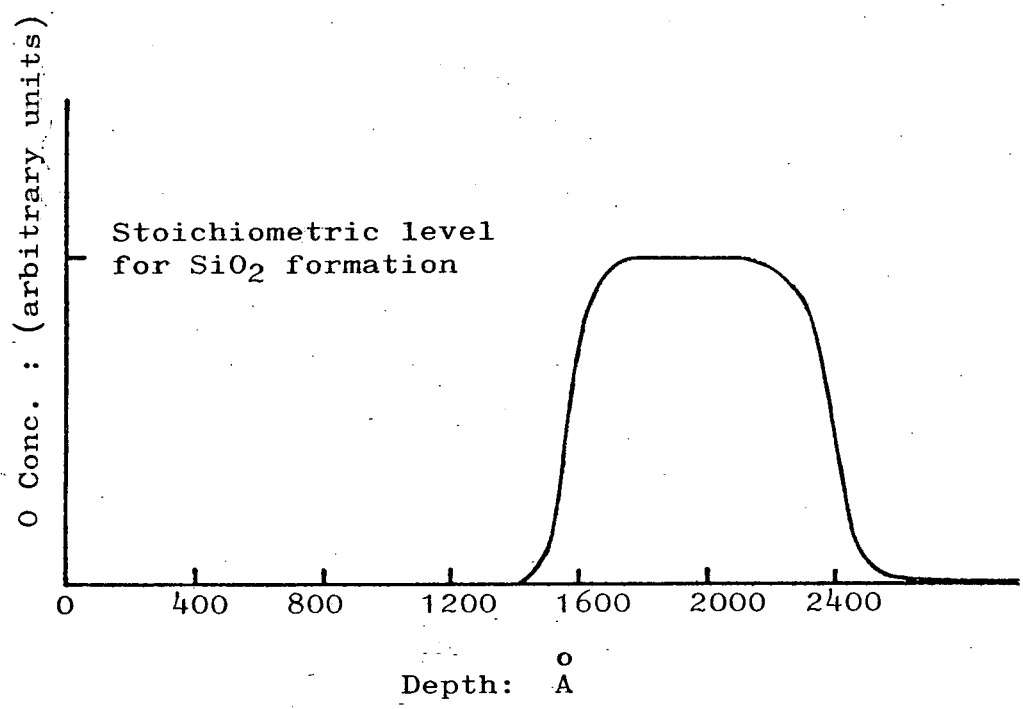

Fig. 4.52. Approximate oxygen profile obtained from data presented in Fig. 4.51.

TABLE 4.9

Summary of Results

Samples implanted to a dose of 1.4×10^{18} $O^{+}.cm^{-2}$ at 200 keV

Sample	As-implanted			Annealed		Deposited epi-layer RBS $\chi_{min.}$
	Visual appear-ance	IR peak μm	RBS χ_{min}	IR peak μm	RBS χ_{min}	
~Room temp. implant	hazy	10.1	-	9.2	-	-
~200°C implant	hazy	10.0	-	9.2	-	0.13
~275°C implant	hazy	9.9	-	9.2	-	0.07
~550°C implant	almost haze-free	9.7	0.12-0.16	9.2	0.05-0.07	0.03
Epi on unimplanted sample	-	-	-	-	-	0.03

beam energy. The projected range, i.e. the peak of the distribution and the standard deviation agree well with computed figures given by Gibbons, Johnson and Mylroie.[103] For higher doses a box-type distribution, indicating a uniform stoichiometric concentration over a certain thickness, is obtained. A consequent reduction in the interface damage was also observed. Other parameters being equal, at higher substrate temperatures the interface damage was decreased.

The oxide in the as-implanted state and following anneal treatments was characterised by infra-red absorption spectroscopy. For a given dose the position of the absorption peak in the as-implanted state depended on the substrate temperature during implantation. At a given substrate temperature the peak depended on the dose. Substrates implanted at near room temperature to a dose of 1.4×10^{18} O^+. cm^2 at 200 keV showed a peak centred around ~10 μm. Higher temperature implants showed a shift of the peak towards the shorter wavelength indicating in-situ annealing of the implanted oxide during implantation. Also, the implanted oxide spectrum had a broad absorption band in the 2.5 μm - 7.5 μm region. This appears to be due to the buried nature of the implanted oxide. A similar broad band was observed in polycrystalline silicon/thermal oxide/silicon structures. Following an anneal treatment at or above 1000°C (less than 30 minutes at 1000°, about 5 mins. at 1100°C) the as-implanted absorption peak shifted to 9.2 μm and considerable sharpening was observed. Two other peaks at 8.4 μm and 12.5 μm also appeared. All three peaks were at exactly the same position as observed with thermal oxides except that the 9.2 μm peak in implanted oxides was slightly broader. However, these absorption peaks were not observed in samples implanted at room temperature following anneal treatment in a hydrogen ambient.

An equivalent thickness of the implanted oxide in terms of thermal oxide thickness was obtained from a plot of the

thermal oxide absorbance at 9.2 μm as a function of thickness. For a dose of 1.4×10^{18} $O^+ . cm^{-2}$ at 200 keV a thickness of ~ 0.4 μm was obtained from the infra-red absorbance, whereas an estimate from the Rutherford back-scattering spectra and a measurement on angle-lapped samples yielded a thickness of ~ 0.3 μm. Transmission electron micrographs indicated a thickness of 0.38 μm. A 0.3 μm thick oxide layer was expected from a total dose of 1.4×10^{18} $O^+ . cm^{-2}$ assuming that all the oxygen ions contribute to the formation of silicon dioxide. The thickness obtained from the RBS spectra and the angle-lapped samples are in very good agreement with the expected thickness. However, infra-red absorbance measurement would be the preferred technique, although the thickness obtained by this technique is consistently higher than the expected value (see p. 114). The infra-red absorbance measurement is totally non-destructive and also yields a thickness value close to that obtained directly from transmission electron micrographs. The excess thickness, over the expected figure, obtained from the TEM method appears to be due to the presence of unreacted crystallites of silicon within the well-defined B-IMPLOX layer.

In the absence of an infra-red pyrometer, the substrate temperature during implantation was estimated, by comparing the temperature-dependent absorption peak position in as-implanted infra-red spectra with those obtained at each anneal step from an isochronally-annealed sample initially

implanted at near room temperature. For a beam current of 10 - 12 μA at 400 keV a substrate temperature of ~ 550°C was estimated.

A degradation of the surface crystallinity by high dose implantation was qualitatively assessed by the appearance of surface haze when viewed obliquely with a strong focussed white light illumination. Samples implanted at ~ 275°C and at lower temperatures had a hazy/milky surface indicating a degradation. The ~550°C implant had an almost haze-free surface. This indicated that a fair degree of surface crystallinity had been retained. Good quality epitaxial layers were deposited on these substrates implanted at ~550°C. With experience, this technique in conjunction with infra-red absorption could be used for assessing the suitability of a substrate for subsequent epitaxial deposition.

In the back-scattering experiments no channelling was observed in samples implanted at room temperature, ~ 200°C and ~275°C in the as-implanted and annealed states. The as-implanted ~550°C samples showed good channelling yielding a χ_{min} of 0.12 - 0.16 with further improvement to 0.05 - 0.07 upon annealing. Epitaxial layers deposited on ~200°C and ~275°C implants produced channelling spectra. The layer deposited on the

$\sim$ 275°C implant yielded a lower value of χ_{min}. A very low-channelled yield was obtained from the epitaxial layer deposited on substrates implanted at ~550°C, the spectrum being identical to that of epitaxial layers on unimplanted substrates. The corresponding value of χ_{min} was 0.03.

Reflection electron diffraction patterns obtained from the epitaxial layers on the ~550°C implants were identical to those from layers on unimplanted substrates. However, pyramidal overgrowths and stacking fault density of the order of $\sim 1 \times 10^3 . cm^{-2}$ were observed. Epitaxial layers deposited on the ~200°C and ~275°C implant showed a high incidence of growth twins.

Transmission electron micrographs of cross-sectional samples showed the presence of a reasonably well-defined dark-band of thickness ~0.38 μm most probably corresponding to the buried implanted oxide. On either side of this implanted oxide there were heavily damaged layers, the one above the oxide being ~ 0.19 μm thick and the layer below the oxide being ~0.32 μm thick. The corresponding damage peaks, in the back-scattered channelled spectra, particularly the one from the upper interface provide a qualitative assessment of the extent of the damage. The transmission electron micrographs also showed a high density of dislocations $\sim 5 \times 10^8 . cm^{-2}$, originating from the damaged layer above the buried oxide, and a small number of stacking faults were observed in the area examined.

X-ray topography provided a non-destructive technique for the assessment of defects in the deposited epitaxial layer. The topographs shown in Fig.4.47 mainly reflect the interface damage. Contrast arising from the pyramidal overgrowths and stacking faults was also observed.

CHAPTER 5

ELECTRICAL CHARACTERISTICS AND DEVICE STRUCTURES

5.1 Introduction

The main objective of this study was the optimization of implant and anneal parameters in respect of the retention of material characteristics suitable for epitaxial deposition. However, for the sake of completeness, the observed electrical characteristics of the structure are described briefly in this chapter. All the results quoted here relate to an implant dose of 1.4×10^{18} $O^+.cm^{-2}$ at 200 keV. The substrate temperature in all cases was $\sim 550^{o}C$. The following were investigated :

1. Spreading resistance of the B-IMPLOX/EPI structure.
2. I-V characteristics of the B-IMPLOX layer.
3. Characteristics of p-n junction diodes fabricated in an epitaxial layer deposited on a B-IMPLOX substrate.
4. Carrier lifetime from measured storage time of the diodes.

A detailed study of the B-IMPLOX I-V, junction diode and MOST characteristics is reported by Shorthouse[159].

5.2 Spreading Resistance

Spreading resistance measurements were obtained using a Solid State Measurements ASR-100 Automatic Spreading Resistance System.* The samples were bevelled at an angle of $2^{o}53'$, thus giving a depth of 0.125 μm per sampling point for a lateral step of 2.5 μm along the bevel. The plots, a typical example of which is shown in Fig.5.1, show the presence of a

*Work carried out by J F Sheridan, Harris Semiconductor Products Division, Melbourne, Florida.

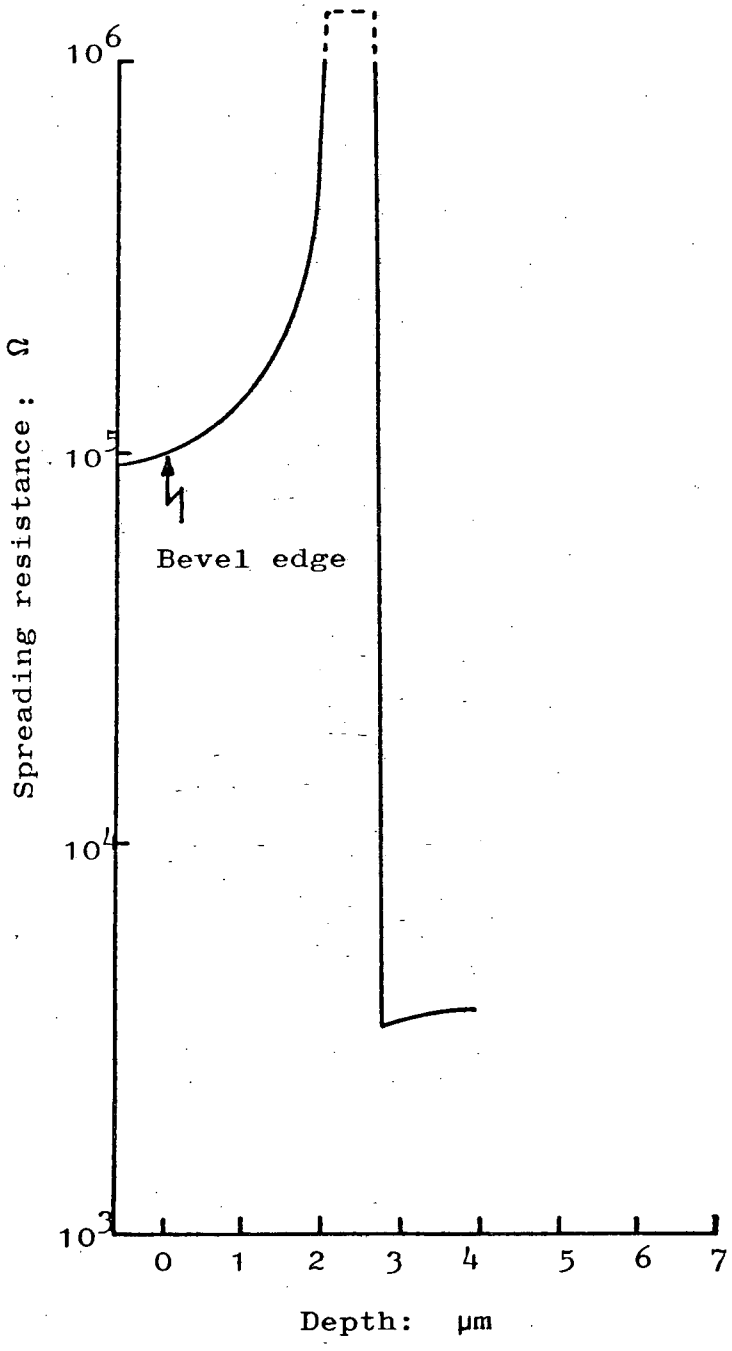

Fig. 5.1. Spreading resistance of the B-IMPLOX-EPI structure.

layer ~0.65 μm in thickness of extremely high resistivity. This thickness figure agrees well with the observed total thickness of 0.69 μm of the B-IMPLOX and associated damaged layers (see section 4.9.1).

5.3 I-V Characteristics

An implanted wafer was annealed at 550°C for 8 hours and at 1150°C for 2 hours both in nitrogen ambients. Mesa structures were formed in the relatively oxygen-free re-crystallized surface layer by plasma etching the silicon down to the oxide using photoengraved aluminium dots of 100 μm diameter as the mask. The B-IMPLOX layer appeared to be highly resistant to plasma etching. It was not removed by repeated exposure to the plasma. I-V curves for connections (a) between mesas and substrate back contact and (b) between neighbouring mesas are shown in Fig. 5.2.

Taking a current of 0.1 μA as a definition of breakdown, voltages in the range 5-13V were obtained from mesa to substrate. This is equivalent to a resistivity of $\sim 2.5 \times 10^{8}$ Ωcm just before breakdown at 10V. Similarly, isolation at 25 V was obtained for adjacent mesas spaced 100 μm apart.

Subsequently, it was discovered that due to a suspected error in dosimetry, the substrates used in the electrical measurements, including this experiment, had been implanted with a lower dose of $\sim 1.0 \times 10^{18}$ $O^{+}.cm^{-2}$. Significant improvement in the isolation characteristics was observed in subsequently processed substrates.(159)

5.4 Diode Characteristics

Diodes of circular geometry, shown schematically in Fig.5.3, were fabricated in a 0.75 μm thick epitaxial layer. Boron and phosphorus were predeposited and diffused to a depth

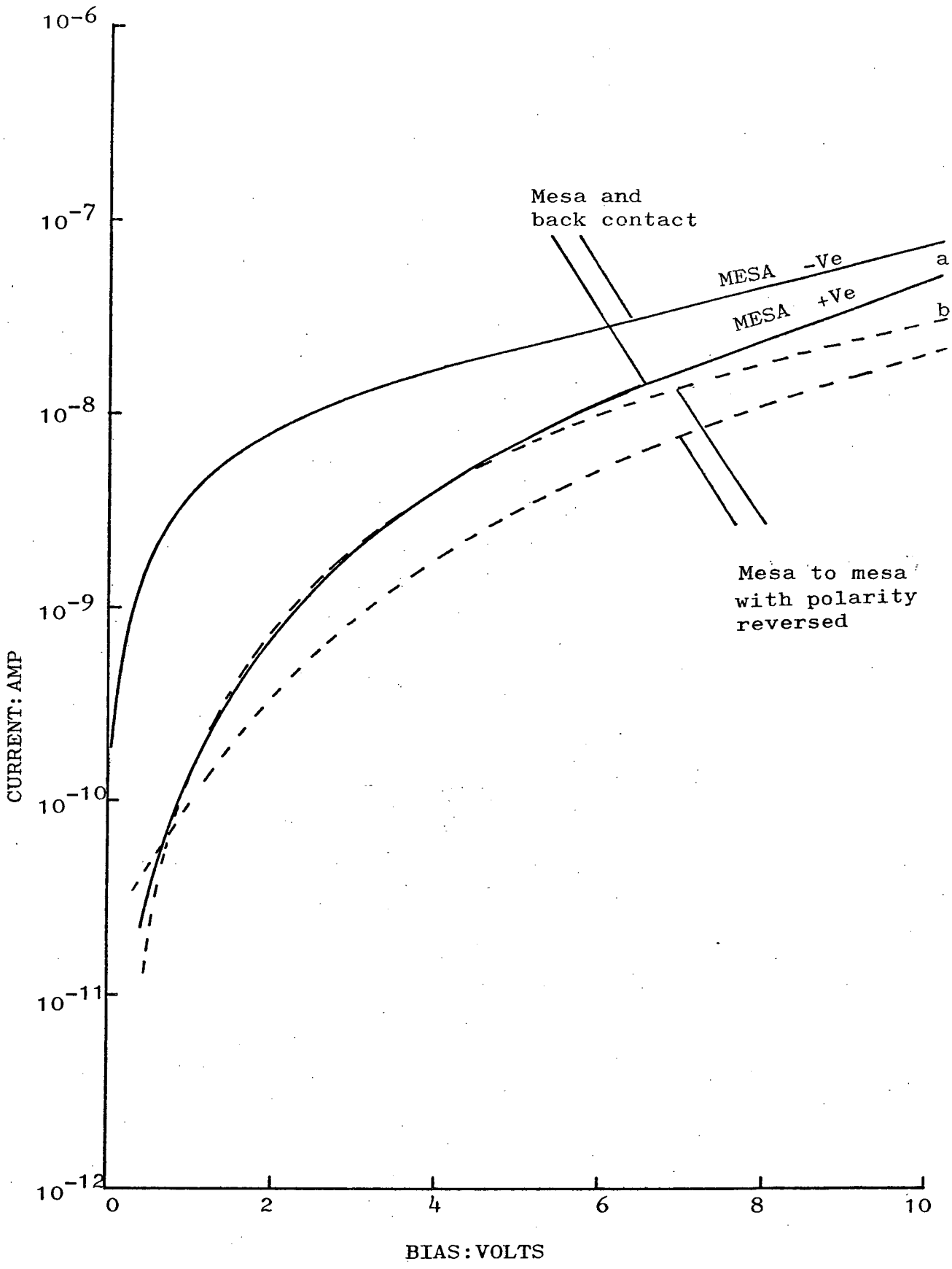

Fig. 5.2. I-V characteristics of the B-IMPLOX layer
(a) Between mesas and substrate back contact;
(b) Between neighbouring mesas.

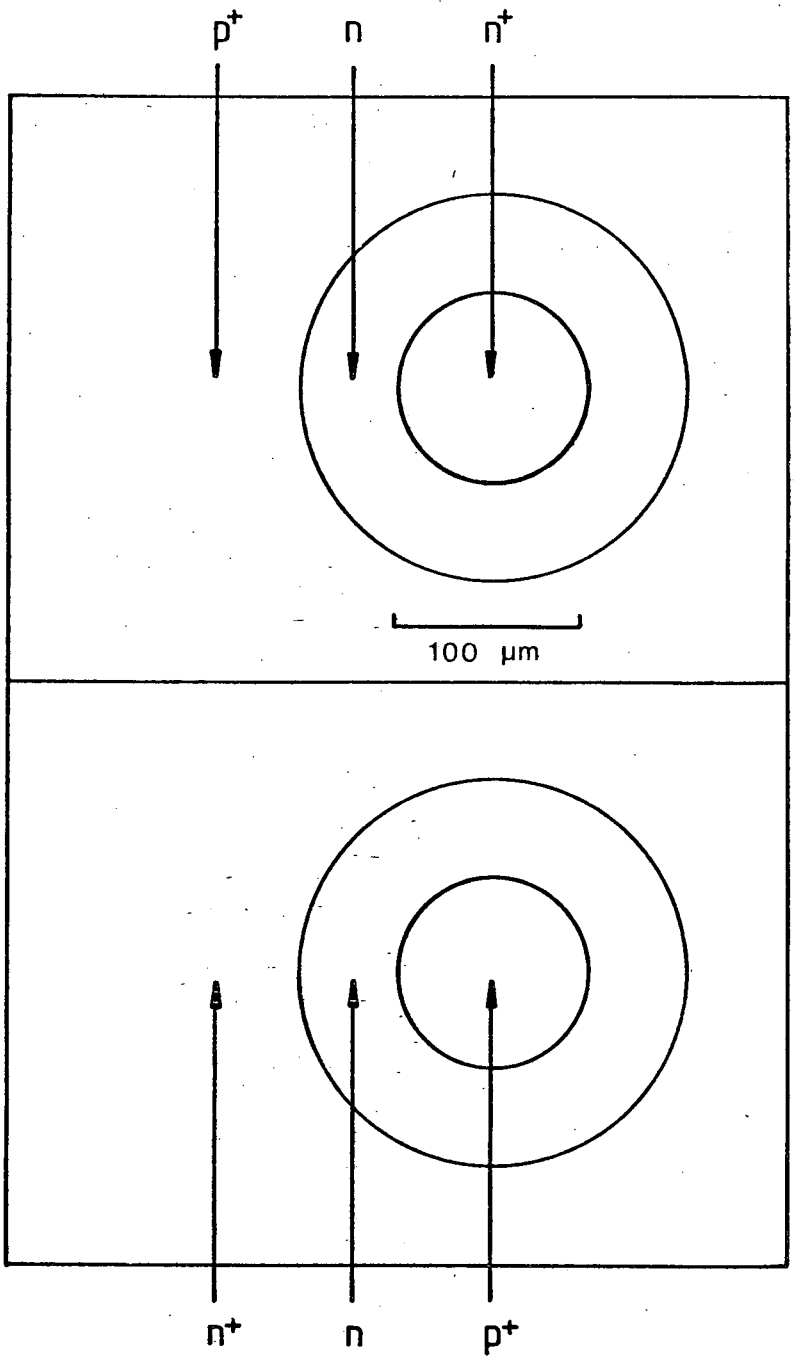

Fig. 5.3. Geometry of the diodes fabricated in the deposited epitaxial layer.

equal to the total silicon thickness (epi + surface silicon) i.e. down to the B-IMPLOX layer.

I-V characteristics of these diodes are shown in Fig.5.4. The diodes in the implanted area start to conduct at a lower forward bias than those in the unimplanted area. The reverse leakage currents in both implanted and unimplanted areas are identical to a bias of 50V. The diode in the implanted area shows a subsequent soft breakdown, whereas the one in the unimplanted area has a sharp breakdown at 100V.

The n^+ diffused areas in the implanted region show reasonable isolation from the substrate comparable to that between the mesa and the substrate (described above), whereas the p^+ areas do not exhibit any isolation whatsoever. A similar effect has been observed in oxygen implanted GaAS [160]. This observation has so far not been explained, but may be due to hole injection into the oxide.*

5.5 Lifetime Measurement

Minority carrier lifetimes, τ , were calculated from the measured storage times, t_s, under linear ramp switching of the above diodes. The following relations hold for various ramp rates R_R [161] :

(1) $t_s = \tau$ when $R_R << I_f/\tau$

(2) $t_s = 0.796\tau$ when $R_R \approx I_f/\tau$

(3) $t_s = 0.7\tau$ when $R_R >> I_f/\tau$

where I_f is the forward current. The condition (2) above is the most convenient to use for lifetime determination, since in this case I_f is the peak reverse current $I_{r_{max}}$, and the lifetime is given by $\tau = 1.25\ t_s$.

---

* (Suspected to be related to the low dose involved, see Sec.5.3).

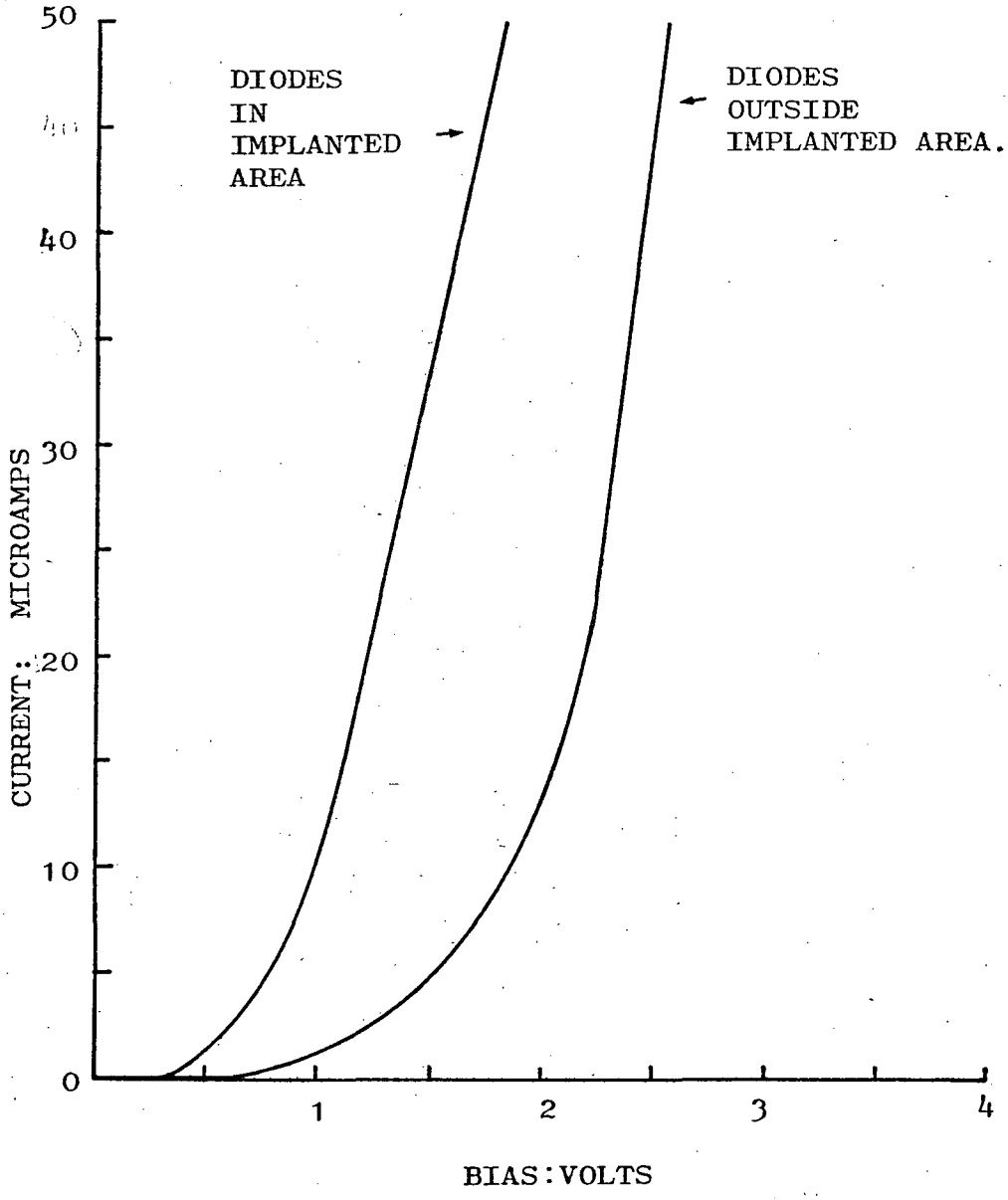

Fig.5.4(a). Diode forward characteristics.

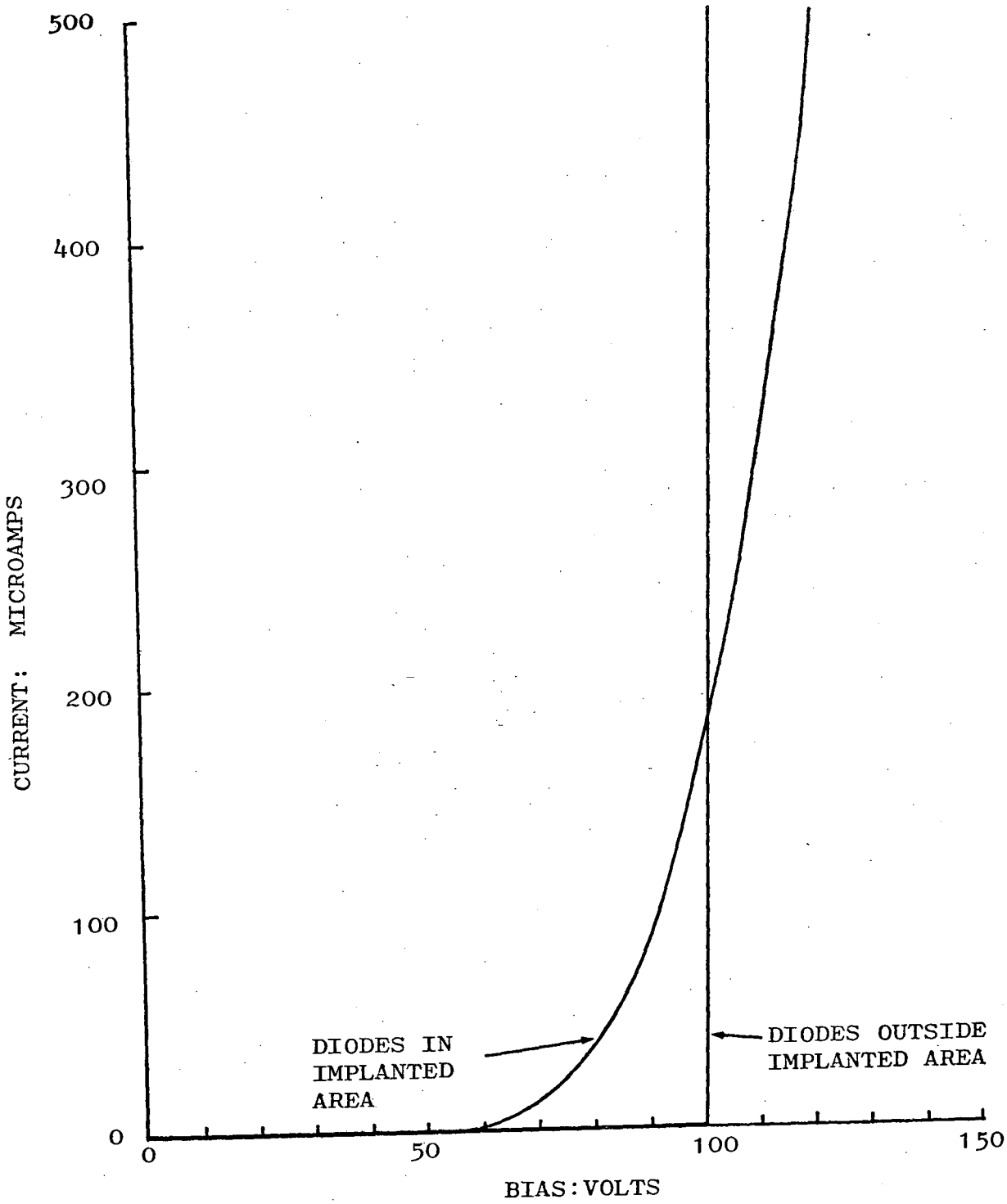

Fig. 5.4(b). Diode reverse characteristics.

The simple arrangement[162], shown in Fig.5.5. was used for measuring the storage time. A negative-going pulse was selected to reverse-bias the diode. The forward bias was obtained by adjusting the offset control which determined the zero-level of the pulse. A current of 0.25 mA ($I_f = I_{r_{max}}$) was obtained with a bias resistor of 10 KΩ and a ramp rate of 2.5×10^2 $A.sec^{-1}$. The CRO traces corresponding to diodes inside and outside the implanted area are shown in Fig.5.6. Lifetime values of 1.25 μs in the implanted area are obtained as opposed to 1.75 μs in the unimplanted area of the substrate. These figures indicate that the lifetime is only marginally degraded in the implanted area, in spite of the observed high defect density of $\sim 5 \times 10^8$ cm^{-2}. (See section 4.9.1.)

5.6 Device Applications of the B-IMPOX/EPI Structure.

Device structures and characteristics which may serve as application areas for IMPLOX are described in this section. This will indicate the potential of the buried implanted oxide along with the deposited epitaxial layer.

5.6.1. N-channel MOS transistor

Lam et al reported the characteristics of an n-channel MOS transistor fabricated in an undoped epitaxial layer[114].

The B-IMPLOX was formed by the implantation of O_2^+ ions to a dose of 6×10^{17} cm^{-2} at 300 keV in 6-8 Ωcm p-type (100) substrates. This dose and energy combination has the same effect as a dose of 1.2×10^{18} $O^+ ions.cm^{-2}$ at 150 keV as used earlier by Izumi, Doken and Ariyoshi[115] (see following section). During implantation the substrate was heated, apparently to a temperature of ~200°C. (The real temperature is suspected to have been much higher, see section 4.5.3.). The substrates were annealed at 750°C for 8 hours followed by 2 hours at 1150°C, both in nitrogen ambients. A B-IMPLOX

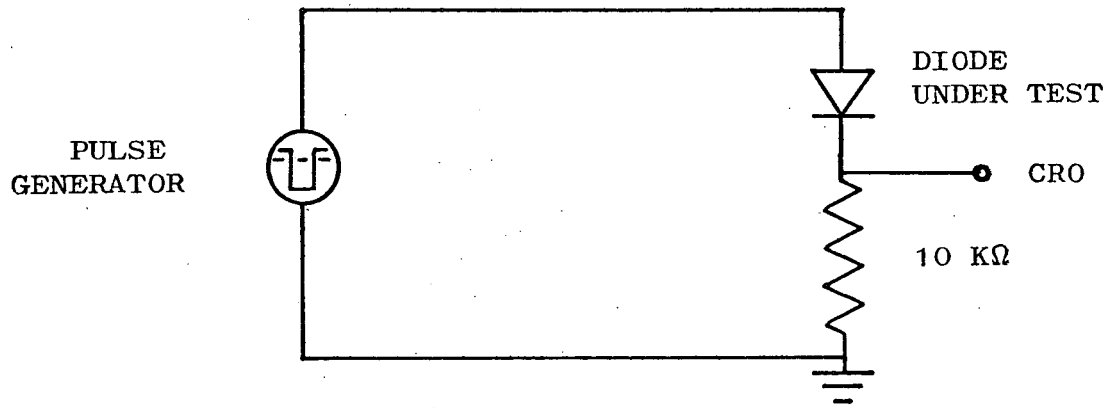

Fig. 5.5. Circuit arrangement used for storage time measurement.

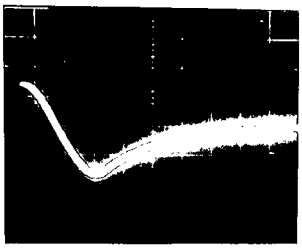

2v
1μs

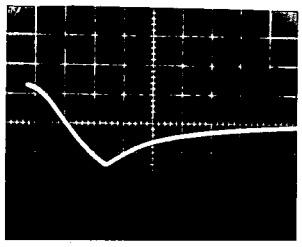

DIODE IN
IMPLANTED AREA

DIODE OUTSIDE
IMPLANTED AREA

Fig. 5.6. Observed storage times.

layer thickness of ~0.25 μm centred at a depth of ~0.38 μm below the surface was obtained.

A self-aligned phosphorus doped polysilicon gate process was used. The source and drain regions were implanted with arsenic. The gate oxide was 0.11 μm thick. The threshold was adjusted by the implantation of boron. The devices had a channel length of 75.6 μm and width of 1121 μm. A threshold voltage of 1.34V was observed. The value of surface electron mobility between 480 $cm^2/V.s$ and 710 $cm^2/V.s$ was obtained. A minimum leakage current of ~10 pA per micron channel width was obtained with a V_{DS} of 2V. The minimum sub-threshold current did not vary with substrate bias, but the threshold voltage was affected. This observation was interpreted as an indication that the IMPLOX-surface silicon interface did not affect the minimum leakage current.

5.6.2 CMOS Devices

CMOS type devices in the B-IMPLOX/EPI structure were the first to be reported by Izumi, Doken and Ariyoshi[115]. The term SIMOX for the Separation by IMplanted OXygen was used to describe the 'technology'.

The B-IMPLOX was formed by implanting $^{16}O^+$ to a dose of 1.2×10^{18}. cm^{-2} at an energy of 150 keV. An IMPLOX layer thickness of 0.21 μm centred at a depth of 0.38 μm was formed. Implanted substrates were annealed at a temperature of 1150°C for 2 hours in a nitrogen ambient. A 600Å layer of thermal oxide was grown and completely etched prior to epitaxial deposition.

A 19-stage CMOS ring oscillator was fabricated in the epitaxial layer. The cross-section of the devices is shown in Fig. 5.7. The gate oxide thickness was 700Å and the thickness of the active silicon was 0.5 μm. The p MOS devices had an aspect ratio, W/L, of $60/5$, whereas the n MOS had a ratio

Parameters of the structure

B-IMPLOX thickness	:	0.21 μm
Gate oxide thickness	:	0.07 μm
Epi-layer thickness	:	0.5 μm
Substrate conc.	:	$1.0 \times 10^{13}.cm^{-3}$
Channel length	:	5.0 μm
Channel width	:	30 - 60 μm

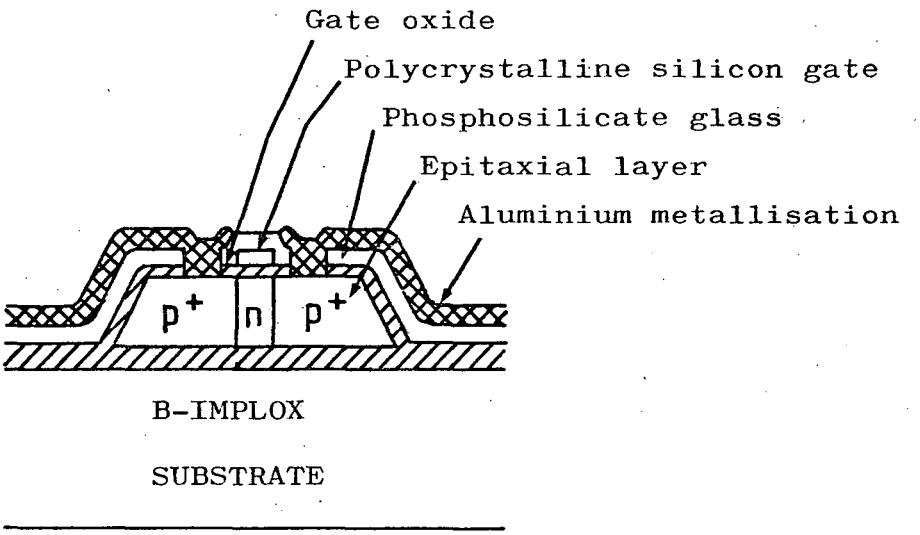

Fig.5.7. Structure of(C)MOS devices fabricated in the epitaxial layer deposited on the substrates with B-IMPLOX layer.(115)

of $^{30}/_{5}$. Threshold voltages of -1.3V and +1.4V were obtained for the p MOS and the n MOS devices respectively.

For a 5V operation a propagation delay of 0.96 ns/stage and a power dissipation of 406 μW/stage were obtained. The speed of operation was about twice as fast as similar devices fabricated in bulk silicon. This increased speed was attributed to the reduction in parasitic capacitance due to the presence of the B-IMPLOX.

5.6.3. High-speed Buried Channel MOS Transistor

Ohwada, Omwia and Sano have reported a high speed, buried channel MOS device[163]. The structure of the device is shown in Fig.5.8.

A 0.47 μm thick B-IMPLOX layer was formed by implanting oxygen to a very high dose (not specified but expected to be $\sim 2 \times 10^{18} O^{+}.cm^{-2}$ at 150 keV) and annealed at a high temperature (not specified). An abrupt interface between the surface silicon and the B-IMPLOX was obtained (Sec.4.6.2.10). The interface charge density was said to be comparable to that of thermally grown oxides.

The device was fabricated using a conventional polysilicon gate MOS process. A p^{+} poly silicon gate was used to obtain a normally-off type operation. A threshold voltage of 0.58V for a drain current of 0.1 μA at 5V was obtained with a device having an aspect ratio of 1. An effective carrier mobility of 750 $cm^2/v.s$ was calculated from the drain conductance. No leakage current was observed in these devices. In submicron MOS transistors fabricated in the B-IMPLOX/EPI structure the threshold voltage shift is much smaller than that in conventional MOS and buried channel MOS devices in bulk silicon. A ring oscillator with 1 μm channel devices had a minimum delay time of 95 ps and a power delay product of 310 fJ at a V_{DD} of 15V.

Parameters of the structure

B-IMPLOX thickness	:	0.47 μm
Gate oxide thickness	:	0.055 μm
Epi-layer thickness	:	0.110 μm
Substrate conc.	:	$1.0 \times 10^{13}.cm^{-3}$
Channel region conc.	:	$1.5 \times 10^{15}.cm^{-3}$
Effective channel length	:	0.7 μm - 5.0 μm
Channel width	:	30 μm

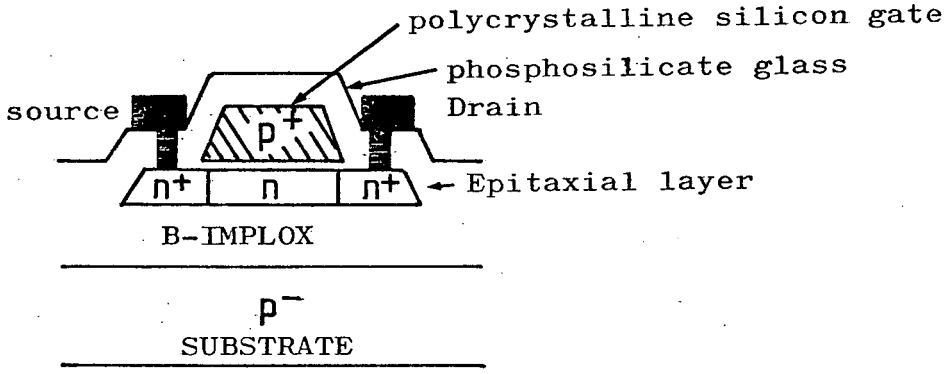

Fig.5.8. A high speed buried channel MOS transistor[163].

5.6.4. High-voltage Buried Channel MOS Transistor

A new offset gate high voltage buried channel MOS device has been reported by Akiya, Ohwada and Nakasima[161]. The structure of the device is shown in Fig.5.9. A process similar to that used for the device described in the previous section was employed.

A 0.53 μm thick B-IMPLOX layer was formed by implanting O^+ ions to a dose of 2.4×10^{18}. cm^{-2} at 150 keV and subsequently annealing at 1150°C for 2 hours. The IMPLOX layer had an average breakdown of 410V, i.e. ~8 $MV.cm^{-1}$.

Using parameters as shown in the Table inset in Fig.5.9 a normally-off buried channel device with a threshold voltage of 0.5V was obtained. For a device with a 10 μm channel and a gate offset of 20 μm a BV_{DS} of 180V was obtained.

This device may be potentially useful for high voltage application and in hybrid integrated circuits including both high voltage and high speed MOS transistors on the same chip.

Parameters of the structure

B-IMPLOX thickness	:	0.53 μm
Gate oxide thickness	:	0.19 μm
Epi-layer thickness	:	0.055 μm
Substrate conc.	:	$1.0 \times 10^{13}.cm^{-3}$
Channel region conc.	:	$1.5 \times 10^{15}.cm^{-3}$
Channel length	:	10.0 μm
Off-set-gate region	:	20 μm

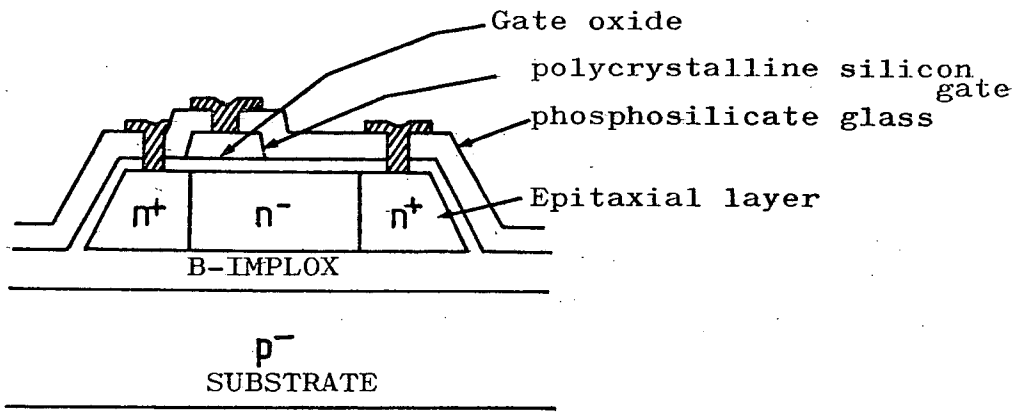

Fig.5.9. A high voltage buried channel MOS transistor(164).

CHAPTER 6

CONCLUSIONS

Buried implanted oxide layers have been formed by high dose implantation of oxygen in silicon. The distribution of oxygen is approximately Gaussian up to doses required to provide the stoichiometric concentration, for the formation of silicon dioxide, at the peak of the distribution. For a given peak concentration, the implanted oxide is buried deeper with increasing energy. The position of the peak, i.e. the projected range, and the standard deviation are in good agreement with computed figures, based on a Gaussian approximation of the LSS projected range distribution, as given by Gibbons, Johnson and Mylroie[103]. At higher doses a box-type distribution, corresponding to a thickness of a stoichiometric silicon dioxide layer, is obtained. This indicates that a given volume of silicon cannot accommodate any more oxygen than that required for the formation of stoichiometric silicon dioxide. The oxide thickness increases with increasing dose of oxygen ions, with the upper interface approaching the substrate surface. The mechanism associated with the transport of the excess implanted oxygen is not clearly understood. A preferential diffusion towards existing nuclei of silicon-oxygen clusters at the upper interface, formed at the early stage of the implantation, is speculated. The degree of interface damage associated with the higher dose implants is lower than that with a dose just sufficient to provide the stoichiometric requirement of oxygen at the peak of the distribution. Other parameters being equal, at higher substrate temperatures the interface damage is reduced.

An anneal treatment is necessary to provide the activation energy for the formation of silicon dioxide and the re-arrangement of bonds. Infra-red absorption characteristics

of implanted oxides annealed at a temperature of 1000°C or above for sufficiently long times (e.g. 5 min. at 1100°C) are almost identical to oxides grown thermally in dry oxygen ambients.

At a high dose of the order of 10^{18} $O^+.cm^{-2}$ considered here, the surface layer is totally amorphized if implanted into substrates held at near room temperature. Once amorphized the surface layer cannot normally be recrystallized, as the crystalline continuity between the surface and the single crystal substrate is lost due to the presence of the implanted oxide layer which is very likely to be amorphous. With a dose of 1.4×10^{18} $O^+.cm^{-2}$ at 200 keV, a good degree of surface crystallinity is retained if the implantation is carried out at an elevated temperature of ~550°C. A short anneal treatment at 1100°C further enhances the crystallinity allowing a subsequent epitaxial deposition. A high density of dislocations originating from the interface damage and some stacking faults are present in the epitaxial layer. In substrate implanted at ~200° and ~275°C a high density of growth twins are initiated by existing recrystallization twins formed during the anneal treatment.

Epitaxial layers deposited on the~550°C implants permit the fabrication of p-n junction diodes with low reverse leakage currents and high breakdown voltages. The minority carrier lifetime in the epitaxial layer on the oxygen implanted area is only marginally degraded from that outside the implanted area.

Further Work

Further work is suggested in the following areas :

1. Direct measurement of the substrate temperature during implantation to establish a 'critical temperature' above which a degree of crystallinity, permitting a subsequent twin-free epitaxial growth, is retained. Any dependence of the 'critical temperature' on the total dose and dose-rate will have to be established. The maximum surface concentration of oxygen compatible with satisfactory epitaxial deposition will also have to be determined experimentally.

2. Optimization of the anneal treatment to minimize the density of interface starts at the B-IMPLOX/EPI interface. It is not certain whether the short anneal treatment of 5 min. at 1100^{o}C achieves this. (See section 3.6.).

3. A study of the mechanisms associated with the saturation in the oxygen concentration under high dose conditions and the associated accumulation at the upper interface. A readioactive tracter technique may provide useful information in this area. Further work is also required for obtaining a modified energy/depth relationship in the RBS spectra.

In obtaining the depth scale from the 'RBS 2' (p.124) programme, it has been assumed that the energy loss and stopping cross-section for helium ions in the composite silicon/B-IMPLOX structure is the same as those in a silicon target. The effect of silicon dioxide on these parameters will have to be taken into account in modifying the energy/depth relationship, Alternative profiling techniques, e.g. AES/ESCA in conjunction with sputter-etching may also be considered.

It is also worth mentioning that variation in the stopping cross-section for oxygen ions will occur when the oxygen concentration approaches that of stoichiometric SiO_2. This leads to a modification of the parameters used in an LSS prediction of the oxygen profile.

4. A study of the mechanism of electrical conduction and diffusion of electrically active impurities through the B-IMPLOX layer.

5. Study of the defects and the observed gettering properties of the epitaxial layer.

6. So far the emphasis has been on the fabrication of MOS type devices (see Chapter 5) for VLSI applications. These devices do not particularly require a material with high minority carrier lifetime. However, the observed

carrier lifetime in the deposited epitaxial layer on substrates with buried implanted oxide layers is about two orders of magnitude higher than that in SOS. Therefore this material should be able to support bipolar and dynamic logic devices etc., in addition to providing dielectric isolation. Further work should be directed in these areas.

7. Study of the relative merits of silane, dichlorosilane and silicon tetrachloride as source chemical and advantages of reduced pressure systems for epitaxial growth on substrates with buried implanted oxides.

8. Development of an implanter capable of producing high oxygen beam currents for increased throughput.

At the present state of development it appears that oxygen implanted silicon with a subsequently deposited epitaxial layer provides a silicon on insulator (SOI) material with a lower density of defects than those produced by other techniques[165]. In strip heater recrystallization, which is another promising technique the possibility of contamination is high[166] and mechanical problems associated with thermal expansion at high temperatures is severe in large wafers. However, oxygen implantation is likely to be a viable technique only with a totally dedicated purpose-built implanter requiring a major capital investment. Only one organisation, so far, is in the process of commissioning such an implanter[167]. Even with the availability of a dedicated machine the cost per chip is likely to be high, largely arising from the very high dose requirement ($\sim \frac{1}{2}$ hour of implantation time per 3" wafer). Alternative SOI technologies when fully developed will no doubt be compared for cost and technical performance.

REFERENCES

(1) K E Bean and W R Runyan
Dielectric isolation: Comprehensive, current and future.
J Electrochem. Soc. Vol. 124, No.1. pp 5C-12C. January 1977.

(2) H M Manasevit, F M Erdmann and A C Thorsen.
The preparation and properties of (111) Si films grown on Sapphire by the SiH_4-H_2 process.
J. Electrochem. Soc. Vol. 123, No.1 pp 52-57.January 1976.

(3)

A E J Boleky.
The performance of complementary MOS transistors on insulating substrates.
RCA Rev. Vol.31, No.2, pp 372-395, June 1970.

B C E Weitzel and R T Smith.
Sapphire substrate misorientation and SOS/MOS transistor performance.
J. Electrochem. Soc. Vol.124, No.7, pp 1080-1086. July 1977.

C C E Weitzel and R T Smith
Silicon-on-sapphire crystalline perfection and MOS transistor mobility.
J. Electrochem. Soc. Vol. 125, No.5 pp 792-798. May 1978.

(4) J L Hutchison, G R Booker and M S Abrahams.
Transmission high-resolution electron microscopy studies of silicon-sapphire epitaxial layer structures.
Microscopy of Semiconducting Materials.
Inst. Phys. Conf. Ser. No.60, pp 139-147. 1981.

(5) M E Roulet, P Schwob, I Golecki and M A Nicolet.
Electrical properties of silicon-implanted furnace-annealed silicon-on-sapphire devices.
Electronics Lett. Vol. 15, No.17, pp 527-529.
16 August 1979.

(6) R S Ronen and P H Robinson.
Hydrogen chloride and chlorine gettering: An effective technique for improving performance of silicon devices.
J. Electrochem. Soc. Vol.119, No.6 pp 747-752. June 1972.

(7) I Golecki.
Furnace and CW Ar induced solid-phase epitaxial regrowth of SOS films implanted Si, Si + B, P and P + B ions.
Proc. 2nd International Conf. on Ion Beam Modification of Materials. Albany, NY. July 1980.

(8) K Imai
A new dielectric isolation method using porus silicon.
Solid-State Electronics. Vol. 24. pp 159-164. 1981.

(9) A Gat, L Gerzberg, J F Gibbons, T J Magee, J Peng and J D Hong.
CW laser anneal of polycrystalline silicon: crystalline structure, electrical properties.
Appl. Phys. Lett. Vol.33, No.8, pp 775-778, 15 October 1978.

(10) J F Gibbons
Beam-recrystallized polysilicon films for integrated circuit applications.
Microscopy of semiconducting materials.
Inst. Phys. Conf. Ser.No.60, pp 431-440, 1981.

(11) T I Kamins and B P Von Herzen.
MOSFET's in electron-beam recrystallized poly-silicon.
IEEE Electron Device Lett. Vol.EDL-2 No.12, pp 313-315.
December 1981.

(12) JCC Fan, M W Geis and B Y Tsaur .
Lateral epitaxy by seeded solidication for growth of single-crystal Si films on insulators.
Appl. Phys. Lett. Vol.38, No.5, pp 365-367. March 1, 1981.

(13) T I Kamins, T R Cass, C J Dell'Oca, K F Lee, R F W Pease and J F Gibbons.
Lateral epitaxial recrystallization of deposited silicon films on silicon dioxide.
J Electrochem, Soc. Vol. 128, No.5, pp 1151-1154. Mary 1981.

(14) M W Geis, D C Flanders and H I Smith.
Grapho-epitaxy of silicon on fused silica using surface micro patterns and laser crystallization.
J Vac. Sci. Tech. Vol.16, No.6, pp 1640-1643.
November/December 1979.

(15) M W Geiss, D A Antomiadis, D J Silversmith, R W Mountain and H I Smith.
Silicon graphoepitaxy using a strip-heater oven.
Appl. Phys. Lett. Vol.37, No.5 pp 454-456.
1 September 1980.

(16) E W Maby, M W Geis, Y L LeCoz, D J Silversmith R W Mountain, D A Antoniadis.
MOSFET's on silicon prepared by moving melt zone recrystallization of encapsulated polycrystalline silicon on an insulating substrate.
IEEE Electron Device Lett. Vol. EDL 2, No.10
pp 241-243. October 1981.

(17) H W Tasch, Jr. T C Holloway, K F Lee and J F Gibbons.
Silicon-on-insulator M.O.S.F.E.T.'s fabricated on laser-annealed polysilicon on SiO_2.
Electron Lett. Vol.15, No.14, pp 435-437.
5th July 1979.

(18) K K Ng, G K Celler, E I Povilonis, R C Frye
H J Leamy and S M Sze.
Effects of grain boundaries on laser crystallized poly-Si MOSFET's.
IEEE Electron Device Lett Vol. EDL2 No.2
pp 316-318 December 1981.

(19) J F Gibbons and K F Lee
One-gate-wide CMOS inverter on laser-recrystallized polysilicon.
IEEE Electron Device Lett Vol. EDL-1 No.6 pp 117-118
1980.

(20) J P Colinge and E Domoulin
A high density CMOS inverter with stacked transistors.
IEEE Electron Device Lett. Vol.EDL-2 No. 10
pp 250-251. October 1981.

(21) R J Dexter, S B Watelski and S T Picraux.
Epitaxial silicon layers grown on ion-implanted silicon nitride layers.
Appl. Phys. Lett. Vol.23, No.8. pp 455-457, 15 Oct. 1973.

(22) M H Badawi and K V Anand.
A study of silicon oxides prepared by oxygen implantation into silicon.
J.Phys. D: App. Phys. Vol.10. pp 1931-1942. 1977.

(23) B M Berry.
'Epitaxy' in Fundamentals of silicon integrated device technology, Vol. 1.
Ed. R M Burger and R P Donovan, Prenctice-Hall Inc.
1967.

(24) J Bloem, L J Giling and M W M Graef.
The Incorporation of phosphorus in silicon epitaxial layer growth.
J Electrochem. Soc. Vol.121, No.10. pp 1364-1361. Oct. 1974.

(25) Y T Lee, N Miyamoto and J Nishizawa.
The lattice misfit and its compensation in the Si-epitaxial layer by doping with germanium and carbon.
J.Electrochem Soc. Vol.122, No.4, pp 530-535. April 1975.

(26) G R Srinivasan.
Autodoping effects in silicon epitaxy.
J. Electrochem Soc. Vol. 127. No.6. pp 1334-1342 June 1980.

(27) A B Phillips
Transistor Engineering p.359
McGraw-Hill Inc. 1962.

(28) A B Glaser and G E Subak-sharpe
Integrated Circuit Engineering p.254.
Addison-Wesley Publishing Company 1977.

(29) B A Joyce
The growth and structure of semiconducting this films.
Reports on Progress in Physics, Vol.37, Part 1.
pp 363-420, 1974.

(30) B A Joyce, J H Neave and B E Watts.
The influence of substrate surface conditions on the nucleation and growth of epitaxial silicon films.
Surface Science 15. pp 1-13, 1969.

(31) B A Joyce, R R Bradley, B E Watts and G R Booker.
A study of nucleation in chemically grown epitaxial silicon films using molecular beam techniques. V. Nucleation kinetic measurements on (100) surfaces.
Phil. Mag. 19, no. 158. pp 403-413. Feb. 1969.

(32) J M Charig and D J Skinner.
Carbon contamination of Si (111) surfaces.
Surface Science 15, pp 277-285. 1969.

(33) B A Joyce, R R Bradley and G R Booker.
A study of nucleation in chemically grown epitaxial silicon films using molecular beam techniques. III. Nucleation rate measurements and the effect of oxygen on initial growth behaviour.
Phil. Mag. Vol.15 No. 138, pp 1167-1187. June 1967.

(34) R J Bennett and R W Gale
Kinetics of the Induction period for the Nucleation of silicon on (111) silicon substrates at U.H.V.
Phil. Mag. Vol.22 No. 175, pp 135-142. July 1970.

(35) M L Hammond
Silicon epitaxy.
Microelectronics J. Vol.10 No.2, pp 4-12. July/Aug. 1979.

(36) Y Avigal and M Schieber
Chemical transport epitaxy of silicon by organic compounds.
J. Electrochem. Soc. Vol. No.12, pp 1585-1586. Dec.1970.

(37) H M Manasevit, W I Simpson and F M Erdmann
Trimethylstibine as a source of Sb for doping epitaxial Si layers.
J Electrochem. Soc. Vol.232, No.7, pp 967-968, July 1974.

(38) F C Eversteyn, P J W Severin, C H J v.d. Brekel, H L Peak
A stagnant layer model for the epitaxial growth of silicon in a horizontal reactor.
J Electrochem. Soc. Vol.117, No.7, pp 925-931. July 1970.

(39) M L Hammond
Introduction to chemical vapour deposition.
Solid St. Tech. pp 61-65. December 1979.

(40) V S Ban
Chemical processes in vapour deposition of silicon.11.
Deposition from Si Cl_3 H and Si Cl_4
J Electrochem. Soc. Vol.122 No.19, pp 1389-1391.
October 1973.

(41) H C Theuerer
Epitaxial silicon films by the hydrogen reduction of $SiCl_4$.
J Electrochem Soc. Vol.108, No.7, pp 649-653. July 1961.

(42) E G Bylander
Kinetics of silicon crystal growth from $SiCl_4$ decomposition.
J Electrochem. Soc. Vol. 109, No.12 pp 1171-1175.
Dexember 1962.

(43) A M Stein.
The kinetics of epitaxial growth of silicon from the trichlorosilane-hydrogen reduction.
J. Electrochem. Soc. Vol.111. No.4, pp 483-484. April 1964.

(44) A Lekholm.
Epitaxial growth of silicon from dichlorosilane.
J. Electrochem. Soc. Vol. 119, No.8, pp 1122-1123.
August 1972.

(45) D J Delong
Advances in dichlorosilane epitaxial technology.
Solid State Tech. pp 29-34, October 1972.

(46) V S Ban and S L Gilbert.
Chemical Processes in Vapour deposition of silicon. 1.
Deposition from SiH_2Cl_2 and etching by HCl.
J.Electrochem. Soc. Vol.122 No. pp 1382-1388, 1975.

(47) Y S Chiang
Silicon epitaxial growth via dichlorosilane in a barrel reactor.
RCA Rev. Vol.38, pp 500-511, December 1977.

(48) B A Joyce and R R Bradley
Epitaxial growth of silicon from the prolysis of monosilane on silicon substrates.
J. Electrochem. Soc. Vol.110 No.12 pp 1235-1240, Dec. 1963.

(49) S R Bhola and A Mayer
Epitaxial deposition of silicon by thermal decomposition of silane.
RCA Rev. Vol.24, pp 511-522. Dec. 1963.

(50) J Bloem
Trends in the chemical vapour deposition of silicon.
'Semiconductor Silicon 1975 pp 180-190.
Eds. H R Huff R R Burgers
Electrochem. Soc. 1973.

(51) D Richman, Y S Chiang and P H Robinson
Low-temperature vapour growth of homepitaxial silicon.
RCA Rev. Vol.31, pp 613-619, December 1970.

(52) D C Gupta and R Yee
Silicon epitaxial layers with abrupt interface impurity profiles.
J Electrochem. Soc. Vol.116, No.11 pp 1561-1565, 1969.

(53) K Das, E Franks, K V Anand
A small scsle silicon epitaxial film deposition system.
Microelectronics J. Vol.9, No.2 pp 8-12. 1978

(54) J Bloem
Silicon epitaxy from mixtures of SiH_4 and Hcl.
J Electrochem. Soc. Vol. 117, No.11, pp 1397-1401. 1970.

(55) J Bloem, L J Giling, M W M Graef
The incorporation of phosphorus in silicon epitaxial layer growth.
J Electrochem. Soc. Vol.121 No.10, pp 1354-1357.
October 1974.

(56) R Reif, T I Kamins and K C Saraswat
A model for dopant incorporation into growing silicon epitaxial films: I. Theory, II.Comparison of theory and experiment.
J Electrochem. Soc. Vol. 125, No.4, pp 644-660.
April 1979.

(57) R Reif, T I Kamins and K C Saraswat
Transient and study-state response of the dopant system of a silicon epitaxial reactor: Transfer function approach.
J. Electrochem. Soc. Vol. 125, No.11 pp 1860-1866,
November 1973.

(58) J Bloem
Band bending at a growing silicon surface.
"Semiconductor Silicon 1973"
Eds. H R Huff and R R Burgess pp 213-226.
Electrochem. Soc. 1973.

(59) S Prussin and J W Cleland
Application of neutron transmutation doping for production of homogeneous epitaxial layers.
J Electrochem. Soc. Vol.125, No.2 pp 350-352. February 1973.

(60) T Ishii, K Takahashi, A Kondo and K Shirahata.
Silicon epitaxial wafer with abrupt interface by two-step epitaxial growth technique.
J Electrochem. Soc. 122, Vol. No.11 pp 1523-1531.
November 1975.

(61) G R Srinivasan
Autodoping effects in silicon epitaxy.
J Electrochem. Soc, Vol.127, No.6, pp 1334-1342.
June 1980.

(62) G Skelly and A C Adams
Impurity atom transfer during epitaxial deposition of silicon.
J Electrochem. Soc. Vol.120, No.1 pp 116-122.
January 1973.

(63) P H Langer and J I Goldstein
Impurity redistribution during silicon epitaxial growth and semiconductor device processing.
J. Electrochem. Soc. Vol. 121, No.4, pp 563-571.
April 1974.

(64) P H Langer and J I Goldstein
Boron autodoping during silane epitaxy.
J Electrochem. Soc. Vol. 124, No.4, pp 591-598.
April 1977.

(65) M Tabe and H Nakamura
Adsorbed layer model for autodoping mechanism in silicon epitaxial growth.
J Electrochem. Soc. Vol. 126, No.5, pp 822-826. May 1979.

(66) G R Srinivasan
Kinetics of lateral autodoping in silicon epitaxy.
J Electrochem. Soc. Vol. 125, No.1 pp 146-151. January 1978.

(67) C O Bozler
Reduction of autodoping.
J Electrochem. Soc. Vol. 122, No.12, pp 1705-
December 1975.

(68) M Ogirima, H Saida, M Suzuki and M Maki
Low pressure silicon epitaxy.
J. Electrochem. Soc. Vol. 124, No.6, pp 903-908. June 1977.

(69) M J-P Duchemin, M M Bonnet, M F Koelsch
Kinetics of silicon growth under low hydrogen pressure.
J Electrochem. Soc. Vol. 125, No. 4, pp 637-644.
April 1978.

(70) Y Ota.
Si Molecular beam epitaxy (n on n^+) with wide range doping control.
J Electrochem. Soc. Vol. 124, No. 11, pp 1795-1802.
1977.

(71) B J Baliga
Kinetics of epitaxial growth of silicon from a tin melt.
J.Electrochem. Soc. Vol.124, No.10, pp 1627-1631, 1977.

(72) B J Baliga
Liquid phase epitaxial silicon diodes: N-epitaxial layers on boron-doped substrates.
J.Electrochem. Soc. Vol.127, No.5 pp 1168-1172, 1980.

(73) U Cohen and R A Huggins
Silicon epitaxial growth by electrodeposition from molten fluorides.
J.Electrochem. Soc. Vol.123, No.3, pp 381-388, 1976.

(74) S S Lau, J W Mayer and W Tseng
Solid phase epitaxial growth of Si and Ge
Handbook on Semiconductors. Ed T S Moss and S P Keller pp 531-562. North-Holland Publishing Company, 1980.

(75) J E Davey, A Christou and H M Day
Solid phase epitaxial studies using vacuum deposition on heated silicon substrates.
Appl. Phys. Lett. Vol.28, No.7, pp 365-367. April 1976.

(76) A Christou, J E Davey and W Tseng
Cyrstalline defects in solid phase epitaxy Si films deposited at elevated temperatures.
Appl. Phys. Lett. Vol. 32, No.10, pp 683-685, 15 May 1978.

(77) P H Lee, M T Wawk, R S Rosler and W C Benzing
Epitaxial pattern shift comparison in vertical, horizontal and cylindrical reactor geometrics.
J.Electrochem. Soc. Vol. 124, No.11, pp 1824-1826, 1977.

(78) H Koyawa D B Wittry and T Kato
Propagation of residual dislocations during silicon epitaxy.
J.Appl. Phys. Vol. 46, No.7, pp 2899-2902, July 1975.

(79) R A Moline, R Leiberman, J Simpson and A U MacRae
The growth of high quality epitaxial silicon over ion implanted buried arsenic layers.
J.Electrochem. Soc. Vol. 121, No.10, pp 1362-1366, October 1974.

(80) J Nishizawa, T Teraski, K Yagi and N Miyamoto
Perfect crystal growth of silicon by vapour deposition.
J.Electrochem. Soc. Vol. 122, No.5, pp 664-669, May 1975.

(81) W R Runyan
Semiconductor measurements and Instrumentation
p.199, McGraw-Hill Book Company, 1975.

(82) P F Kane and G B Larrabee
Characterization of semiconductor Materials.
p.169, McGraw-Hill Book Company 1970.

(83) G R Booker and R Stickler
Crystallographic imperfections in epitaxially grown silicon.
J.Appl. Phys. Vol. 33, No.11, pp 3281-3290. November 1962.

(84) G A Rozganyi, R P Deysher and C W Pearce
The identification, annihilation and suppression of nucleation sites responsible for silicon epitaxial stacking faults.
J.Electrochem. Soc. Vol.123, No.12, pp 1910-1915, December 1976.

(85) K V Ravi, C J Varker and C E Volk
Electrically active stacking faults in silicon.
J.Electrochem. Soc. Vol. 120, No.4, pp 533-541. April 1973.

(86) R B Marcus, M Robinson, T T Sheng, S E Haszko and S P Murarka.
Electrical activity of epitaxial stacking faults.
J.Electrochem. Soc. Vol. 124, No.3, pp 425-430, March 1977.

(87) R Ogden and J M Wilkinson
Characterization of crystal defects at leakage sites in charge-coupled devices.
J.Appl. Phys. Vol.48, No.1, pp 412-414, January 1977.

(88) V G K Reddi and A Y C Yu
Ion implantation for silicon device fabrication.
Solid State Technology, pp 35-41.
October, 1972.

(89) G Carter and W A Grant
Ion implantation of semiconductors. Chapter 7.
Edward Arnold 1976.

(90) A B Glaser and G E Subak-Sharpe
Integrated circuit engineering.
p.221 and Chapter 6. Addidon-Wesley Publishing Company.

(91) H S Rupprecht
New advances in semiconductor implantation.
J. Vac. Technol. Vol.15, No.5, pp 1669-1674.
September/October 1979.

(92) M Watanabe and A Tooi
Formation of SiO_2 films by oxygen-ion bombardment.
Jap. J.Appl.Phys. Vol. 5, No. pp 737-738, 1966.

(93) J H Freeman
Proc. Eur. Conf. on Ion Implantation, Raading 1970.
p.74. P. Peregrinus, Hitchin 1974.

(94) P V Pavlov and E V Shitova
The structure of oxide films obtained by oxygen ion bombardment of a silicon surface.
Sov. Physc. - Dokl., Vol.12, No.1, pp 11-13, July 1967.

(95) J Dylewski and M C Joshi
Formation of thin SiO_2 films by high dose oxygen ion implantation into silicon and their investigation by I R techniques.
Thin Solid Films, Vol. 35, No. pp 327-336, 1976.

(96) J Dylewski and M C Joshi
Thin SiO_2 films formed by oxygen ion implantation in silicon: Electron microscope investigations of the $Si-SiO_2$ interface structures and their C-V characteristics.
Thin Sold Films. Vol. 37, No. pp 241-248, 1976,

(97) J Dylewski and M C Joshi
The Dielectric breakdown properties and I-V characteristics of thin SiO_2 films formed by high dose oxygen ion implantation into silicon.
Thin Sold Films Vol. 42, No. pp 227-235, 1977.

(98) K I Kirov, F D Atanasova, S P Alexandrova, B G Amov and A E Djakov.
Properties of SiO_2 films formed by oxygen implantation into silicon.
Thin Solid Films. Vol. 48, No. pp 187-192, 1978.

(99) S S Gill and I H Wilson
Rutherford back scattering analysis of oxide layers formed by ion implantation into single crystal silicon.
Thin Solid Films, Vol. 55, No. pp 435-448, 1978.

(100) A D Yadav and M C Joshi
Formation of thin Si_3N_4 films by nitrogen ion implantation into silicon.
Thin Solid Films, Vol. 59, No. pp 313-317, 1979.

(101) P H Rose and A R Kirkpatrick.
Formation of oxide and nitride layers on silicon by dose implantation.
Presented at the Intl. Workshop on Ion-based Techniques for Film Formation, Tokyo, 2-3 June 1981.

(102) J F Gibbons
Ion implantation in semiconductors - Part I: Range distribution theory and experiments.
Proc. IEEE, Vol.56, No.3, pp 295-319, March 1968.

(103) J F Gibbons. W S Johnson and S W Mylroie
Projected range statistics: Semiconductor and related materials.
Dowden, Hutchinson and Ross, Inc. 1975.

(104) J F Gibbons
Ion implantation in semiconductors - Part II:
Damage production and annealing.
Proc. IEEE, Vol.60, No.9, pp 1062-1096. September 1972.

(105) B L Crowder, R S Title, M H Broadsky and G D Petit
ESR and optical absorption studies of ion-implanted silicon.
App. Physic. Lett. Vol.16, No.5, pp 205-208. 1 March 1970.

(106) B L Crowder
The influence of the amorphous phase on ion distribution and annealing behaviour of group III and V ion implanted in silicon.
J.Electrochm. Soc. Vol. 118, No.6, pp 943-952. June 1971.

(107) F F Morehead and B L Crowder
A model for the formation of amorphous Si by ion bombardment.
Radiation effects, Vol. 6, No. pp 27-32, 1970.

(108) F F Morehead and B L Crowder and R S Title.
Formation of amorphous silicon by ion bomardment as a function of ion, temperature and dose.
J.Appl. Phys. Vol.43, No.3, pp 1112-1118, March 1972.

(109) J R Dennis and E B Hale
Energy dependence of amorphizing implant dose in silicon.
Appl. Phys. Lett. Vol.29, No.9, pp 523-524. November 1976.

(110) J W Mayer, L Eriksson and J A Davies
Ion implantation in semiconductors.
Academic Press, 1970.

(111) H J Stein, F L Vook, D K Brice, J A Borders and S T Picraux.
Infra red studies of crystallinity in ion-implanted Si.
Proc. 1st Internl. Conf. Ion Implantation.
Ed. L Chadderton and F Eisen, pp 17-24,
Gordon and Breach 1971.

(112) P Capper, A W Jones, E J Wallhouse and J W Wilkes
The effects of heat treatment on dislocation-free oxygen-containing silicon crystals.
J.Appl.Phys. Vol. 48, No.4, pp 1646-1655. April 1977.

(113) H Ming Liaw
Oxygen and carbon in Czochralski-grown silicon.
Microelectronics Journal, Vol.12, No.3, pp 33-36, 1981.

(114) H W Lam, R F Pinizzotta, H T Yuan and D W Bellavance
Characteristics of MOSFETs fabricated in silicon-on insulator material formed by high-dose oxygen ion implantation.
Electron. Lett. Vol.17, No.10, pp 356-358, 14 May 1981.

(115) K Izumi, M Doken, H Ariyoshi,
C MOS devices fabricated on buried SiO_2 layers formed by oxygen implantation into silicon.
Electron. Lett. Vol. 14, No.18, pp 593-594.
31 August 1978.

(116) S S Gill
Ion implnatation machines.
Internal report, Dept. Electronic and Electrical Engineering, University of Surrey, 1978.

(117) P J Cracknell, M Gettings and K G Stephens.
Use of low-energy accelerators for ion implantation.
Nucl.Instr. Vol. 92, No.4, pp 465-469. April 15,1971.

(118) L E Collins, P A O'Connell, J G Perkins, F R Powlet and P T Stroud.
Effects produced by bombardment and implantation into thin films and surfaces.
Nucl. Instr. Vol. 92, No.4, pp 455-459, April 1971.

(119) P E Freeland
Oxygen precipitation in silicon at 650°C.
J.Electrochem. Soc. Vol.127, No.3, pp 754-756.
March 1980.

(120) W Kaiser, H L Fresch and H Reiss
Mechanism of the formation of donor states in heat-treated silicon.
Phys. Rev. Vol.112, No.5, pp 1546-1554, December 1, 1958.

(121) V H Garski
I-r studies on the structure of annealed silicon oxide evaporated films.
Naturforsch, Vol. 19A, pp 1219-1225, 1964.

(122) Csepregi, W K Chu, H Muller, J W Mayer and T W Sigmon.
Influence of thermal history on the residual disorder in implanted 111 silicon.
Radiation Effects, Vol.28, pp 227-233, 1976.

(123) S S Lau
(University of California, San Diego, CA 92093)
Private communication, May 1981.

(124) K Uda and M Kamoshida
Annealing charactieristics of highly P^+ - ion - implanted silicon crystal - two - step anneal.
J.Appl. Physc. Vol.48, No.1, pp 18-21, January 1977.

(125) C Feldman and R Plachy
Vacuum deposited silicon devices on fused silica substrates.
J.Electrochem. Soc. Vol. 121, No.5, pp 685-688, May 1974.

(126) H Kressel , P Robinson, S H McFarlane,
R V D'Aiello and V L Dalal
Epitaxial silicon p-n junctions on polycrystalline "ribbon substrates.
Appl. Phys. Lett. Vol.25, No.4, pp 197-199,
15 August 1974.

(127) C Daey Onwens and H Heijligers
Recrystallization processes in polycrystalline silicon.
Appl. Phys. Lett. Vol.26, No.10, pp 569-571
15 May 1975.

(128) W J H Schins, J Bezemer, H Holtrop, S Radelaar.
Recrystallization of polycrystalline CVD grown silicon.
J.Electrochem.Soc. Vol.127, No.5, pp 1193-1199
May 1980.

(129) G Hass and C D Salzberg
Optical properties of silicon monoxide in the wavelength region from 0.24 to 14.0 microns.
J.Opt. Soc. Am. Vol.44, No.3, pp 181-187, March 1954.

(130) L E Howarth and W G Spitzer
Infra red properties of silicon monox and evaporated SiO films.
J.Am. Ceramic Soc. Vol.44, No.1, pp 26-28
January 1961.

(131) K Das, J Butcher and K V Anand
Silicon/oxide/Silicon structure by oxygen implantation and epitaxy for dielectric isolation in ICs.
Proc. 8th Intnl. Conf. CVD 1981, pp 427-437.
Ed. J M Blocher Jr, G E Vuillard and G Wahl
Electrochemical Society, Proc. Vol. 81-7, 1981.

(132) L Csepregi, E F Kennedy, S S Lau, J W Mayer and T W Sigmon.
Disorder produced by high-dose implantation in Si.
Appl. Phys. Lett. Vol.29, No.10, pp 645-648.
15 November 1976.

(133) T E Seidel, G A Pasteur and J C C Tsai.
Visible interference effects in silicon caused by high-current-high-dose implantation.
Appl. Phys. Lett. Vol.29, No.10, pp 648-651,
15 November 1976.

(134) S P Murarka, T E Seidel, J V Dalton, J M Mishman and M H Read.
A study of stacking faults during CMOS processing: Origin, elimination and contribution to leakage.
J.Electrochem. Soc. Vol.127, No.3, pp 716-724.
March 1980.

(135) W Kaiser
Electrical and optical properties of heat-treated silicon.
Phys. Rev. Vol.105, No.5, pp 1751-1756, March 15, 1957.

(136) F Matossi
Vibration frequencies and binding forces in some silicate groups.
J.Chem.Phys. Vol.17, No.8, pp 679-685. August 1949.

(137) E R Lippincott, A Van Valkenburg, C E Weir and E N Bunting.
Infra red studies on polymorphs of silicon dioxide and germanium dioxide.
J.Res. Nat. Bureau of Standards, Vol.61, No.1 pp 61-70. July 1958.

(138) R Hanna
Infrared absorption spectrum of silicon dioxide.
J.Am. Ceramic Soc. Vol.48, No.11, pp 595-599, November 1965.

(139) D S Alam and K E G Pitt
The structure of evaporated silicon oxide films and its effect on the electrical and optical properties.
Thin Solid Films, Vol.1, pp 245-254, 1967/68.

(140) P D Parry
Target heating during ion implantation.
J.Vac.Sci.Technol. Vol.13, No.2, pp 622-629, March/April 1976.

(141) Y Wada, H Usui and M Ashikawa
Substrate temperature measurement during ion implantation.
Japanese J. of Appl.Phys. Vol.14, No.9 pp 1351-1356, September 1975.

(142) J W Mayer and B M Ullrich
Material analysis by nuclear back scattering applications.
Chapter 2B, New uses of ion accelerators.
Ed. J F Ziegler, Plenum Publishing Corp. 1975.

(143) J W Mayer and M A Nicolet
Backscattering analysis with MeV ^{4}He ions.
From Material characterization using ion beams.
Ed. J P Thomas and A Cachard
Plenum Publishing Corp. 1978.

(144) D E Davies, E F Kennedy and J P Lorenzo.
Pulse annealing of implanted InP with minimal phosphorus loss.
IEEE Electron Device Lett. Vol. EDL 3, No.1
January 1982.

(145) G W B Ashwell and R Heckingbottom
Interdiffusion of titanium and gold: A comparison of thin films deposited in technical vacuum and ultra high vacuum.
J.Electrochem. Soc. Vol.128, No.3, pp 649-654.
March 1981.

(146) D W Morgan, H Ohno, C E C Wood, L F Eastman and J D Berry.
Ion beam analysis of molecular beam epitaxy.
In AlAs/InGaAs layer structures.
J.Electrochem.Soc. Vol.128, No.11 pp 2419-2424.
November 1981.

(147) R L Ruth and N Schwatz
A Rutherford backscattering analysis of anodic tantalum - titanium oxides.
J.Electrochem.Soc. Vol.123, No.12, pp 1860-1867.
December 1976.

(148) D W Wellby
RBS data collection and analysis.
Internal report Dept. Electronic and Electrical Eng. University of Surrey, 1981.

(149) T Hayashi, H Okamoto and Y Homma
Formation of abrupt interfaces between surface silicon and buried SiO_2 layers by very high dose oxygen ion implantation.
Jpn J. Appl.Phys. Vol.19, No.5, pp 1005-1006, May 1980.

(150) T Hayashi, S Maeyama and S Yashii
TEM, AES and XPS studies of Si layers on buried SiO_2 layer formed by high-dose oxygen ion-implantation.
Jpn J.Appl.Phys. Vol.19, No.6, pp 1111-1116, June 1980.

(151) J S Halliday
Reflection electron microscopy
in 'Techniques for electron microscopy' Ed. D H Kay pp 525-545, Blackwell Scientific Publications 1965.

(152) L E Murr
Electron optical applications in materials science.
pp 223-302. McGraw-Hill Book Company 1970.

(153) J Fletcher, J M Titchmarsh and G R Booker
Experimental procedures for preparing 90^{o} cross-section and 1^{o} angle TEM specimens of semiconducting materials.

(154) M H Loretto and R E Smallman
Defect analysis in electron microscopy
Chapman and Hall, 1976.

(155) K Das, J B Butcher, M C Wilson, G R Booker
D W Wellby, P L F Hemment, K V Anand.
RBS and TEM studies of silicon/oxide/silicon structures formed by oxygen implantation and epitaxy.
Microscopy of Semiconducting Materials, 1981.
Inst. Phys. Conf. Ser. No.60, pp 307-312, 1981.

(156) P F Kane and G B Karrabee
Characterization of semiconductor materials.
pp 182-187, McGraw-Hill Book Company 1970.

(157) J M Walls
'Methods of surface analysis'. Short course notes.
Dept. of Physics. Loughborough University of Technology. March 1980.

(158) W Runyan
Semiconductor measurements and instrumentation.
pp 259-261, McGraw-Hill Book Company, 1975.

(159) G P Shorthouse.
M.Sc. Dissertation.
Middlesex Polytechnic, 1982.

(160) H Beneking, N Grote, H Kratle
On the behaviour of buried oxygen implanted layers in highly doped GaAs.
Solid-State Electronics, Vol.22, pp 1039-104, 1979.

(161) Y C Kao and J R Davis
Correlation between reverse recovery time and lifetime of p-n junction driven by a current ramp.
IEEE Trans. E.D. Vol. ED 17, No.9, pp 652-657.
September 1970.

(162) K Das
M.Phil. Thesis, Hatfield Polytechnic, 1977.

(163) K Ohwada, Y Omwra and E Sano
A high-speed buried chennel MOSFET isolated by an implanted silicon dioxide layer.
IEEE Trans.ED. Vol. ED 28, No.9, pp 1084-1087.
September 1981.

(164) M Akiya, K Ohwada, S Nakashima.
High-voltage buried-channel MOS fabricated by oxygen implantation into silicon.
Electronics Lett. Vol.17, No.18, pp 640-641.
3 September 1981.

(165) R F Pinizzotto.
Microstructural defects in laser recrystallized, graphite strip heater recrystallized and buried oxide silicon-on-insulator systems.
Presented at the Electronic Materials Conference, Fort Collins, Colorado, June 1982.

(166) B-Y Tsaur
(Lincoln Lab., MIT, Lexington, MA 02173).
Private communication, June 1982.

(167) K Izumi.
(MEC Lab., NTT, 3 - 9 - 11 Midori-cho,
Musashino-shi, Tokyo 180, Japan.)
Private communication, June 1982.

APPENDIX 1

PUBLICATIONS ARISING FROM THE PROGRAMME OF STUDY

1. A small scale silicon epitaxial film deposition system.
   With E. Franks and K V Anand.
   Microelectronics Journal, Vol.9, No.2, pp 8-12,
   December 1978.

2. RBS and TEM studies of silicon/oxide/silicon structures formed by oxygen implantation and epitaxy.
   With J B Butcher, M C Wilson, G R Booker, D W Wellby, P L F Hemment and K V Anand.
   Inst. Phys. Conf. Ser. No.60: Section 6, pp 307-312.
   Paper presented at Microsc. Semicond. Mater. Conf. Oxford, 6-10 April 1981.

3. Characteristics of silicon/oxide/silicon structure produced by oxygen implantation and epitaxy.
   With G P Shorthouse, J B Butcher and K V Anand.
   Recent News Paper presented at the Minneapolis, Minnesota, Meeting of the Electrochem. Soc. May 1981.

4. Silicon/oxide/silicon structure by oxygen implantation and epitaxy for dielectric isolation in ICs.
   With J B Butcher and K V Anand.
   Proc. Eighth International Conf. on Chemical Vapor Deposition 1981.
   Electrochem. Soc. Proc. Vol. 81-7. pp 427-437, 1981.

5. Silicon/oxide/silicon structures using high dose oxygen implantation.
   With G P Shorthouse and J B Butcher.
   Paper presented at the Electronic Materials Conference, June 1982. Colorado State University, Fort Collins, Colorado, to be published.